Linear Optics Quantum Computing with single photons from an atom-cavity system

Annemarie Ingrid Holleczek

University College, Oxford

Submitted for the degree of Doctor of Philosophy
Trinity Term 2015

Supervised by
Dr. Axel Kuhn

Clarendon Laboratory
University of Oxford
United Kingdom

Publications

---

* A. Holleczek, A. Aiello, C. Marquardt, and G. Leuchs
Optics Express **19** 9714 (2011).

P. B. R. Nisbet-Jones, J. Dilley, A. Holleczek, O. Barter, and A. Kuhn
New Journal of Physics **15** 053007 (2013).
IOPselect

A. Holleczek, O. Barter, G. Langfahl-Klabes, and A. Kuhn *Proc. SPIE 9377, Advances in Photonics of Quantum Computing, Memory, and Communication VIII* 937709 (2015).

A. Holleczek, O. Barter, A. Rubenok, J. Dilley, P. B. R. Nisbet-Jones, G. Langfahl-Klabes, G. D. Marshall, C. Sparrow, J. L. O'Brien, K. Poulios, A. Kuhn, J. C. F. Matthew
arXiv:1508.03266 (2015). [submitted]

* when still at Max-Planck-Institute for the Science of Light, Erlangen, Germany

Conference Proceedings

---

* A. Holleczek, A. Aiello, C. Marquardt, and G. Leuchs
CLEO EUROPE/EQEC EA_P14 (2011).

A. Holleczek, O. Barter, P. B. R. Nisbet-Jones, J. Dilley, and A. Kuhn
CLEO EUROPE/EQEC IB_4_2 (2013).

Abstract

One of today's challenges to realise computing based on quantum mechanics is to reliably and scalably encode information in quantum systems. Here, we present a photon source to on-demand deliver photonic quantum bits of information based on a strongly coupled atom-cavity system. The source operates intermittently for periods of up to 100 μs, with a single-photon repetition rate of 1 MHz, and an intra-cavity production efficiency of up to 85%. Our ability to arbitrarily control the photons' wavepackets and phase profiles, together with long coherence times of 500 ns, allows to store time-bin encoded quantum information within a single photon. To do so, the spatio-temporal envelope of a single photon is sub-divided in d time bins which allows for the delivery of arbitrary qu-d-its. This is done with a fidelity of > 95% for qubits, and 94% for qutrits verified using a newly developed time-resolved quantum-homodyne measurement technique.

Additionally, we combine two separate fields of quantum physics by using our deterministic single-photon source to seed linear optics quantum computing (LOQC) circuits. As a step towards quantum networking, it is shown that this photon source can be combined with quantum gates, namely a chip-integrated beam splitter, a controlled-NOT (CNOT) gate as well as a CNOT4 gate. We use this CNOT4 gate to entangle photons deterministically emitted from our source and observe non-classical correlations between events separated by periods exceeding the travel time across the chip by three orders of magnitude. Additionally, we use time-bin encoded qubits to systematically study the de- and re-phasing of quantum states as well as the the effects of time-varying internal phases in photonic quantum circuits.

Statement of Originality

This thesis is entirely my own work, except for Chapter 4, which is based on Nisbet [65]. I contributed to these experiments in my first year and the text of the publication was partially written by me. My contribution to this project is published in [66], where I am first author.

I am also first author of [84], from which Section 5.2 and Section 5.3 of Chapter 5 are adapted. The work presented in these two Sections was carried out as a collaborative effort and all authors contributed.

Oxford, October 2015

Annemarie Holleczek

Contents

Chapter 1

Introduction

Feynman's and Deutsch's idea to realise versatile computers and networks with the help of quantum-mechanical systems [1, 2] marked the beginning of a novel research area, namely quantum information science [3, 4]. To process quantum information in physical units, single quantum-mechanical systems are necessary where the quantum information can be produced, manipulated, distributed and stored. The smallest unit of quantum information is the qubit which is a two-state quantum mechanical system being in a superposition of both of these states at the same time. The classical analogue to the qubit is the bit which can only be in one state or the other at the same time.

To manipulate quantum bits of information, a universal set of quantum gates is necessary which acts on one single or more qubits [5]. Single photons commonly act as carriers of quantum information [6, 7, 8] as they are not too strongly susceptible to decoherence. This allows for the transport of information over large distances in free space [9] or in fibre [10]. The information itself can be imprinted on a superposition state of a particular degree of freedom such as for example their polarisation or their photon number in a particular

mode.

In this thesis, we introduce a single-photon source based on a strongly coupled atom-cavity system with which it is possible to encode quantum information in the time domain. As a prerequisite, we show theoretically and experimentally that it is possible to *arbitrarily* shape the spatio-temporal envelope of the single photons emitted from this source. We imprint *time bins* onto each photon directly in the cavity by dividing the photon's spatio-temporal envelope into d separate peaks, putting each photon in a coherent superposition of the respective number of d peaks. Two-peaked photons can be interpreted as time-bin encoded qubits, three-peaked as qutrits and four-peaked as ququads.

Up to 2001, it was believed that the realisation of a quantum gate based on an optical approach would require a nonlinear effect as one quantum state needs to influence the state of another one. Effectively, this means that two single photons need to interact nonlinearly, which is a very weak effect as traditionally, optical nonlinear effects [11] such as for instance second harmonic generation [12] require high-intensity laser pulses containing many photons. In 2001, Knill, Laflamme and Milburn [13] (KLM) discovered that quantum gates can indeed be realised without the necessity of a nonlinear interaction between two single photons. Their approach is based on the use of linear optical elements and the measurement of auxiliary photons which provides for the required nonlinearity. Therefore, this is a *conditioned* version of a quantum gate. For an all-optical KLM quantum computer, deterministic sources of indistinguishable single photons in pure states are required. In addition to the source of quantum bits of information, one only needs beam splitters, phase shifters, and mirrors to process and efficient single-photon detectors, feedback from photo-detector outputs and quantum memories to store quantum information.

The KLM approach is the foundation of the area of research now commonly referred to as linear optical quantum computing (LOQC). To date, several quantum gates have been demonstrated experimentally [14, 15, 16]. However, the scalability of these demonstrations – a feature which is key to constructing real quantum computers [5] – is often limited by the probabilistic nature of the spontaneous parametric down conversion (SPDC) photon sources that are commonly used.

In this thesis, a single-photon source which is intrinsically different from SPDC sources is introduced to linear optics quantum computing. This source produces narrowband photons deterministically from an atom-cavity system with a 200 ns coherence time and a 1 MHz repetition rate. As a step towards quantum networking, it is shown that this photon source can be combined with quantum gates, a chip-integrated beam splitter, a chip-integrated controlled-NOT (CNOT) gate [17] as well as a CNOT4 gate. We use this CNOT4 gate integrated into a photonic chip to entangle our photons, and observe non-classical correlations between events separated by periods exceeding the travel time across the chip by up to three orders of magnitude. Additionally, we use time-bin encoded qubits to systematically study the impact of dephasing of quantum states on the fidelity and errors of photonic quantum circuits. In particular, we evaluate the CNOT functionality for time-bin encoded qubits with various imprinted phases.

In Chapter 2, we focus on the physical and theoretical prerequisites to generate single photons from an atom-cavity system. We discuss different types of photon sources and put our single-photon source into a broader context. Also, we introduce the vacuum-stimulated Raman adiabatic passage (V-STIRAP) used to generate single photons in our experiment. Additionally, we explain how to shape the spatio-temporal envelopes of atom-

cavity photons and how that enables us to encode quantum information in this type of information carrier. Finally, we theoretically investigate the atom preparation in our system, in particular how atoms can be cooled and trapped in a magneto-optic trap (MOT) and how we can make these atoms interact with the cavity to form the strongly coupled atom-cavity system.

We explain the prerequisites to deterministically produce single photons with an arbitrary spatio-temporal envelope from a strongly coupled atom-cavity system in Chapter 3. We discuss the technical details of our experiment, in particular the laser system, the cavity and the cooling and trapping of Rubidium atoms with the help of a MOT as well as their launching with the help of an atomic fountain. Also, we describe how all parts of the experiments need to be put in sync to achieve the overall goal of producing single photons.

Chapter 4 introduces the experimental work. We discuss the production of novel quantum bits of information encoded in the time domain refered to as time-bin encoded photonic qubits, qutrits and ququads. To determine their properties, we introduce the novel method of quantum homodyning. A thorough discussion about the differences between quantum and 'classical' homodyning can be found in the Appendix, Chapter 7.

Chapter 5 discusses the second set of experiments. We demonstrate quantum logic using our single photons from our strongly coupled atom-cavity system. We link two fields of physics which have not been linked to date – namely cavity quantum electrodynamics (c-QED) and LOQC – and demonstrate the ability to do so with the help of a simple chip-integrated beam splitter, CNOT and CNOT4 gate. With a defining feature of two-qubit logic being the ability to generate entanglement from separable input states, we demonstrate the generation of a maximally entangled Bell state with the help of this chip-

integrated CNOT4 circuit. Additionally, we use time-bin encoded qubits to systematically study the de- and re-phasing of quantum states as well as the the effects of time-varying internal phases in photonic quantum circuits. Chapter 6 concludes this work with a discussion of potential ways of continuing experiments regarding a strongly coupled atom-cavity system.

Chapter 2

Theory – How to produce photons from an atom-cavity system

In this Chapter, the main focus is on the physical and theoretical basics necessary to understand the single-photon source experiment. We discuss different types of photon sources in Sec. 2.1 and put our single-photon source based on a strongly coupled atom-cavity system into a broader context. Also, we investigate the question of why we utilise a cavity to produce single photons from a single emitter as well as the necessary prerequisites to achieve this in Sec. 2.2. We moreover learn how to shape the spatio-temporal envelopes of atom-cavity photons in Sec. 2.3 and how that helps us to encode quantum information in this type of carrier. Additionally, we investigate the atom preparation in Sec. 2.4, in particular how atoms can be cooled in Sec. 2.4.1 and trapped in a magneto-optic trap (MOT) in Sec. 2.4.2. How we can make these atoms interact with the cavity to form

the strongly coupled atom-cavity system is discussed in Sec. 2.4.3.

2.1 Introduction to single-photon sources

Before discussing different types of single-photon sources, we need to define what a photon is in the first place. A photon is an excitation of one single mode of the quantised electromagnetic field [18]. Mode m of the quantised electro-magnetic field is described by its frequency ν_m and a photon – one excitation of this mode – possesses the energy of $h\nu_m$, with h being the Planck constant. Let us continue with defining what an ideal source for these photons is: An ideal single-photon source emits photons at the push of a button, at a user-defined point in time. The probability of emitting *only one* photon at a time is 1 and the probability of emitting *more than one* is 0. Additionally, the emitted single photons are indistinguishable, and the repetition rate is as fast as the user wishes and only potentially limited by the duration of the single-photon pulse. To date, no single-photon source has yet met these criteria.

In practice, there are various schemes [19] for producing single photons in modern quantum optics. These non-ideal photon sources can be based on colour centres [20, 21], quantum dots [22, 23], single atoms [24], single ions [25], single molecules [26] and atomic ensembles [27]. In theory, these sources produce a single photon in response to an external control or trigger, therefore, these sources are often referred to as *deterministic*[1]. The alternative approach is to *probabilistically* produce single photons. These sources can rely on photons created in pairs via spontaneous parametric downconversion (SPDC) in bulk crystals [28, 29], waveguides [30] and by four-wave mixing (FWM) in optical fibers

[1]Please note that due to extraction loss, these sources – which are in theory deterministic – become probabilistic in reality.

[31, 32] or waveguides [33]. One property of these sources is that the photons are created in pairs, allowing for one photon to be used as a signal and one as a herald photon. In theory, the distinction between deterministic and probabilistic delivery of single photons is clear, however, in practice, this is not so much the case. In this thesis, we will focus on a deterministic single-photon emitter based on a strongly coupled atom-cavity system which we for this reason also refer to as *photon pistol*.

2.2 Single photons from an atom-cavity system

The technique to produce single photons from an atom-cavity system is based on a coherent Raman process pioneered by Kuhn et al. [8, 34, 35, 36, 37]. The idea is to emit exactly one single photon from a single emitter into a single mode of a radiation field when being triggered to do so. This corresponds to the 'on-demand' criteria of an ideal photon source. The single emitter is identified as an atom strongly coupled to a high-finesse optical cavity, the single mode as a mode of the radiation field of such a cavity and the trigger as a classical light pulse. This technique combines cavity quantum electro-dynamics (c-QED) with an adiabatic transfer technique.

We start this Section with a description of an optical resonator in the form of a cavity in Sec. 2.2.1, and motivate why we are using such an element in our experiment in Sec. 2.2.2. We learn how single emitters and cavities interact in Sec. 2.2.3 in general and why it is necessary to have an atom-cavity system in the *strong coupling* regime in Sec. 2.2.4. We conclude this Section with how we have to treat this system if the single emitter is a ^{87}Rb atom in Sec. 2.2.5.

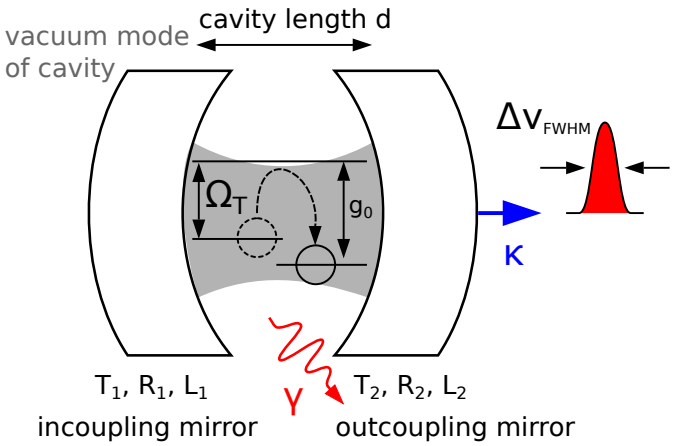

Figure 2.1: Cavity of length d with mirrors of reflectivity $\{R_1, R_2\}$, transmittivity $\{T_1, T_2\}$ and loss $\{L_1, L_2\}$. Around resonance transmission, one can determine the linewidth $\Delta\nu_{\mathrm{FWHM}}$ of the cavity. If one strongly couples an atom with the vacuum mode of the cavity (grey), one can produce a single photon in this mode as described in Sec. 2.2.4. There are two potential loss channels to lose this excitation, denoted κ and γ, also discussed in Sec. 2.2.4.

2.2.1 What is a cavity?

A cavity or Fabry-Pérot resonator consists of two reflective surfaces or 'mirrors' separated by a distance d. Light, that hits the surface of a mirror can either be reflected, transmitted or lost by absorption or scattering. Therefore, we can describe our resonator by the coefficients $R_{\mathrm{i}}, T_{\mathrm{i}}$ and L_{i}, where $\mathrm{i} \in \{1, 2\}$ identifying the reflected, the transmitted and the lost amount of light on the mirror. Due to energy conservation we find that $R_{\mathrm{i}} + T_{\mathrm{i}} + L_{\mathrm{i}} = 1$. An illustration of a cavity and the key parameters can be found in Fig. (2.1).

Light coupled into the resonator must fulfil the resonance condition and that the electric field is zero at the mirror surfaces. The resonance condition arising from boundary conditions at each mirror reads

$$m\frac{\lambda_m}{2} = d, \tag{2.1}$$

where m is an integer. The length of the resonator is consequently the m-times half the wavelength of the incoupled light. Therefore, the resonant frequencies are

$$\nu_m = \frac{c}{\lambda_m}. \tag{2.2}$$

The spacing between resonant frequencies thus is $\Delta\nu = \nu_{m+1} - \nu_m$. This parameter is called the free spectral range $\Delta\nu_{\text{FSR}}$ of the cavity. With Eqs. (2.1) and (2.2) we can calculate the free spectral range to be

$$\Delta\nu_{\text{FSR}} = \nu_{m+1} - \nu_m = \frac{c}{2d}. \tag{2.3}$$

Another important property of the resonator is the linewidth $\Delta\nu_{\text{FWHM}}$ which describes the spectral width of the resonance transmission, or more precisely, the spectral full-width-half-maximum (FWHM) value of the transmitted Lorentzian profile. The cavity's finesse $\mathcal{F}$ is defined as

$$\mathcal{F} = \frac{\Delta\nu_{\text{FSR}}}{\Delta\nu_{\text{FWHM}}} = \frac{\pi\sqrt{R}}{1-R}, \tag{2.4}$$

where $R = \sqrt{R_1 R_2}$. The finesse is commonly used as a measure of the quality of the resonator as it can be thought of as the mean number of round trips of a photon in the cavity. Assuming no absorption or scattering loss, in the vicinity of the resonance we find twice the decay rate of the cavity [37] to be

$$2\kappa = \Delta\nu_{\text{FSR}}/\mathcal{F}. \tag{2.5}$$

The experimentally determined parameters for the cavity used in the photon-pistol experiment, such as its length d, its linewidth $\Delta\nu_{\mathrm{FWHM}}$ and the free spectral range $\Delta\nu_{\mathrm{FSR}}$ can be found in Secs. 3.2.6 and 3.2.7, respectively.

2.2.2 Why using a cavity?

The first question which needs to be asked is why we want to put a single emitter inside a high-finesse optical cavity to produce our single photons. There are two reasons to do so: Firstly, we want to eliminate the possibility that the photons are emitted in all directions, which clearly reduces the versatility of a photon source as the photons need to be collected from a large solid angle. Secondly, as already stressed in the introduction, we do not want to spontaneously emit our photons into free space but into one well-defined mode of the electro-magnetic field. As discovered by Purcell in 1946[2] [38], the spatial mode density inside a cavity changes if a single emitter is placed inside it. Therefore, the spontaneous emission rate into the cavity mode can be either enhanced or suppressed [36]. The equation for the Purcell factor f describing this phenomenon reads

$$f = \frac{3Q\lambda^3}{4\pi^2 V}, \tag{2.6}$$

where V is the mode volume of the cavity, λ the wavelength of the emitted radiation and Q the quality factor of the resonator. The quality factor is defined as $Q = \nu/\nu_{\mathrm{FWHM}}$, the ratio of the resonance frequency ν and the cavity linewidth ν_{FWHM}. For $f < 1$, the spontaneous emission rate is enhanced or, if $f > 1$, suppressed. Moreover, the probability

[2] The original finding was that the spontaneous emission of a fluorescent molecule can be enhanced by putting it into a matched resonant cavity.

of spontaneous emission of a photon into the cavity reads [37]

$$\beta = \frac{f}{f+1}, \tag{2.7}$$

where f is the Purcell factor introduced in Eq. (2.6). Therefore, it can be seen easily that for a large value of f – obtained by a very small mode volume V or a very high quality factor Q – the probability of a photon being emitted into the vacuum mode of the cavity is significantly larger than the probability of a photon being emitted into free space, which is traditionally referred to as γ. This effect has first been demonstrated by Carmichael [39] and DeMartini [40].

2.2.3 Atom-photon interactions inside an optical resonator

Having already motivated the use of a cavity when we want to produce single photons, this Section discusses what happens when a single emitter is placed inside a resonator. Any single quantum system which exhibits discrete energy levels can be coupled to a quantised mode of a radiation field inside an optical cavity [37]. The interaction with a monochromatic, resonant light field of frequency ω_{cav} can be described by the Jaynes-Cummings model [41], however, this model only applies for two-level systems. This is thoroughly discussed for instance in [42].

In extension to the Jaynes-Cummings model, we are here considering the atom as a Λ-type three-level system[3] with two long-lived ground states $|u\rangle$, $|g\rangle$ and one excited state $|e\rangle$ taking part in the interaction. An abstract depiction of the scheme can be found in Fig.

[3]This will be of help for the discussion in Sec. 2.2.4.

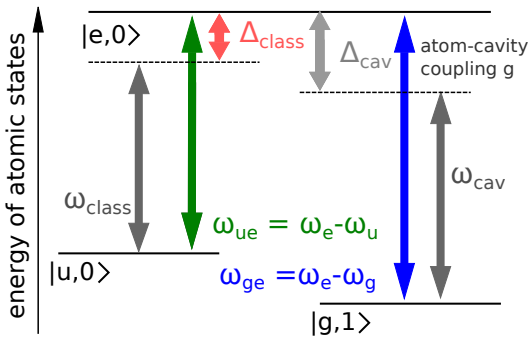

Figure 2.2: A Λ-type three-level system with two ground states $|u\rangle$, $|g\rangle$ and one excited state $|e\rangle$: The transition frequencies between the levels are $\omega_{\mathrm{ge}} = \omega_{\mathrm{e}} - \omega_{\mathrm{g}}$ and $\omega_{\mathrm{ue}} = \omega_{\mathrm{e}} - \omega_{\mathrm{u}}$. To address the states, we use a classical light field ω_{class} with Rabi frequency Ω_{T}. The detunings are $\Delta_{\mathrm{cav}} = \omega_{\mathrm{eg}} - \omega_{\mathrm{cav}}$ and $\Delta_{\mathrm{class}} = \omega_{\mathrm{eu}} - \omega_{\mathrm{class}}$.

(2.2). The transition frequencies between the levels are $\omega_{\mathrm{ge}} = \omega_{\mathrm{e}} - \omega_{\mathrm{g}}$ and $\omega_{\mathrm{ue}} = \omega_{\mathrm{e}} - \omega_{\mathrm{u}}$. To address the states, we use a classical light field ω_{class} with Rabi frequency Ω_{T}, where the subscript T stands for trigger. The detunings read $\Delta_{\mathrm{cav}} = \omega_{\mathrm{eg}} - \omega_{\mathrm{cav}}$ and $\Delta_{\mathrm{class}} = \omega_{\mathrm{eu}} - \omega_{\mathrm{class}}$.

The cavity field is quantised and can be expressed by a superposition of number states $|n\rangle$, where n denotes the number of photons inside the cavity. As the corresponding energy spacing is equidistant, we can treat the cavity as a quantum mechanical harmonic oscillator. Therefore, the cavity's Hamiltonian reads

$$\hat{H}_{\mathrm{cavity}} = \hbar\omega_{\mathrm{cavity}}\left(\hat{a}^{\dagger}\hat{a} + \frac{1}{2}\right), \tag{2.8}$$

where $\hat{a}^{\dagger}$ and $\hat{a}$ are the creation and annihilation operators of a photon inside the cavity. The Hamiltonian of the atom reads

$$\hat{H}_{\mathrm{atom}} = \hbar\omega_{\mathrm{u}}|u\rangle\langle u| + \hbar\omega_{\mathrm{g}}|g\rangle\langle g| + \hbar\omega_{\mathrm{e}}|e\rangle\langle e|. \tag{2.9}$$

The three-level-extended Jaynes-Cummings Hamiltonian of the whole system is given by

the sum of the cavity's, the atom's and the interaction Hamiltonian

$$\hat{H}_{\text{JC,3}} = \hat{H}_{\text{cavity}} + \hat{H}_{\text{atom}} + \hat{H}_{\text{interaction}}, \tag{2.10}$$

of which we already know $\hat{H}_{\text{cavity}}$ and $\hat{H}_{\text{atom}}$. A complete discussion of the process can be found in [36]. The interaction Hamiltonian in the interaction picture reads

$$\begin{aligned}\hat{H}_{\text{interaction}} = \frac{\hbar}{2}\Big(&2\Delta_{\text{class}}|u\rangle\langle u| + 2\Delta_{\text{cav}}|g\rangle\langle g| - \Omega_{\text{T}}(|u\rangle\langle e| + |e\rangle\langle u|) \\ &- 2g_0(|e\rangle\langle g|\hat{a} + \hat{a}^\dagger|g\rangle\langle e|)\Big),\end{aligned} \tag{2.11}$$

from which we can see that only the states $|u, n-1\rangle$, $|e, n-1\rangle$ and $|g, n\rangle$, where n denotes the photon number in the cavity, are coupled. In the following, we assume that the detunings $\Delta_{\text{cav}} = \Delta_{\text{class}} = \Delta$. The eigenfrequencies of the interaction Hamiltonian given in Eq. (2.10) depending on the photon number n in the rotating wave approximation read

$$\omega_{\text{n}}^0 = \omega_{\text{cav}}(n + 1/2), \tag{2.12}$$

$$\begin{aligned}\omega_{\text{n}}^{\pm} &= \omega_{\text{cav}}(n + 1/2) + 1/2\Big(\Delta \pm \sqrt{4ng_0^2 + \Omega_{\text{T}}^2 + \Delta^2}\Big) = \\ &= \omega_{\text{n}}^0 + 1/2\Big(\Delta \pm \sqrt{4ng_0^2 + \Omega_{\text{T}}^2 + \Delta^2}\Big).\end{aligned} \tag{2.13}$$

If we assume the photon number n to be exactly equal to one, we find the eigen- or dressed states to be

$$\begin{bmatrix} |a^-\rangle \\ |a^+\rangle \\ |a^0\rangle \end{bmatrix} = \begin{pmatrix} \sin\theta\cos\phi & \sin\theta\sin\phi & \cos\theta \\ \cos\theta\cos\phi & \cos\theta\sin\phi & -\sin\theta \\ -\sin\phi & \cos\phi & 0 \end{pmatrix} \begin{bmatrix} |g,1\rangle \\ |u,0\rangle \\ |e,0\rangle \end{bmatrix}. \tag{2.14}$$

So, the definition of the dressed states is nothing else than a rotation of the states $|g,1\rangle$, $|u,0\rangle$, and $|e,0\rangle$. The rotation angles ϕ and θ are defined as

$$\tan\phi = \frac{\Omega_\mathrm{T}}{2g_0}, \tag{2.15}$$

$$\tan\theta = \frac{\sqrt{4g_0^2+\Omega_\mathrm{T}^2}}{\sqrt{4g_0^2+\Omega_\mathrm{T}^2+\Delta^2}-\Delta}. \tag{2.16}$$

We conclude that the interaction with a classical light field of Rabi frequency Ω_T lifts the degeneracy of the eigenstates. However, as we can see from Eq. (2.14), there is one of the dressed states $|a^0\rangle$ which does not contain a component of the excited state $|e,0\rangle$, so it cannot decay spontaneously – it is a 'dark' state. If Ω_T = 0, the dark state is equal to the initial state $|u,0\rangle$. By applying a classical light field of Rabi frequency Ω_T, we find that there is a mixture of states $|u,0\rangle$ and $|g,1\rangle$. In case of $\Omega_\mathrm{T} \gg 2g$, the term $1/(\tan\phi)$ will go to zero and the eigenstate reduces to $|g,1\rangle$. With a suitably chosen light field of Rabi frequency Ω_T it is possible to transfer the atom from the initial state $|u,0\rangle$ to the end state $|g,1\rangle$, without populating the excited state. This only works if the adiabaticity is kept [43]. The three-level-extended Jaynes-Cummings Hamiltonian as shown in Eq. (2.10) does not include any coupling to an environment leading to decay. To include loss mechanisms such as the spontaneous decay γ into free space – also referred to as atomic polarisation decay rate – as well as the field decay rate out of the cavity κ, one has to use a master

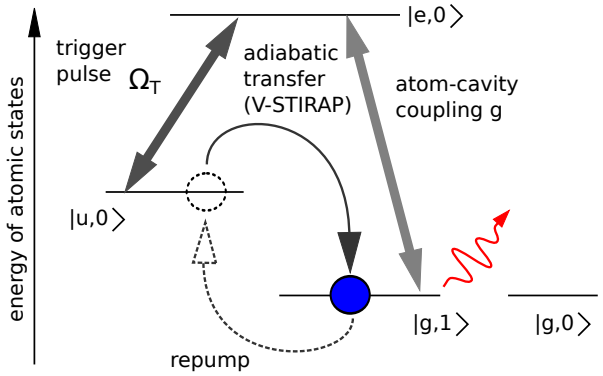

Figure 2.3: Single photon production via an adiabatic Raman process: Ground state $|u,0\rangle$ of the atom is coupled to the excited state $|e,0\rangle$ via the trigger pulse Ω_T. The other ground state, $|g,1\rangle$ is coupled to the excited state $|e,0\rangle$ via the vacuum mode of the cavity. The atom is prepared in one ground state $|u,0\rangle$ and with the help of a trigger pulse of Rabi frequency Ω_T and experiencing the two couplings, it is pumped to $|g,1\rangle$ without populating the excited state $|e,0\rangle$. To restart the process, the atom is transferred to the initial ground state $|u,0\rangle$. Please note that the states $|0\rangle$ and $|1\rangle$ denote the population of the cavity mode with no or exactly one photon.

equation approach. These two decay channels are pictorially represented in Fig. (2.1). For a complete discussion of this system please refer to [34].

2.2.4 Producing a single photon from a strongly coupled atom-cavity system

To produce single photons from an atom-cavity system, we drive the vacuum-stimulated Raman adiabatic passage (V-STIRAP). As Sec. 2.2.3 has discussed this scheme purely theoretically, we briefly summarise the principle in words and without equations: In an idealised atomic Λ-type system with ground states $|u,0\rangle$, $|g,1\rangle$ and excited state $|e,0\rangle$, we choose the resonance frequency of the used cavity to be close to the atomic transition between states $|g,1\rangle$ and $|e,0\rangle$, coupling both states. The other ground state, $|u,0\rangle$, is coupled to the excited state $|e,0\rangle$ with the help of an external laser pulse with the Rabi

frequency Ω_T as it can be seen in Fig. (2.3). If the atom is prepared in this ground state $|u,0\rangle$ in the cavity with no photon present, it is possible to coherently transfer the atom between both ground states without populating the excited state as well as emitting a single photon into the cavity mode. A constraint is that the control fields change sufficiently slowly (adiabatically)[4] [34].

Up to this point, we have considered the system's Hamiltonian in Eq. (2.10), in particular its interaction Hamiltonian in (2.11), the associated eigenvalues in Eqs. (2.12) and (2.13) and dressed states in Eqs. (2.14) that we obtain when coupling a Λ-type three-level atom to a cavity. However, we have not discussed any couplings to an environment leading to decay. In Sec. 2.2.3, we already hint at the spontaneous decay from the excited state $|e,0\rangle$, γ, into free space as well as the cavity decay rate κ. The cavity decay rate leads to the loss of the excitation out of the cavity which reduces the state $|g,1\rangle$ to $|g,0\rangle$ and decouples this state from further evolution.

Therefore, the most important requirement for the V-STIRAP process to occur is that the atom-cavity system is in the *strong-coupling regime* [36, 37] during the V-STIRAP process. This means that the coherent interaction with the cavity dominates over the decay. The important parameters are the atom-cavity coupling $g(\boldsymbol{r})$ and the two decay channels γ and κ.

In general, the atom-cavity coupling constant depending on the position of the atom $\boldsymbol{r}$

[4] This adiabaticity will be of great help when it comes to 'shaping' of single photons which will be discussed in Sec. 2.3.

is given by [36]

$$g(\boldsymbol{r}) = g_0\, \Psi_{\text{cavity}}(\boldsymbol{r}), \text{ with } g_0 = \frac{|\boldsymbol{\mu}| \cdot |\boldsymbol{E}|}{\hbar},$$

where g_0 is the maximum coupling constant, $\Psi_{\text{cavity}}(\boldsymbol{r})$ the mode function of the cavity mode, $\boldsymbol{E}$ is the electric field in the cavity and $\boldsymbol{\mu}$ the electric dipole moment of the respective atomic transition. For the vacuum mode of the cavity, the amplitude of $\boldsymbol{E}$ can be rewritten as $|\boldsymbol{E}| = \sqrt{\hbar\omega_{\text{cav}}/2\epsilon_0 V}$, where V is the volume of the mode and ω_{cav} the resonance frequency of the cavity. In particular, for the cavity coupling the transition between the excited state $|e\rangle$ and ground state $|g\rangle$ of the atom, the atom-cavity coupling constant $g(\boldsymbol{r})$ reads

$$g(\boldsymbol{r}) = \sqrt{\frac{\mu_{\text{eg}}^2\, \omega_{\text{ge}}}{2\hbar\epsilon_0 V}}\, \Psi_{\text{cavity}}(\boldsymbol{r}). \tag{2.17}$$

In the case of maximum coupling, $\Psi_{\text{cavity}}(\boldsymbol{r}) = 1$ and we find $g(\boldsymbol{r}) = g_0$, which is for instance the case in an anti-node of the cavity.

Potential decay channels have been introduced above as the spontaneous emission rate γ and the cavity decay rate κ. The strong-coupling regime constraint [36] is fulfilled if

$$g \gg \{\gamma, \kappa\}, \tag{2.18}$$

where g is the coupling strength of the atom with the vacuum mode of the cavity as it has already been introduced in Eq. (2.17). To obtain a high g, we therefore need a short cavity with a resulting small mode volume V as $g \propto 1/V$. Additionally, we want to influence

the loss rate κ and keep it at a low level. This is experimentally done by the right choice of reflectivities of the cavity mirrors and qualified by the cavity finesse $\mathcal{F}$ as it is shown in Eq. (2.5). The finesse has already been introduced in Sec. 2.2.1 and Eq. (2.4). As $\mathcal{F} \propto \sqrt{R}/\sqrt{1-R}$, where $R = \sqrt{R_1\, R_2}$ and R_1 and R_2 are the reflectivities of the cavity mirrors, we can see that we need highly reflective mirrors. The relation between the decay rates and the coupling constant of atom and vacuum mode of the cavity can be described by the cooperativity parameter

$$C = \frac{g^2}{2\kappa\gamma}, \tag{2.19}$$

which determines the effect of one single atom inside a cavity [44]. We can use the cooperativity parameter to determine the maximum possible photon production efficiency

$$\eta_{\text{max}} = \frac{2C}{2C+1}, \tag{2.20}$$

which is solely dependent on the cooperativity. As it can be seen from Eq. (4.5), the

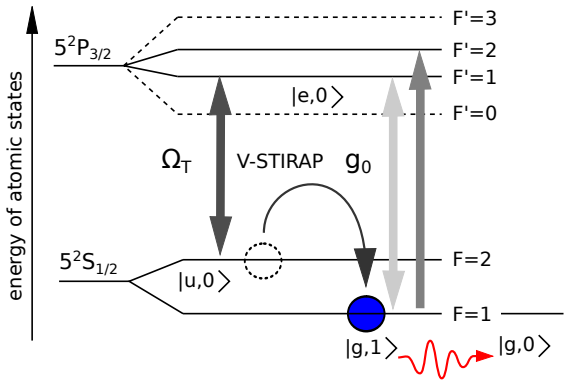

Figure 2.4: V-STIRAP process on the D_2-line between states 5^2 $S_{1/2}$ and 5^2 $P_{3/2}$ of ^{87}Rb. The atom is prepared in the F = 2 hyperfine state and pumped to the F = 1 state via emitting one single photon into the vacuum mode of the cavity. With a repump laser, the atom is excited to the F' = 2 state from where it probabilistically decays into the initial state F = 2. From there, the V-STIRAP process can be restarted.

stronger the atom-cavity coupling, the closer the photon production probability is to 1.

2.2.5 Producing a single photon from a ^{87}Rb atom

The atom that we want to strongly couple to our high-finesse optical cavity is a ^{87}Rb atom[5] due to the fact that it has the lowest nuclear spin and therefore the simplest hyperfine structure. Additionally, we can address its hyperfine levels with cheap commercial[6] diode laser systems. Also, cavity mirrors are better in the near infrared. From other groups, we know that the reflectivities of the mirrors in the blue or much beyond 800 nm in the red are not as good. In our particular case, we use Rubidium's D_2-line (5^2 $S_{1/2} \rightarrow 5^2$ $P_{3/2}$), which is illustrated in Fig. (2.4).

We identify the states $|u,0\rangle$, $|e,0\rangle$ and $|g,1\rangle$ introduced in Secs. 2.2.3 and 2.2.4 as the

[5]Historically, all the Alkalis have been of interest in atomic physics due to the fact that these atoms only possess one valence electron. Therefore, one could also think of Lithium (671 nm) or Sodium (589 nm) as an Alkali. Their atomic structure could be addressed with visible light, however, there are practically no laser systems at these wavelengths. Another option would be Cesium, in which case one would have to go to higher hyperfine energy levels, F = 4 and F = 5. Instead of ^{87}Rb, one could also think of ^{85}Rb. The advantage here would be that ^{85}Rb is more naturally abundant than ^{87}Rb and cheap commercial laser systems are also available. However, the scheme to produce photons of alternating polarisation wouldn't work on this atomic structure.

[6]Thanks to the CD-ROM player there are cheap laser diodes available at around 785 nm.

hyperfine energy levels F = 2, F' = 1 and F = 1. Therefore, we find that the V-STIRAP process starts with the ^{87}Rb atom prepared in the F = 2 hyperfine ground state. This atom experiences two couplings, one to a classical light field of Rabi frequency $\Omega_{\mathrm{T}}(t)$ resonant to the atomic transition from the F = 2 to the F' = 1 hyperfine energy level ($|u,0\rangle \rightarrow |e,0\rangle$). We refer to this light field as *STIRAP*, *drive* or *pump* laser field. The other coupling is to the vacuum mode of the cavity the atom is placed in. The cavity's resonance frequency is close to the F = 1 $\rightarrow$ F' = 1 hyperfine transition of the atom originally introduced as $|g,1\rangle \rightarrow |e,0\rangle$ and therefore far off-resonance to the atomic transition F = 2 $\rightarrow$ F = 1. With the help of these couplings as well as a suitably chosen light field of Rabi frequency Ω_{T}, it is possible to transfer the atoms, we can create a photon in the vacuum mode of the cavity. The photon leaks out of the cavity with a rate of κ, as it has also been thoroughly discussed in Sec. 2.2.4.

After this, the system is in state F = 1 corresponding to $|g,0\rangle$ and has to be repumped to its initial state F = 2 introduced as $|u,0\rangle$ in order to restart the single photon production process. We achieve this with the help of the *repump* laser, resonant to the F = 1 $\rightarrow$ F' = 2 transition, which optically pumps the atom to the hyperfine state F' = 2 from where it probabilistically decays back to its initial state of F = 2. At that point, the photon generation process can be restarted and the next single photon can be produced. All the experimental details such as for instance how the laser beams need to be prepared to drive the V-STIRAP process can be found in the experimental Chapter 3 in Sec. 3.1, in particular in Figs. (3.1) and (3.3).

2.3 Arbitrarily 'shaped' single photons from an atom-cavity system

Having shown theoretically that we can produce single photons from an atom-cavity system in Sec. 2.2, we discuss how we can imprint an arbitrarily shaped spatio-temporal envelope on the photon, which we also sloppily refer to as their 'shape'. This Section is based on the analytic recipe of how to drive an atom-cavity system to have such a photon delivered, published in [45]. A proof of principle test of this recipe can be found in Fig. (2.5).

The idea is to start from the desired spatio-temporal envelope of the photon in final state $|g,1\rangle$ and to work backwards to calculate the required driving pulse of Rabi frequency $\Omega_{\mathrm{T}}(t)$ acting on initial state $|u,0\rangle$. The abstract level scheme we base our nomenclature on can be found in Figs. (2.3) and (2.4). The atom-cavity system is described by the time-dependent Schrödinger equation

$$i\hbar\frac{d}{dt}\mathbf{c}(t) = -\frac{\hbar}{2}\underbrace{\begin{pmatrix} 0 & \Omega_{\mathrm{T}}(t) & 0 \\ \Omega_{\mathrm{T}}(t) & 2i\gamma & 2g \\ 0 & 2g & 2i\kappa \end{pmatrix}}_{\hat{H}(t)}\mathbf{c}(t), \tag{2.21}$$

where $\mathbf{c}(t) = [c_{\mathrm{u}}(t),\, c_{\mathrm{e}}(t),\, c_{\mathrm{g}}(t)]^{\mathrm{T}}$ are the probability amplitudes for the two ground states $|u,0\rangle$ and $|g,1\rangle$ and the excited state $|e,0\rangle$. The cavity decay rate κ as well as the atomic polarisation decay rate γ have been phenomenologically introduced by non-hermitian damping terms as opposed to for instance in Eq. (2.11). Please note that this Hamiltonian is in the interaction picture and that the rotating wave approximation has been applied. Also, all detunings and higher number photon states have been neglected. As the Hamilto-

nian $\hat{H}(t)$ is known, the calculation of the time-dependent Rabi frequency is more or less straightforward [45]. The coupled equation system can be written out explicitly

$$i\frac{d}{dt}c_{\mathrm{u}}(t) = -\frac{1}{2}\Omega_{\mathrm{T}}(t)c_{\mathrm{e}}(t), \tag{2.22}$$

$$i\frac{d}{dt}c_{\mathrm{e}}(t) = -\frac{1}{2}\Omega_{\mathrm{T}}(t)c_{\mathrm{u}}(t) - i\gamma c_{\mathrm{e}}(t) - gc_{\mathrm{g}}(t), \tag{2.23}$$

$$i\frac{d}{dt}c_{\mathrm{g}}(t) = -g\,c_{\mathrm{e}}(t) - i\kappa c_{\mathrm{g}}(t). \tag{2.24}$$

By inverting Eq. (2.22), one obtains

$$\Omega_{\mathrm{T}}(t) = -2i\frac{\frac{d}{dt}c_{\mathrm{u}}(t)}{c_{\mathrm{e}}(t)}. \tag{2.25}$$

Now, we define the desired shape of the photon's probability amplitude $\Psi_{\mathrm{Photon}}(t)$

$$\Psi_{\mathrm{Photon}}(t) = \sqrt{\eta}\,\Psi_0(t), \tag{2.26}$$

where $\Psi_0(t)$ denotes the normalised photon wavefunction with $\int dt|\Psi_0(t)|^2 = 1$ and η is the total probability for a single-photon emission from the cavity. The photon's field amplitude is only defined by the probability amplitude of the final ground state $|g,1\rangle$ with one photon being present, scaled by $\sqrt{2\kappa}$

$$c_{\mathrm{g}}(t) = \frac{\Psi_{\mathrm{Photon}}(t)}{\sqrt{2\kappa}}, \tag{2.27}$$

where κ is the cavity decay rate which has been phenomenologically introduced in Sec. 2.2.3. From this equation, it can be seen that the probability amplitude $c_{\mathrm{g}}(t)$ is directly

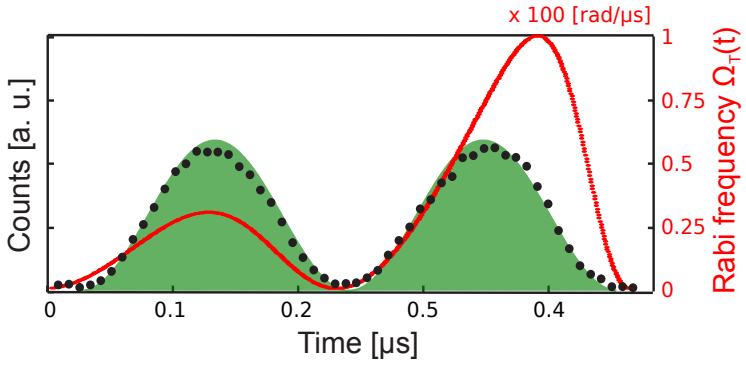

Figure 2.5: Twin-peak single photon from atom-cavity systems: The red line shows the calculated Rabi frequency $\Omega_{\mathrm{T}}(t)$ required to obtain twin-peak photons for values (g, κ, γ) = 2 π (15, 12, 3) MHz and a photon emission probability of η = 0.81. Also, we show the experimentally measured twin-peak photon data. We actively use this shaping method in Chapter 4.

proportional to the desired photon's probability amplitude. From re-arranging Eq. (2.24), one obtains

$$c_{\mathrm{e}}(t) = -\frac{i}{g}\Big(\frac{d}{dt}c_{\mathrm{g}}(t) + \kappa c_{\mathrm{g}}(t)\Big). \tag{2.28}$$

As a next step, the probability amplitude of the excited state taking part in the interaction $c_{\mathrm{u}}(t)$ needs to be determined. As a clear expression cannot be obtained from the Hamiltonian [45], a different approach has to be taken which uses the diagonal elements of the density matrix – the population. The population of the system can only be lost via the two channels γ and κ – the atomic polarisation decay rate γ which as well as the cavity decay rate κ also has been phenomenologically been introduced in Sec. 2.2.3. The probability to find the system in its initial state $|u, 0\rangle$ can be written as

$$\rho_{\mathrm{uu}}(t) = 1 - \rho_{\mathrm{ee}}(t)\rho_{\mathrm{gg}}(t) - \int_0^t dt[2\gamma\rho_{\mathrm{ee}}(t) + 2\kappa\rho_{\mathrm{gg}}(t)], \tag{2.29}$$

where the density matrix element $\rho_{\mathrm{uu}} = c_{\mathrm{u}}^* c_{\mathrm{u}}$ and analogously $\rho_{\mathrm{ee}} = c_{\mathrm{e}}^* c_{\mathrm{e}}$ and $\rho_{\mathrm{gg}} = c_{\mathrm{g}}^* c_{\mathrm{g}}$.

As $c_{\mathrm{g}}(t)$ and $c_{\mathrm{u}}(t)$ are purely real and $c_{\mathrm{e}}(t)$ purely imaginary, one can write

$$c_{\mathrm{u}}(t) = \sqrt{\rho_{\mathrm{uu}}(t)}. \tag{2.30}$$

Inserting this result into Eq. (2.25), the Rabi frequency – a real function that defines the driving pulse to obtain the desired photon shape $\Psi_{\mathrm{Photon}}(t)$ – can be calculated

$$\Omega_{\mathrm{T}}(t) = -i\frac{\frac{d}{dt}\rho_{\mathrm{uu}}(t)}{c_{\mathrm{e}}(t)\sqrt{\rho_{\mathrm{uu}}(t)}}. \tag{2.31}$$

This is the analytical recipe of how to calculate the Rabi frequency in order to produce a single photon with an a-priori defined spatio-temporal mode from a Λ-type three-level system. To calculate the Rabi frequency on a daily basis, a Mathematica script is used to solve Eq. (2.31) numerically. If we put this recipe to the test, the result can be seen in Fig. (2.5).

2.4 How to get atoms inside a cavity

Having studied theoretically how to produce single photons from a strongly coupled atom-cavity system in Secs. 2.2 and 2.3 of this Chapter, we are focussing on how the atoms as such need to be prepared. In the following, we discuss the principles of cold neutral atoms in Sec. 2.4.1, in particular how to create a magneto-optical trap (MOT) in Sec. 2.4.2. The MOT has become a standard tool in contemporary atomic-physics experiments when cold, neutral atoms are required as it both laser cools and magneto-optically traps them [46]. The first MOT has been realised in 1987 by Raab [47]. Additionally, we answer the

question how to make cold atoms interact with the cavity in Sec. 2.4.3.

2.4.1 Doppler-cooling – the optical molasses technique

The technique to laser-cool atoms is based on the principle that laser light can experimentally slow moving atoms down and also manipulate them. We assume a two-level system[7] with a transition frequency ω_0 and shine near-resonant laser light of frequency ω onto it with $\omega = \omega_0 \pm \Delta$, where $\pm\Delta$ is the detuning. Due to the Doppler shift, atoms of a certain velocity class $v = \Delta/k$ see resonant light with their transition of frequency ω_0. With k we denote the photon's wave vector. Assuming a red-detuned laser light, it is ensured that any atom which moves *towards* the laser sees Doppler-shifted light on resonance and experiences a momentum transfer opposite to its direction of motion. This momentum transfer can occur when an atom absorbs and re-emits a photon of Doppler-shifted resonant light. Conversely, an atom moving in the opposite direction – *away* from the light source – sees Doppler-shifted light *away* from resonance. As the photons are strictly coming out of one direction and can be re-emitted non-directionally in 4π, the atoms are slowed down. Therefore, two counter-propagating laser beams help to reduce the atoms' momentum in both directions of motion in one dimension. Three *pairs* of counter-propagating beams ensure the cooling of atoms in three dimensions. This technique is referred to as optical molasses [46, 48].

Naturally, the closer the Doppler-shifted light is to the transition frequency of the atoms, the higher is the scattering rate $R_{\pm,\,\mathrm{scatt}}$ of the atom. Mathematically, with $R_{0,\mathrm{scatt}}$

[7] This assumption is justified in our case as the linewidth of the laser is small enough to not address a different energy level.

being the scattering rate on resonance, we find

$$R_{\pm,\,\text{scatt}} = R_{0,\text{scatt}} \cdot \frac{1}{1 + \frac{1}{\Gamma^2/4}\left(\frac{\delta_\pm^2}{I/I_{\text{sat}}+1}\right)^2}, \tag{2.32}$$

where Γ is the linewidth of the transition corresponding to the transition frequency ω_0, ω the frequency of the laser, $\delta_\pm = \omega - \omega_0 \pm kv = \Delta \pm kv$ the difference between laser frequency ω and atomic transition frequency ω_0 taking into account the Doppler shift. For lower power, indicating that intensity I is much smaller than the saturation intensity ($I/I_{\text{sat}} \ll 1$), we obtain as a velocity-dependent force on the atoms in the molasses phase

$$F_{\text{mol}}(v) = \underbrace{\hbar k}_{\text{photon momentum}} \underbrace{(R_{-,\text{scatt}} - R_{+,\text{scatt}})}_{\text{scattering rate}} = \tag{2.33}$$

$$= \hbar k\, R_{0,\text{scatt}} \cdot \left(\frac{1}{1 + \left(\frac{\delta_-}{\Gamma/2}\right)^2} - \frac{1}{1 + \left(\frac{\delta_+}{\Gamma/2}\right)^2} \right). \tag{2.34}$$

Due to momentum transfer, the atoms can be cooled by absorbing and re-emitting photons. What we have not taken into account is – when emitting the photon into 4π – the atom receives a momentum 'kick' in a random direction which leads to a random walk in velocity space [46] and therefore to heating. The minimum temperature we can cool the atoms in the optical molasses technique is determined by the balance of this heating process and the cooling of the laser is referred to as Doppler temperature T_{Doppler} which is 146 μK for the ^{87}Rb D_2-line [49]. To both cool and trap the atoms at the same time, we have to go to even lower temperatures. How we achieve this is discussed in Sec. 2.4.2.

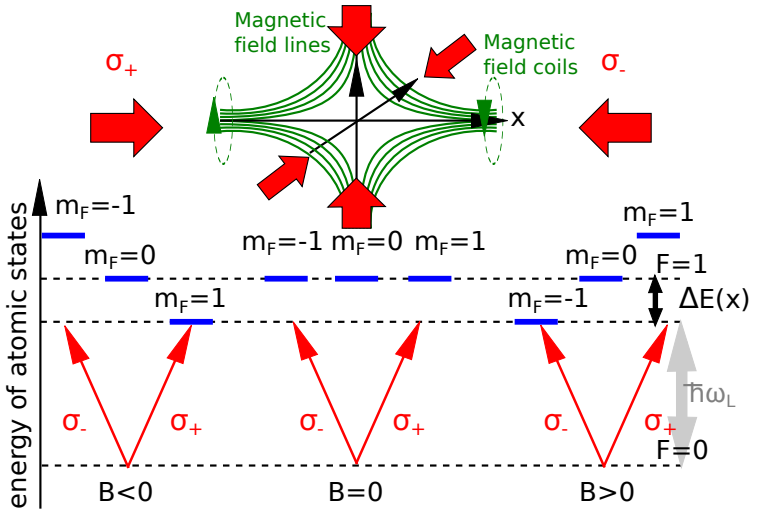

Figure 2.6: By applying a magnetic field to our optical molasses technique, we can also confine our atoms: The magnetic field is generated with the help of two anti-Helmholtz coils and is – if the earth magnetic field is compensated for – 0 in the centre of the trap. By the magnetic field, the degeneracy of the m_F states is lifted the further the atom moves away of the centre of the trap. With the help of red-detuned laser light and the correct polarisation, we can 'kick' the atoms back towards the centre of the trap.

2.4.2 Sub-Doppler-cooling – the magneto-optical trap (MOT)

In Sec. 2.4.1, we have discussed the optical molasses technique to cool atoms, however, this cooling technique does not trap these atoms at the same time. To implement a trap, a spatially dependent quadrupole magnetic field is introduced [46] with the help of two coils in anti-Helmholtz configuration (currents in opposite direction). To explain the principles of a magneto-optical trap, we are considering an atom with a ground state and an excited state with angular momentum F = 1 and three degenerate energy levels namely $m_F = \{-1, 0, 1\}$ in the following.

As it can be seen in Fig. (2.6, upper), there is no magnetic field at the centre of the two anti-Helmholtz coils. Discussing this problem in only one dimension, we refer to this centre point as $x = 0$. With $B(x) = 0$, atoms do not experience any magnetic field and their atomic energy levels remain unperturbed. However, if they are displaced from

this position, they experience a Zeeman shift in their magnetic sub-levels m_F and their degeneracy is lifted according to

$$\Delta E(x) = g_F \, \mu_B \, m_F \, B(x), \tag{2.35}$$

where μ_B is the magnetic moment, and g_F is the Landé factor[8]. A schematic illustration can be found in Fig. (2.6, lower). To form a magneto-optical trap, we shine three counter-propagating laser beams intersecting each other at $x = 0$. The laser beams are circularly polarised and red-detuned from the atoms' resonance frequency. Analogously to the scattering force for the optical molasses technique in Eq. (2.33), one can deduce the velocity-dependent force the atoms experience with respect to their scattering rates $R_{\sigma_+,\text{scatt}}$ and $R_{\sigma_-,\text{scatt}}$ for both incoming σ_+, σ_- circularly polarised laser beams

$$\begin{aligned} F_{\text{MOT}}(v,x) &= \hbar k (R_{\sigma_-,\text{scatt}} - R_{\sigma_+,\text{scatt}}) = \\ &= \hbar k R_{0,\text{scatt}} \cdot \left(\frac{1}{1 + \left(\frac{\delta_- - \Delta E(x)/\hbar}{\Gamma/2} \right)^2} - \frac{1}{1 + \left(\frac{\delta_+ + \Delta E(x)/\hbar}{\Gamma/2} \right)^2} \right), \end{aligned} \tag{2.36}$$

where $\delta_+ = \omega - \omega_0 + kv$ and $\delta_- = \omega - \omega_0 - kv$. Please note that $\omega_0 + \Delta E(x)/\hbar$ is the resonant transition frequency in the m_F = 1 and $\omega_0 - \Delta E(x)/\hbar$ in the m_F = -1 case. Therefore, we find

$$F_{\text{MOT}}(v,x) = \hbar k (R_{\sigma_-,\text{scatt}}(\omega - \omega_0 - \Delta E(x)/\hbar - kv) \tag{2.37}$$

$$- R_{\sigma_+,\text{scatt}}(\omega - \omega_0 + \Delta E(x)/\hbar + kv). \tag{2.38}$$

[8] For most of the transitions used in laser cooling experiments g ≈ 1 [46].

For the velocity-dependent part of the force, we find using the Taylor expansion[9]

$$\begin{aligned} F_{\text{MOT}}(v) &= F_{\sigma_-,\text{scatt}}(\omega-\omega_0-kv) - F_{\sigma_+,\text{scatt}}(\omega-\omega_0+kv) = \\ &\sim F_{\text{scatt}}(\omega-\omega_0) - kv\frac{\partial F_{\text{scatt}}}{\partial\omega} - \left(F_{\text{scatt}}(\omega-\omega_0) + kv\frac{\partial F_{\text{scatt}}}{\partial\omega}\right) = \\ &= -2kv\frac{\partial F_{\text{scatt}}}{\partial\omega} = -\alpha v, \end{aligned} \tag{2.39}$$

assuming small velocities.

For the position-dependent part force on the atoms in the MOT phase, in the approximation of small values of x and a linear magnetic field $B(x)$, we find

$$\begin{aligned} F_{\text{MOT}}(x) &= F_{\sigma_-,\text{scatt}}(\omega_0-\Delta E/\hbar) - F_{\sigma_+,\text{scatt}}(\omega_0+\Delta E/\hbar) = \\ &= -2\frac{\Delta E}{\hbar}\frac{\partial F_{\text{scatt}}}{\partial\omega_0} \sim -\beta'\frac{\partial B(x)}{\partial x}\,x = -\beta\,x, \end{aligned} \tag{2.40}$$

assuming small detunings and a small Zeeman shift. The prefactor $\beta'\partial B(x)/\partial x$ with $\partial B(x)/\partial x = const.$ looks like a spring constant. This indicates that the further the distance of the atoms to the $x = 0$ point, the more they are forced back. Taking Eqs. (2.39) and (2.40) into account, we find the total force on the atoms to be $F_{\text{MOT}}(v,x) = -\alpha v - \beta x$, which is similar to the structure of a damped harmonic oscillator [46]. This leads to the cooling of atoms as well as to their local confinement.

[9] $f(x)|_{x=x_0} = f(x_0) + f'(x_0)(x-x_0)$. We identify f' as $\frac{\partial f}{\partial\omega}$.

2.4.3 The atomic fountain

Having discussed how to cool and trap atoms in Secs. 2.4.1 and 2.4.2, the final question to answer is how we can make the atoms interact with the vacuum mode of the cavity and form a strongly coupled atom-cavity system. To do so, we use an atomic fountain technique, which launches the atoms towards the cavity after having cooled them down in a MOT to sub-Doppler temperatures as described above. If the momentum is applied correctly to the atoms, their upper turning point is equivalent to the centre of the cavity mode. This guarantees reasonably long interaction times. This technique is called *moving molasses* technique.

To launch the atoms, the upper and lower MOT beams are frequency detuned $\omega \pm \Delta\omega$, with respect to each other. In a moving reference frame with velocity [46]

$$\mathbf{v} = \frac{\Delta\omega}{k}\mathbf{e}_z, \tag{2.41}$$

the Doppler shift amounts to $\Delta\omega$, such that all beams appear to have the same frequency and the atoms are cooled into a moving rest frame. After the launch of the atoms, all MOT beams are switched off, the cloud of atoms ballistically moves towards the cavity and eventually interacts with the cavity mode. For all the experimental parameters of the MOT and cold atoms please refer to the experimental Sec. 3.3. In this referenced Section, we show stationary pictures of the MOT such as in Fig. (3.16), how the atoms slowly move upwards after being launched in Fig. (3.19), demonstrate the MOT's loading, expansion and temperature in Sec. 3.3.2, and its dynamic properties in Sec. 3.3.3.

Chapter 3

Technical discussions – The nitty-gritty details of photon pistols

One of our primary goals is to deterministically produce single photons with an arbitrary spatio-temporal envelope from a strongly coupled atom-cavity system. To do so, we first need to deliver one single ^{87}Rb atom between two mirrors of a high-finesse optical cavity. This is done by first cooling roughly 10^6 atoms to μK regime with the help of a magneto-optical trap (MOT) and then launch them upwards with an atomic fountain. The cavity itself needs to be locked to a Rubidium resonance with the help of a reference laser. This cavity frequency couples one ground and one excited state of our atomic Λ-type level scheme taking part in the interaction to drive the V-STIRAP process. The other ground state is coupled to the excited state with a driving laser. This V-STIRAP process delivers the single photon deterministically in the vacuum mode of our cavity.

In Sec. 3.1 of this Chapter, we describe the diode laser system and their locking procedure, common to all the elements of the setup. Next, we discuss the cavity, its properties and its locking scheme in Sec. 3.2. In Sec. 3.3, we focus on the atoms in the experimental setup. Finally, we discuss the repetitive experimental sequence used for single-photon

generation in Sec. 3.4.

3.1 The laser system

The key to the photon pistol experiment is a well-characterised and stably operating laser system. Our infrared diode laser system consists of two Toptica DL100s. In the following, we discuss how to actively stabilise them to a frequency reference and the way they are aligned in the lab to operate a magneto-optical trap, lock the cavity and drive the V-STIRAP process.

3.1.1 Frequency stabilising the laser system and Rubidium spectroscopy

Two DL100 Toptica diode lasers in Littrow configuration are sufficient to provide all necessary frequencies to generate a MOT, to launch the atoms towards the cavity, to lock the cavity and to drive the V-STIRAP process. An overview of the complete level and laser locking scheme can be found in Fig. (3.1). We use the F = 2 $\rightarrow$ F' = 3 transition in the Rubidium D_2-line [49] to cool and trap the atoms. We refer to the laser addressing this transition as the *MOT cooling*. Atoms could also potentially be excited into the F' = 2 state. From there, they can decay into the F = 1 state and are lost from the MOT cycle as they do not interact any more with the cooling laser. Therefore, a *MOT repump* laser is needed in addition which drives the atoms from state F = 1 to state F' = 2. From there, they may decay into F = 2 and again participate in the magneto-optical trap's cooling cycle. Additionally, we need laser beams of certain frequencies to lock our cavity to and to drive the photon generation process. As already described in Chapter 2, the cavity couples

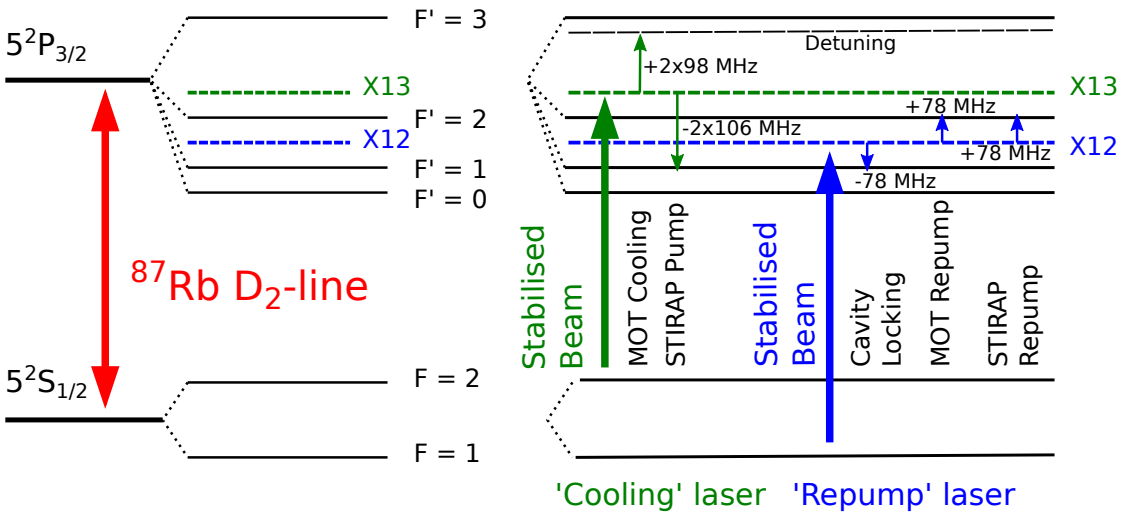

Figure 3.1: Hyperfine level scheme of the D_2-line of ^{87}Rb (left) and necessary frequencies to drive the V-STIRAP process as well as to provide for the MOT cooling and repumping light (right): The laser system consists of two DL100 Toptica diode lasers. With the help of its commercial Pound-Drever-Hall locking circuit the laser used for cooling is locked to the crossover point X13, the midpoint between the F = 2 $\rightarrow$ F' = 1 and F = 2 $\rightarrow$ F' = 3 transitions, whereas the repump laser is locked to the crossover point X12, the midpoint between the F = 1 $\rightarrow$ F' = 1 and F = 1 $\rightarrow$ F' = 2 transitions. To prepare the laser beams at the correct frequencies, the respective laser beam frequency is shifted with double- or single-passed acousto-optic modulators (AOMs). The measured spectra and error signals can be found in Fig. (3.2).

one of the two ground and one excited state of our Rubidium atom idealised as a Λ-type levels scheme. We refer to this transition as the *cavity locking* transition. To drive the atomic photon generation process, we need the *STIRAP pump* laser and, after the atom has generated one single photon, the *STIRAP repump* laser to restart the process.

The two DL100 grating-stabilised diode lasers are locked via a Doppler-free saturated absorption spectroscopy of Rubidium in a room-temperature vapour cell, which is a standard technique in atomic physics [50]. As it can be seen in Fig. (3.1), the cooling laser is locked to the crossover point that is halfway between transitions F = 2 $\rightarrow$ F' = 1 and F = 2 $\rightarrow$ F' = 3, referred to as X13. The repump laser is locked to the crossover point of transitions F = 1 $\rightarrow$ F' = 1 and F = 1 $\rightarrow$ F' = 2, referred to as X12. The locking scheme of

the lasers consists of the commercial Toptica Pound-Drever-Hall (PDH) and proportional-integrative-derivative (PID) action controller. The PDH modulates the laser current at 20 MHz via the BIAS-T of the laser head which gives rise to sidebands of $\pm$20 MHz spectral distance to the centre frequency of the laser.

The locking circuit operates as follows: A small amount of light is double-passed through a cell filled with natural abundance Rubidium vapour in the pump-probe scheme. With the term 'pump-probe scheme' we mean that we send a beam of around 1 mW laser power through the vapour cell – the pump beam – and counter-propagatingly the probe beam of the same frequency. The probe beam is registered on a photodiode. Only if the laser beams are close to the atomic resonance within the natural linewidth Γ, the two beams address atoms of the same velocity class and direction of motion. Close to resonance, the pump beam will excite the atoms and as soon as the number of atoms in the excited state and the number of atoms in the ground state are equal, the transition is called *saturated*. When the transition is saturated, the rate of absorption is equal to the rate of stimulated emission and so the probe beam is barely attenuated. Hence, the saturation of the absorption by the pump beam leads to a narrow peak in the intensity of the probe beam transmitted through the vapour cell. Therefore, we see a peak in the absorption spectrum on the photodiode, e.g. at the hyperfine resonances.

Additionally, we observe strong peaks at frequencies exactly between two hyperfine transitions which are called *crossover resonances* [46, 50]. In the case of the cooling laser, there are two transitions involved, namely F = 2 $\rightarrow$ F' = 1 and F = 2 $\rightarrow$ F' = 3 which clearly share the F = 2 energy level. As two transitions and one common ground state are involved, we have to apply a three-state picture. On resonance with either transition F = 2

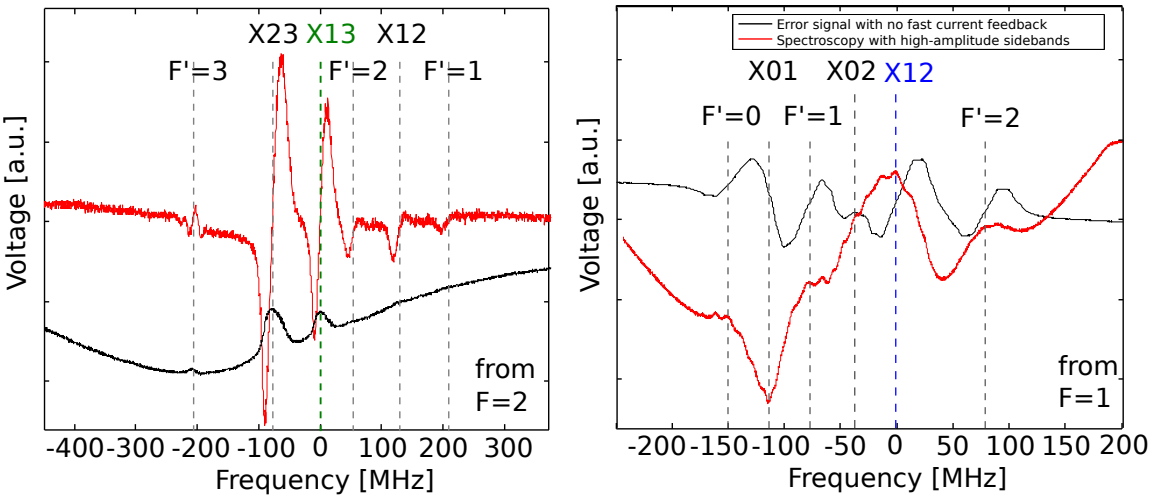

Figure 3.2: Measured signal of the Doppler-free saturated absorption spectroscopy: The black line corresponds to the measured spectrum of the probe beam on a photodiode, the red trace is the error signal from the laser's Pound-Drever-Hall action controller. (Left) We lock the cooling laser to the crossover point X13 (marked in green), corresponding to the midpoint between the transitions F = 2 → F' = 1 and F = 2 → F' = 3. (Right) The repump laser is locked to the crossover point X12 (marked in blue), corresponding to the midpoint between the transitions F = 1 → F' = 1 and F = 1 → F' = 2.

→ F' = 1 and F = 2 → F' = 3, the pump beam depletes the atom population at the velocity class around v ≈ 0. Therefore, we see an intensity peak in the probe beam as its light gets barely absorbed and consequently barely attenuated. Additionally, exactly at the midpoint between the two transitions, the pump beam burns a hole in the population of two different velocity classes corresponding to either transition F = 2 → F' = 1 or F = 2 → F' = 3. The probe beam absorption gets attenuated at inverse velocity classes of transitions F = 2 → F' = 3 or F = 2 → F' = 1 which gives rise to a strong intensity peak on the photodiode, the crossover resonance. Similarly, this principle holds for the X12 crossover resonance, where two transitions F = 1 → F' = 1 and F = 1 → F' = 2 which share the F = 1 energy level are involved. As we can observe in Fig. (3.2, black trace), the absorption peaks in the probe spectrum originating from these crossover resonances can be quite strong. Therefore, we use them in our laser locking circuits.

Coming back to our initial question of frequency stabilising our laser system, we need to know how far the laser has drifted from the crossover point of the atomic resonance at any point in time. The problem is that the atomic resonance itself is symmetric and does not contain any information about in which direction in frequency space the laser frequency has drifted. To obtain this information, we apply the Pound-Drever-Hall technique [51]. In this technique, we need the ± 20 MHz sidebands modulated around the centre frequency of the laser as a reference. This component in the signal transmitted through the Rubidium vapour cell is subject to a π phase shift above the resonance, and to zero phase shift below. Hence frequency mixing of the transmitted AC component at 20 MHz with a reference signal of the same frequency results in an effective phase measurement. The deviation from $\pi/2$ is used as the error signal feeding the PID locking circuit which keeps the laser on the resonance. Both the initial absorption signal from the photodiode as well as the error signal for both cooling and repump laser can be found in Fig. (3.2).

This error signal is fed into the PID action controller in the laser's electronics rack that processes the error signal of the laser frequency and then amplifies is to the power level sent to the piezo-electric transducer. The latter acts on the angle of the grating as well as the length of the external cavity.

This locking scheme reduces the frequency fluctuations of both the cooling and repump laser around their respective centre frequencies to around 500 kHz and 400 kHz. These two values are referred to as the lasers' linewidths. Techincally, the linewidth of a diode laser is limited by noise sources such as for instance fluctuations in the length of the resonator, the the current going to the laser diode or the temperature of the laser diode.

3.1.2 The laser beam preparation

The two lasers of our infrared laser system provide for the MOT pump and repump beams, the beams to drive the V-STIRAP process as well as the locking beam for the cavity. Additionally, the setup comprises a MOT and atomic fountain imaging system. In the following, we discuss how these beam lines need to be set up on the optical table such that each beam can be switched individually at the correct point in time. A complete overview of all beam lines can be found in Fig. (3.3).

As a first element in the setup, an anamorphic prism pair can be found that helps to transform an elliptical laser beam[1] into a nearly circular one by magnifying it in one dimension. With the help of a subsequent Rubidium vapour cell, we can lock our lasers to the crossover points in the Rubidium spectroscopy as thoroughly discussed in Sec. 3.1.1. Another control mechanism is the use of Fabry-Perot cavities as monitoring devices which show whether the lasers are running single-mode spectrally or not.

On the cooling laser's beam line, the MOT cooling beams need to be subdivided into two sets of beams, namely the cooling upper and the cooling lower ones as we have to detune these beams relatively to each other when intending to launch the atoms upwards. The technique is more thoroughly discussed in Sec. 3.3.3. A double-passed acousto-optic modulator (AOM) provides for both the correct frequency detuning as shown in Fig. (3.1) as well as the on- and off-switching. This is analogously the case for the STIRAP pump and the saturated absorption imaging beam. The importance of the latter as a monitoring device is explained in Sec. 3.3.1. All these beams are fibre coupled before they reach the vacuum chamber where the cavity and the MOT are located. As we want

[1] Intrinsic problem of these type of lasers due to their diode.

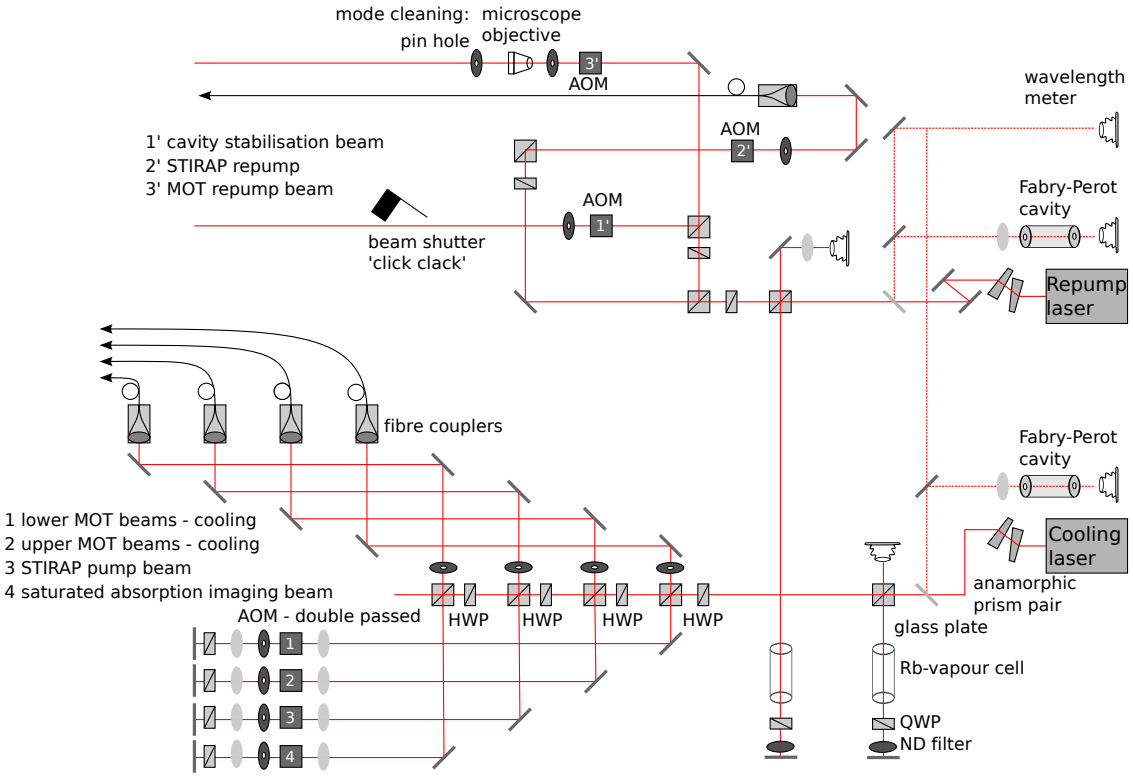

Figure 3.3: Complete overview of beam preparation lines of the photon pistol experiment: The cooling laser (lower) provides for the two MOT cooling beams, the STIRAP pump beam, and the illumination beam to do absorption imaging of the MOT and the fountain in flight. The repump laser (upper) provides for the cavity stabilisation, the MOT repump, the STIRAP repump and the MOT repump beam. Being locked to the crossover resonances X12 and X13 of the Rubidium spectrum, respectively, the laser light is shifted to the correct wavelength with the help of an AOM. The frequencies have already been shown in Fig. (3.1).

an intrinsically stable MOT as well as STIRAP alignment, the beam preparation stage is completely decoupled from the actual experimental stage with the help of this fibre coupling.

The repump laser's side is similar to the cooling laser's one. However, there is one experimental quirk in place – a physical shutter which is used in the cavity locking beam line. We refer to this device as *AOM click clack*. Light is needed to lock the cavity to a certain resonance, however, as soon as the V-STIRAP process happens inside the cavity, it needs to be completely field-free. An AOM can switch light but never guarantee that

there is absolutely zero light travelling towards the cavity. Therefore, we need a physical shutter operated in front of the cavity. Additionally, it also serves as a protecting device as when the photon generation process is taking place in the cavity and the single-photon counting modules (SPCMs) are switched on, the power level used to lock the cavity would destroy these sensitive devices instantly. The click clack device itself is based on a relay (Tyco-T9AS/V) [52, 53] and a simple control circuit. To minimise vibrations, the shutter is screwed to the laser table with a neoprene mount. More on the actual switching and safety measures can be found in Sec. 3.4.

3.2 The cavity

The cavity is the core element of the photon-pistol experiment. Its key physical properties are the free spectral range ν_{FSR}, its mechanical stability, its linewidth ν_{FWHM} and the quality of its active stabilisation. In the following, we discuss how to choose, control and characterise these.

In particular, we discuss the chosen cavity design for our experiment in Sec. 3.2.1. As we need to actively vary the length of the cavity, we touch upon the properties of the piezo-electric transducers the cavity mirrors are mounted on in Sec. 3.2.2. The active stabilisation technique to keep the cavity on or close to the atomic resonance for the photon production process is discussed in Sec. 3.2.3. Also, we determine the properties of the cavity if the active stabilisation is not in use in Sec. 3.2.4. We introduce a new element to the active stabilisation chain, the new 'cavity lock box' in Sec. 3.2.5. This lock box enables us to run various characterisation measurements on the cavity, such as the above

mentioned free spectral range ν_{FSR} as well as its linewidth ν_{FWHM}. These measurements are presented in Secs. 3.2.6 and 3.2.7.

3.2.1 The best of all possible cavities

Loosely adapted from Gottfried Leibnitz, we discuss the properties of our high-finesse optical cavity. There are two properties the design of our high-finesse optical resonator needs to provide. First of all, we want our atom-cavity interactions to take place in the strong coupling regime [36] as it has been discussed in Sec. 2.2.4. This means that the coherent interaction of atom and cavity mode dominates over the incoherent decay, as expressed by $g \gg \{\kappa, \gamma\}$. We therefore need cavity mirrors with the highest possible reflectivity. Secondly, we also want to be able to detect our single photons eventually. This means they need to leak out of the cavity at some point in time, which clearly requires low reflectivity mirrors. As these two properties seem to be contradictory, both constraints can be fulfilled with the help of an *asymmetric* cavity design. This means, for our cavity, we choose one almost perfect mirror, the incoupling mirror – in the convention of Fig. (2.1) – and one with larger transmission, the outcoupling mirror. The design chosen has been similarly used by the Kimble [54] and the Meschede [55] group. By choosing an asymmetric cavity design, the overall finesse of the cavity is reduced, however, one is still in the strong coupling regime.

The mirrors we use in the experiment are of transmissions $T_1 = 0.5$ ppm[2] and $T_2 \approx 40$ ppm [52]. The mirrors[3] consist of a cylindrical BK7 substrate with a diameter of 7.75 mm and a length of 4 mm [52]. The front facet is polished to obtain a spherical concave surface

[2] ppm = parts per million = 10^{-6}.
[3] Manufactured by Research-Electro-Optics Inc., Boulder, Colorado.

of radius of curvature R_c = 50 mm. A dielectric reflective coating has been deposited on the front and an anti-reflective coating on the back of the lower-reflectivity mirror. In addition to that, the mirrors were machined down to a cone with a surface diameter of 1.5 mm[4]. The cavity and its parameters is thoroughly characterised in Sec. 3.2.6, determining its length d, its free spectral range $\Delta\nu_{\mathrm{FSR}}$, its linewidth $\Delta\nu_{\mathrm{FWHM}}$ as well as the spacing of the transverse modes $\Delta\nu_{\mathrm{trans}}$. In Sec. 3.2.4, we also determine its mechanical stability.

3.2.2 The cavity piezo

As the cavity resonance frequency needs to be chosen close to the atomic transition between the atomic states $|g\rangle$ and $|e\rangle$ as introduced in Sec. 2.2.4, we need to make sure experimentally that the cavity stays close to this atomic resonance over a certain period of time. With the help of a piezo-electric transducer (Noliac CSAP03), the cavity's length can be varied. The two cavity mirrors are mounted on two shear piezos which gives a 1.5 μm peak-to-peak stroke at $\pm$320 V, respectively. Each of these two piezos is sufficient to scan the cavity over a free spectral range with respect to distance. To span the complete spectral range, the peak-to-peak stroke needs to be around 0.4 μm. In earlier stages of the photon-pistol experiment, it was intended to use the two piezos independently [52], but one of the piezos was electrically shorted. This leaves one of the two mirror fixed to one position and only the other mirror can be displaced and therefore alter the length of the cavity.

In Fig. (3.4), the stroke versus applied voltage relationship for the shear plates can be found. According to [56], the polynomial trend follows the experimental relationship

[4]Machining done by Hellma Optics GmbH, Jena.

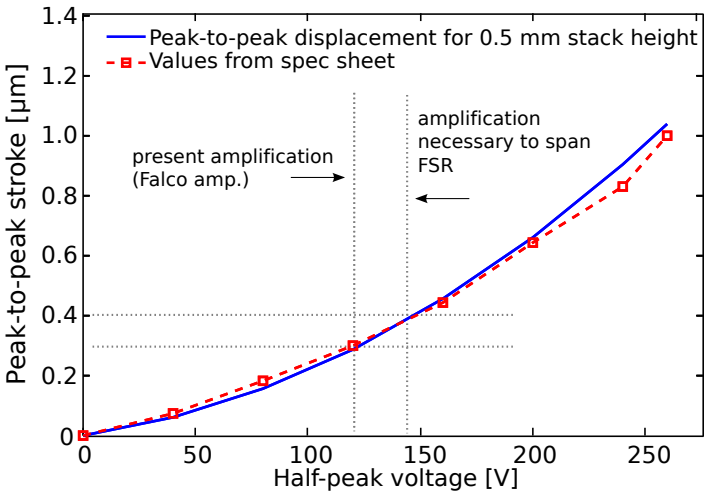

Figure 3.4: Characterisation of the cavity's piezo-electric transducer (Noliac CSAP03): As it can be seen, the stroke versus applied voltage relationship for shear plates is not linear. A typical measurement taken from [56] is shown. The displacement per voltage unit increases when the actuator is used close to the maximum recommended voltage. In this graph, the current possible voltage is shown (Falco amplifier) as well as the necessary voltage to span the full free spectral range (FSR) of the cavity. The Noliac terminology has been used in this graph (half-peak voltage = amplitude, peak-to-peak stroke = 2x displacement δ).

$\delta = 2.88 \cdot 10^{-15} tE^2 + 5.0 \cdot 10^{-10} tE$, where δ is the displacement, t the height of the actuator (0.5 mm) and E the applied electrical field (Voltage/height). The graph also shows that the present amplification (see Sec. 3.2.5) we can achieve is insufficient to scan the full free spectral range of the cavity.

3.2.3 The cavity's active stabilisation

To keep the cavity's resonance frequency close to one atomic resonance as described in Sec. 3.2.3, we need to actively stabilise it on this resonance. This is achieved with the help of the shear piezo-electric transducer described in Sec. 3.2.2 and an electric locking mechanism similar to the one used to lock the lasers as described in Sec. 3.1.1. In particular, we use the repump laser's Pound-Drever-Hall module, a home-buit PID regulator, a sample-and-hold circuit and a newly designed cavity lock box as shown in Fig. (3.9).

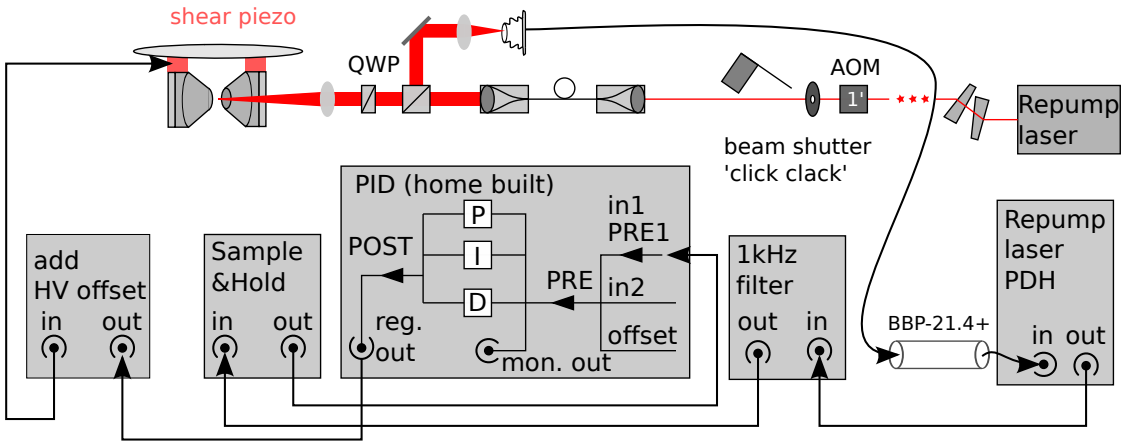

Figure 3.5: Active feedback loop for the stabilisation of the cavity: The cavity locking beam, tapped of the repump laser system, is frequency shifted with the help of an AOM. As the cavity needs to be completely dark in the time the single photons are produced, a mechanical shutter is in place behind the AOM output. After passing through the mode-cleaning fibre, the stabilisation beam hits the end facet of the cavity and is reflected in the non-resonant case. The interesting frequency component is detected with the help of a Thorlabs photodiode and further processed in the repump laser's PDH module, the home-built PID and added onto a high-voltage offset generated in the cavity lock box until it reaches the cavity's piezo.

An illustration of the complete experimental cavity locking circuitry can be found in Fig. (3.5).

The beam to stabilise the cavity on is tapped off the repump laser system which is stabilised on the crossover resonance X12 of the Rubidium spectroscopy as shown in Fig. (3.1). After shifting its centre frequency with the help of an AOM, a mechanical beam shutter is put in place to make sure the cavity remains completely dark in the time the single photons are produced. Before the laser beam hits the end facet of the cavity, it is mode cleaned with the help of a 10 cm single-mode fibre. Due to imperfect optical impedance[5] and mode matching[6] [57], most of the light is reflected back the same way it came from *even* in the resonant case. As there is also a QWP in front of the cavity which the light passes through in twice – once when leaving the fibre as well as when being

[5]Perfect impedance matching is achieved when the transmission through the input mirror equals all losses of the resonator.

[6]Mode matching means that the beam's size, shape and wavefront curvature match the cavity mode.

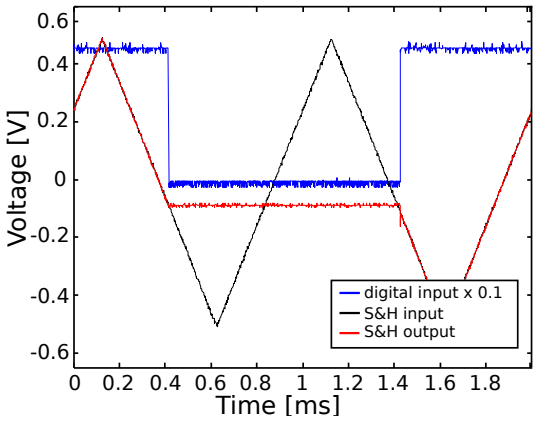

Figure 3.6: Functionality of sample-and-hold circuit (S&H) used to lock the cavity in a running experiment. While the actual photon production is taking place 25,000 times in a row, no light from the cavity locking beam is supposed to be inside the cavity. To keep the cavity on resonance in this time period, the S&H circuit freezes the voltage of the cavity piezo and as soon as the photon production phase of 25 ms is finished, the the electronic signal is un-frozen and the PID regulator works again to keep the cavity on resonance. The black signal is the signal going into the sample-and-hold circuit. The blue signal is the S&H gate (which decides whether the signal goes through or is frozen) and the red signal is the S&H output. It can easily be seen that the circuit does exactly what it is supposed to do when the gate is switched off.

reflected off the end facet of the cavity – it accumulates a polarisation phase shift of π and, when passing through a PBS, it is sent out off the beam line and onto an adequate photodiode[7].

To lock the cavity, we use the laser's commercial Pound-Drever-Hall action controller where the signal from the photodiode is mixed to base-band [57] and therefore generates the necessary error signal. The abstract functionality of the PDH module [51] has already been discussed with respect to the locking procedure of the laser system in Sec. 3.1.1.

As a next step in the feedback chain, the error signal filtered with a 1 kHz lowpass filter to remove high-frequency noise. As a next step, it passes through a sample-and-hold circuit (S&H). This element is necessary, as – while single photons are produced – the cavity needs to be completely empty of photons as we need the vacuum mode of the

[7] Thorlabs PDA 10A

cavity to drive our transition. Therefore, the cavity stabilisation beam has to be switched off in this period and the regulating signal has to be held or 'frozen' at this locking point for 25 ms while 25,000 1 μs STIRAP drive pulses are fired. The freezing of the regulating signal is the task of the sample-and-hold circuit, which operates computer controlled. A measured trace of its functionality can be seen in Fig. (3.6). More on the experimental timings can be found in Sec. 3.4.

Having passed the S&H, the error signal enters the home-buit PID regulator. The PID regulator generates a regulating signal according to the error signal sent into it to keep the cavity on resonance. After the PID regulator, the regulating signal is added onto a high-voltage offset generated in the cavity lock box thoroughly described in Sec. 3.2.5 and thus controls the cavity length via the piezo-electric transducer. The elements of the feedback chain such as PID regulator, S&H, as well as the cavity lock box are powered with four 24 V lead-acid batteries which were initially put in place to remove the 50 Hz noise of the mains[8].

This is how we frequency-stabilise our cavity – on 'good' days we can observe a locked cavity for several hours. With 'locked' cavity we refer to the cavity constantly staying on resonance with the light of the repump laser and transmitting it. If this is the case and the cavity is locked, the PDH and PID regulator account for all drifts occurring in the environment such as for instance temperature drifts in the laboratory, vibrations or laser frequency drifts. It would be interesting to determine the locked cavity's linewidth over time, however, this is not possible as we cannot lock and scan it at the same time. This

[8] ... and most probably saved the authors' PhD when a surge peak in Dec. 2013 damaged several parts of the lab electronics such as laser and Fabry-Perot-cavity piezo-electric transducers, laser diodes and various other parts.

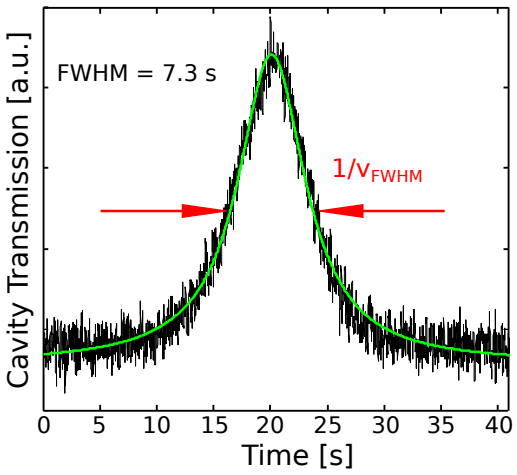

Figure 3.7: Demonstration of the cavity's mechanical stability: We decouple the active locking circuitry shown in Fig. (3.5) from the HV-amplifier and the voltage going to the cavity is put close to resonance. We measure the cavity's transmission on a long oscilloscope trace until the cavity has drifted over the resonance. The data displayed is not post-processed, therefore, we display the data with respect to time in seconds. From this, we can determine drift speed of the cavity spectrally. We see that the cavity's mechanical stability is not a limiting factor experimentally.

topic of scanning the cavity is thoroughly discussed in Sec. 3.2.5.

The most probable causes for an 'unstable cavity lock' is an unstable laser lock caused by mode hops e.g. due to temperature fluctuation in the lab or heavy mechanical vibrations in the building[9].

3.2.4 The cavity's mechanical stability

When we drive the V-STIRAP process, we need the cavity to be completely field-free. Therefore, we need to interrupt the locking circuit, switch off the cavity's active locking procedure described in Sec 3.2.3 for the photon production time of 25 ms. Nevertheless, the cavity needs to stay on or close to the atomic resonance. This is why we also investigate the cavity's passive or mechanical stability.

To measure this potentially limiting factor of the cavity's overall stability, we set the cavity close to resonance with the help of the high voltage offset[10] while the regulating signal coming from the active feedback loop shown in Fig. (3.5) is unplugged from the

[9] The mechanical workshop is close to the lab – the cavity is known to lock much better after 5 pm.
[10] This high-voltage offset is thoroughly discussed in Sec. 3.2.5.

setup. We measure the laser power after the outcoupling mirror of the cavity with the help of a photodiode and a long oscilloscope trace. Fig. (3.7, black) shows a characteristic measurement of the passive or mechanical stability of the cavity. The trace shown in green in Fig. (3.7) is a fitted Lorentzian with a determined full-width half maximum value of 7.3 s. Therefore, we can determine the drift-speed as a function of frequency-drift over time for this characteristic measurement. Taking into account the measurement shown in Fig. (3.7), the ν_{FWHM}, corresponding to the measured 30 MHz in Fig. (3.10) is being traversed in 7.3 s. So, the cavity's frequency drift is on average less than 4.2 MHz/s.

This result shows that – although having its fundamental problems as described above – the cavity is mechanically stable on 'long' timescales and therefore ideal for our purpose as no active feedback can be applied in the $\approx$ 25 ms while the atoms are being driven with the STIRAP pump and repump beams. We conclude that it is the *best of all possible cavities*.

3.2.5 Scanning and frequency locking the cavity

To gain full control of the photon production process, it is essential to know every single parameter of the setup. Characterising the cavity to every respect is therefore crucial. The ability to scan the cavity mirror separation d – which means applying a high-voltage ramp to its piezo-electric transducer – provides a clear picture of its properties. One of its most important parameters which needs to be determined is its linewidth ν_{FWHM}, theoretically introduced in Sec. 2.2.1. To obtain information about the cavity, the resonance condition $m \cdot \lambda_m/2 = d$ needs to be fulfilled. As it can be seen from the equation, we can do this by either varying the the length of the cavity d or change the wavelength λ of the light

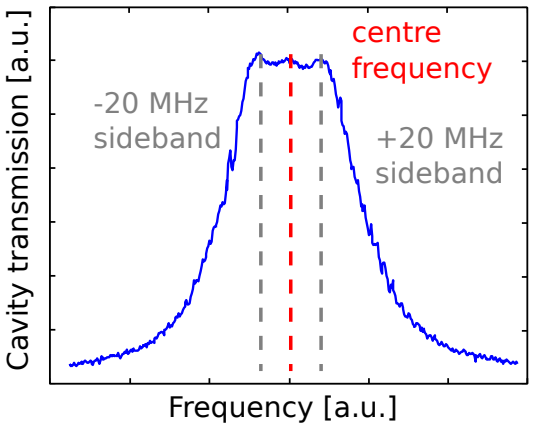

Figure 3.8: In a previous version of the photon-pistol experiment [52, 53], the cavity linewidth has only been determined with frequency markers at ±20 MHz being modulated around the centre frequency of the repump laser. To obtain transmission through the cavity, the laser needed to be scanned. The alternative – scanning the cavity externally – was not available at that point. Reproducing this method's result, it can be seen that the linewidth cannot be measured precisely as the sidebands are hardly separated from the centre transmission. A measurement with the cavity being scanned externally and frequency markers at ±100 MHz can be seen Fig. (3.10).

impinging on the cavity ('scanning the laser').

The first approach that we take to measure the linewidth of the cavity is to vary the wavelength of the laser. In this technique, the sidebands on the repump laser at ±20 MHz around the centre frequency are used as frequency markers. As it can be seen in Fig. (3.8), this technique leads to a rather unsatisfying result as the frequency markers are hardly distinguishable from the centre frequency – they cannot be clearly resolved spectrally. A conclusive fit of three superposed Lorentzians to the data is therefore unsatisfactory. We conclude that the laser's intrinsic 20 MHz sidebands cannot be used to determine this 'broad' cavity's properties.

The second possibility is that we vary the cavity length d. In the setup that the author took over from the previous DPhil students, this was not possible. For this reason, a new electronic circuit had to be designed and constructed to modulate the length of the cavity externally without scanning the laser. This circuitry is presented in the following.

In addition to the ability to modulate the cavity length, we also need to monitor the cavity performance on a daily basis. Therefore, the electronic circuit needs to operate in

two different modes – the *debug* and the *default* mode. In the *debug mode*, the input into the circuit is electronically amplified by a factor of 20. This mode – also referred to as Case I – is only used for characterisation purposes and not on a daily basis. The second operational mode is the *default mode* or Case II. The input into the circuit is not amplified but added on an internal voltage offset which is a user set value between -6 V and +6 V amplified by a factor of 20. The circuit diagram and its operational principle can be found in Fig. (3.9). We refer to the whole electronic circuitry being located after the home-built PID regulator and before the cavity's piezo-electric transducer as the *cavity lock box*. Externally, we see that the box has an input and an output which goes to the piezo. The respective operational mode is chosen by the user with the help of a two-way switch on the front plane of the cavity lock box.

We start with discussing the *debug* mode in detail. In this mode, the Falco amplifier amplifies the user-set *offset* as well as the input signal by a factor of 20. The user-set value of the offset is any value from -6 V to +6 V, which is fed by two standard battery blocks and changed by trimpots on the front panel of the cavity lock box. The battery used as an input into the Falco amplifier is a free-floating potential and never on case ground. However, the Falco[11] amplifier's 0, the signal ground, is on case ground. This mode has been mainly used for externally scanning the cavity to measure its linewidth.

In the *default mode*, the input signal into the cavity lock box is added on top of the user-set HV-offset. The HV-offset is generated by the user by setting any value between -6 V and +6 V multiplied by a factor of 20. This is the standard setting for the experiment being operated on a daily basis. Both the amplifier's 0 as well as the battery's 0 are on the

[11] Low voltage DC/battery powered high voltage amplifier WMA-01, Falco Systems

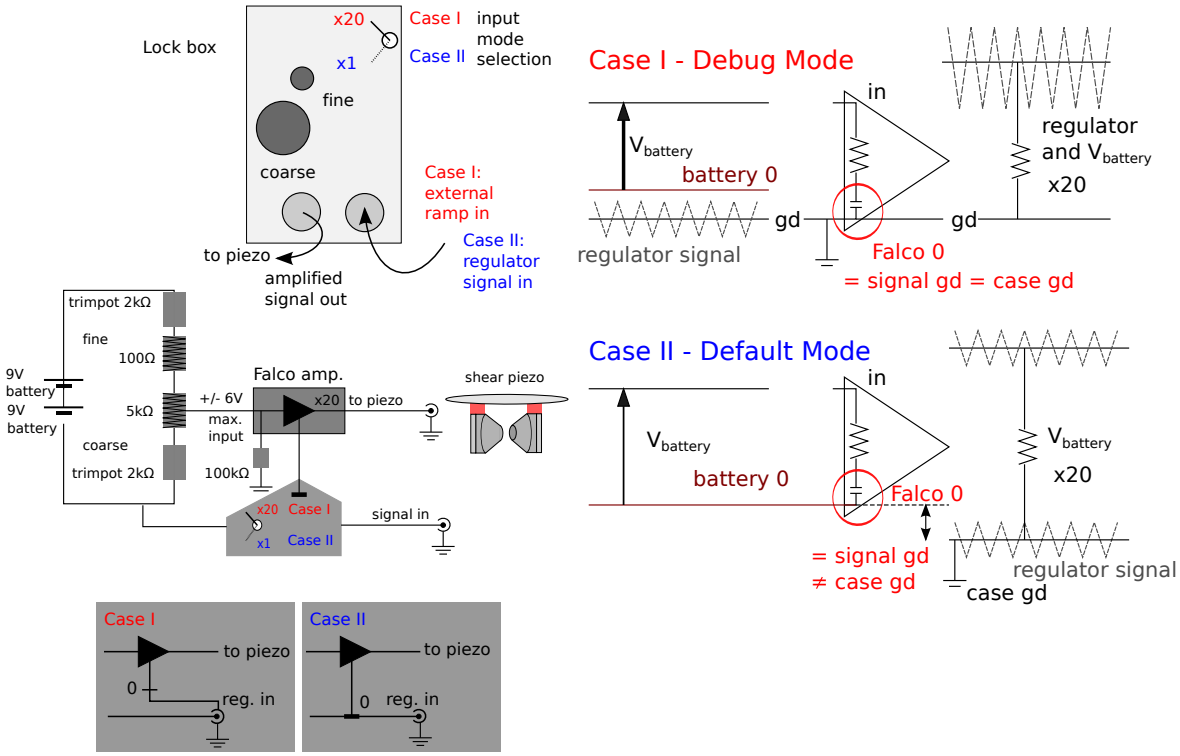

Figure 3.9: The new lock box can be operated in two different modi – labelled Case I and II in this graph. In the *debug mode* (Case I, x20), the user plugs a signal input on the front plane of the cavity lock box, most probably a voltage ramp from a standard function generator. This voltage ramp is amplified by a factor of 20 with the help of the Falco amplifier. The user has to make sure that the battery offset is set to V = 0 to be able of being in complete control with the function generator offset. It has to be noted that there is an additional Zener diode circuit (not displayed) in place to make sure that there in not more that ± 6 V going towards the Falco amplifier. The *default mode* (Case II, x1) provides the daily operational mode. The user sets a voltage from -6 V to +6 V with the help of two batteries and variable resistors. The chosen offset value is then amplified by a factor of 20 with the help of the Falco amplifier. After that, the input signal e.g. the regulating signal from the home-built PID regulator is added on the amplified high-voltage offset.

same level – the signal ground – but not on case ground.

With the possibility of externally scanning the cavity it is also possible to observe the transverse mode spectrum of the cavity which can be seen in Fig. (3.14). Ideally, one would be able of scanning the complete free spectral range of the cavity which could be verified by observing two TEM00 mode. Due to the fact that there is only one piezo-electric transducer one mirror is glued on working as described in Sec. 3.2.2, this is not possible in the current piezo-amplifier-configuration.

3.2.6 The cavity linewidth, length and free spectral range

As already briefly discussed in Sec. 3.2.5, there are two different ways of determining the cavity linewidth. One can for instance scan the laser over the cavity resonance and make use of the laser's side bands at 20 MHz as frequency markers. As the cavity linewidth $\Delta\nu_{\mathrm{FWHM}}$ is of the order of 30 MHz for the TEM00 mode, it is hard to properly calibrate the frequency reference of 40 MHz as the 20 MHz sidebands peaks are not well resolvable. This can be observed in Fig. (3.8). A different approach is to scan the cavity over resonance externally and at the same time modulate frequency sidebands of $\pm$100 MHz onto the laser. The sidebands are used to calibrate the frequency axis.

In Fig. (3.10), a least-squares fit and experimental data for the linewidth of a TEM00

mode[12] of the cavity is shown. A triple Lorentzian (green line) of the form

$$y = y_0 + \frac{2A_\mathrm{l}}{\pi}\frac{w_\mathrm{l}}{4(x-x_{0\mathrm{l}})^2+w_\mathrm{l}^2} + \frac{2A_\mathrm{m}}{\pi}\frac{w_\mathrm{m}}{4(x-x_{0\mathrm{m}})^2+w_\mathrm{m}^2} + \frac{2A_\mathrm{r}}{\pi}\frac{w_\mathrm{r}}{4(x-x_{0\mathrm{r}})^2+w_\mathrm{r}^2}, \tag{3.1}$$

is fitted to the data with the help of a self-programmed Matlab routine based on the Matlab internal function *nlinfit*. A_i refers to the amplitude, w_i to the FWHM width, and $x_{0\mathrm{i}}$ to the position of the respective Lorentzian, $\mathrm{i} \in \{\mathrm{l}, \mathrm{m}, \mathrm{r}\}$ corresponding to left, middle and right. The results for the respective fit parameters have been printed into the figure as it can be seen in Fig. (3.10). The shown data is one linewidth measurement with the scan frequency of the cavity piezo of 20 Hz and a 190 mV peak-to-peak scan amplitude[13]. Before the data is taken, it is made sure that the incoupling of the TEM00 mode into the cavity is maximised. To estimate an error on the determined linewidth value, we take several measurements with different scan speeds between 10 Hz and 65 Hz with a constant, minimal peak-to-peak scan amplitude and at the correct wavelength of 780.2±0.1 nm measured with a Highfinesse[14] wavelength meter. The given error corresponds to the manufacturer's specified error. The result can be found in Fig. (3.11). As cavity linewidth we find $\Delta\nu_\mathrm{FWHM}$ = 29.6±0.4 MHz[15].

While characterising the cavity, it is is observed that there is a dependence of the cavity's linewidth on

[12] The 100 MHz sideband modulation on the laser has been added with an experimental trick by not using the regular 20 MHz sideband modulation but instead the VCO of one of the cooling laser's AOMs at 98.1 MHz as a frequency reference. Obviously, the laser has to be operated free running and not locked for these measurements.

[13] Measured data taken on 22/07/2013.

[14] That is the brand.

[15] Error calculation: Δ = max. value - value at 0 sweep rate (extrapolated).

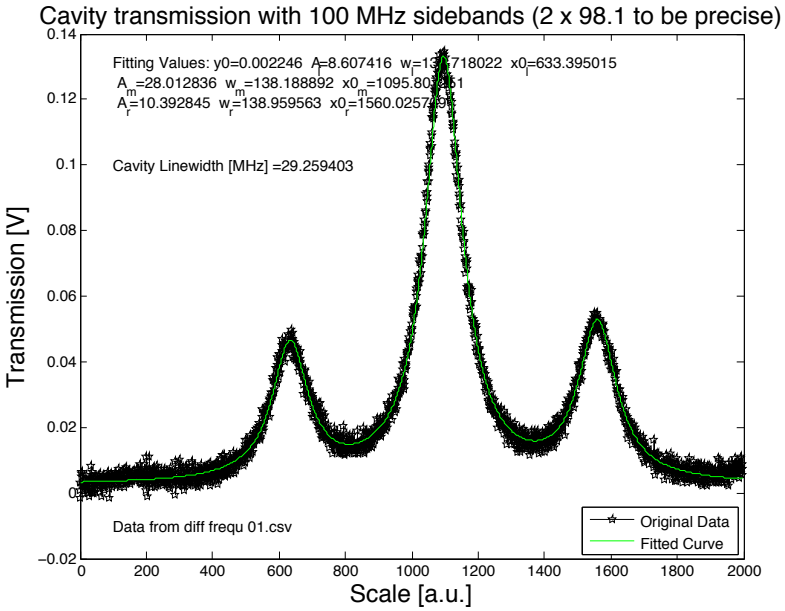

Figure 3.10: Fit to determine the linewidth of the cavity [example, measurement with 190 mV peak-to-peak amplitude on the cavity piezo, 20 Hz scan frequency]: 100 MHz sidebands are modulated onto the Bias-T of the laser with the help of an independent RF-source. The trace (black stars) has been taken by a fast photodiode, monitoring the output of the cavity. The incoming wavelength of the laser light is 780.2±0.1 nm (measured with a wavelength meter). A sum of three Lorentzians as shown in Eq. (3.1) is fitted to the data with a self-programmed fit routine in Matlab. We observe a ν_{FWHM} of $\approx$ 30 MHz.

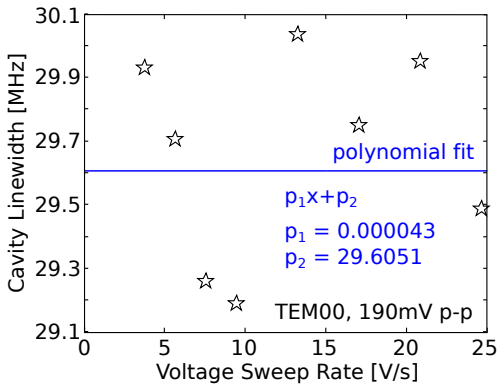

Figure 3.11: Cavity linewidth at the correct laser wavelength: We do not see a clear dependence of the linewidth on the voltage sweep rate if we change the scan frequency and keep the peak-to-peak amplitude of the voltage ramp constant. The extrapolated value at 0 V/s corresponds to the actual linewidth.

- the laser wavelength (equivalently the laser current),
- the voltage sweep rate of the scan on the piezo-electric transducer, not based on the variation of the scan frequency but on the variation of the peak-to-peak voltage amplitude,
- the transmitted optical mode.

However, we need to distinguish between an 'apparent' and 'real' linewidth change. An example for this difference between these two can be found in Fig. (3.12).

We observe a strong dependence of the cavity's linewidth on which mode is transmitted as shown in Fig. (3.12, left). We take these measurements with the minimal experimentally possible peak-to-peak voltage amplitude of 190 mV on a function generator going towards the lock box. There, the peak-to-peak voltage is multiplied by 20 as we are in the *debug mode* as introduced in Sec. 3.2.5. The peak-to-peak voltage as well as the incoupling into the cavity remains untouched such that we are able of comparing the measurements to each other. We observe that the TEM00 linewidth is quite high, then the value drops for

the TEM01 and TEM02 modes. For the TEM03 and TEM04 it increases again but not to the full TEM00 linewidth. We stop determining the linewidth for TEM modes beyond the TEM04 mode, as the electronic signal on the photodiode gets too small and we abstain from maximising the incoupling on a different higher-order mode, as we want to keep the comparability between measurements as already mentioned. The observed behaviour is consistent with the theory that a defined dirt particle has ended up on the cavity mirrors. This behaviour can be explained in the following way: The location of the TEM00 mode inside the optical resonator is only dependent on the incoupling of the light. With a certain incoupling into the cavity, a local dirt spot on the mirrors results in a higher loss rate, a lower finesse and ultimately a broader linewidth locally. If we therefore hit the dirt particle with our incoupling, the TEM00 modes will see a higher loss rate which ultimately results in a higher measured linewidth. But the question is why we see different linewidths for different TEM modes. An ideal cavity with perfect cylindrical symmetry shows Laguerre-Gauss modes. As soon there is an imperfection in the substrate with which the mirrors are coated, the prefect symmetry will be lost and Hermite-Gauss modes will form which are not rotationally invariant[16]. This is what we see in almost every resonator. Consequently, a local area of increased loss can act as a symmetry breaker which defines the coordinate system of the modes. The higher-order modes have the ability of rotating around their centre to avoid the area of increased loss and therefore, we see a lower linewidth for instance for the TEM01 mode than the TEM00 mode. This is why one could potentially map out the areas on the mirror with a higher loss rate such as caused by dirt.

[16]A different reason why Hermite-Gauss modes could form inside the cavity is that the mirrors are not aligned coaxially perfectly. In this case, not the dirt spot acts as a symmetry breaker but the alignment of the mirrors. Nevertheless, the argument that the Hermite-Gauss modes can avoid the areas of the mirrors with increased loss still holds.

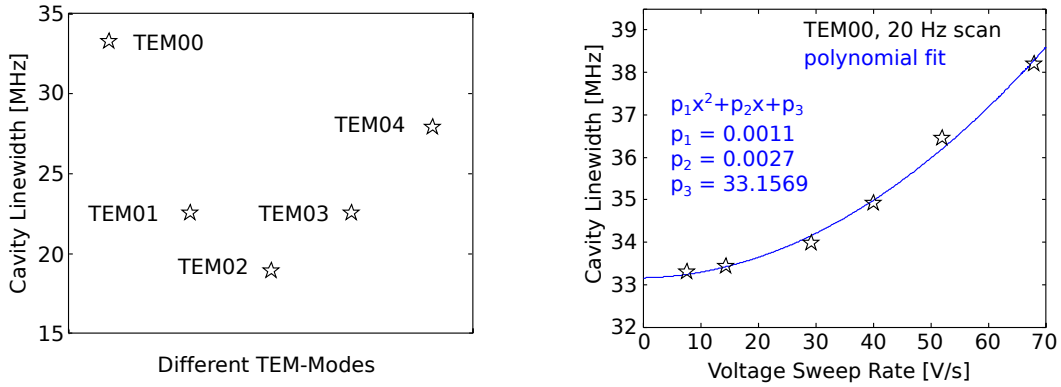

Figure 3.12: Difference between 'real' (left) and 'apparent' (right) cavity linewidth change: Dependency of the linewidth on which mode is transmitted by the cavity (left). We take this data with constant laser power and peak-to-peak scanning voltage at 20 Hz scanning frequency. Additionally, we do not recouple the mode between measurements to rule out addressing different parts of the cavity mirrors. This measurement result is consistent with a dirt spot being one the high-reflective cavity mirrors. (Right) An example of an 'apparent' linewidth change: We determine the linewidth for the TEM00 mode and different voltage sweep rates. The 'actual' linewidth is the one extrapolated for 0 V/s voltage sweep rate. For this wavelength, it was found to be around 33 MHz.

An example for an 'apparent' change of the cavity's linewidth can be found in Fig. (3.12, right). We observe an increase of linewidth the higher our cavity sweep rate is. The sweep rate is determined by the peak-to-peak scan amplitude (in Volts) the cavity's piezo-electric transducer is being scanned with and the time taken to do so. Please note that these measurements are taken in the *debug mode* of the cavity lock box. We observe that the linewidth apparently increases, the higher the voltage sweep rate is. This does not seem to happen in a linear but in a polynomial way. By fitting a second order polynomial function $\propto p_3x^2 + p_2x + p_1$ to the data in Matlab[17], we can extract the value for the linewidth at 0 V/s voltage sweep rate which is 33 MHz. Calculating the residual variance R^2[18] from this fitted model, we find that the second order polynomial equation predicts 99.4% of the variance in the linewidth. We believe that this is not an actual change in

[17] Internal Matlab function polyval

[18] $R^2 = 1 - SS_{resid}/SS_{total}$, where SS_{resid} is the residual sum of squares and SS_{total} is the total sum of squares of the linewidth multiplying by the variance of the linewidth by the number of observations minus 1.

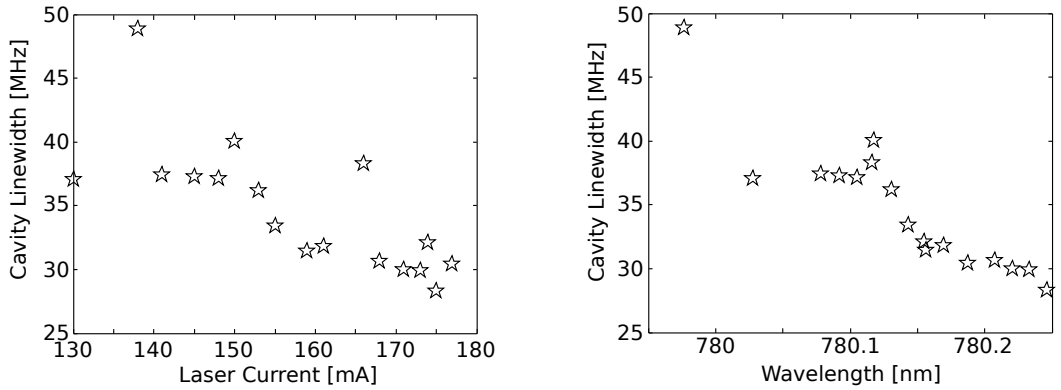

Figure 3.13: Dependence of linewidth on laser current and laser wavelength, respectively. We scan the cavity with a 190mV peak-to-peak voltage amplitude and a 20 Hz scan frequency. The incoupling remains constant over the whole measurement and we detect the TEM00 mode.

linewidth but that we actually see the photodiode's limit in bandwidth of 300 kHz[19] we use to measure the linewidth. This behaviour can be seen clearly experimentally when the resonance is scanned too quickly. This is why we also use the voltage sweep rate – the transversed voltage per time unit – as a parameter due to the fact that it includes both the scan amplitude and the scan frequency.

As a final investigation, we measure the dependence of the cavity's linewidth on the wavelength of the laser. We do this by changing the laser current and the respective results can be found in Fig. (3.13). Two potential influence factors that could explain this behaviour are the optimised coating of the cavity mirrors to our experimental wavelength as well as the fact that different laser currents imply different laser powers which lead to different intensities inside the cavity.

We conclude this experimental Section with a measurement of a 'comb' of transverse modes of the cavity as shown in Fig. (3.14). We scan the cavity with a function generator over a voltage of 80 V peak-to-peak amplitude. By observing the output of the cavity, we can see the transmission of several transverse modes, from the TEM00 to the TEM06,

[19]Homebuilt device with OPT210 photodiode.

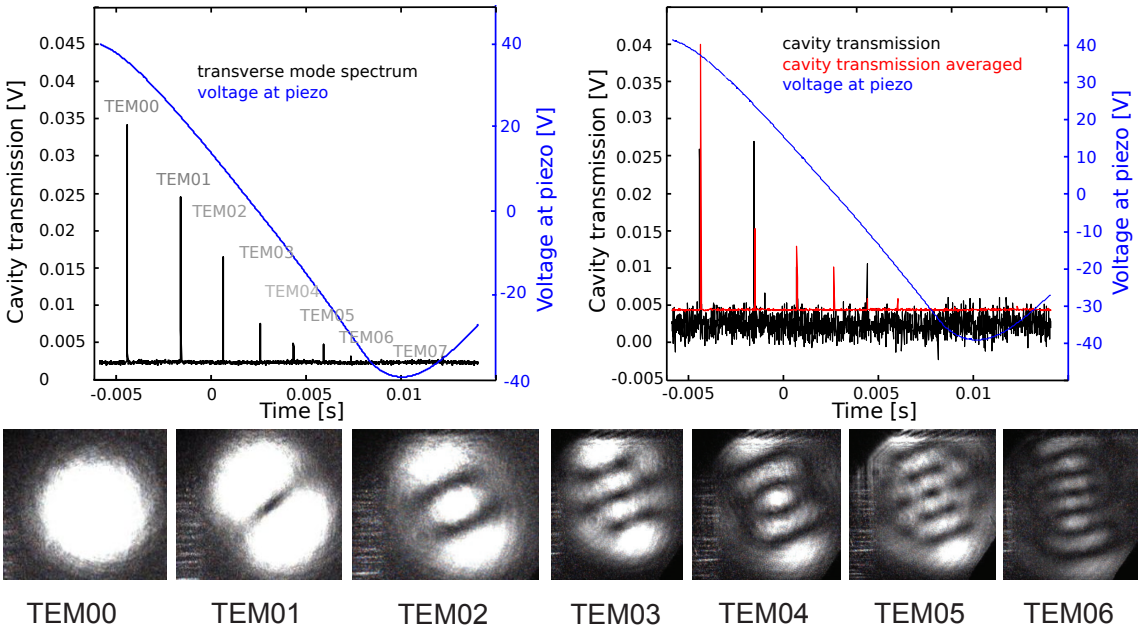

Figure 3.14: Spectrum of transverse modes: The cavity is scanned with the help of a function generator and the cavity lock box introduced in Sec. 3.2.5 over a distance of about 200 nm in 15 ms, corresponding to a change in piezo voltage between ± 40 V. This corresponds to a peak-to-peak voltage amplitude of 80 V. The light input power into the cavity has to be set to about 1 mW, just below the theoretical damage threshold of the cavity mirror coating. The cavity input beam is aligned such that it couples into all transverse modes, in contrast to the otherwise preferred coupling into the TEM00 mode only. The images below the graphs show the transverse modes the cavity transmits for each transmission peak. The output power is in the range of 10 - 100 nW. The blue trace shows the voltage which goes to the piezo and therefore modulates its length. The black trace corresponds to the transmission of the cavity. No post-processing has been applied in these two sets of data, only the oscilloscope's internal 'averaging' mode has been used in the plot on the left but not on the right. The images shown are taken with an Imagesource Camera observing the output of the cavity.

which we also show below the graphs. In reality, the transverse modes are equally spaced on their time axis, however, due to the nonlinearity of the piezo-electric transducer which we discuss in Sec. 3.2.2, they are not. We do not apply any post-processing on the data, simply use the oscilloscope's interal averaging function to obtain these traces.

Potential room for error in all of these measurements are the frequency noise and the linewidth of the laser, also the detector bandwidth as well as acoustic noise and nonlinearity of both the applied voltage ramp and the cavity piezo. The linewidth of the laser has

been determined to be around 400 kHz, so this is well below the measured linewidth of the cavity around 30 MHz. The nonlinearity of the piezo-electric transducer is discussed in Sec. 3.2.2, but due to the present amplification, we can only scan in the linear regime. A final potential error are imperfections in the voltage ramp we apply to the piezo. The cavity lock box including the Falco amplifier described in Sec. 3.2.5 acts as a low pass filter. This is why the edges of the voltage ramp are rounded after passing the amplifier setup which can for instance be seen in Fig. (3.14). We circumvent this problem in linewidth measurements by experimentally making sure that the transmission of the cavity is always halfway between both peaks of the voltage ramp.

3.2.7 Frequency spacing of the transverse modes

To fully characterise the cavity's properties and to therefore calculate its length and finesse, the spacing of the transverse modes has to be determined. This can be achieved with the help of the diode laser which is usually used to lock the cavity. If this laser is scanned over the maximum possible range, we are capable of seeing the TEM00 and TEM01 modes of the cavity being transmitted. While the laser is scanned, its error signal of the Rubidium spectroscopy – normally used to lock the laser frequency to – is taken as a frequency marker of 6.8 GHz, the hyperfine splitting in the F = 1 to the F = 2 energy level. With the frequency marker of 6.8 GHz, the separation of the TEM00 and TEM01 transverse mode is calculated to be 36.8$\pm$0.1 GHz, which can be seen from the experimental data displayed in Fig. (3.15).

In principle, this is sufficiently precise because the hyperfine splitting is of the same order of magnitude as the expected 30 to 40 GHz mode splitting. It would be better to use

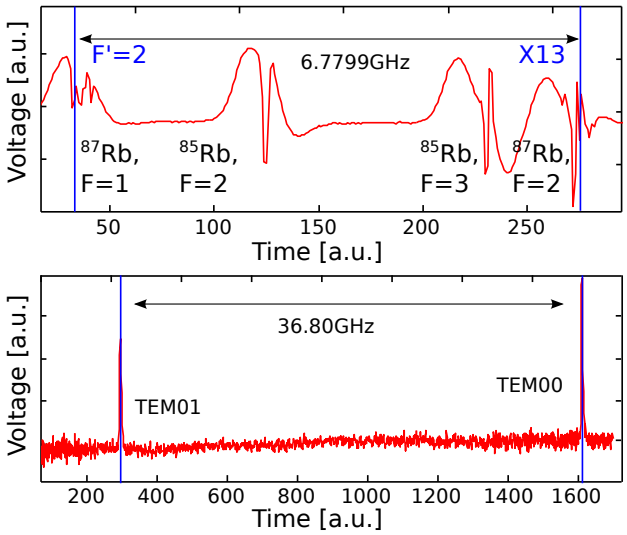

Figure 3.15: Determining the frequency spacing of the transverse modes: The laser is scanned (mode-hop free) such that the TEM00 and the TEM01 mode are clearly identified on the cavity transmission photodiode. For practical reasons, the error signal of the Rubidium spectroscopy is used as a 'frequency marker'. The frequency difference in the Rubidium spectrum between the F = 1 $\rightarrow$ F' = 2 energy level to the crossover resonance F = 2 $\rightarrow$ X13 is calculated to be 6.7799 GHz. This calibration results in a frequency spacing of the TEM00 and TEM01 mode of 36.8$\pm$0.1 GHz.

a Fabry-Perot test cavity instead with equally spaced 'frequency markers'[20]. However, the explained method can be quickly implemented and just needs a well set-up laser system.

To complete the characterisation of our cavity, we extend the formalism already introduced in Section Sec. 2.2.1. Having determined the spacing of the transversal modes experimentally, it is possible to determine the length of the cavity as well as its free spectral range (FSR), finesse, and number of modes within the free spectral range. From the following equation we learn the relationship of ν_{trans} and ν_{FSR}

$$\Delta\nu_{\text{trans}} = \frac{1}{\pi}\Delta\nu_{\text{FSR}} \arccos\left(1 - \frac{d}{R_{\text{c}}}\right), \tag{3.2}$$

where $\Delta\nu_{\text{trans}}$ is the splitting of the transverse modes, $\Delta\nu_{\text{FSR}}$ is the free spectral range, d is the cavity length and R_{c} the radius of curvature of the cavity mirrors. The radius of curvature is assumed to be a constant, R_{c} = 5 cm, as specified by the company which

[20] There is room for error as we have to operate the laser system at its maximum capacity, in particular, we have to operate the laser piezo at its maximum amplitude for a certain amount of time until the measurement is taken.

fabricated the mirrors. In addition to that, the free spectral range of the cavity can be written as

$$\Delta\nu_{\text{FSR}} = \frac{c}{2d}, \tag{3.3}$$

where c is the speed of light. Therefore, the Eq. (3.2) calculates to

$$\Delta\nu_{\text{trans}} = \frac{1}{\pi}\frac{c}{2d}\arccos\left(1 - \frac{d}{R_{\text{c}}}\right). \tag{3.4}$$

We cannot calculate the length d of the cavity by just inverting this Equation, we have to solve it numerically with the help of Mathematica. The result is a cavity length d = 67.36±0.40 μm. The error is calculated by the error of the spacing of the transverse modes $\Delta\nu_{\text{trans}}$ and by converting this into a length error. By taking the result for the cavity length and inserting it into Eq. (3.3), we can determine the free spectral range to be $\Delta\nu_{\text{FSR}}$ = 2.33±0.01 THz. As a final characterisation measurement, the finesse – the quality factor of the cavity – is determined. It is a fraction of $\Delta\nu_{\text{FSR}}$ over $\Delta\nu_{\text{FWHM}}$ and has already been introduced in Sec. 2.2.1 in Eq. (2.4). The linewidth of the cavity $\Delta\nu_{\text{FWHM}}$ is determined in Sec. 3.2.6 to be $\Delta\nu_{\text{FWHM}}$ = 29.61±0.43 MHz.

To conclude, we summarise all characterisation measurements in the following

d	=	67.35±0.40 μm
$\Delta\nu_{\text{trans}}$	=	36.80±0.11 GHz
$\Delta\nu_{\text{FSR}}$	=	2.23±0.01 THz
$\Delta\nu_{\text{FWHM}}$	=	29.61±0.43 MHz
$\mathcal{F}$	≈	74 700
$\#_{\text{modes}}$	≈	61

In previous work [52], the latter values were determined [sic]

d	=	74 μm
$\Delta\omega_{\text{trans}}$	=	$2\pi \cdot 35$ GHz
$\Delta\omega_{\text{FSR}}$	=	$2\pi \cdot 2.0$ THz
$\Delta\omega_{\text{FWHM}}$	=	$2\pi \cdot 23.74$ MHz
$\mathcal{F}$	=	85 000

From these values, it seems as if the cavity has 'shrunk' miraculously by about 10 μm. We can think of two possible explanations for this difference. The first explanation is that one local dirt spot ended up on the cavity mirrors increasing the linewidth by about 6 MHz. A second explanation is that the fit of three Lorentzians to the measurement with 20 MHz sidebands as demonstrated in Fig. (3.8) was imprecise and the calculated length difference is just resulting from this imprecision.

3.3 Loading atoms into the cavity

In this Section, we describe the operation of the atomic fountain which is used to introduce cold Rubidium atoms into the cavity. The theory has been already described in Secs. 2.4.2 and 2.4.3. In Sec. 3.3.1, we discuss the absorption imaging technique to characterise the cold atoms. We determine all important parameters of the magneto-optical trap in Sec. 3.3.2, in particular its loading, expansion and temperature. The respective parameters of the atomic fountain are discussed in Sec. 3.3.3.

3.3.1 Absorption imaging

The absorption imaging technique is a powerful tool to observe a cold atomic cloud – may it be in its stationary or dynamic phase. An example of this imaging technique can

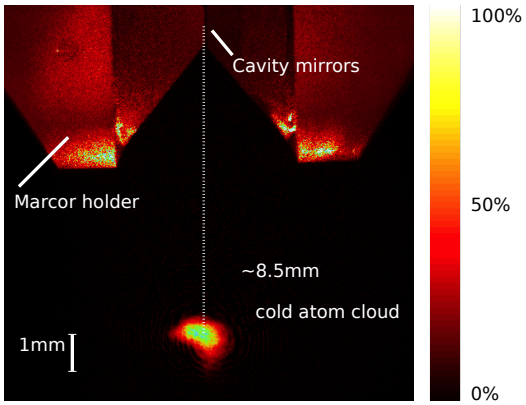

Figure 3.16: Position of cold atom cloud and cavity, the picture is taken with the help of the absorption imaging technique: In a magneto-optical trap, the atoms are cooled down at a position roughly 8 to 9 mm below the centre of the vacuum mode of the cavity. After being cooled, the atoms are launched upwards.

be found in Fig. (3.16) as well as the experimental setup in Fig. (3.17). The absorption imaging method works on the cooling transition F = 2 to F' = 3 of the Rubidium atoms. We illuminate the cold atomic cloud with an atomic resonance frequency of ω_0 with light of frequency ω, where ω - ω_0 = 1.2 MHz[21]. Therefore, the incoming light is blue-detuned from the cooling resonance. This is done by shifting the cooling laser locked to the crossover resonance X13 by 106.5 MHz twice in an AOM double-pass configuration. Having passed the AOM, the frequency-shifted light is coupled into a fibre and sent into the absorption imaging beam line in front of the vacuum chamber. There, the beam is enlarged with the help of a telescope, such that it illuminates the whole area between the position of the MOT and the cavity inside the vacuum chamber. After leaving the vacuum chamber, the light is detected with the help of a camera (Imaging source DMK 21BF04). As the cold atomic cloud absorbs light from the absorption beam, it leaves a shadow on the image taken by the camera. This can for instance be seen in Fig. (3.18, left). After having taken a first image, a second image is taken with the cooling beams switched off. The picture shown in Fig. (3.18, middle) serves as a reference image as it basically shows us the background of the measurement, in particular the absorption beam with no cold

[21]This detuning has been found experimentally to give the highest contrast in the absorption imaging pictures.

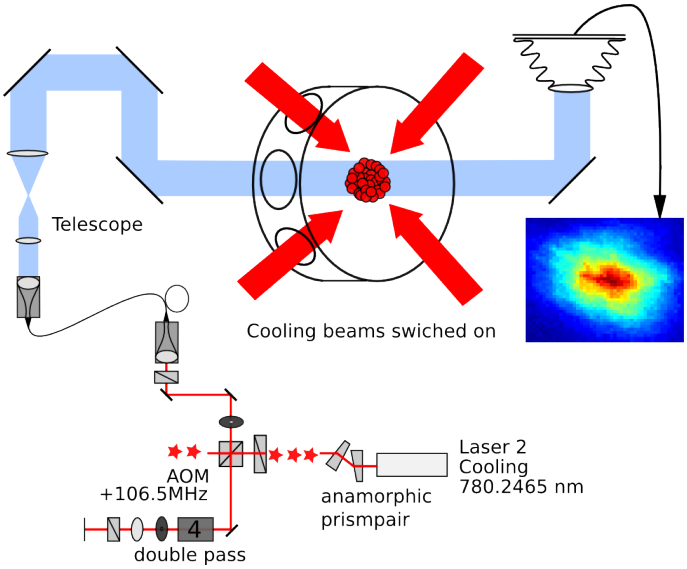

Figure 3.17: Absorption imaging setup: To provide the 1.2 MHz blue-detuned light for imaging, we tap off light from the cooling laser, frequency-shift it by twice 106.5 MHz and couple it into a fibre. When coupled out of the fibre, the beam is enlarged with the help of a telescope-type setup and enters the vacuum chamber via the middle viewport. Inside the chamber, it illuminates the cold atomic cloud. With the help of an Imagesource camera we take two pictures: One with all MOT beams as well as the illumination switched on and a reference picture just with the illumination do determine the background in the measurement.

atom cloud present.

For post-processing, we need to look into the attenuation of laser light by the atomic cloud. The intensity of the beam, attenuated by the absorption of the atomic cloud, reads

$$I(O.D.) = I_0 \cdot \exp\Big(-\frac{O.D.\,\Gamma^2}{4(\omega-\omega_0)^2+\Gamma^2}\Big), \tag{3.5}$$

where $O.D.$ is the optical density of the cloud, I_0 the initial intensity of the beam, Γ the linewidth of the transition, ω_0 the frequency of the transition and ω the frequency illuminating the cold atomic cloud. The optical density is defined as $O.D. = N_{\text{pixel}}\sigma_0 l$, where σ_0 is the resonant cross section of the transition, l is the thickness of the cloud and

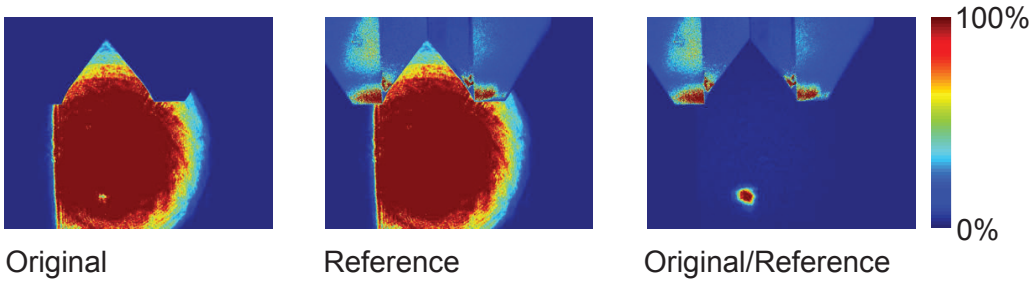

Figure 3.18: Absorption images: (Left) camera image of the absorption. The beam displayed in red is the illumination beam. The area where a yellow shadow is visible is the area where the cold atomic cloud absorbs light from it. To properly correct for the background of the measurement, a reference picture with no cold atomic cloud present is also taken (middle). While the reference image is taken, one of the cooling beams is still switched on such that the light scatters off the cavity mirrors and their mounts, to give a hint about where with respect to the cavity the cold atomic cloud is located. (Right) This image is the result of dividing the left picture by the second one according to Eq. (3.5).

N_{pixel} the number of atoms per observed pixel. By applying Beer's law

$$dI/dz = -\sigma_0\,\rho(x,y,z)\,I, \tag{3.6}$$

$$\text{we can see that } I = I_0\,\exp(-\sigma_0\,n(x,y)), \tag{3.7}$$

where $n(x,y) = \int_{-\infty}^{\infty} dz\,\rho(x,y,z)$ is the density of atoms in the (x,y) plane. Accordingly, we can calculate

$$\ln\Big(\frac{I(O.D.)}{I_0}\Big) = 0.97\cdot O.D., \text{ where } O.D. = -\sigma_0\,n(x,y). \tag{3.8}$$

Therefore, the number of atoms in one pixel is $N_{\text{pixel}} = n_{\text{pixel}}\cdot A_{\text{pixel}}$[22], where n_{pixel} is the atom density measured per pixel and A_{pixel} is the corresponding area. The total number of atoms therefore is $N_{\text{tot}} = \sum_{\text{all pixels}} N_{\text{pixel}} = \sum_{\text{all pixels}} n_{\text{pixel}}\,A_{\text{pixel}}$. These calculations are

[22] We use $A_{\text{pixel}} = l_{\text{pixel}}^2 = (0.0257\text{ mm})^2$. This number is not the area of a 'physical' pixel but the area the pixel observes. This calibration is done with the help of the diameter of the tips cavity mirrors which is well known.

carried out with a Matlab routine and we typically find atom numbers of $4 \cdot 10^6$ atoms in the MOT phase.

To optimise the performance and repetition rate of the apparatus, we use this absorption imaging technique. In particular, we measure the MOT's loading speed, its expansion velocity as well as its temperature in Sec. 3.3.2. We also characterise the speed of the atoms in the atomic fountain in Sec. 3.3.3. To conclude, we show a routine application of the absorption imaging technique in Fig. (3.19).

3.3.2 The MOT loading, expansion and temperature

The quicker we are able of loading the magneto-optical trap, the better[23]. Besides the alignment of the MOT cooling beams, their intensity, their radius and the B-field which we assume optimised before operating the experiment on a daily basis, there is one crucial factor which increases the loading rate of the MOT – the background pressure of Rubidium in the vacuum chamber. The Rubidium atoms in the chamber are provided by Alvatec getter[24]. We can influence the amount of Rubidium getting into the chamber by changing the current going to the dispenser manually. In Fig. (3.20), we see the Rubidium pressure increasing over the course of the day as the getter is left running. This leads to a larger number of atoms in the MOT and also shorter loading times. However, these timescales are much too slow to *instantaneously* increase the background pressure of Rubidium inside the chamber to rapidly load the MOT. A much quicker way to do so is to apply light-induced atom desorption (LIAD) [58, 59]. Atoms are adsorbed to the walls of the vacuum

[23] This is easy to see taking our experimental sequence into account which is introduced in Sec. 3.4. Shorter MOT loading times lead to a higher experimental repetition rate.

[24] Alvasource AS-5-Rb-160-S

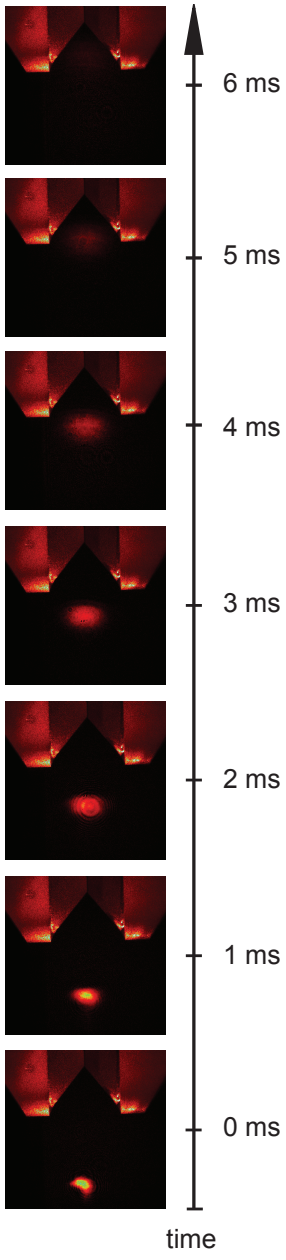

Figure 3.19: This Figure shows a routine application of the absorption imaging technique: It is an easy way to check whether the atoms are flying straight up towards and eventually reach the cavity. The time between each picture is 1 ms. The detuning of the upper and lower MOT beams is 1 MHz, which results in an approximate speed of the atoms of 1 m/s. The pictures are false colour images (LabView's 'temperature map').

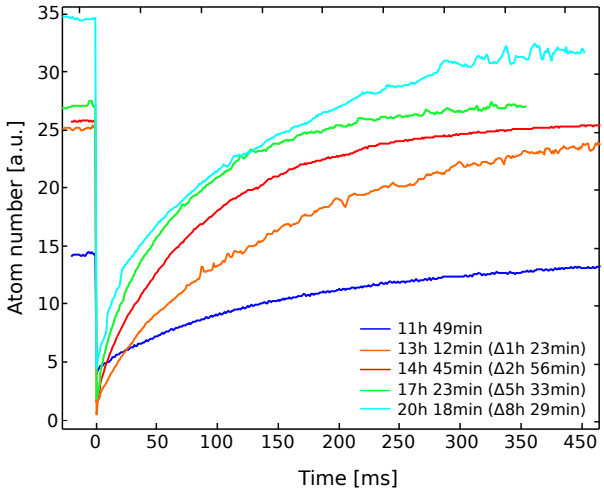

Figure 3.20: MOT loading velocity: At time t = 0 ms, the MOT beams are briefly switched off and back on again with the help of an AOM. This graph shows empirically how quickly and how full the MOT loads according to the amount of Rubidium atoms inside the vacuum chamber during the day. The time Δ is the time elapsed from the switch on time of the dispenser. The Rb-dispenser has been switched on before the first measurement and has been running on the same settings all day.

chamber and by shining strong UV light, they can be desorbed and again take part in the MOT cooling cycle. This leads to a temporary increase of the Rubidium pressure in the chamber. It has been experimentally found [59], the shorter the wavelength, the more atoms can be desorbed. In our experiment, we use an LED array at 400 nm wavelength to load the atoms faster into the MOT.

As a next step, we want to determine the temperature of the MOT cloud, which we do with the help of its expansion velocity after having switched off the MOT cooling beams. The diameter $\sigma_{\mathrm{x}}(t)$ of the cloud after a certain period of time t in one dimension can be calculated by

$$\sigma_{\mathrm{x}}(t) = \sqrt{\sigma_0^2 + v_{\mathrm{x}}^2 t^2}, \tag{3.9}$$

where σ_0 is the initial diameter of the cloud and v_{x} is the RMS (root mean square) velocity in one dimension. According to the kinetic gas theory, v_{x} can be expressed by

$$v_{\mathrm{x}}^2 = \frac{k_{\mathrm{B}} T}{m}, \tag{3.10}$$

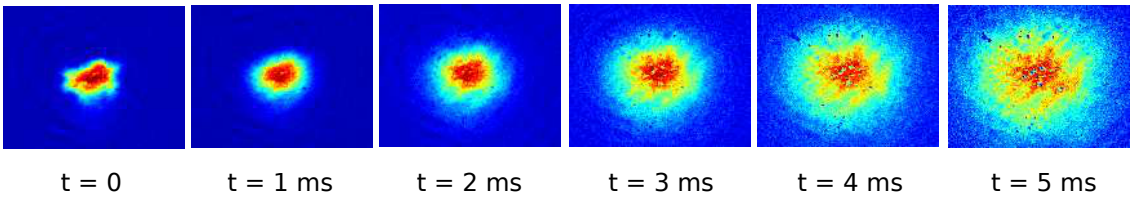

Figure 3.21: Determining the temperature of the atomic cloud with the help of its expansion velocity: At time t = 0 ms, the MOT beams are switched off and the cold atom cloud expands. By fitting a 2D-Gaussian to the image of the MOT, the expansion velocity of the cloud and therefore its temperature can be calculated.

where k_B is the Boltzmann constant, m = 144 · 10^{-27} kg, and T the temperature of the atoms. By inserting Eq. (3.10) into Eq. (3.9) and fitting the resulting function to the pictures acquired with the help of the absorption imaging technique, we can find the temperature of the atomic cloud. For the sequence of pictures in Fig. (3.21), we find temperatures of 78±36 μK and 124±42 μK, evaluating the data for the expansion in x- and y-direction, respectively. By decreasing the time between the measurements and choosing a smaller step size for time t, one could decrease the error bars.

3.3.3 The MOT in motion – the atomic fountain

There are different ways of getting an atom between the mirrors of a high-finesse optical cavity. They can be prepared above the cavity and dropped [8], or below the cavity and launched upwards [60]. The latter approach has the advantage that the gravitational force acts in the opposite direction compared to the direction of motion of the atoms. Therefore longer interaction times can be achieved as compared to the first approach, where gravity speeds the atoms up even more.

Another approach is to trap the atoms inside the cavity using a blue-detuned auxiliary laser [61]. This approach means the atoms are trapped for an extremely long time. How-

ever, the atoms are subject to an ac-Stark shift due to the E-field of the dipole trapping laser which can affect the photon production process. Furthermore, this approach suffers from the disadvantage that the atoms heat up inside the trap and a cooling cycle needs to be run to cool the atom back down.

In the earlier stages of this experiment, it had been decided to follow the atomic-fountain approach. The atoms are first cooled down to temperatures of around 100 μK then launched upwards. This low temperature is necessary as otherwise the spread of the atomic cloud due to the atom's thermal velocity would be too pronounced. It has to be stated that in our experiment the loading into the cavity is probabilistic, however, as soon as one single atom interacts with the vacuum mode of the cavity, the single photon production is deterministic. On the time-scales of the photon production, the atom is quasi-stationnary – experimentally, we observe interaction times of atoms and cavity of 80 μs whereas the production of a photon takes 1 μs. The two-atom contribution can be kept negligible experimentally due to low atom densities, e.g. short MOT loading times and low Rubidium background pressure.

In this Section, we want to discuss how our actual atomic fountain behaves experimentally. We already know that the velocity of the atoms can be expressed by $v = \sqrt{2}\lambda\Delta f$, where v is the velocity of the atoms, λ is their wavelength, and Δf is the frequency detuning of the MOT beams with respect to each other [46, 60]. This equation describes that the atoms are cooled into a *moving* rest frame. The atoms see the incoming light on resonance with the F = 2 to F' = 3 transition due to the Doppler shift as they move upwards with the finite velocity v in the laboratory frame. The factor $\sqrt{2}$ can be explained by the geometric arrangement of our MOT cooling beams (45° to the vertical).

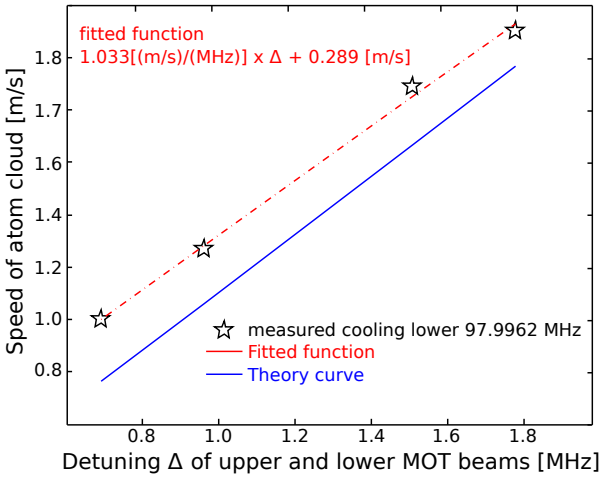

Figure 3.22: Comparing the real cold atom cloud velocity with the expected one: We observe a linear behaviour in both the experimental as well as in the expected data. The gradients are comparable. However, there is an offset of 0.3 m/s, meaning the atoms are quicker than expected. This can be explained by an intrinsic frequency offset of 150 kHz between upper and lower cooling beams or an offset in the calibration of the CCD pixel size/imaged area.

By observing the flight of the cold atoms towards the cavity and taking a picture every millisecond for the following six milliseconds, we can determine the diameter of the MOT in vertical and horizontal direction (x,y) by fitting a 2D-Gaussian to the shape of the atom cloud. This allows to characterise

1. the velocity of the real atomic cloud compared to the expected velocity $v = \sqrt{2}\lambda\Delta f$.

2. the detuning Δf between upper and lower MOT beams in the launch phase leading to the slowest atoms.

3. the best MOT-cooling parameters to obtain an atomic cloud with the least expansion (or homogenic expansion) in both the horizontal and vertical direction during the flight.

When measuring the velocity, we chose the frequency of the cooling lower beam as our master frequency and detune the frequency of the upper beam accordingly. As described above, we take one picture per millisecond while launching the atoms such that we can determine the speed of the atomic cloud with respect to the detuning of the upper MOT beam. The result of the measurement can be found in Fig. (3.22) as well as the theory

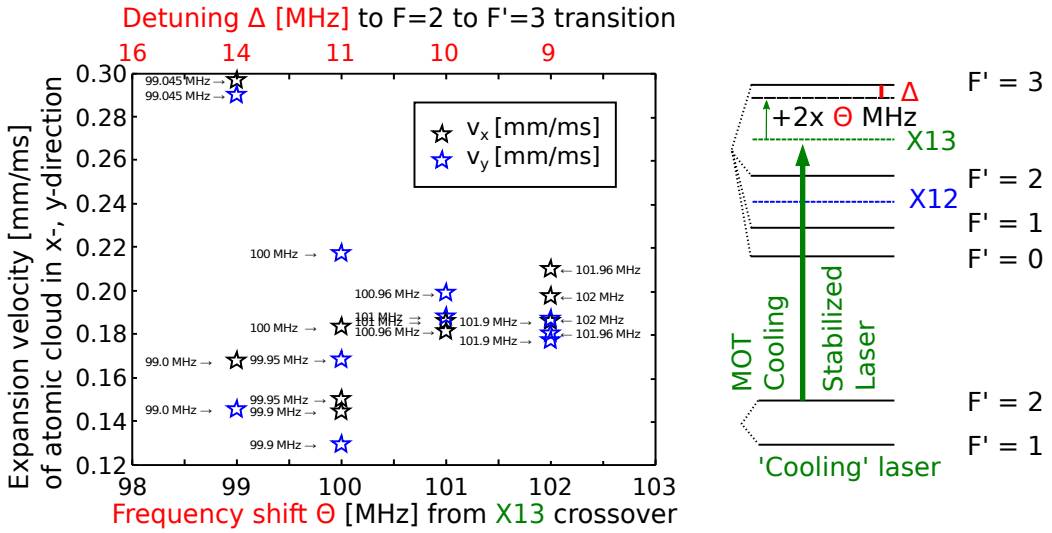

Figure 3.23: Different values for red-detuning the MOT cooling beams by a frequency Δ: We have chosen the cooling lower MOT beam frequency to be our master frequency and calculate the detuning Δ in MHz (marked in red) from the cooling transition. The cooling lower beam has been chosen such that the cold atoms are not launched but remain at their initial position when switching off the cooling beams. For a red-detuning of 10 MHz from the cooling transition F = 2 to F' = 3, we observe the most homogeneous expansion of the atomic cloud after switching off the MOT beams. For a detuning of 11 MHz, we observe smaller expansions velocities, however, the MOT gets also squeezed in one direction.

curve. Calculating the gradient in the theory curve $v = \sqrt{2}\lambda\Delta f$ = 1.1034 m/sΔf [MHz] and comparing it to the measured value of 1.033 (m/s)/MHz indicates that there is good accordance. The offset between the theory and experimental curve can be explained by an intrinsic frequency offset between upper and lower cooling beams of 150 kHz or an intrinsic offset introduced by the calibration of the CCD pixel versus imaged area.

Coming back to the enumeration above and having already learned how the expected atomic velocity compares to the experimentally measured one, we study the detunings between the upper and lower MOT cooling beams. The result is as simple as it is expected, the smallest detuning results in the slowest MOT.

To finalise the discussion about the MOT in motion, we want to investigate which overall detuning from the atomic cooling transition we want to run our MOT and atomic

fountain. To get as many atoms as possible towards the cavity, the atomic cloud should stay confined locally during flight as much as possible. We have chosen different detunings for upper and lower MOT beams such that the atomic cloud is not launched but stays at its initial position. An illustration can be found in Fig. (3.23). We observe the best local confinement of the MOT in motion at a 10 MHz red-detuning from the F = 2 to the F' = 3 transition.

All these investigations are carried out for one reason. This reason 'in action' – a slow, big MOT moving straight upwards towards the cavity with a velocity of 1 m/s – can be seen in Fig. (3.19). As a next step, we need to put everything from cavity locking to cooling and launching atoms together, to produce single photons from our system. This is discussed in the following Section.

3.4 The experimental photon-production sequence

In this Section, we put together all the experimental information that we have gathered in this Chapter: To produce single photons from an atom cavity system, we need to first cool Rubidium atoms down in a magneto-optical trap as introduced in Sec. 3.3.2. Subsequently, we need to launch the atoms upwards, as shown in Sec. 3.3.2. Eventually, one single Rubidium atom is interacting with the cavity that is held on the correct frequency by its locking circuit as explained in Sec. 3.2.3. As soon as an atom interacts with the cavity, STIRAP pump and repump pulses need to be fired at this atom to trigger the single-photon production process as described theoretically in Sec. 2.2.5. The single photon – due to the cavity loss rate κ – leaks out of the cavity and needs to be detected by single-

photon counting modules and stored digitally for post processing. This is, in principle, the experimental photon production sequence, which needs to be repeated many times in a row. How this is technically done is the topic of this Section. An outline of this simplified version of events can be found in Fig. (3.24) and an overview of the nitty-gritty technical details in Fig. (3.25).

In the default state of the experiment, the MOT beams are switched on, the cavity is locked and the battery of single-photon counting modules is switched off ('gated'). As a safety precaution, there are two so-called click clacks in place, already described in Sec. 3.1.2. The click clack in front of the cavity ('AOM click clack') lets light pass as a default whereas the one on the outcoupling side of the cavity ('SPCM click clack') is blocking the light such that it does not hit the sensitive SPCMs when the cavity is held on resonance. To control the experiment, in particular all the switching of various elements, a LabView routine is used which is connected to an Adlink I/O board. An overview of this routine is shown in Fig. (3.25).

If we want to start the photon-production process, we start with loading our MOT for about 500 ms which is enough to gather a sufficient amount of atoms. For 1 ms, the cooling beams are detuned to the according frequencies and subsequently switched off. We set the detuning to 0.6 MHz giving a launch velocity of about 1 m/s. As the MOT is located about 9 mm below the centre of the cavity mode, as it can be seen in Fig. (3.16), it takes the atoms about 11 ms to reach the cavity due to the slowing effect of gravity[25]. Then, we fire a STIRAP pump and repump laser with a certain profile onto the atoms according to which photon shape we want to generate. A Matlab routine controls the signal going to

[25]These values are experimentally determined, a measurement can for instance been found in Fig. (5.27).

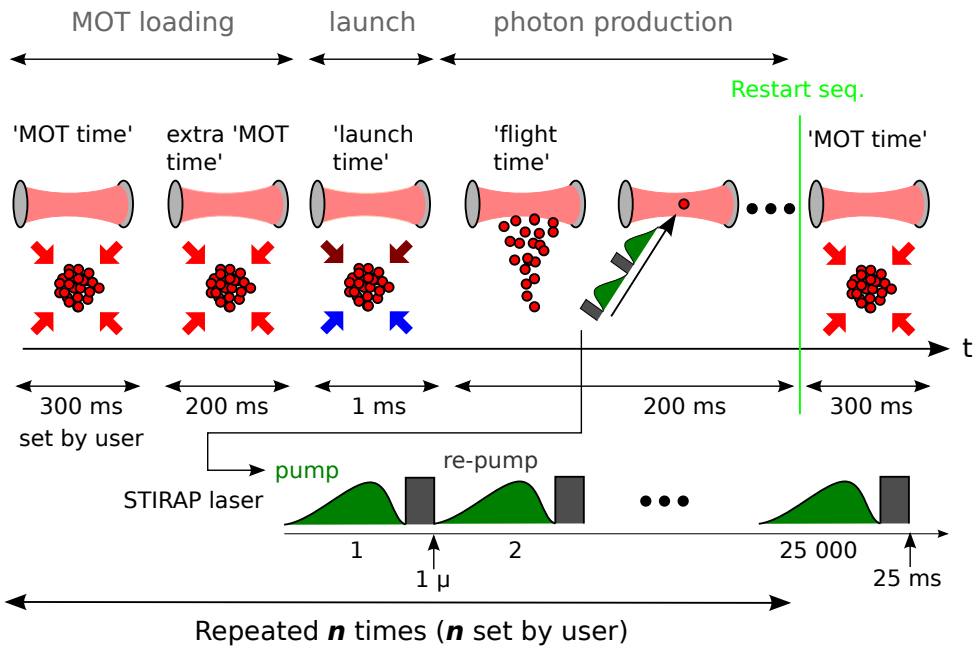

Figure 3.24: Simplified MOT loading, launch and photon production phase (time axis not to scale): At first, roughly 10^6 atoms are cooled in the MOT to about 100 μK. Standardly, this cooling phase lasts for 300 ms and can be adjusted by the user to obtain sufficient cold atoms. The number of atoms depends on technical factors such as the Rubidium background pressure inside the vacuum chamber or the quality of the alignment of the MOT cooling beams. The cooling beams are left switched on for an additional 200 ms as part of the LabView sequence used to control the experiment. Then, MOT beams are detuned relatively to each other which exerts an upwards force on the atoms. After a flight time of roughly 8 ms, the quickest atoms of the cloud start interacting with the vacuum mode of the cavity. Then, a STIRAP or pump laser is applied in order to drive the Raman adiabatic passage. As a single photon is emitted from the atom – after several roundtrips in the cavity – it leaks out of one cavity mirror. The photon production phase lasts for 25 ms and after that, the sequence is reconfigured for the next MOT loading cycle. The overall length of one cycle is therefore 700 ms.

the respective AOMs to produce these light pulses and receives its start trigger from the LabView program. The theoretical discussion of pump pulse and resulting photon shape can be found in Sec. 2.3. We repeat the Matlab sequence of pump and repump pulse 25,000 times in a row. In this photon production phase, the cavity needs to be completely field free as well as the cavity click clack needs to let these single photons pass towards the SPCMs. Therefore, the cavity AOM is switched off as well as the respective click clack is down at this point in time. This double protection mechanism guarantees that no cavity locking light is inside the cavity in the photon production phase as well as no light can reach the detectors when they are switched on. This mechanism is mandatory as saturation power is around 120 pW and the cavity locking beam of the order of 10 nano watts[26].

As soon as the single photon counters detect a single photon in the photon production phase, they send a TTL pulse towards a registering device, a time-to-digital converter[27] (TDC), where the TTL pulses receive a time stamp and a number according to which of the detectors fired when. The TDC records four pieces of information for every TTL pulse: First of all, it records which detector clicks – in the 'qu-bits, qu-trits, qu-quads'-experiment either 1 or 2 (see Chapter 4) or 1 to 6 in the 'LOQC with long photons'-experiment (see Chapter 5). The next information recorded is *when* the click occurred with respect to the start of the STIRAP pulse. It also records the *total* time from the start of the launch phase. The fourth piece of information which is recorded is *which pulse* of the STIRAP pump pulses (1 - 25,000) produced the detected photon.

After the photon production phase, the sequence is reconfigured to its initial state, for

[26] We have not experimentally verified the damage threshold of the detectors – luckily.
[27] Agilent U1051A/TC890

instance the gate of the detectors is turned off, the SPCM click clack blocks the beam line towards the SPCMs, the AOM click clack opens and the cavity locking beam is switched back on and travels towards the cavity. Also, the MOT is reloaded and the cycle starts again. As it can be seen in Fig. (3.24), one full cycle takes 700 ms.

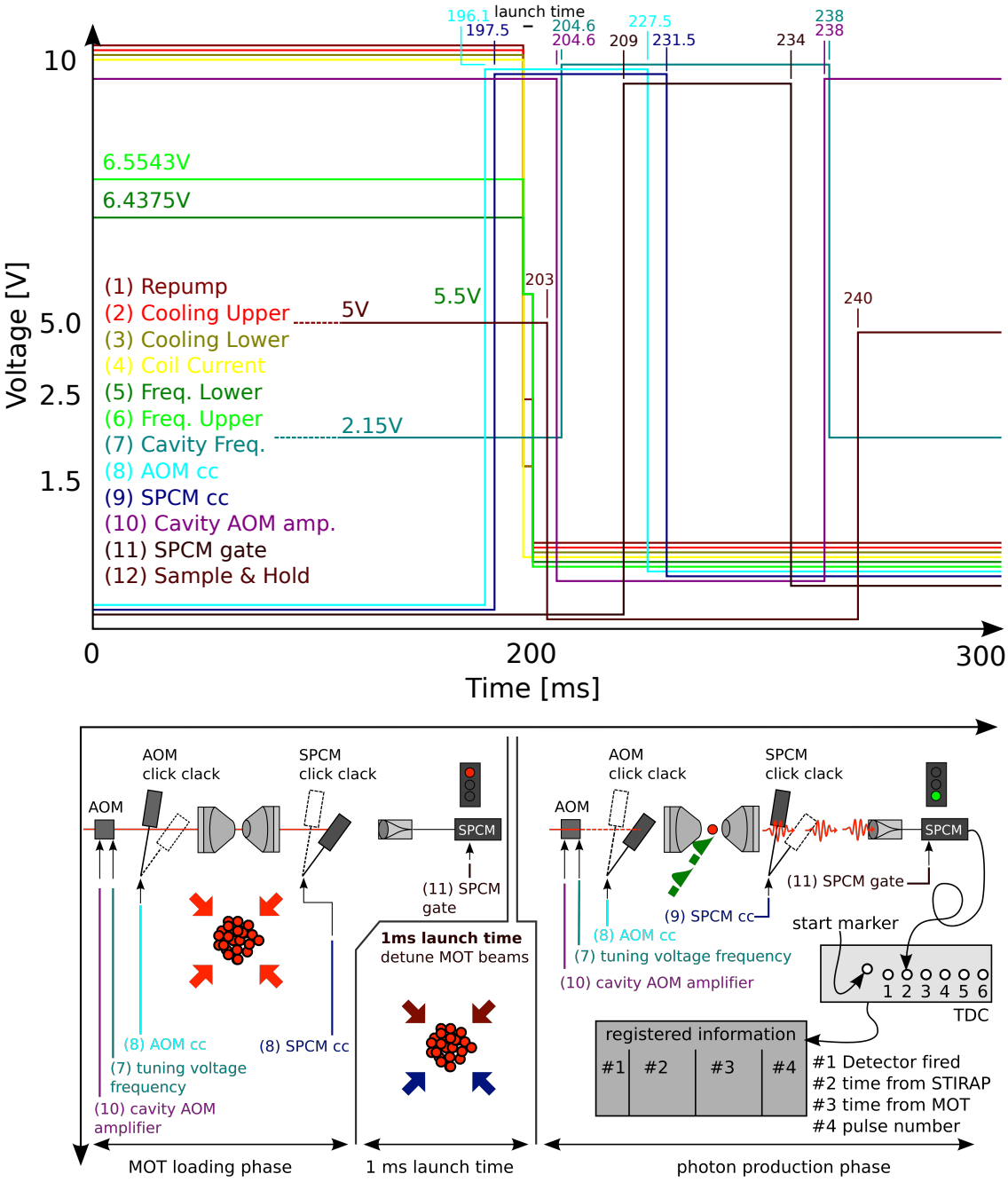

Figure 3.25: Experimental sequence: The upper picture shows the timings of the experimental sequence which has to be carried out by the LabView routine. How often the routine is repeated is set by the user. As it can be seen in the lower picture, we can define three parts of the experimental sequence: The first part – the MOT loading phase – is identical to the free running experiment. The second phase only lasts very shortly – in the 1 ms long launch time the upper and lower MOT beams are detuned against each other and the cold atomic cloud is launched upwards. In the third phase, the photon production phase, the STIRAP pump beam is fired onto the atom inside the cavity and the photons are produced. They are detected with the help of single photon counters.

Chapter 4

Quantum experiments I – qubits, qutrits, and ququads

The main goal of this thesis is to perform quantum networking or even linear optics quantum computing [13, 62, 63, 64] with the help of temporally long photons. Ideally, to perform LOQC measurements, elementary 'quantum' bits (qubits) of information have to be initialised and delivered in a non-probabilistic, versatile, reconfigurable fashion which is not subject to systematic photon losses. The focus of this experimental Chapter is on our approach to achieve these goals. We report on the on-demand production of quantum bits of information encoded in the time domain of more than 100 m in length. We refer to them as time-bin encoded photonic qubits, qutrits and ququads. This Chapter is based on [65] and [66].

4.1 Production of time-bin encoded qu-d-its

Encoding quantum information in time goes back a long way [67], time-bin encoded qubits were first demonstrated in the Gisin group in 1999 [68]. With a Michelson interferometer setup first splitting 300 ps pulses, then adding a phase shift in its longer arm and finally re-interfering the pulses on a second beam splitter, a two time-bin photon with the time bins being separated by 1.2 ns is generated. This photon is used to pump a nonlinear

crystal, generating two time-binned photons at a longer wavelength. This scheme is later extended to femtosecond pulses [69].

Our approach to time-bin encoding is based on the theoretical [45] and experimental [60] demonstrations of arbitrarily shaping the spatio-temporal envelope of the single photons emitted from our source based on a strongly coupled atom-cavity system. Therefore, we are able to shape photons in a way that they represent time-bin encoded *qubits*, *qutrits* or even *ququads*. More generally, we refer to this type of quantum bits of information as *qu-d-its*[1]. The number of time bins we can encode in our photons is fundamentally limited by the coherence time of the system and the minimal temporal length of the time bins not violating the adiabaticity constraint introduced in Sec. 2.2.3. From [70], we learn that the adiabaticity constraint in the case of full state transfer from $|u,0\rangle$ to $|g,1\rangle$ is

$$\frac{g^2}{\gamma} \gg \frac{\pi}{2T} + \frac{\kappa}{2}, \tag{4.1}$$

where T is the length of the adiabatic transfer, g the atom-cavity coupling strength, κ the cavity decay rate and γ the polarisation decay rate. For (g, κ, γ) = (12, 12, 3) MHz, we obtain $T \gg 38$ ns. The actual length of the photon's wave packet Ψ_{Photon}, keeping the process adiabatic and assuming a quick adiabatic transfer $\kappa \cdot T < 1$[2] is given by $\Psi_{\text{Photon}}(t) = \sqrt{2\kappa}e^{-\kappa t}$ [70]. Therefore, the lower bound for the length of the photon's wave packet is defined by the lifetime $1/\kappa$ of the resonator. For κ = 12 MHz, the lifetime of the resonator equals 83 ns. Experimentally, we observe 230 ns as the shortest possible

[1] With $d = b$ in the qu-b-its case and $d = tr$ in the qu-tr-its case. Strictly speaking, this scheme breaks down in the ququads case.

[2] 12 MHz · 38 ns ≈ 0.5

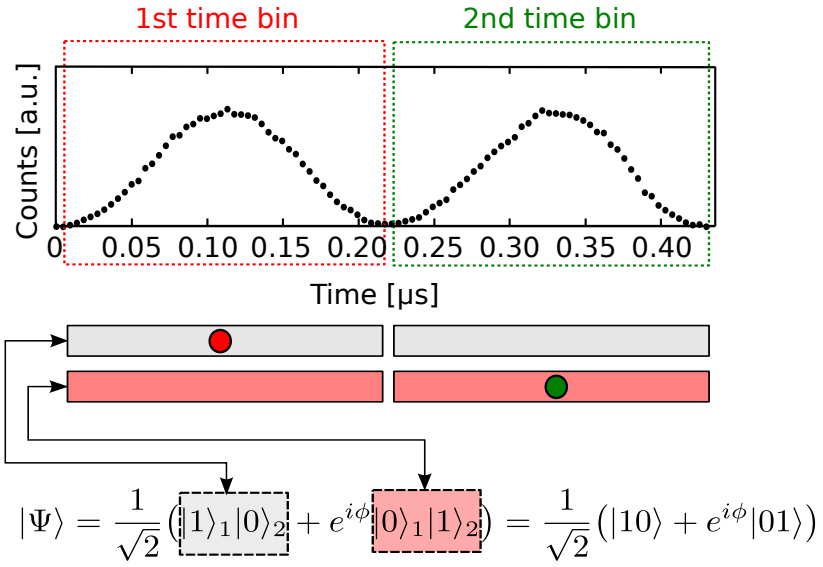

Figure 4.1: Time-bin encoded qubit: The spatio-temporal envelope of a single photon is subdivided into two separate time bins of 230 ns length. Therefore, the state of the single photon is equivalent to a quantum superposition of a photon being in the first or second time bin, respectively.

temporal length of the time bin[3]. Assuming a 500 ns coherence time [65], we can ideally imprint two time bins into our photon's wave packed but also three. It is also possible to encode four time bins, but the lack of coherence is going to be visible, as it can for instance be seen in Fig. (4.12).

Having explored the history of encoding information in time as well as the limitations of our system, we continue with how we can encode quantum bits of information into time-bin encoded photons. The quantum mechanical analog to the classical *bit* and therefore the elementary unit in quantum information processing is a *qubit* [3]. For a single photon, its initialisation is often achieved via dual-rail encoding [71], where a single photon is split

[3]This value is determined experimentally by running HOM measurements for different lengths of the time bins. We make sure to minimise the ratio of coincidences we observe for parallely polarised over perpendicular polarised photons per time bin. This is the case for a temporal length of 230 ns per time bin.

by a 50:50 beam splitter into the non-separable state of the form

$$|\Psi\rangle = \frac{1}{\sqrt{2}}\left(|10\rangle + e^{i\phi}|01\rangle\right), \tag{4.2}$$

where $|10\rangle$ and $|01\rangle$ correspond to the two spatial modes, with ϕ being the relative phase delay in the transmitted mode. In our case, the photonic qubits are not encoded *spatially* but *temporally*. As it can be seen in Fig. (4.1), this means that the spatio-temporal envelope of the single photon has been subdivided into two different time bins of equal temporal length. Therefore, the total single-photon state is a quantum superposition of a photon being in the first or second time bin, respectively. Please note that there is a well-defined phase relationship and coherence between the two time bins in our experiment, this is why we can regard the single photon as a photonic qubit. The same holds for qutrits and ququads accordingly, with additional time bins for each. We are therefore able of encoding arbitrary qubits into single photons as we are able of controlling the probability amplitudes of these states and their relative phase, ϕ. However, in the following, the discussion is restricted to time bins with equal amplitudes as we only want to show a proof of principle experiment.

4.2 Quantum-homodyne measurements

To verify that the quantum state of the photon corresponds to the desired qubit, the relative phase ϕ between individual time bins has to be determined. This is achieved with the help of a newly developed quantum-homodyne technique. A similar technique for SPDC photons has been introduced by Wasilewski et al. [72].

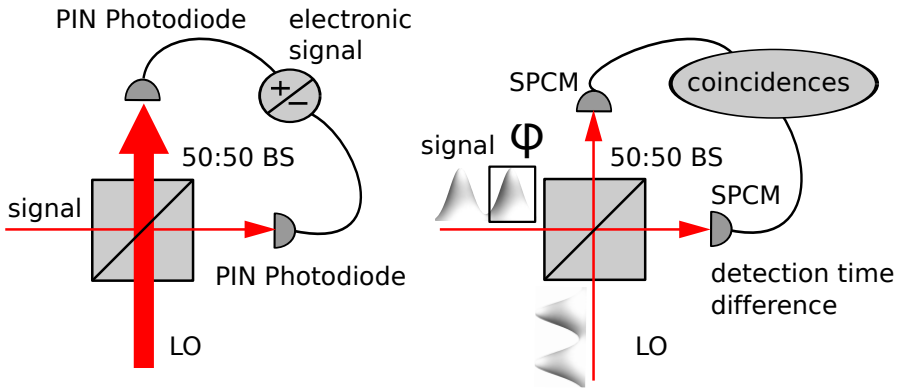

Figure 4.2: Homodyne vs. quantum-homodyne technique: In the homodyne measurement, a weak *signal* beam as well as a bright *local oscillator* (LO) of the same frequency is sent on a 50:50 non-polarising beam splitter (BS) where they interfere. The detectors transform the AC signals of the photocurrents coming from the respective photodiode into voltages. These two voltages can subsequently be electronically added or subtracted. The "+" operation delivers information about an arbitrarily rotated quadrature variable of the signal beam. In the quantum-homodyne case, two single photons are sent on a 50:50 BS such that they arrive there simultaneously and interfere with each other. If both photons are indistinguishable, bunching or the Hong-Ou-Mandel effect [73] can be observed. In our quantum-homodyne measurement, clicks on both single-photon counting modules (SPCMs) are measured. During post-processing, correlation events can be evaluated in a time-resolved manner as our photons are much longer than the detector time resolution.

Usually, the term *homodyne* stands for a technique used in the continuous variable (CV) regime. The difference between the *homodyne* and the *quantum-homodyne* technique is shown in Fig. (4.2). In the continuous variables, a weak signal beam interferes with a 'classical' local oscillator (LO) [74] of the same frequency[4] on a non-polarising beam splitter (BS). In the two output ports of this beam splitter, the respective signal is measured with the help of a PIN photodiode and then electronically added or subtracted from one another. In this way, information about an arbitrarily rotated quadrature of the signal beam and a quadrature of the LO can be obtained. This technique is essential when measuring non-classical CV light and more information about it can be found in the Appendix, Chapter 7.

[4] In the case of signal and LO beam having different frequencies, the technique is referred to as *heterodying*.

In the quantum-homodyne case, we also deal with non-classical light, namely single photons in both the signal and the local oscillator beam. The standard technique to detect and obtain information about these photons is two-photon interference [75]. In particular, as our photons are very long, all measurements can be carried out in a time-resolved manner [76, 77] – the photons are of the length of several 100 ns whereas the detector time resolution is roughly three orders of magnitude smaller. With our quantum-homodyne technique we extend the well-known Hong-Ou-Mandel interference [73] as it can be seen in Fig. (4.3): The signal photon interferes on a beam splitter with a single LO photon of state

$$|\Psi_{\mathrm{LO}}\rangle = \hat{a}^{\dagger}_{\mathrm{LO}}|00\rangle = \left(|10\rangle + |01\rangle\right)/\sqrt{2}, \text{with its creation operator being} \tag{4.3}$$

$$\hat{a}^{\dagger}_{\mathrm{LO}} = \frac{1}{\sqrt{2}}\left(\hat{a}^{\dagger}_{\mathrm{TB\ 1}} + \hat{a}^{\dagger}_{\mathrm{TB\ 2}}\right). \tag{4.4}$$

This photon exhibits no phase shift between its time bins. In particular the creation operator for the LO shown in Fig. (4.3, right), is $1/\sqrt{2}\left(\hat{a}^{\dagger}_{\mathrm{B1}} + \hat{a}^{\dagger}_{\mathrm{B2}}\right)$. In the traditional HOM interference as shown in Fig. (4.3, left), the photons arrive simultaneously at the beam splitter in spatio-temporal modes A and B. The creation operators in the respective output ports of the beam splitter read

$$\hat{a}^{\dagger}_{\mathrm{C}} = \frac{1}{\sqrt{2}}\left(\hat{a}^{\dagger}_{\mathrm{A}} + \hat{a}^{\dagger}_{\mathrm{B}}\right), \text{and} \tag{4.5}$$

$$\hat{a}^{\dagger}_{\mathrm{D}} = \frac{1}{\sqrt{2}}\left(\hat{a}^{\dagger}_{\mathrm{A}} - \hat{a}^{\dagger}_{\mathrm{B}}\right), \tag{4.6}$$

such that the input states $\hat{a}^{\dagger}_{\mathrm{A}}|0\rangle$ and $\hat{a}^{\dagger}_{\mathrm{B}}|0\rangle$ translate into a superposition of output states

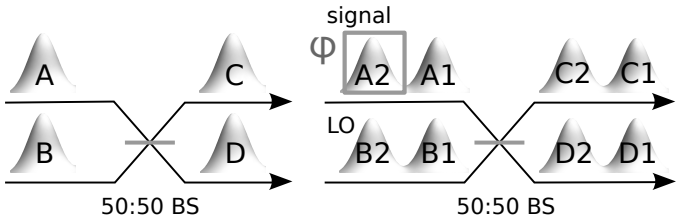

Figure 4.3: Quantum homodyning (right) extends standard Hong-Ou-Mandel interferometry (left): Photons of identical spatio-temporal envelope arrive simultaneously at a 50:50 beam splitter and interfere. The local oscillator (LO) photon exhibits no phase differences between its time bins, while any phase or frequency changes within the signal photon give rise to correlation events in detection-time resolved measurements.

$\hat{a}_{\mathrm{C}}^{\dagger}|0\rangle$ and $\hat{a}_{\mathrm{D}}^{\dagger}|0\rangle$ using the operator relation of the beam splitter. Inversely, we find

$$\hat{a}_{\mathrm{A}}^{\dagger} = \frac{1}{\sqrt{2}}\left(\hat{a}_{\mathrm{C}}^{\dagger} + \hat{a}_{\mathrm{D}}^{\dagger}\right), \text{and} \tag{4.7}$$

$$\hat{a}_{\mathrm{B}}^{\dagger} = \frac{1}{\sqrt{2}}\left(\hat{a}_{\mathrm{C}}^{\dagger} - \hat{a}_{\mathrm{D}}^{\dagger}\right), \tag{4.8}$$

Applied to twin-peak signal and LO photons, in the Heisenberg picture, the input states read

$$|\Psi_{\mathrm{A}}\rangle = |\Psi_{\mathrm{signal}}\rangle = \frac{1}{\sqrt{2}}\left(\hat{a}_{\mathrm{A1}}^{\dagger} + e^{i\phi}\hat{a}_{\mathrm{A2}}^{\dagger}\right)|00\rangle_{\mathrm{A}} = \frac{1}{\sqrt{2}}\left(|10\rangle_{\mathrm{A}} + e^{i\phi}|01\rangle_{\mathrm{A}}\right), \tag{4.9}$$

$$|\Psi_{\mathrm{B}}\rangle = |\Psi_{\mathrm{LO}}\rangle = \frac{1}{\sqrt{2}}\left(\hat{a}_{\mathrm{B1}}^{\dagger} + \hat{a}_{\mathrm{B2}}^{\dagger}\right)|00\rangle_{\mathrm{B}} = \frac{1}{\sqrt{2}}\left(|10\rangle_{\mathrm{B}} + |01\rangle_{\mathrm{B}}\right), \tag{4.10}$$

The input state into the beamsplitter in the quantum homodyne measurement reads

$$|\Psi_{\mathrm{in}}\rangle = \frac{1}{2}\left(\hat{a}_{\mathrm{A1}}^{\dagger} + e^{i\phi}\hat{a}_{\mathrm{A2}}^{\dagger}\right)\left(\hat{a}_{\mathrm{B1}}^{\dagger} + \hat{a}_{\mathrm{B2}}^{\dagger}\right)|00\rangle_{\mathrm{A}}00\rangle_{\mathrm{B}}, \tag{4.11}$$

which can be converted into the output state

$$|\Psi_{\text{out}}\rangle = \frac{1}{4}\Big(\hat{a}^\dagger_{\text{C1}} + \hat{a}^\dagger_{\text{D1}} + e^{i\phi}\hat{a}^\dagger_{\text{C2}} + e^{i\phi}\hat{a}^\dagger_{\text{D2}}\Big)\Big(\hat{a}^\dagger_{\text{C1}} - \hat{a}^\dagger_{\text{D1}} + \hat{a}^\dagger_{\text{C2}} - \hat{a}^\dagger_{\text{D2}}\Big)|00\rangle_{\text{C}}|00\rangle_{\text{D}}. \tag{4.12}$$

This output state can be simplified to

$$\begin{aligned}
|\Psi_{\text{out}}\rangle \propto \quad & \Big((\hat{a}^\dagger_{\text{C1}})^2 - (\hat{a}^\dagger_{\text{D1}})^2\Big)|00\rangle_{\text{C}}|00\rangle_{\text{D}} && (4.13)\\
& + e^{i\phi}\Big((\hat{a}^\dagger_{\text{C2}})^2 - (\hat{a}^\dagger_{\text{D2}})^2\Big)|00\rangle_{\text{C}}|00\rangle_{\text{D}} && (4.14)\\
& + (1 + e^{i\phi})\Big(\hat{a}^\dagger_{\text{C1}}\hat{a}^\dagger_{\text{C2}} - \hat{a}^\dagger_{\text{D1}}\hat{a}^\dagger_{\text{D2}}\Big)|00\rangle_{\text{C}}|00\rangle_{\text{D}} && (4.15)\\
& - (1 - e^{i\phi})\Big(\hat{a}^\dagger_{\text{C2}}\hat{a}^\dagger_{\text{D1}} - \hat{a}^\dagger_{\text{D2}}\hat{a}^\dagger_{\text{C1}}\Big)|00\rangle_{\text{C}}|00\rangle_{\text{D}}, && (4.16)
\end{aligned}$$

where the subscripts $\{1, 2\}$ refer to the respective time bin, $\{\text{C}, \text{D}\}$ to the respective output port of the beam splitter and ϕ to the phase difference between the two time bins of the signal photon.

The terms of the output state referenced (4.13) and (4.14) contain the creation operator pairs where both photons are detected in the same time bin and output port of the beam splitter. This is the case when photons coalesce. The terms referenced as Eqs. (4.15) and (4.16) describe the situation where the photons are detected in different time bins. No cross-correlations between outputs C and D are witnessed for identical photons ($\phi = 0$) in theory, which corresponds to the well-known Hong-Ou-Mandel effect. If one chooses $\phi = \pi$, the photons are actively forced into opposite output ports, provided the detections occur in different time bins. This means that if for instance the first photon is detected in

C1, the second *must* be detected in D2. The photon correlations, which normally follow bosonic statistics, are projected into a quasi-fermionic state by the first detection and the change in relative phase. By examining the number of cross-correlations found in different time bins, the relative phase difference, ϕ, between any pair of time bins can be determined.

4.3 Experimental setup

Having thoroughly discussed all details of the experiment in Chapter 3, we use our well-characterised setup for the production of photonic qubits, qutrits and ququads. An outline of the experimental arrangement is shown in Fig. (4.4). We alternatingly produce signal and LO photons from the atom-cavity system[5] by imprinting the respective phase (zero or ϕ) on the photons with the help of the STIRAP driving pulse's phase. This STIRAP driving pulse is generated by light passing through an AOM which gets its signal from an arbitrary waveform generator.

The stream of photons produced from the atom with the help of the STIRAP driving pulse is split by a polarising beam splitter (PBS) between long (upper) and short (lower) beam paths, causing successively emitted photons to arrive simultaneously at the non-

[5] In practice, we alternatingly imprint a phase shift of ϕ and no phase shift onto the STIRAP driving pulse with the help of an AWG. To exclude any technical error in the AWG, we carefully check the (electronic) driving pulse's pattern and imprinted phase shift before starting each individual measurement. In this way, we determine the *imprinted phase difference* between signal (phase shift) and LO (no phase shift) photon. What we additionally check is to only produce signal *or* LO photons and measure the HOM interference. The outcome of these two separate measurements is identical in both cases – for perpendicularly polarised photons, the cross-correlation function is given by the auto-convolution of the photon's shape (for no and ϕ phase shift) and for parallely polarised photons (ideally) the cross-correlation function is zero. This is how we are sure that we measure the phase *difference* between signal and LO photon in a quantum homodyne measurement.

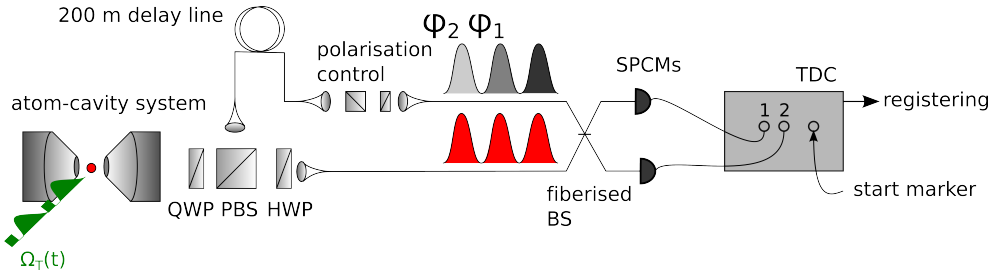

Figure 4.4: Experimental arrangement for quantum-homodyne measurements: As described in Section 2.1, to create a single photon of a pre-defined spatio-temporal envelope, a single ^{87}Rb atom is placed inside a high-finesse optical cavity where a Raman transition is driven within this atom. A 200 m long fibre is used to delay this generated photon such that it arrives simultaneously at the beam splitter (BS) with the subsequently emitted photon that travels the direct path. The two output modes of the fiber BS are monitored for detection events with the help of two SPCMs. The detection events are subsequently sent to the time-to-digital converter (TDC) where they are registered, provided with a time stamp and stored for post-processing.

polarising 50:50 beam splitter[6]. In the two output ports of the fiber beam splitter, there are two single-photon counting modules (SPCMs). These detectors[7] are gated and quenched avalanche photodiodes with a timing resolution of 350 ps and a dead-time of 50 ns. Both of them are connected to a time-to-digital converter (TDC)[8] with a timing resolution of 50 ps which registers the clicks in the detectors as well as provides them with a timestamps as described in Sec. 3.4.

In this experiment, we therefore use a standard 6-beams magneto-optical trap and an atomic fountain which has been already discussed in Secs. 3.3.2 and 3.3.3. In the MOT, about 10^6 atoms are prepared at about 100 μK 8.5 mm below the centre of the cavity mode as it can be seen in Fig. (3.16). The loading of the MOT takes about 300 ms and is assisted by UV light-induced desorption (LIAD) of Rubidium from the walls of the vacuum chamber. This procedure allows for effective loading of the MOT in a relatively

[6] As the beam splitter randomly distributes the photons between the paths, this occurs with a probability of 25%. This probability can be increased to unity using fast switching optics or generating polarisation-controlled single photons.

[7] Perkin-Elmer, SPCM AQRH-14.

[8] Agilent TC890

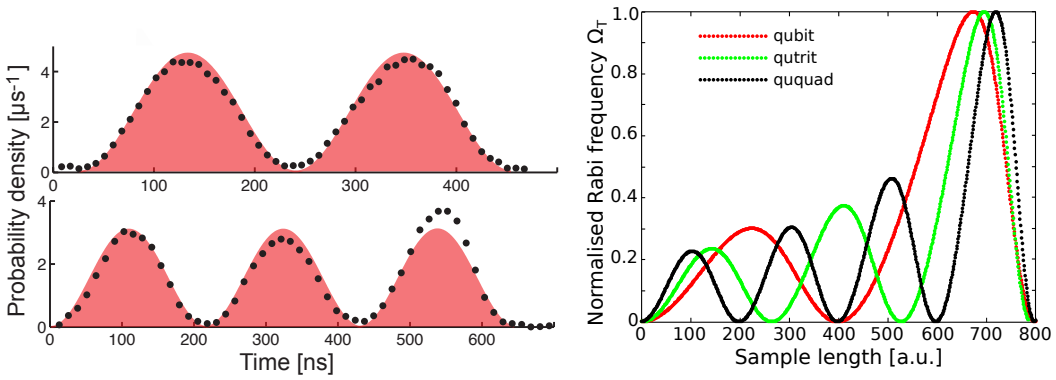

Figure 4.5: (Left) Probability density of twin- and triple-peak photons, taken from [65]. The red-filled area indicates the desired $\sin^2$-shaped probability density in every time bin. (Right) Normalised Rabi frequency Ω_T to generate qubits, qutrits and ququads for $(g, \kappa, \gamma) = 2\,\pi(15, 12, 3)$ and an efficiency of $\eta = 0.81$.

short time. In order to subsequently load atoms into the cavity, the MOT beams are detuned relative to each. This ballistically launches the cold atomic cloud. A complete discussion can be found in Sec. 3.3.3. It has to be made sure that the launched atoms' position coincides with the centre of the cavity mode. Experimentally, about 100 μs of interaction time [60] of the atom with the cavity is achieved.

As soon as one of the ^{87}Rb atoms interacts with the cavity, the Raman transition can be driven as it has been shown in Chapter 2, in particular in Secs. 2.2.4 and 2.2.3. Also, it has been discussed in Sec. 2.3 that it is possible to engineer the photon's shape both theoretically and experimentally [45, 60]. For this experiment, we generate time-bin encoded qubits, qutrits and ququads with each time bin being 230 ns long – their waveform can be found in Fig. (4.5, left) as well as their driving pulse of Rabi frequency Ω_T in Fig. (4.5, right). In practice, the limiting factor to produce these photons are decoherence effects upon their generation inside the cavity as well as the bandwidth of the acousto-optic modulator (AOM) modulating the driving pulse's amplitude.

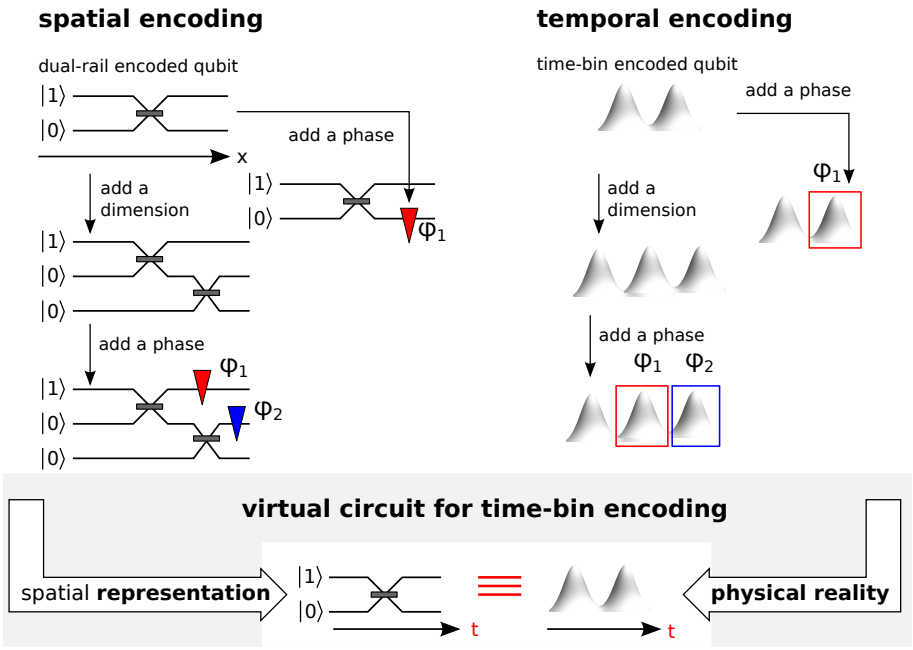

Figure 4.6: Comparison between spatially and temporally encoded quantum bits of information: Conventionally, quantum circuits are producing spatially entangled qubits (left). However, our quantum bits of information are encoded temporally (right). In our *virtual* circuits representation (lower), we depict our temporally encoded information *as is it was spatially encoded*.

4.4 Excursion I: Virtual-circuit representation

With our photons, we have a new domain to encode information on our hand – the time. To increase the understanding of the experiment we are carrying out, we introduce a novel way of displaying the physical reality with the help of a virtual circuit. An illustration comparing the traditionally used and well-known spatially encoded qubit with the temporally encoded ones can be found in Fig. (4.6). As time-bin encoding quantum bits of information is non-intuitive, we chose to represent the modes as if they were spatial ones. We can see all different virtual circuits for the experiments we are carrying out in Fig. (4.7).

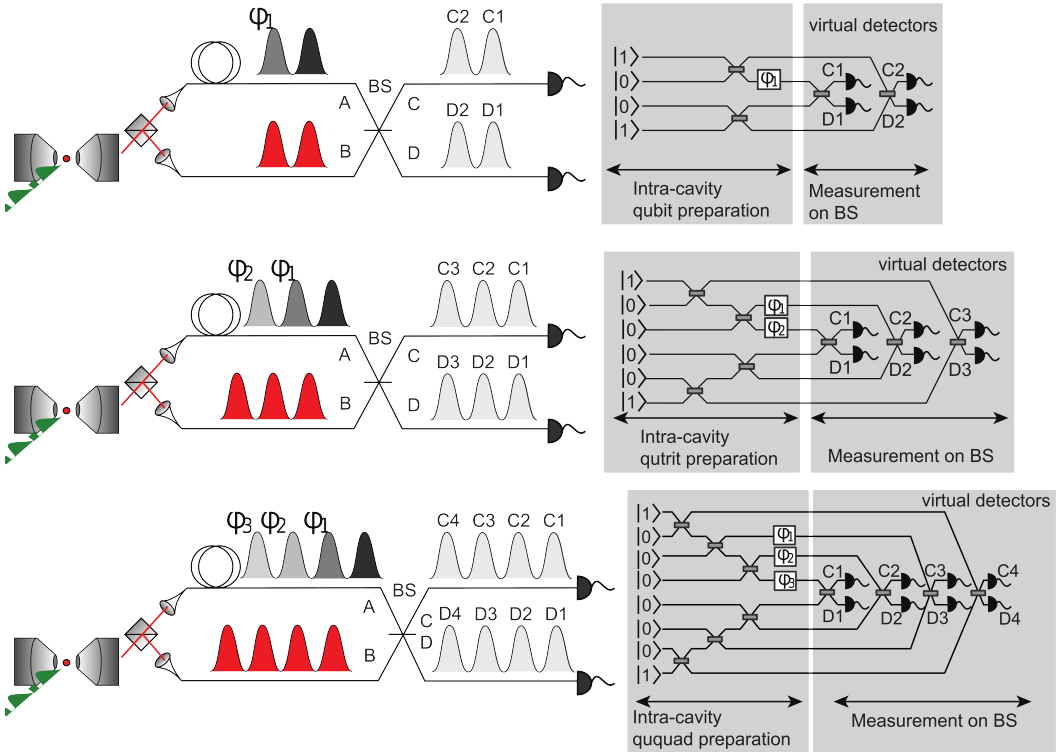

Figure 4.7: Real vs. virtual-circuit representation for qubits, qutrits and ququads experiments: In the qubit case, we subdivide the spatio-temporal envelope into two time bins, and observe them on four virtual detectors, one in each output arm of the BS and in two separate time bins. This number analogously increases to three time bins and six virtual detectors in the qutrit case. The most extreme case we measure is the ququad case, where we generate two subsequent single photons subdivided into four time bins and observe these on eight virtual detectors.

4.5 Excursion II: Data acquisition and post-processing

This Excursion discusses the data acquisition and post-processing in our experiment. This equivalently holds for qubits, qutrits and ququads experiments described in this Chapter as well as for experiments with LOQC described in Chapter 5.

The single photon counters register a click and emit a TTL pulse, which is registered in the TDC. As discussed in Sec. 3.4, the TDC registers four pieces of information about this TTL pulse, namely (1) the number of the detector that clicks, the time *when* the click occurred with respect to (2) the start of the particular STIRAP pulse (0 – 1 μs) and with respect to (3) the time of the first STIRAP pulse firing (0 – 25 ms) after launching the MOT. The fourth piece of information is (4) the pulse number of the fired STIRAP sequence the detection is associated with (1 – 25,000). One file is saved in the TDC of all clicks that occurred in all SPCMs per MOT throw in the sequence, containing the mentioned four pieces of information for the registered TTL pulses, each SPCM being connected to one input of the TDC. The next question is how we actually count correlations.

During post-processing, we look for counts occurring in the same pulse number per registered file (per MOT throw). Is there another click detected in this particular pulse number and in the same detector, it is most probably an event caused by after-pulsing in the SPCM. Is the click detected in a different detector (but having the same registered plulse number), we count this as a correlation and register the time between these detections. This is what is called *detection-time difference* in the characteristic plots.

Let us discuss an example with a real registered count, please note that the time parameters are given in picoseconds:

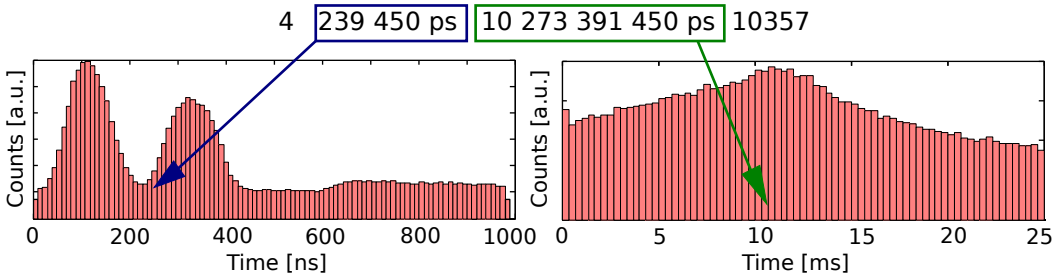

Figure 4.8: Example of a registered count in the TDC coming from the SPCM. Assuming a two time-bin photon, the click is detected in detector 4, 239 ns from the beginning of the STIRAP pulse, 10 ms from the beginning of the MOT throw and this click was produced by the 10,357-th STIRAP pulse fired.

(1)	(2)	(3)	(4)
4	239450	10273391450	10357

This means, we detected a click in detector 4, 239 ns from the beginning of the STIRAP pulse, 10 ms from the beginning of the MOT throw and this click was produced by the 10,357-th STIRAP pulse fired. What this means is illustrated in Fig. (4.8). If we for instance observe two clicks in the same detector for the same pulse number, such as

4	239450	10273391450	10357
4	301762	10273453762	10357

it is most probably one real photon click and one after pulse with a time difference of 62 ns. These after pulses can come from two different sources. The SPCMs can spit out a photon after the detection of a photon which leaves the module, travels the inverse optical path, is back reflected on an optical element and is detected once again. The other possibility is that this after pulse is caused by charge impurities of the detectors itself. In any case, it is a source of noise, this is why we discard all clicks in one detector for one pulse number after the first detection.

If our detection pattern looks like this

4	515350	14156355350	14271
5	301762	10273453762	10357

we most probably detected one correlation between detector 4 and 5 with a detection-time difference of 62 ns. This gives rise to one correlation event in a standard detection-time difference graph.

If we want to display our data in a different way – alluding to the well known truth tables used in the LOQC community – we carry out the same evaluation but add another piece of information. This time, we are interested in which part of the pulse the detection occurred. According to Fig. (4.8), we separate for instance a two time-bin photon into two parts. We define all detections in time t according to $t_{\text{pulse}} > \text{t} > t_{\text{pulse}}/2$ as detections in time bin 2 and accordingly, detections in $t_{\text{pulse}}/2 > \text{t} > 0$ as detections in time bin 1. If we detect one photon for instance in time bin 1 in detector C and *for the same pulse number* in detector D in time bin 2, we observe a correlation between *virtual detectors* C1 and D2. This scheme is illustrated in Fig. (4.9).

4.6 Experimental results

As it has been shown in Fig. (4.4), the experimental setup is simple and is not being changed in course of the qubits, qutrits and ququads measurements. Signal and LO photons interfere on a fiber BS and in its output ports, the interference signal is monitored with the help of two SPCMs. The virtual circuits for all measurements we carry out can be found in Fig. (4.7). The results for measured twin-peak photons are presented in Fig. (4.10), for triple-peak photons in Fig. (4.11) and for quadruple-peak photons in Fig. (4.12) as well as in [65].

Perpendicularly polarised photons do not interfere, and their cross-correlation function

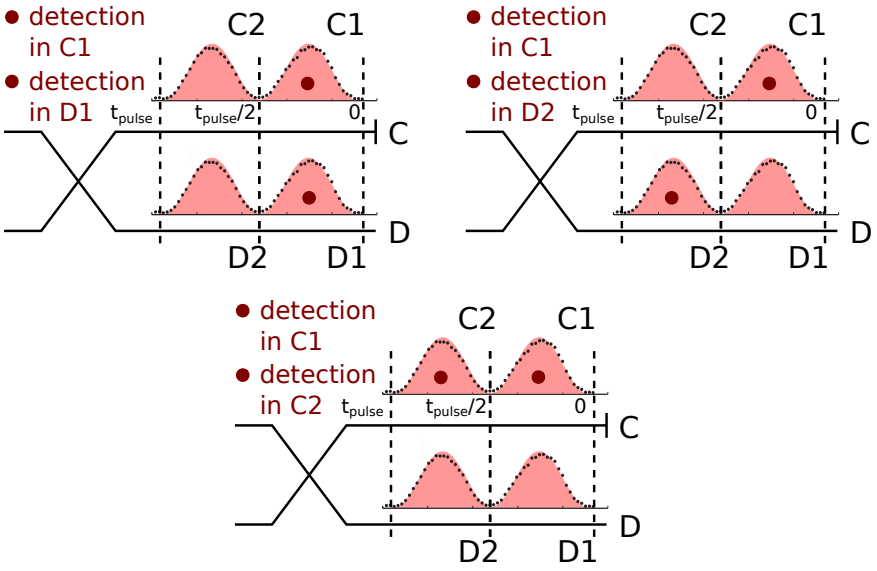

Figure 4.9: We bin our measured data such that it matches the well known truth table from LOQC measurements: We define time bins for the detection time of our photon. If we detect the photon in time $t_{\text{pulse}}/2 > \text{t} > 0$, we define it is detected in time bin 1 of detector C (upper left). If we register a second count for the same pulse number in the other detector D also in time $t_{\text{pulse}}/2 > \text{t} > 0$, this is a correlation event between *virtual detectors* C1 and D1. If we detect a photon in C1 and in time $t_{\text{pulse}} > \text{t} > t_{\text{pulse}}/2$ in the other detector, it is a correlation event between detectors C1 and D2 (upper right). If we register two counts in the same pulse number in the same detector (lower), we discard this event as it is most probably an after pulse and therefore noise.

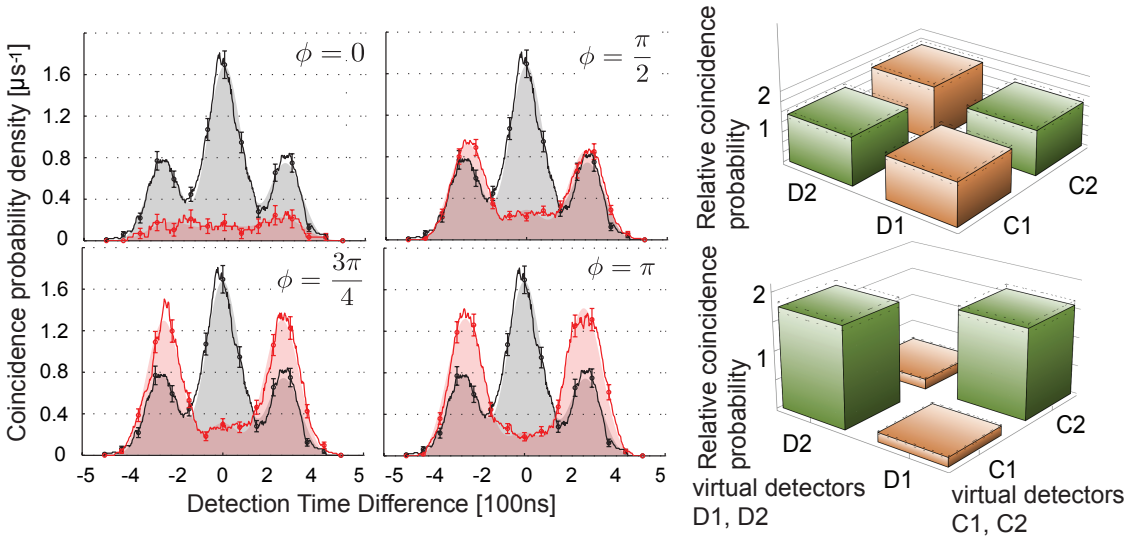

Figure 4.10: (Left) Results of the time-resolved quantum-homodyne measurement for qubits [65]: The reference signal (perpendicular polarisation) is shown in grey, the homodyne signal (parallel polarisation) in red. The relative phase shift ϕ between the signal-photon peaks has been stepped between 0 and π. Real time-resolved detector clicks can be mapped to virtual detectors C1, C2, D1, and D2 firing, the respective virtual circuit to identify the virtual detectors can be found in Fig. (4.7). (Right) Relative coincidence probabilities (RCPs) between virtual detectors for perpendicular polarisation (reference measurement) and for a phase shift of $\phi = \pi$. The colour brown indicates both virtual detectors firing in the same time bin whereas green means they fire in successive time bins.

is given by the auto-convolution of the photon's shape. For twin-peak photons, a triple-peak convolution is witnessed as it can be seen in grey in Fig. (4.10, left), with a large central peak caused by detector clicks in identical time bins which are represented by the annihilation operators $\hat{a}_{C1}\hat{a}_{D1}$ and $\hat{a}_{C2}\hat{a}_{D2}$. The additional two side peaks of equal height arise from correlations between adjacent time bins represented by $\hat{a}_{C1}\hat{a}_{D2}$ and $\hat{a}_{C2}\hat{a}_{D1}$, respectively. With parallel polarisation, the photons do interfere and the cross-correlation function marked in red in Fig. (4.10, left) varies with the relative phase between the peaks of the signal photon. As discussed above, no correlations are found within identical time bins, so the central peak at zero detection-time difference vanishes. This is not the case for the two side peaks at ± 230 ns, where the number of counts depends strongly on ϕ and

is expected to vary between zero and twice the value found with perpendicularly polarised photons.

In order to exploit the data measured with the help of the quantum-homodyne technique, the virtual-circuit representation introduced in the Excursion in Sec. 4.4 is of great help. As it can be seen in Fig. (4.7), two photons are generated, each existing in a superposition of two time bins with a possible phase shift in the signal and no phase shift in the local oscillator photon. These photons are interfered on one single beam splitter with detectors C and D monitoring the respective output modes. This physical reality is equivalent to the representation of spatial superposition of a beam splitter's output with an extra phase shift imprinted in the transmitted mode as shown in Fig. (4.6). In the experiment which is virtually represented in Fig. (4.7), the real beam splitter and detectors are used twice – once per time bin – and so the equivalent virtual circuit consists of two beam splitters and four virtual detectors C1, C2, D1, and D2.

Due to the photons being much longer than the detector time resolution, the absolute time at which the real detectors fire can be recorded with the help of the time-to-digital converter (TDC). Therefore, the four possible cross-correlations – represented by either the annihilation operators $\hat{a}_{\mathrm{C1}}\hat{a}_{\mathrm{D1}}$ and $\hat{a}_{\mathrm{C2}}\hat{a}_{\mathrm{D2}}$ (same time bin) or $\hat{a}_{\mathrm{C1}}\hat{a}_{\mathrm{D2}}$ and $\hat{a}_{\mathrm{C2}}\hat{a}_{\mathrm{D1}}$ (different time bins) – can be retrieved. This is shown in Fig. (4.10, left) for both perpendicularly (black) and parallelly polarised (red) photons with a $\phi = \pi$ phase shift in the signal photon. The full time-resolved correlation function – which depends strongly on the photon shape – can now be time-binned and normalised to give the *correlations between virtual detectors*, which is shown in Fig. (4.10, right). The relative coincidence probability (RCP) used as a measure to compare the amount of correlations between virtual detectors is defined

by the ratio of quantum-homodyne correlations to the number of reference correlations retrieved from the measurements of perpendicularity polarised photons. The RCP ranges from zero to two, indicating the respective extreme case of photons coalescing (no correlations) or anti-coalescing (correlations). By comparing these measured correlations to the expectation, the *fidelity* of the qubit state preparation is found to be F = 0.96±0.01. How to calculate this result is explained in Sec. 4.7.

The quantum-homodyne technique which has been applied to *qubits* in the previous paragraph, it is now extended to time-bin encoded *qutrits* and *ququads*. These qutrits and ququads are generated by adding more time bins with in general arbitrary amplitudes and relative phases. The states are now of the form

$$|\Psi_3\rangle \propto |100\rangle + e^{i\phi_1}|010\rangle + e^{i\phi_2}|001\rangle, \tag{4.17}$$

$$|\Psi_4\rangle \propto |1000\rangle + e^{i\phi_1}|0100\rangle + e^{i\phi_2}|0010\rangle + e^{i\phi_3}|0001\rangle. \tag{4.18}$$

In Fig. (4.7), the virtual circuits for the preparation and analysis of the qutrit $|\Psi_3\rangle$ as well as the ququad $|\Psi_4\rangle$ is shown. Although the physical apparatus remains unchanged, the virtual circuit has expanded and now consists of six detectors C1 - C3 and D1 - D3. The time-resolved quantum-homodyne correlations for the qutrit and ququad photons are shown in Figs. (4.11, left) and (4.12, left), respectively. Additionally, the recorded data is also separated into the correlations between the virtual detectors which can be seen in Figs. (4.11, right) and (4.12, right), respectively. The correlations between these time bins all depend on the relative phases, as predicted. A procedure to determine the fidelities analogously to the one introduced in Sec. 4.7 yields fidelities of 0.94±0.01 and 0.89±0.02

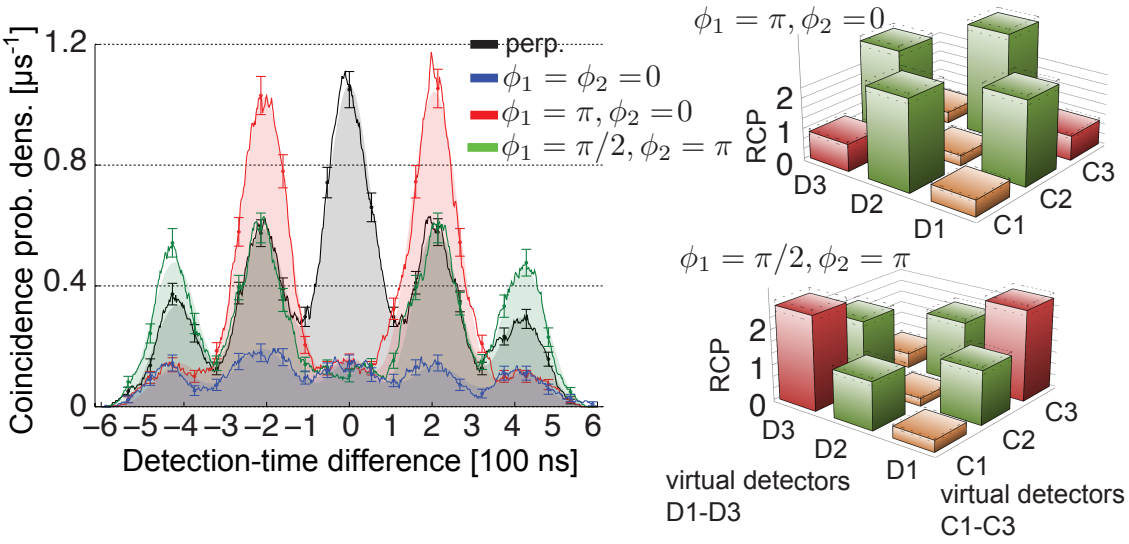

Figure 4.11: Results for the qutrits experiment [65, 66]: (Left) Time-resolved quantum-homodyne measurement for photons with perpendicular (black) and parallel (blue) polarisation with a phase shift in the central time bin of $\phi_1 = \pi$ (red) and with phase shifts of $\phi_1 = \pi/2$ in the central and $\phi_2 = \pi$ in the final time bins (green). (Right) Relative coincidence probabilities (RCPs) between virtual detectors for qutrits of phase $\phi_1 = \pi$ as well as $\phi_1 = \pi/2$, $\phi_2 = \pi$: The colour brown indicates the virtual detectors firing in the same time bin, green in successive time bins and red in time bins separated by one. The respective virtual circuit for the qutrit measurements can be found in Fig. (4.7, middle).

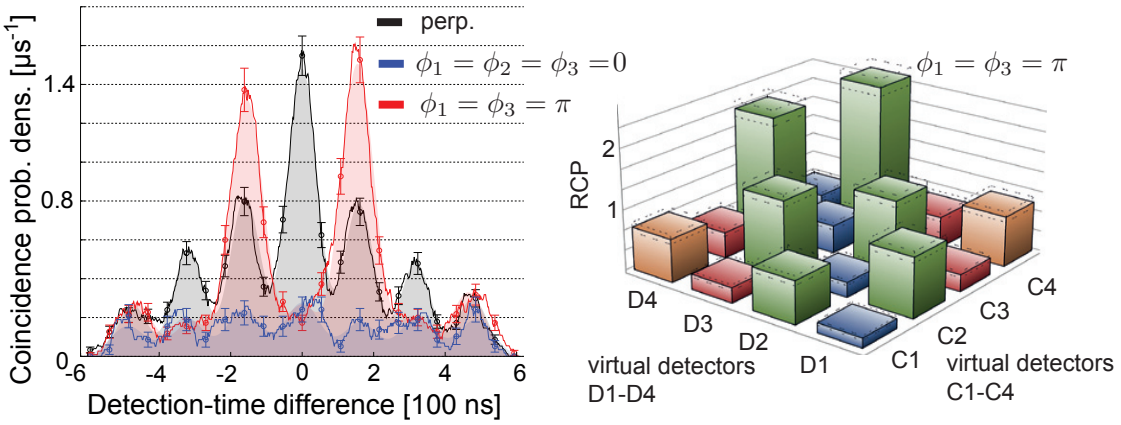

Figure 4.12: Results for the ququads experiment [65]: (Left) time-resolved homodyne signal of perpendicular (black), parallel (blue) polarisation and for phase shifts of $\phi_1 = \phi_2 = \pi$ in the signal photon (red). As before, the solid traces are obtained from summing all coincidences found within an 60 ns wide interval around each point of the trace and for some of these data points, we show the statistical error. The shaded areas in the plot correspond to the fit of seven auto-correlated $\sin^2$-pulses to the measured coincidence probabilities. (Right) Relative coincidence probabilities (RCPs) between the eight virtual detectors for the $\phi_1 = \phi_2 = \pi$-case, the respective virtual circuit can be found in Fig. (4.7).

for qutrits and ququads [65], respectively.

However, the increase in the size of the states is not infinite. The limiting factor of how many peaks a photon can have is the intrinsic coherence time of 500 ns and evolution rates of the system $(g,\ \kappa) = 2\pi \cdot (15,\ 12)$ MHz [60].

4.7 Calculating the fidelity

Determining the fidelity [3] of a prepared quantum state is a popular tool to determine how "close" this state is to the ideal one. To do so, the density matrix $\hat{\rho}$ of the generated state has to be reconstructed.

For our qubit state with the imprinted phase flip $\phi = \pi$, $\hat{\rho}$ calculates to be [65]

$$\hat{\rho} = \frac{1}{2}\begin{pmatrix} 1.01 & -0.85 \\ -0.85 & 0.99 \end{pmatrix}. \tag{4.19}$$

The values on the diagonal are obtained using photons of perpendicular polarisation in the quantum-homodyne measurement, for instance shown in Fig. (4.10, left). The numbers are proportional to the square root of the number of correlations detected in time bin 1 and 2, respectively, and then normalised to one. We further assume that signal and LO photons only differ in phase, such that their off-diagonal elements only differ in sign. Their magnitude is given by the ratio of the square root of the maximum observed to the maximum possible side-peak visibility, as shown in Fig. (4.10, left). Having obtained the density matrix of the single photon state, the fidelity [3] itself is is calculated with $F(|\Psi\rangle, \hat{\rho}) = \sqrt{\langle\Psi|\hat{\rho}|\Psi\rangle}$, where F is the value for the fidelity, $|\Psi\rangle$ is the reference state with $|\Psi\rangle = (|10\rangle - |01\rangle)/\sqrt{2}$, and $\hat{\rho}$ is the reconstructed density matrix of the single photon's quantum state.

4.8 Outlook – Quantum feedback

In this Section, we discuss what promising route could extend the qu-d-it production demonstrated in this Chapter. Although being an outlook, very preliminary 'proof of principle'-data has already been acquired[9], as shown in Fig. (4.13, right).

Assuming time-bin encoded qubits, the idea is to make a measurement on the first time bin of two interfering photons while the second time bin of the second photon is still being produced inside the cavity. The state of the second photon is – according to the

[9] In the earlier stages of the author's time in Oxford.

outcome of the measurement in the first time bin – actively influenced upon its generation process inside the cavity by changing its imprinted phase from default $\phi = 0$ to $\phi = \pi$. In Fig. (4.13, left), the virtual circuit of this idea is shown. Two twin-peak photons are subsequently emitted from the cavity such that they arrive at the fiber beam splitter at the same time. If there is a detection on the detector marked in red in Fig. (4.13, left) – the detector we condition on – a phase change is imprinted on the photonic time bin still being created inside the cavity.

Experimentally, a detection in the first time bin needs to trigger a circuitry which flips the phase of the STIRAP driving pulse as quickly as possible. The experimental means to do so can for instance be a latch circuit triggered by the TTL output of our SPCM and an electro-optic modulator to interact with this circuit, changing the STIRAP driving phase when receiving the input from the circuit to do so.

As soon as the first detection has occurred, which sets the phase between both photons to zero, the second time bin of the second photon gets imprinted a phase shift of π. Therefore, the second detection – provided it occurs in the second time bin – must occur in the other detector. We refer to this process as quantum feedback.

However, this feedback only delivers the desired result if the first photon emitted from the cavity takes the long path and the second one the short path of our setup. Additionally, the first detection must occur on the detector we choose to condition on and in the first time bin of the photon. The second photon must be detected in the second time bin. Only under theses circumstances, the second click occurs in the other detector. This quantum feedback shows great promise in view of LOQC experiments, however, it is beyond the

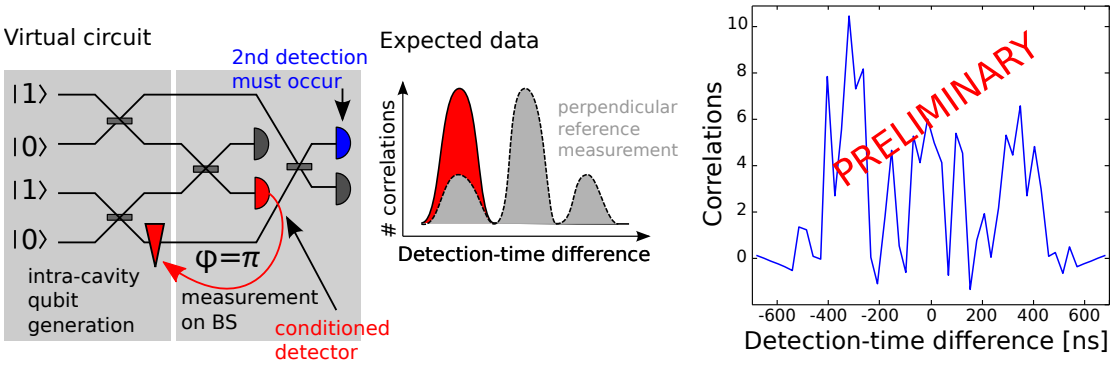

Figure 4.13: Quantum feedback experiment and very preliminary data: Two time-bin encoded qubits are generated successively from the cavity and sent towards a fiber BS. If there is a detection in the first time bin on the detector displayed red, this triggers a latch circuit to impose a phase flip of π upon the generation of the second time bin of the second photon. Therefore, if the second detection occurs in the second time bin, it *must* occur in the other detector, as this photon is forced into the opposite output mode due to the phase shift between the two time bins. In very preliminarily measured data (right), the expected peak from -230 ns to -560 ns suggests that this experiment can work when more experimental data is taken as this displayed set of data has been taken with only one experimental run ($\approx$ 30 min).

scope of this project[10].

[10]Please refer to my colleague Oliver Barter's thesis for more experimental details as well as first measurement results.

Chapter 5

Quantum experiments II – LOQC with long photons

Thirteen years ago, atom-cavity systems were proposed by Kuhn et al. [8] as an ideal photonic source for operating optical quantum technology devices [78] based on quantum interference of many photons [73] and post-selection to induce nonlinear controlled operations [15, 17, 79]. Recently, integrated optics have been developed to realise complex, miniature and mobile circuits for quantum information processing that manipulate the quantum states of single photons [16, 80].

Up to now, optical quantum logic has been performed with short photons – photons that have coherence length orders of magnitude smaller than the physical quantum circuits. For instance, photons from parametric down conversion traditionally have coherence lengths of 100 μm, but also 10 cm long photons from quantum dots have been reported [81]. In our case, photons are several orders of magnitude longer and consequently, they are much longer than the actual physical circuit.

In the following Chapter, these two systems, a photon "pistol" consisting of a strongly coupled atom-cavity system (Kuhn group, Oxford) is combined with a quantum information processing device, a photonic integrated circuit (O'Brien group, Bristol) as shown in

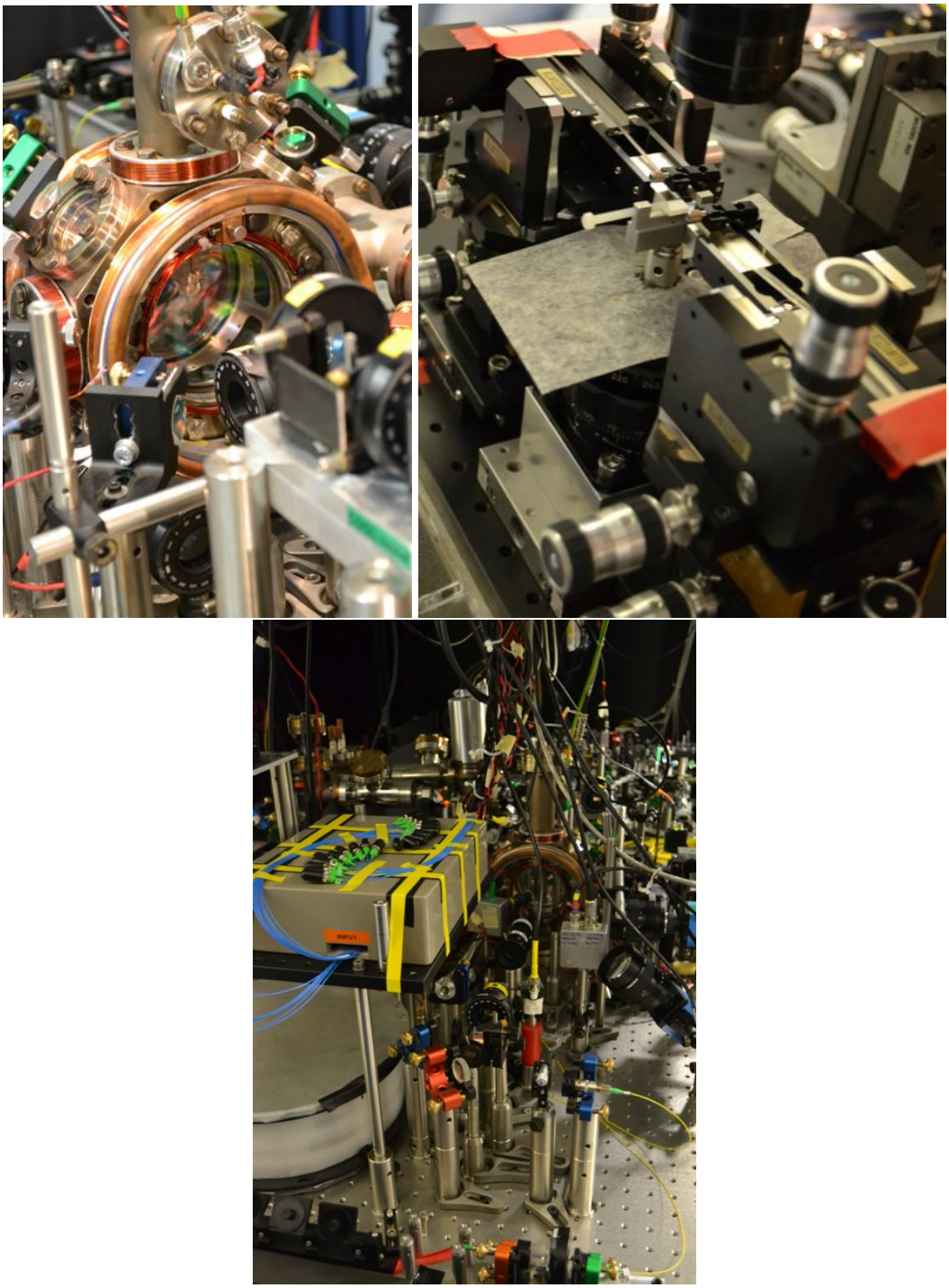

Figure 5.1: Linear optics quantum computing with ultra-long photons: The upper pictures show the experimental setup which is in place for the first data acquisition phase (2012). The respective data is presented in Sec. 5.1. Photons from the atom-cavity system represented by the vacuum chamber that contains the cavity (upper left) are coupled into the LOQC circuit. The picture (upper right) shows the translation stages for free-space coupling in and out of the chip. The lower picture shows the much more advanced setup, used for the second data acquisition phase (2014/2015). The respective data can be found in Sec. 5.2, Sec. 5.3, and Sec. 5.4. As it can be seen in the lower picture, the chip has been boxed up and a fibre array accessible to the experimentalist outside the box has been glued to the chip itself. This allows for comfortable data acquisition.

Fig. (5.1). As these LOQC devices are portable, the experiments described in the following have been carried out in Oxford in May 2012 and two years later from August to October 2014. Sec. 5.1 describes our first steps towards linear optics quantum computing with ultra-long photons and preliminary results when measuring a chip-integrated beamsplitter and CNOT gate. After two years of experimental down-time, the experiments were resumed in August 2014. The results of these measurements can be found in Sec. 5.2 to 5.4. We demonstrate a CNOT operation with ultra-long photons in Sec. 5.2 and additionally verify that we can generate entanglement from separable input states on our integrated circuit. The latter can be found in Sec. 5.3. We conclude this Chapter with operating a LOQC circuit with temporally encoded qubits in Sec. 5.4.

5.1 First data

Operating a LOQC circuit with photons from an atom-cavity system has never been carried out before. Traditionally, these circuits are operated with inherently probabilistic single-photon sources. This Section describes our first steps towards using a deterministic single-photon source to seed these circuits and the lessons we have to learn on the route towards a more professional use of narrowband single-photon sources and integrated quantum photonics described later in this Chapter.

In particular, in Sec. 5.1.1, we describe the experimental setup constructed of an atom-cavity system as a single-photon source and the LOQC circuit as the quantum processing unit. As these two systems have never been combined before, we also touch upon experimental difficulties. In Sec. 5.1.2, we measure Hong-Ou-Mandel interference on a simple LOQC beam splitter and therefore test how the performance of these systems compares.

Finally, we show first data of operating a controlled-NOT gate with long photons Sec. 5.1.3 as well as with twin-peak photons.

5.1.1 Experimental setup

To carry out LOQC experiments with ultra-long photons, we begin in the traditional way of how to produce photons from an atom-cavity system as already thoroughly discussed in Chapter 4. In Fig. (5.2), the traditional outline of the experimental setup with a LOQC circuit in form of either a chip-integrated beam splitter or a CNOT gate can be found. These are the circuits we are going to measure in Sec. 5.1.2 and Sec. 5.1.3, respectively. Two single photons are subsequently emitted from the single atom strongly coupled to a high-finesse optical cavity. A polarising beam splitter (PBS) directs the unpolarised stream of photons into two paths of different optical lengths chosen to delay one photon by its own length. To obtain a photon pair at the input of the circuit, the first photon has to take the path including the 200 m delay line corresponding to its 1 μs temporal length, the second one has to take the short path.

The fibres used are polarisation maintainig except for the delay arm of a non-polarisation maintaining fibre which is additionally polarisation controlled with the help of manual fibre polarisation controllers ('paddles'). The photons are coupled into the circuit in free space, with the fibre array leading up to the circuit mounted on translation stages. After passing through the photonic circuit, the photons are collected with a second fibre array and sent onto single-photon counting modules (SPCMs)[1]. With the help of refractive index matching liquid, the coupling efficiencies are about 60% from the fibre into the circuit

[1] In the CNOT case: Two Laser Components COUNT modules and two Perkin-Elmer SPCMs AQRH-14.

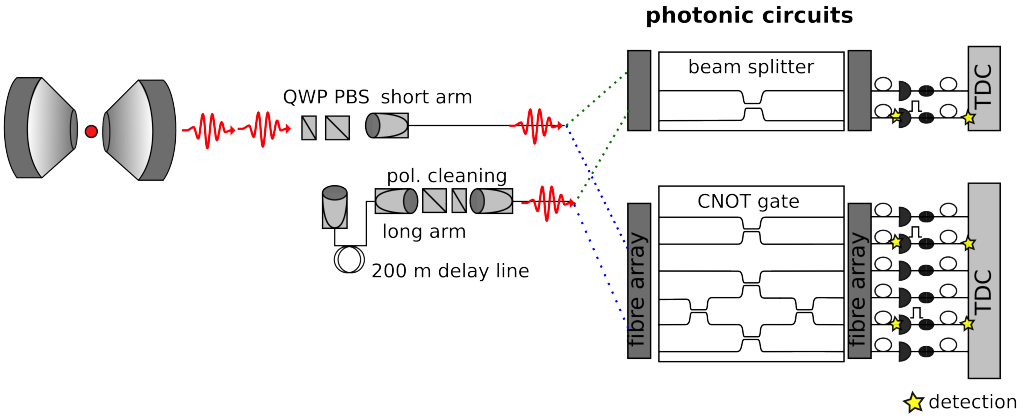

Figure 5.2: Schematic experimental setup for measuring a LOQC circuit, in particular a beam splitter or CNOT gate: The single photons are emitted from the optical cavity. With the help of a delay line, the first photon is delayed by its own length such that it arrives at the beam splitter simultaneously with the subsequently emitted photon. The photons are coupled into the photonic integrated circuit in free space. There, the quantum computation takes place. Leaving the chip, the photons are coupled into a fibre array and sent towards single-photon counting modules (SPCMs). As soon as the SPCMs detect a single photon, a TTL pulse is sent to the TDC where it is registered together with a time stamp and stored for post-processing.

and back into a fibre array. This part of the experiment is shown in Fig. (5.1, upper right). The TTL signals from the SPCMs are registered by the time-to-digital converter (TDC) which records all the information necessary for post-processing the data.

Experimentally, the challenges lie in the spatial and temporal length of the photons. As we learn when setting up the experiment, etaloning can potentially cause self-interference arising from reflection off perpendicular optical surfaces, such as for instance from the PC fibre connectors[2], polished chip facets or the back facet of the cavity mirrors. As PC fibre connectors have a flat surface, it is naturally prone to self-interference of the photon as it can be reflected from this surface as the coherence length of the photons is much longer than any optical path length within the circuit. These effects decrease the quantum interference which is necessary to operate these photonic devices. A solution to this particular problem is to replace all PC fibre connectors by APC ones. These APC

[2]FC/PC: Physical Contact polish of the fibre end. FC/APC: Angled Physical Contact.

connectors are polished at an angle of 8°, although they have higher insertion losses than the PC ones[3], they greatly reduce back reflections.

5.1.2 Chip-integrated beam splitter

As a first compatibility check between the photon pistol and the LOQC devices, a chip-integrated 50:50 beam splitter is tested with photons emitted from the strongly coupled atom-cavity system. The corresponding experimental setup is depicted in Fig. (5.2, upper). As in previous measurements, the photons are much longer than the detector resolution, this is why we can have a look at the interference in a time-resolved manner [75, 77]. As the properties of our source have been already determined in a separate HOM measurement [60], we need to determine whether their indistinguishability is preserved across the spatial and polarisation overlap inside the waveguide. This means we investigate whether the LOQC circuit and the photon pistol are compatible.

In a traditional Hong-Ou-Mandel (HOM) measurement, we send indistinguishable single photons of parallel polarisation into the two inputs of the circuit and compare the data to the reference measurement of distinguishable photons which are perpendicularly polarised. In Fig. (5.3), we can directly compare these two sets of data of a HOM measurement on chip and on a fiber beam splitter. The preliminary HOM-visibility in the photonic circuit case is estimated to be $\approx 60\%$ as opposed to $87\pm5\%$ [60][4] on a fiber BS. This value shows that both systems, the atom-cavity system to generate single photons and the photonic chip to carry out quantum gate operations, is suitable to be used as a *hy-*

[3] As specified by the supplier, FC/PC patch cables have an 'typical' insertion loss of 0.3 dB, whereas for FC/APC patch cables it is 1.5 dB.

[4] Please not that this HOM data is taken from Peter Nisbet-Jones' paper [60].

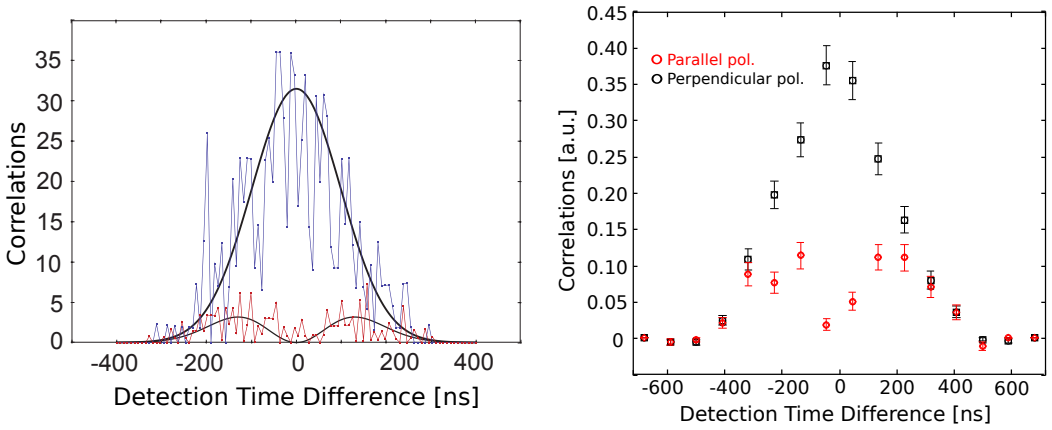

Figure 5.3: Time-resolved Hong-Ou-Mandel interference for both the fiber beam splitter (left, data from [60]) and chip-integrated (right) beam splitter: The red data in both cases corresponds to parallely polarised single photons interfering. Ideally, no correlations between both detectors are observed which corresponds to the Hong-Ou-Mandel effect. However, the 'wings' around the zero detection-time difference arise from decoherence effects upon generation of the photons. The black data points are the reference measurement with perpendicular polarised photons. The shape of the envelope is equivalent to the convolution of the shapes of the two single photons.

brid source-chip system. The HOM-visibility difference between fiber beam splitter and chip-integrated beam splitter can be explained by an imperfect splitting ratio in the circuit, decoherence effects upon the generation of the photons or imperfect polarisation alignment. In due course we see that this HOM-visibility can be increased to values around 85% as demonstrated in Sec. 5.2.2 by for instance careful polarisation alignment.

5.1.3 Chip-integrated CNOT gate

Having demonstrated that both systems can be joined together, the next step is to introduce a more sophisticated photonic chip to the system: A controlled-NOT (CNOT) gate [17] integrated within a silica-on-silicon circuit, the respective experimental setup can be found in Fig. (5.2, lower).

The architecture of the circuit which is depicted in Fig. (5.4) has been introduced theoretically by Ralph et al. [17] in 2002. It is a gate that only consists of linear optical

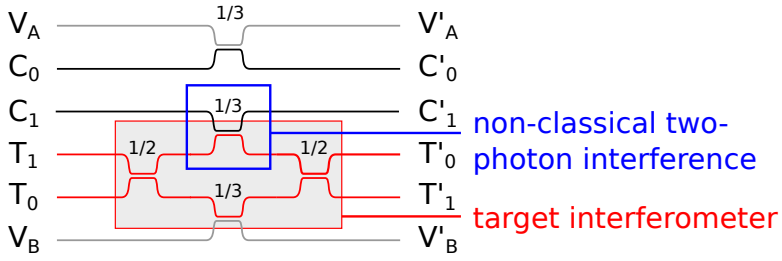

Figure 5.4: Schematic of Ralph's coincidence controlled CNOT gate (theory [17], experiment in bulk optics [15] and on chip [80]): V stands for vacuum input, C for control qubit and T for target mode. Please note that the target modes T_0 and T_1 on the output of the circuit are inverted compared to the input ones. This is due to the generation process of the photonic chip and, with the help of this labelling, it leads to the well-known truth table.

elements and needs a two-photon input, one in the control and one in the target mode. It operates in the coincidence basis, which means that if one detects a coincidence between target and control modes[5] on the output of the circuit, the computation has been successful. The complete circuit consists of two vacuum, two control and two target modes. By inserting a single photon in one mode of both target and control we *spatially* encode our target and control *qubits*. The fundamental principle of the CNOT gate is, that according to which state the control qubit is in it flips the target qubit or leaves it unchanged. The potential input states in the logical basis are $|0_C 0_T\rangle$, $|0_C 1_T\rangle$, $|1_C 0_T\rangle$ and $|1_C 1_T\rangle$, corresponding to a single photon occupation of mode C_0 and T_0, C_0 and T_1, C_1 and T_0 or C_1 and T_1, respectively.

Experimentally, this gate works as described in the following: The two target modes T_0 and T_1 are mixed on a 50:50 beam splitter, then enter an interferometer and are subsequently recombined on a second 50:50 beam splitter. The interferometer has two additional 1/3:2/3 beam splitters in the upper and lower interferometer arm. If the interfer-

[5]This means that we detect a click (a photon) in one of the detectors connected to the target modes and one click in the detectors connected to the control modes. We refer to this as a correlation event between control and target modes.

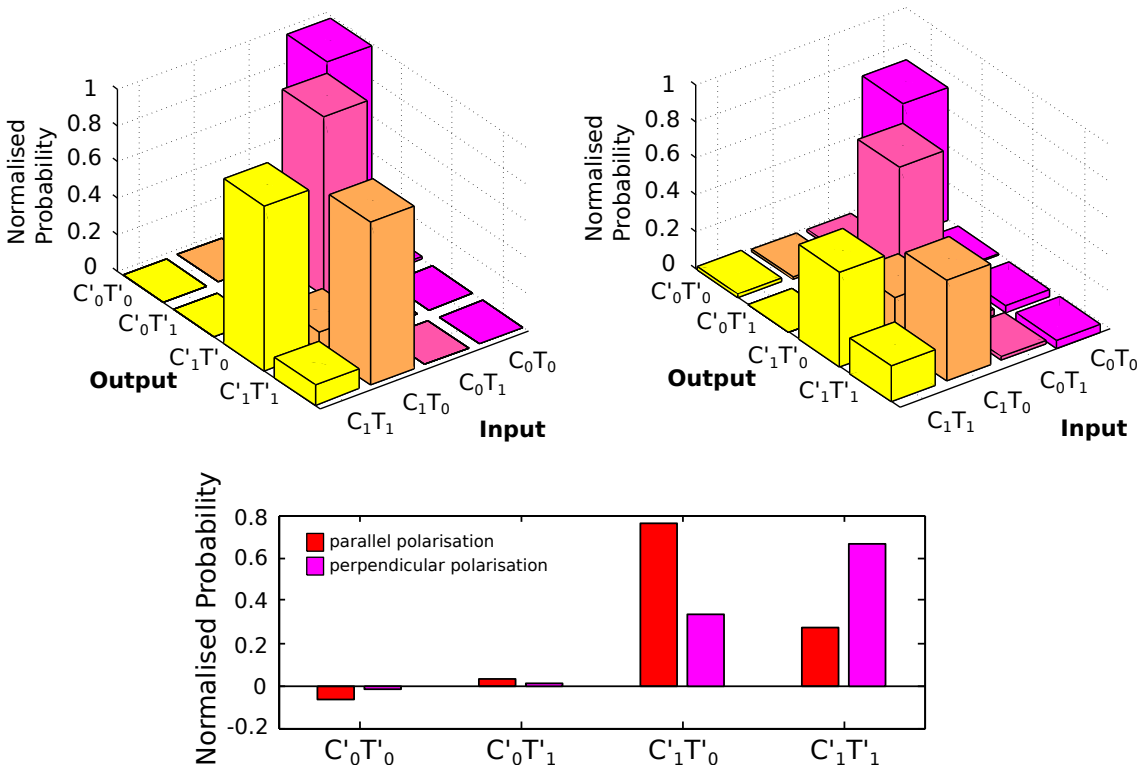

Figure 5.5: (Upper left) Theoretical truth table values (calculated by J. C. F. Matthews) for an imperfect photonic CNOT integrated circuit, which includes an imperfect 50:50 (simulated as 55:45) and an imperfect 1/3:2/3 BS (simulated as 40:60). (Upper right) Best measured data for the complete truth table with single-peaked photons in the hybrid source-chip system. (Lower) By comparing the output of the circuit for both parallely and perpendicularly polarised photons in the C_1T_0 input case we see that quantum interference does steer the output of the circuit.

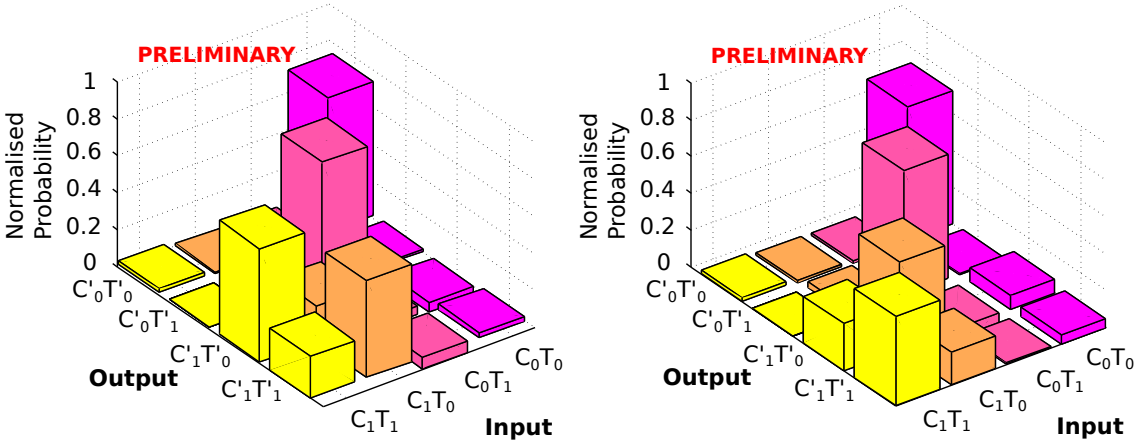

Figure 5.6: Preliminary measurements of a two time-bin photon with a phase shift of π on one of the time bins: (Left) Evaluation of the data in the same time bin (right) as well as in different time bins. In the different time-bin case we observe quasi-fermionic behaviour whereas in the same time-bin case we observe a standard CNOT operation.

ometer is balanced, the target qubit will leave the interferometer in the same state that it entered in. From Fig. (5.4), we can clearly see that this is the case if the control qubit is in state $|0_C\rangle$, meaning that we send the photon into input C_0. However, if there is a single photon sent into input C_1, indicating that the control is in state $|1_C\rangle$, target and control photons interfere non-classically on the 1/3:2/3 BS. This non-classical two-photon interference causes a phase shift of π in the upper arm of the target interferometer. Therefore, the target leaves the circuit in the respective other state, whereas the control remains unchanged. The gate has an overall success probability of 1/9. As soon as a coincidence between control and target is detected, we know that the computation has been carried out successfully. The gate has been firstly demonstrated using bulk optics by O'Brien et al. [15] and with the help of an integrated circuit by Politi et al. [80]. The chip we use in these preliminary measurements is grown and lithographically masked using germanium- and boron-doped buried square Silica waveguides on a Silicon substrate [82].

The schematic of the experimental setup can be seen in Fig. (5.2) and the preliminary measured results in Figs. (5.5) and (5.6). To display all measured outputs for all input combinations in the logical basis we use a 'quantum logic' *truth-table* representation. As input states, we choose a single photon pair with only one time bin as well as a two time-binned photon pair.

In the photon-pair case, we observe that the CNOT operation works – however, not ideally. For instance in the C_1T_1 input case we observe most of the counted correlations between output modes $C'_1T'_0$, however, there are also some between the output modes $C'_1T'_1$. As the model in Fig. (5.5, upper left) shows, this can be explained by non-ideal beam splitter ratios on the chip. Also, the circuit has not been designed for the 780 nm

wavelength but for 804 nm.

Additionally, we send our two time-bin photons introduced in Chapter 4 into the CNOT circuit with a phase shift of π imprinted on one of the time bins of one photon of the photon pair. If we evaluate the data only taking coincidences detected in the *same* time bin into account, we can reproduce the standard CNOT functionality, as it can be seen in Fig. (5.6, left). This means if we insert a pair of photons into input modes C_1 and T_0, we find a coincidence event[6] between output modes C'_1 and T'_1 and vice versa for pair of photons being sent into input modes C_1 and T_1. This means the photons behave as expected – as bosons.

However, if we evaluate the identical data for coincidences in *different* time bins, the CNOT operation breaks down, as shown in Fig. (5.6, right). Choosing C_1 as the control input, this means – provided that we detect one photon in one time bin and the second one in the other time bin in the coincidence basis – we are able of actively forcing the photon into the respective other target output than the one we would expect if we had bosonic behaviour. This means if we insert a pair of photons into input modes C_1 and T_1, we find a coincidence event between output modes C'_1 and T'_1 and vice versa for pair of photons being sent into input modes C_1 and T_0. This is why we refer to this behaviour as quasi-fermionic.

Interpreting these findings, we find that we can mimic both bosnic behaviour (evaluation of the data in the same time bin) and fermionic behaviour (evaluation of the data in different time bins) with the same measurement [83]. A similar behaviour has already been observed with respect to our quantum homodyne measurement in Sec. 4.2.

[6] Only for coincidences detected in the same time bin.

The results are referred to as 'preliminary' and have never been published as each row of the truth table has been normalised separately to one. This is due to the fact that in this measurement session, we did not carry out an overall normalisation measurement. Therefore, different lines of the truth table cannot be compared to each other. We conclude, that this is a valid 'proof of principle'-experiment – we can demonstrate that we can use the atom-cavity source and the LOQC circuit as a hybrid source-chip system – but nothing more than that. However, these normalisation measurements have to be repeated as well as the data acquisition. The respective results including a proper calibration of the system can be found in Sec. 5.2.3 for the CNOT operation an in Sec. 5.4 for the two-qubit measurements on chip.

5.2 The CNOT4 chip

As the preliminary data acquisitions lack a proper normalisation measurement, we need to repeat and extend the experiment described above. There is two-year downtime of the photon-pistol experiment until this plan can spring into action. In August 2014, the collaborative experimental work of Bristol and Oxford is resumed by the author. The results are published in [84].

In the following, we begin with the description of our particular circuit in Sec. 5.2.1. We introduce different types of experiments, ranging from characterising the hybrid source-chip system by a simple Hanbury-Brown-Twiss measurement (*single-photon* experiments) and Hong-Ou-Mandel measurements (*two-photon* experiments) on chip in Sec. 5.2.2. Also, we demonstrate that it is possible to do a CNOT operation with long photons in

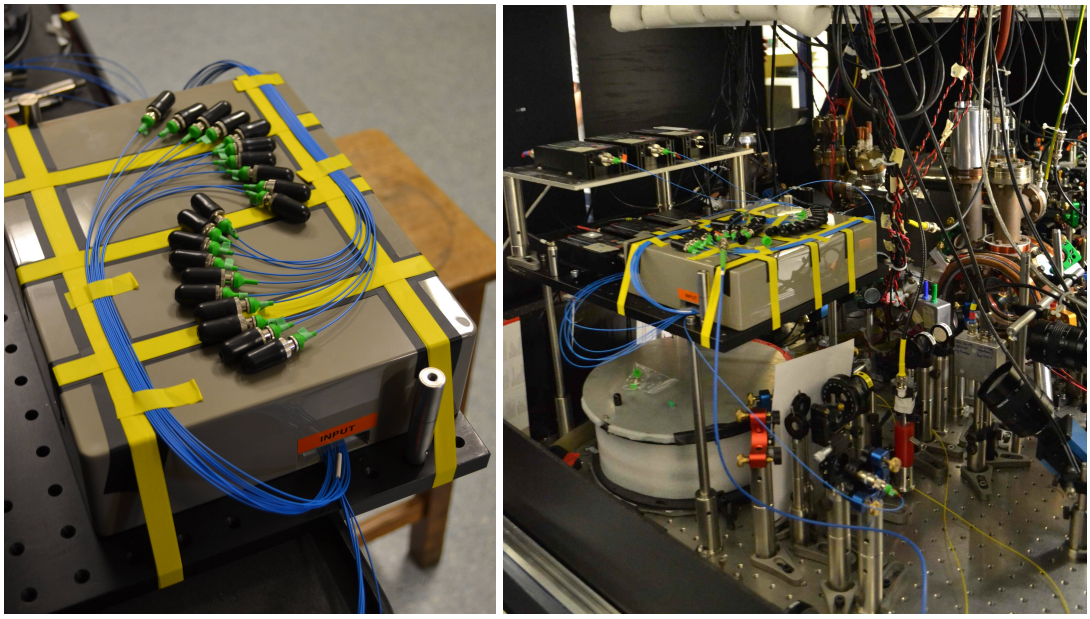

Figure 5.7: State-of-the-art chip packaging (left) as well as this package embedded in the photon-pistol experiment (right): Inside the plastic box (left) visible from the outside, a PM fibre array is glued to the actual waveguide which allows for easy input changing when carrying out the experiments. The different input modes can be selected by coupling the ends of these fibres to the long and the short arm of the photon pistol. In the actual setup (right), we can identify the spooled delay fibre of 200 m length below the bread board. On the bread board, we mount the six single-photon counters as well as the packged chip right next to the counters. For safety reasons, we tape the box the chip is in to the bread board (yellow). Also, we see the photon pistol's vacuum chamber.

Sec. 5.2.3.

5.2.1 Introduction

The experiments that follow are carried out with the help of a different chip design, not the standard CNOT as described above, but the so-called CNOT4 chip[7]. The photonic circuit itself, shown in Fig. (5.8), is a network of single-mode waveguide directional couplers designed to operate with near-infrared (NIR) photons and fabricated lithographically using germanium and boron doped silica on a silicon substrate [80]. The buried square 3.5 μm x 3.5μm waveguides of refractive index contrast Δn = 0.5 support only the fundamental mode at 780 nm. For photons from spontaneous parametric down conversion with a coherence length in the 100 μm range, the full quantum process for single- and two-qubit logic using exactly this architecture has been carried out [85]. The input and output facets of the integrated circuit are glued with an optical adhesive to polarisation maintaining fibre arrays to simplify coupling into and out of the circuit. This makes the handling of the device much more experimentalist-friendly as it can be seen in Fig. (5.7). The integrated circuit sits in a much larger plastic package to guarantee strain relief on the fibres. If one wants to change input modes, only coupling the respective input of the circuit to the long and short arm of the photon pistol is necessary. The average loss across the chip from input to output fibre amounts to 3.3 dB.

The CNOT4 circuit is in principle a CNOT one with two additional Hadamard gates on the control modes as depicted in Fig. (5.8). The target interferometer is similar to the one used in a standard CNOT gate. As we use the CNOT4 chip in various different ways

[7]This was due to the fact that Bristol decided to have a fibre array glued to the end facet of the traditional CNOT chip and something went wrong in the gluing process which made the circuit no longer available.

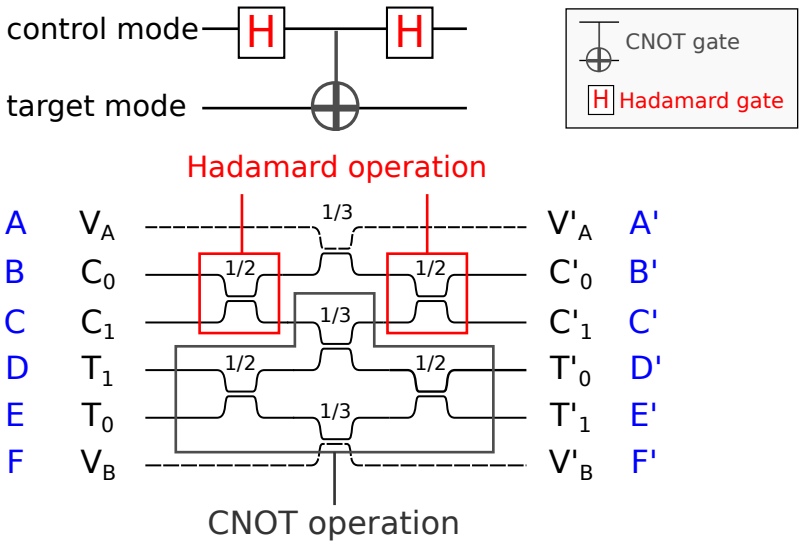

Figure 5.8: Circuit diagram and architecture of the used CNOT4 circuit. The CNOT4 circuit is similar to a standard CNOT one but with two additional Hadamard gates mixing the control modes. As we use this circuit in various different ways in the following, we therefore introduce an non-descriptive nomenclature for our input and output modes. The input modes are referred to as A, B, C, D, E, and F and the output modes as A', B', C', D', E', and F'.

in the following, we introduce a new nomenclature for the input modes which we refer to as A, B, C, D, E, and F. The respective output modes are A', B', C', D', E', and F'. In Sec. 5.2.2, we see that we can characterise our source with the help of this circuit itself. We determine that we obtain one single photon at a time from the source as well as learn about their indistinguishability and polarisation and spatial overlap on chip.

5.2.2 Characterising the source – on chip

As a first experiment, we want to do characterisation measurements of the experimentally crucial parts of the hybrid source-chip system. This Section discusses how we can do this with the help of the system itself. We have to demonstrate two fundamental properties of the source, namely that we have *single photons* as well as that these photons are *indistinguishable* from each other – otherwise no quantum interference is possible.

We begin with the demonstration of the singleness [37] of the photons. This measurement is a 'single-photon' measurement in a Hanbury-Brown-Twiss (HBT) setup [86]. The function that we measure is the second-order intensity correlation function $g^{(2)}(\Delta\tau)$ of the source. A sketch of the experimental setup can be found in Fig. (5.9). In this measurement, all the single photons coming from the cavity are sent into one particular input mode of the CNOT4 chip – in our case we choose input mode F – while all six outputs are monitored by single-photon counters. The second-order intensity correlation function $g^{(2)}(\Delta\tau)$ is defined by [24, 60]

$$g^{(2)}(\Delta\tau) = \frac{\langle P_{\mathrm{D1}}(t) P_{\mathrm{D2}}(t-\Delta\tau)\rangle}{\langle P_{\mathrm{D1}}(t)\rangle \langle P_{\mathrm{D2}}(t)\rangle}, \tag{5.1}$$

where we refer to $\Delta\tau$ as the detection-time difference, $P_{\mathrm{D1}}(t)$ and $P_{\mathrm{D2}}(t)$ are the probabilities of detecting a photon in the corresponding detector D1 and D2. The photon's singleness is defined as $g^{(2)}(\Delta\tau = 0)$ [37, 52]. As the single photons can potentially be observed in more than two outputs compared to the standard $g^{(2)}(\Delta\tau)$ measurement on a simple beam splitter, we count correlations in outputs D', E', and F' and add them up during post-processing. The result of each individual output combination and the total result is shown in Fig. (5.9). Please note that in this measurement, although it includes – besides photon-photon correlations – photon-dark count correlations as well as dark count-dark count correlations, the singleness is still demonstrated. The main source of noise is dark counts from the detectors. The only correction that has been applied during post-processing is that all detections which are outside the single photons' arrival time have been gated out in the analysis programme. The absence of a peak around $\Delta\tau = 0$ –

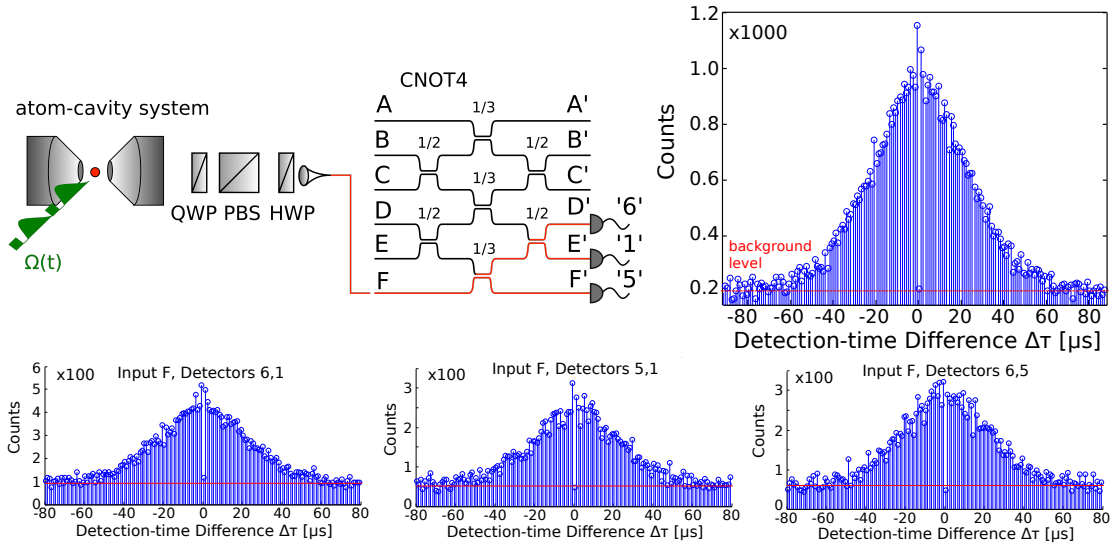

Figure 5.9: Determining the singleness of our single photons: We use our hybrid source-chip system to carry out a Hanbury-Brown-Twiss measurement, where all the photons from the source are sent into the circuit's input F and all six outputs of the CNOT4 chip are observed. However, as the single photon stream that is sent into the circuit can only be observed by detectors D, E, and F due to the chip's architecture, only these outputs are correlated during post-processing. We determine the $g^{(2)}(\Delta\tau)$ function by adding up all the correlations between D' and E', D' and F' and E' and F'. The detector connected to output D' has the number 6, E' the number 1 and F' the number 5 – the numbers refer to the input modes of the time-to-digital converter which registers the single photon clicks. Please note, there is no background subtracted. 6,000 MOT throws have been used to obtain this result which corresponds to 1,800 s = 30 min of time-integration.

which corresponds to zero detection-time difference – indicates that there is exactly one photon emitted for one pump pulse sent onto the atom. Normalising the data from Fig. (5.9), we find at zero detection-time difference $g^{(2)}(0) = 0.15$ [84] indicating the reduction in probability of detecting two events during one single STIRAP pump pulse. These residual correlations can be fully attributed to detector dark counts, the shot noise of which imposes an upper limit of $g^{(2)}(0) < 0.02$ to the photon stream at the one-sigma confidence level [84].

From Fig. (5.9), we can also determine the interaction time of the atom producing the photon which corresponds to the envelope of the $g^{(2)}(\Delta\tau)$ function. We can see that if the first click is registered at $\Delta\tau = 0$, there is the probability that this atom still emits a photon at t' = t + 60 μs. It has to be stated that this is the source characteristics of a 'day-to-day measurement' and not particularly optimised on a long interaction time of the atom with the cavity. Each bar in the graph corresponds to a time window of 1 μs – the repetition rate of the photon production. Having demonstrated the first property of our photons, their singleness, we subsequently investigate their indistinguishability.

The HOM measurement quantifies whether the source prepares single photon pairs as well as whether their indistinguishability is preserved across the coherence time of the photons *including* the spatial and polarisation overlap in the waveguide. In a measurement similar to a traditional atom-cavity system where we use a fiber beam splitter, we send the first photon of a pair down the delay arm of the system, the second one down the short arm. In this way, both photons of the pair arrive at the LOQC circuit simultaneously. As we want to characterise our hybrid system with the help of the system itself – we do not check for instance the HOM visibility or the singleness of the photons on a finer beam

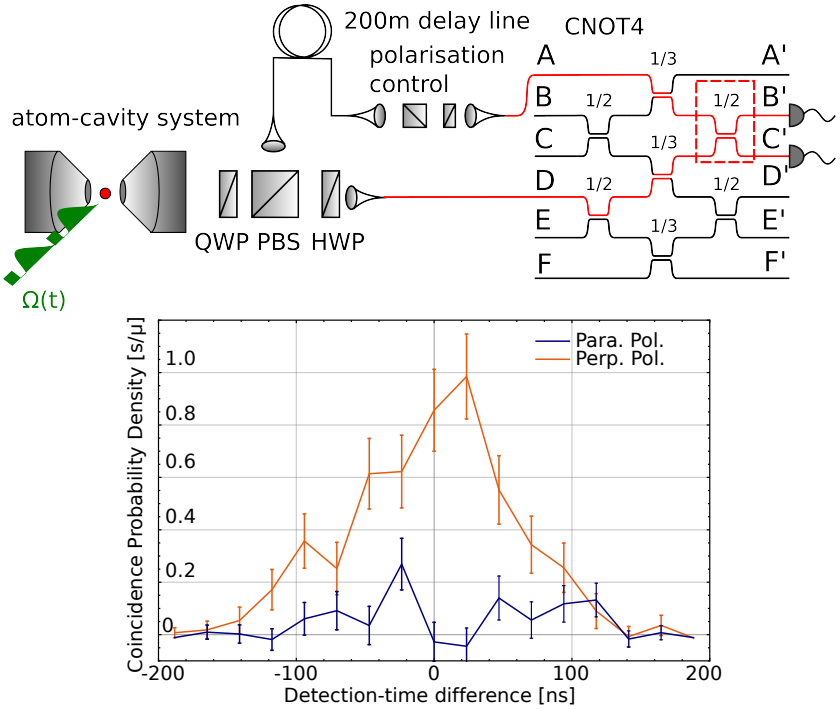

Figure 5.10: Determining the indistinguishability of our single photon pairs as well as their spatial and polarisation overlap on chip with the help of our hybrid source-chip system: On our chip, we choose the input modes A and D and interfere them on the beam splitter marked in red. We monitor the outputs B' and C'. If a photon does not end up in the monitored outputs is is considered as loss. We observe a HOM-visibility of 0.85±0.05 [84].

splitter[8] – we chose the input modes A and D of our circuit and the beam splitter marked in red in Fig. (5.10). We monitor the output modes B' and C'. The other potential output modes the photons could be registered in are considered as loss. This does not change the physics but – due to increased measurement time – decreases the signal-to-noise ratio due to dark counts in the detectors. To determine the degree of inseparability of our single photons, we need to carry out two measurements and compare them. At first, a reference is established by generating and measuring perfectly *distinguishable* single photons. The easiest way of doing this is to use perpendicularly polarised photons. By switching to parallelly polarised photons, one can demonstrate their degree of *indistinguishability* by comparing this measurement to the one with perfectly distinguishable photons. As it can be seen in Fig. (5.10), we observe a HOM-visibility of 85±5%.

5.2.3 CNOT operation with long photons

A CNOT gate is a two-qubit logic gate in which the state of a target qubit is flipped, dependent upon the state of a control qubit. The standard architecture has been introduced by Ralph [17] in 2002 and can be seen in Fig. (5.11, left). This gate operates on spatial mode encoded qubits, with the control qubit encoded into modes C_0 and C_1 and the target qubit encoded into modes T_0 and T_1. The gate's mechanism is based on two core principles of linear optical quantum circuits: single photon interference – requiring complete circuit stability – and two-photon interference. The principles of a standard CNOT gate is thoroughly discussed in Sec. 5.1.3.

As the standard CNOT circuit is not available, we have to carry out our measurements

[8] This would be less demanding experimentally but one would not learn as much about the coupled system.

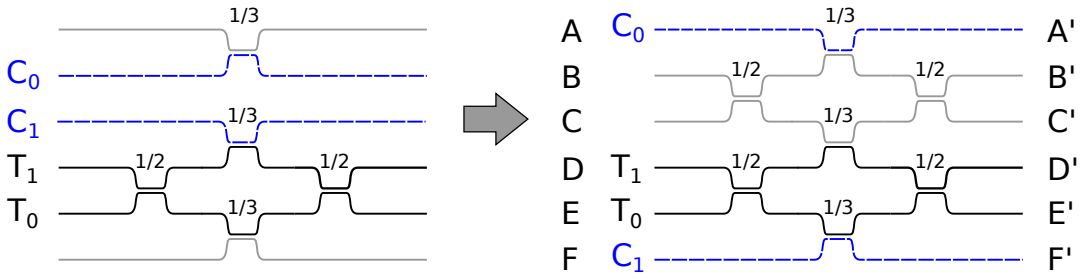

Figure 5.11: Comparison between a well-known architecture of a CNOT gate (left) and a CNOT4 gate (right). We use the CNOT4 gate *as if it was* a CNOT gate. As it can be seen from the circuits, the C_0 mode does not take part in the computation and the C_1 mode couples to the target interferometer of modes T_0 and T_1. By a non-classical interference, a phase shift is introduced in the interferometer and the target output is flipped.

on a different circuit, namely the CNOT4 one. By comparing the circuits' architectures as shown in Fig. (5.11), it is easy to see that the CNOT4 gate is a CNOT gate mixing the control inputs. This is how the gate is originally intended to be used. However, as we want to verify our standard CNOT operation on the CNOT4 circuit, we identify input mode A of the circuit as our new C_0, the input modes B and C as the respective vacuum modes V_A and V_B, input mode D and E correspond to the respective target input modes T_1 and T_0 and input mode F corresponds to the C_1 input mode. We see that our new C_0 mode only interferes with the vacuum modes and if we insert a photon into this input mode, it can only reach the vacuum outputs which we solely monitor for the sake of completeness. The target interferometer is similar to the one on the standard CNOT circuit. The only difference is that the interesting beam splitter is not located in the upper arm of the interferometer but in the lower arm. Due to the architecture of the circuit, it is impossible that one single photon potentially inserted into input A interferes with a target photon. This is why it is possible to use this CNOT4 as a standard CNOT circuit. Identifying input mode F as C_1, we find that – identically to the standard CNOT configuration – there can be non-classical

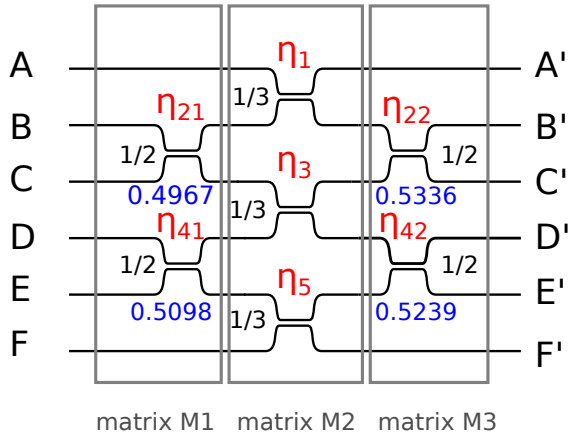

Figure 5.12: CNOT4 circuit used in our experiment comprising beam splitters with general (η_{xy}, red), ideal (black) and measured (blue) reflectivities. Accordingly, (1-η_{xy}) refers to the transmittivity of the beam splitter. The matrices M1, M2 and M3 describe the linear transformation of the input modes through the circuit.

two-photon-interference on the beam splitter in the lower target interferometer arm. This introduces a phase-shift of π in the target interferometer and flips the output mode of the circuit.

How to calculate the output of a CNOT4 gate

Having already experimentally demonstrated the two fundamental properties of our hybrid source-chip system – single as well as indistinguishable photons – we discuss what we expect to measure if we operate a CNOT operation on a CNOT4 chip in this Section. En passant, we establish a formalism of how to calculate photonic circuits which is of help as soon as we deal with Sagnac loops on chip in Sec. 5.3.

In the following, we extend the formalism developed by Ralph [17] in the Schrödinger picture in order to determine the output modes of a LOQC gate to our CNOT4 circuit. The input modes A, B, C, D, E, and F are transformed into the output modes A', B', C', D', E', and F' via the transformation matrices M1, M2 and M3

$$\begin{pmatrix} A' \\ B' \\ C' \\ D' \\ E' \\ F' \end{pmatrix} = M3 \cdot M2 \cdot M1 \cdot \begin{pmatrix} A \\ B \\ C \\ D \\ E \\ F \end{pmatrix}. \tag{5.2}$$

The successive transformations describing the circuit are depicted in Fig. (5.12). The transformation matrices explicitly read

$$M1 = \begin{pmatrix} 1 & 0 & 0 & 0 & 0 & 0 \\ 0 & \sqrt{\eta_{21}} & \sqrt{1-\eta_{21}} & 0 & 0 & 0 \\ 0 & \sqrt{1-\eta_{21}} & -\sqrt{\eta_{21}} & 0 & 0 & 0 \\ 0 & 0 & 0 & \sqrt{\eta_{41}} & \sqrt{1-\eta_{41}} & 0 \\ 0 & 0 & 0 & \sqrt{1-\eta_{41}} & -\sqrt{\eta_{41}} & 0 \\ 0 & 0 & 0 & 0 & 0 & 1 \end{pmatrix}, \tag{5.3}$$

$$M2 = \begin{pmatrix} \sqrt{\eta_1} & \sqrt{1-\eta_1} & 0 & 0 & 0 & 0 \\ \sqrt{1-\eta_1} & -\sqrt{\eta_1} & 0 & 0 & 0 & 0 \\ 0 & 0 & \sqrt{\eta_3} & \sqrt{1-\eta_3} & 0 & 0 \\ 0 & 0 & \sqrt{1-\eta_3} & -\sqrt{\eta_3} & 0 & 0 \\ 0 & 0 & 0 & 0 & \sqrt{\eta_5} & \sqrt{1-\eta_5} \\ 0 & 0 & 0 & 0 & \sqrt{1-\eta_5} & -\sqrt{\eta_5} \end{pmatrix}, \tag{5.4}$$

$$M3 = \begin{pmatrix} 1 & 0 & 0 & 0 & 0 & 0 \\ 0 & \sqrt{\eta_{22}} & \sqrt{1-\eta_{22}} & 0 & 0 & 0 \\ 0 & \sqrt{1-\eta_{22}} & -\sqrt{\eta_{22}} & 0 & 0 & 0 \\ 0 & 0 & 0 & \sqrt{\eta_{42}} & \sqrt{1-\eta_{42}} & 0 \\ 0 & 0 & 0 & \sqrt{1-\eta_{42}} & -\sqrt{\eta_{42}} & 0 \\ 0 & 0 & 0 & 0 & 0 & 1 \end{pmatrix}, \tag{5.5}$$

where η_{xy} refers to the reflectivity and accordingly (1-η_{xy}) to the transmittivity of the respective beam splitter. To subsequently calculate the output modes A', B', C', D', E', and F' one applies these matrices M1, M2 and M3 on the input modes A, B, C, D, E, and F. In the *ideal case*, we find

$$\begin{pmatrix} A' \\ B' \\ C' \\ D' \\ E' \\ F' \end{pmatrix} = M3 \cdot M2 \cdot M1 \cdot \begin{pmatrix} A \\ B \\ C \\ D \\ E \\ F \end{pmatrix} = \frac{1}{\sqrt{3}} \begin{pmatrix} A+B+C \\ A-C+\frac{1}{\sqrt{2}}D+\frac{1}{\sqrt{2}}E \\ A-B-\frac{1}{\sqrt{2}}D-\frac{1}{\sqrt{2}}E \\ \frac{1}{\sqrt{2}}B-\frac{1}{\sqrt{2}}C-E+F \\ \frac{1}{\sqrt{2}}B-\frac{1}{\sqrt{2}}C-D-F \\ D-E-F \end{pmatrix}, \tag{5.6}$$

relating the input modes to the output modes. Switching from the modes A', B', C', D', E' and F' in the Schrödinger picture to the corresponding creation/annihilation operators $\hat{A}'^{\dagger}$, $\hat{B}'^{\dagger}$, $\hat{C}'^{\dagger}$, $\hat{D}'^{\dagger}$, $\hat{E}'^{\dagger}$ and $\hat{F}'^{\dagger}$ in the Heisenberg picture we explicitly find

$$\hat{A}'^{\dagger} = \frac{1}{\sqrt{3}}(\hat{A}^{\dagger} + \hat{B}^{\dagger} + \hat{C}^{\dagger}), \tag{5.7}$$

$$\hat{B}'^{\dagger} = \frac{1}{\sqrt{3}}(\hat{A}^{\dagger} - \hat{C}^{\dagger} + \frac{1}{\sqrt{2}}\hat{D}^{\dagger} + \frac{1}{\sqrt{2}}\hat{E}^{\dagger}), \tag{5.8}$$

$$\hat{C}'^{\dagger} = \frac{1}{\sqrt{3}}(\hat{A}^{\dagger} - \hat{B}^{\dagger} - \frac{1}{\sqrt{2}}\hat{D}^{\dagger} - \frac{1}{\sqrt{2}}\hat{E}^{\dagger}), \tag{5.9}$$

$$\hat{D}'^{\dagger} = \frac{1}{\sqrt{3}}(\frac{1}{\sqrt{2}}\hat{B}^{\dagger} - \frac{1}{\sqrt{2}}\hat{C}^{\dagger} - \hat{E}^{\dagger} + \hat{F}^{\dagger}), \tag{5.10}$$

$$\hat{E}'^{\dagger} = \frac{1}{\sqrt{3}}(\frac{1}{\sqrt{2}}\hat{B}^{\dagger} - \frac{1}{\sqrt{2}}\hat{C}^{\dagger} - \hat{D}^{\dagger} - \hat{F}^{\dagger}), \tag{5.11}$$

$$\hat{F}'^{\dagger} = \frac{1}{\sqrt{3}}(\hat{D}^{\dagger} - \hat{E}^{\dagger} - \hat{F}^{\dagger}). \tag{5.12}$$

However, we want to determine the output with respect to the input. Therefore, we have

to invert (M3 · M2 · M1) to find the matrix $(\mathrm{M3} \cdot \mathrm{M2} \cdot \mathrm{M1})^{-1}$. This results in

$$\hat{A}^\dagger = \frac{1}{\sqrt{3}}(\hat{A}'^\dagger + \hat{B}'^\dagger + \hat{C}'^\dagger), \tag{5.13}$$

$$\hat{B}^\dagger = \frac{1}{\sqrt{3}}(\hat{A}'^\dagger - \hat{C}'^\dagger + \frac{1}{\sqrt{2}}\hat{D}'^\dagger + \frac{1}{\sqrt{2}}\hat{E}'^\dagger), \tag{5.14}$$

$$\hat{C}^\dagger = \frac{1}{\sqrt{3}}(\hat{A}'^\dagger - \hat{B}'^\dagger - \frac{1}{\sqrt{2}}\hat{D}'^\dagger - \frac{1}{\sqrt{2}}\hat{E}'^\dagger), \tag{5.15}$$

$$\hat{D}^\dagger = \frac{1}{\sqrt{3}}(\frac{1}{\sqrt{2}}\hat{B}'^\dagger - \frac{1}{\sqrt{2}}\hat{C}'^\dagger - \hat{E}'^\dagger + \hat{F}'^\dagger), \tag{5.16}$$

$$\hat{E}^\dagger = \frac{1}{\sqrt{3}}(\frac{1}{\sqrt{2}}\hat{B}'^\dagger - \frac{1}{\sqrt{2}}\hat{C}'^\dagger - \hat{D}'^\dagger - \hat{F}'^\dagger), \tag{5.17}$$

$$\hat{F}^\dagger = \frac{1}{\sqrt{3}}(\hat{D}'^\dagger - \hat{E}'^\dagger - \hat{F}'^\dagger). \tag{5.18}$$

To test this formalism, we take a simple measurement and compare it to the expectation. Sending photons into input D of the CNOT4 circuit[9], we expect an output state of the form

$$\hat{D}^\dagger|000000\rangle = \frac{1}{\sqrt{3}}(\frac{1}{\sqrt{2}}\hat{B}'^\dagger - \frac{1}{\sqrt{2}}\hat{C}'^\dagger - \hat{E}'^\dagger + \hat{F}'^\dagger)|000000\rangle = \tag{5.19}$$

$$= \frac{1}{\sqrt{6}}|010000\rangle - \frac{1}{\sqrt{6}}|001000\rangle - \frac{1}{\sqrt{3}}|000010\rangle + \frac{1}{\sqrt{3}}|000001\rangle. \tag{5.20}$$

To find the probability of detecting these single photons in output B', we need to determine the probability $\langle \hat{n}_{\mathrm{B}'} \rangle$

$$\langle \hat{n}_{\mathrm{B}'} \rangle = \langle \hat{B}'^\dagger \hat{B}' \rangle = \frac{1}{6}. \tag{5.21}$$

[9]We choose this input (and later input E) into the circuit as they send photons into the target interferometer where the non-classical two-photon-interference takes place. We want to see whether the circuit works as expected by comparing the output of the circuit when using one input or two inputs.

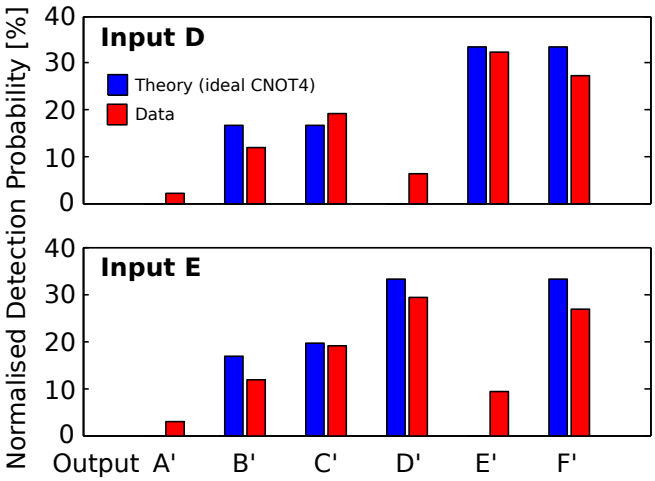

Figure 5.13: Experimental verification of theory model introduced according to Ralph [17]. We measure the output with respect to inputs D (upper) and E (lower) as we can at the same time determine whether our target interferometer works as soon as we obtain the data of the two-photon input. Please note that the theory data has been determined from the ideal beam splitter reflectivities, not the measured ones.

Accordingly, this means that we find the single photon with a probability of 1/6 in output C' and with probability of 1/3 in output E' or F'. If we want to verify this experimentally, we input a stream of single photons into input D, and observe all six outputs, we see after 500 times loading and launching the MOT that in the percentage of counts[10] in the respective output mode are the following

$$A' \rightarrow 2.61 \pm 0.07\% \text{ observed}, \qquad 0\% \text{ expected in ideal case}, \tag{5.22}$$

$$B' \rightarrow 11.90 \pm 0.14\% \text{ observed}, \qquad 16.67\% \text{ expected in ideal case}, \tag{5.23}$$

$$C' \rightarrow 19.15 \pm 0.18\% \text{ observed}, \qquad 16.67\% \text{ expected in ideal case}, \tag{5.24}$$

$$D' \rightarrow 6.27 \pm 0.1\% \text{ observed}, \qquad 0\% \text{ expected in ideal case}, \tag{5.25}$$

$$E' \rightarrow 32.28 \pm 0.23\% \text{ observed}, \qquad 33.33\% \text{ expected in ideal case}, \tag{5.26}$$

$$F' \rightarrow 27.26 \pm 0.22\% \text{ observed}, \qquad 33.33\% \text{ expected in ideal case}. \tag{5.27}$$

[10] Please note that there is no background subtracted but all counts which are counted outside the single photons' arrival time have been gated out in the analysis programme.

The difference of the measured to the ideal data derives from the fact that we assume perfect on-chip beam splitters as well as we do not subtract noise arising from detector dark counts to get a realistic picture of the system. An identical measurement can also be carried our for input E. Again, we load and launch the MOT 500 times and record the signal on our six output channels. This is what we find

$$A' \rightarrow 2.98 \pm 0.07\% \text{ observed}, \qquad 0\% \text{ expected in ideal case}, \tag{5.28}$$

$$B' \rightarrow 11.84 \pm 0.15\% \text{ observed}, \qquad 16.67\% \text{ expected in ideal case}, \tag{5.29}$$

$$C' \rightarrow 19.61 \pm 0.19\% \text{ observed}, \qquad 16.67\% \text{ expected in ideal case}, \tag{5.30}$$

$$D' \rightarrow 29.41 \pm 0.24\% \text{ observed}, \qquad 33.33\% \text{ expected in ideal case}, \tag{5.31}$$

$$E' \rightarrow 9.24 \pm 0.13\% \text{ observed}, \qquad 0\% \text{ expected in ideal case}, \tag{5.32}$$

$$F' \rightarrow 26.90 \pm 0.23\% \text{ observed}, \qquad 33.33\% \text{ expected in ideal case}. \tag{5.33}$$

A complete overview of measured and ideally expected data can be found in Fig. (5.13). These results show us that if we only input a stream of single photons into the CNOT4 chip's target input mode D and E respectively, they will leave the chip in the respective other output mode referred to as E' and D'. Subsequently, we need to show that single-photon interference on one of the beam splitters in the target interferometer really steers the output of the photonic circuit. This is done by applying the same formalism as introduced above.

The potential input mode combinations are (A, E), (A, D), (D, F) and (E, F), where A and F correspond to the control input modes and E and D to the target ones. Instead of just counting detector clicks, we now need to count correlations between detector clicks in the respective output modes (A', E'), (A', D'), (D', F') and (E', F'). By carrying out the

calculations and post-selecting in the coincidence basis we find

$$\begin{aligned}\hat{A}^\dagger\hat{E}^\dagger|000000\rangle &= \frac{1}{3}(\hat{A}'^\dagger+\hat{B}'^\dagger+\hat{C}'^\dagger)\Big(\frac{1}{\sqrt{2}}\hat{B}'-\frac{1}{\sqrt{2}}\hat{C}'^\dagger-\hat{D}'^\dagger-\hat{F}'^\dagger\Big)|000000\rangle = \\ &= \frac{1}{3}\Big(\frac{1}{\sqrt{2}}\hat{A}'^\dagger\hat{B}'^\dagger+(\hat{B}'^\dagger)^2-\frac{1}{\sqrt{2}}\hat{A}'^\dagger\hat{C}'^\dagger-\frac{1}{\sqrt{2}}(\hat{C}'^\dagger)^2\cdots \\ &\quad -\hat{A}'^\dagger\hat{D}'^\dagger-\hat{C}'^\dagger\hat{D}'^\dagger-\hat{A}'^\dagger\hat{F}'^\dagger-\hat{B}'^\dagger\hat{F}'^\dagger-\hat{C}'^\dagger\hat{F}'^\dagger\Big)|000000\rangle \\ &\overset{\text{post-selecting in coincidence basis}}{\equiv} -\frac{1}{3}\hat{A}'^\dagger\hat{D}'^\dagger|000000\rangle = -\frac{1}{3}|100100\rangle. \end{aligned} \tag{5.34}$$

As a value for the coincidence expectation in outputs A' and D' for an input in A and E we therefore find

$$\langle\hat{n}_{\mathrm{A}'}\hat{n}_{\mathrm{D}'}\rangle = \langle\hat{A}'^\dagger\hat{A}'\hat{D}'^\dagger\hat{D}'\rangle = \frac{1}{9}. \tag{5.35}$$

Therefore, the probability of detecting a correlation between A and D is 1/9. This result indicates that if we send one single photon into each input modes A and E, respectively, we will observe correlations between output modes A' and D' - this is exactly consistent with the case of only one single photon input as it can be seen in Eq. (5.31). This is the reason why we identify input mode A with C_0 in a standard CNOT.

If we apply this procedure now to all other output combinations in which we are look-

ing for correlations we find for single-photon input in modes A and D

$$\begin{aligned}\hat{A}^\dagger\hat{D}^\dagger|000000\rangle &= \frac{1}{3}(\hat{A}'^\dagger+\hat{B}'^\dagger+\hat{C}'^\dagger)(\frac{1}{\sqrt{2}}\hat{B}'^\dagger-\frac{1}{\sqrt{2}}\hat{C}'^\dagger-\hat{E}'^\dagger+\hat{F}'^\dagger)|000000\rangle = \\ &= \frac{1}{3}\Big(\frac{1}{\sqrt{2}}\hat{A}'^\dagger\hat{B}'^\dagger+\frac{1}{\sqrt{2}}(\hat{B}'^\dagger)^2-\frac{1}{\sqrt{2}}\hat{A}'^\dagger\hat{C}'^\dagger-\frac{1}{\sqrt{2}}(\hat{C}'^\dagger)^2\cdots \\ &\quad -\hat{A}'^\dagger\hat{E}'^\dagger-\hat{B}'^\dagger\hat{E}'^\dagger-\hat{C}'^\dagger\hat{E}'^\dagger+\hat{A}'^\dagger\hat{F}'^\dagger+\hat{B}'^\dagger\hat{F}'^\dagger+\hat{C}'^\dagger\hat{F}'^\dagger\Big)|000000\rangle \\ &\overset{\text{post-selecting in coincidence basis}}{\equiv} -\frac{1}{3}\hat{A}'^\dagger\hat{E}'^\dagger|000000\rangle = -\frac{1}{3}|100010\rangle. \end{aligned} \tag{5.36}$$

This case is consistent with the single-photon input solely into mode D, as it can be found in Eq. (5.26) and the fact that we have already identified that input mode A is equivalent to the C_0 mode in the standard CNOT gate. We continue with the more interesting cases (D, F) and (E, F). For (D, F) we find

$$\begin{aligned}\hat{D}^\dagger\hat{F}^\dagger|000000\rangle &= \frac{1}{3}(\frac{1}{\sqrt{2}}\hat{B}'^\dagger-\frac{1}{\sqrt{2}}\hat{C}'^\dagger-\hat{E}'^\dagger+\hat{F}'^\dagger)(\hat{D}'^\dagger-\hat{E}'^\dagger-\hat{F}'^\dagger)|000000\rangle = \\ &= \frac{1}{3}\Big(\frac{1}{\sqrt{2}}\hat{B}'^\dagger\hat{D}'^\dagger-\frac{1}{\sqrt{2}}\hat{C}'^\dagger\hat{D}'^\dagger-\frac{1}{\sqrt{2}}\hat{B}'^\dagger\hat{E}'^\dagger+\frac{1}{\sqrt{2}}\hat{C}'^\dagger\hat{E}'^\dagger\cdots \\ &\quad +(\hat{E}'^\dagger)^2-\frac{1}{\sqrt{2}}\hat{B}'^\dagger\hat{F}'^\dagger+\frac{1}{\sqrt{2}}\hat{C}'^\dagger\hat{F}'^\dagger+\hat{D}'^\dagger\hat{F}'^\dagger-(\hat{F}'^\dagger)^2\Big)|000000\rangle \\ &\overset{\text{post-selecting in coincidence basis}}{\equiv} \frac{1}{3}\hat{D}'^\dagger\hat{F}'^\dagger|000000\rangle = \frac{1}{3}|000101\rangle. \end{aligned} \tag{5.37}$$

This indicates that if we input two single photons in inputs modes D and F, we are going to detect correlations between outputs modes D' and F' with the probability of 1/9. This is the first case where we see that quantum interference actively steers the output of the photonic circuit. If we had only sent single photons into input mode D, we would expect zero counts in output D' as it can be seen in Eq. (5.25) – this two-photon-interference is

what makes this gate an operable standard CNOT gate. We therefore identify F as C_1 in the original CNOT gate.

As a final combination, we calculate the output for the (E, F) input case

$$\begin{aligned}\hat{E}^\dagger\hat{F}^\dagger|000000\rangle &= \frac{1}{3}(\frac{1}{\sqrt{2}}\hat{B}'^\dagger - \frac{1}{\sqrt{2}}\hat{C}'^\dagger - \hat{D}'^\dagger - \hat{F}'^\dagger)(\hat{D}'^\dagger - \hat{E}'^\dagger - \hat{F}'^\dagger)|000000\rangle = \\ &= \frac{1}{3}\Big(\frac{1}{\sqrt{2}}\hat{B}'^\dagger\hat{D}'^\dagger - \frac{1}{\sqrt{2}}\hat{C}'^\dagger\hat{D}'^\dagger - (\hat{D}'^\dagger)^2 - \frac{1}{\sqrt{2}}\hat{B}'^\dagger\hat{E}'^\dagger + \frac{1}{\sqrt{2}}\hat{C}'^\dagger\hat{E}'^\dagger \cdots \\ &\quad + \hat{D}'^\dagger\hat{E}'^\dagger - \frac{1}{\sqrt{2}}\hat{B}'^\dagger\hat{F}'^\dagger + \frac{1}{\sqrt{2}}\hat{C}'^\dagger\hat{F}'^\dagger + \hat{E}'^\dagger\hat{F}'^\dagger + (\hat{F}'^\dagger)^2\Big)|000000\rangle \\ &\overset{\text{post-selecting in coincidence basis}}{\equiv} \frac{1}{3}\hat{E}'^\dagger\hat{F}'^\dagger|000000\rangle = \frac{1}{3}|000011\rangle. \end{aligned} \tag{5.38}$$

In this particular input mode combination, we see that the target output is steered from output mode D' as it can be seen in Eq. (5.31) in the one-input case to output mode E' in the two-input case. Having carried out this calculation, it is easy to see that also this probability to detect the respective correlations in output modes E' and F' is 1/9 in the *ideal case*.

For the sake of clarity, we summarise the results of this Section. If we send a pair of single photons into (A, E), we observe photons in output modes (A', D'). Analogously, if we input a photon pair into input modes (A, D), we observe a correlation between output modes (A', E'). In both of these cases, no non-classical interference has happened upfront although the output *seems* flipped. The result is the same as if we only had input single photons into modes E or D, respectively and a non-interfering, e.g. perpendicularly polarised photon into mode A. If we choose to send a single photon pair into (E, F), we observe a correlation between (E', F'). Accordingly, if we send a pair into (D, F),

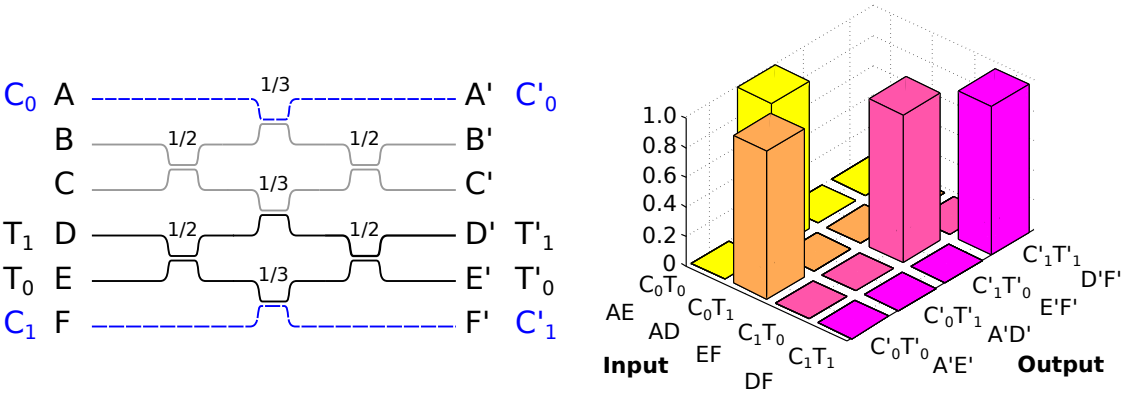

Figure 5.14: Ideal truth table (right) for the operation of the CNOT4 gate (left) normalised to 1. Please note that the output modes are not relabelled in this case. In the following, the output modes are relabelled as it is the fundamental principle of the CNOT gate to flip state of the target qubit if the control qubit is in state $|1_C\rangle$. Relabelling is standardly carried out in the community as it can for instance be seen in [80].

we observe a correlation between (D', F'). In these two cases, quantum interference has steered the process such that we observe an output not in the classically expected target mode but in the respective other one. All correlation events occur with a probability of 1/9, just as in the ideal CNOT circuit case. These results are displayed in form of a truth table in Fig. (5.14).

Please note that if we have two-photon interference for the (D, F) and (E, F) cases, the output does not *appear* to be flipped at a first glance. This is what motivates a relabelling process in the target modes as displayed for instance in Fig. (5.15). This is standard procedure in the community [80] and is implicitly carried out in the following.

Measuring the output of a CNOT4 gate

In order to test the operation of our CNOT4 gate as a CNOT, we relabel the modes of our chip as per Fig. (5.11) which allows us to reproduce the CNOT functionality. The only difference between our CNOT4 circuit and the more traditional CNOT circuit is that in our

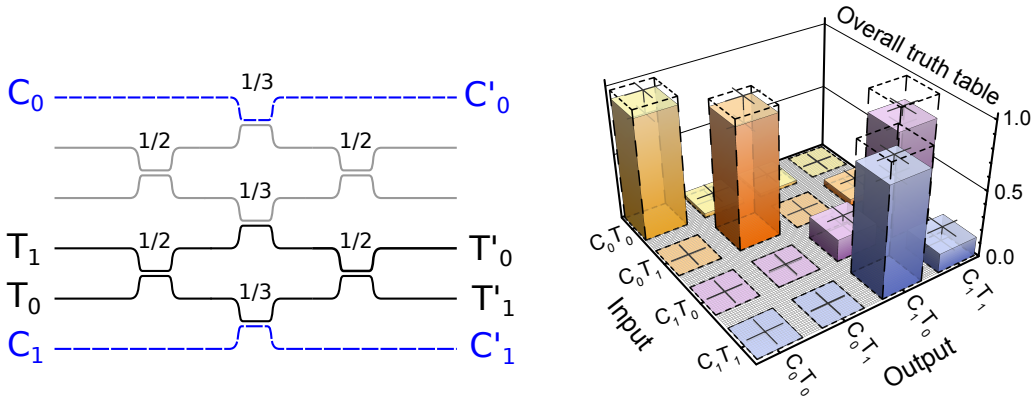

Figure 5.15: Observed truth table published in [84]: (Left) Relabelled circuit diagram. (Right) The ideal CNOT operation is presented by dotted bars and the measured data by coloured bars. This plot is derived from 1110 pairs of control-target correlations detected up to ± 200 ns apart and measured within 20 hours.

circuit, the two vacuum modes are mixed twice before leaving the chip. As a result, they are not independent from each other. However, since the gate is post-selected conditionally upon the detection of one photon in one of the control modes and one photon in one of the target modes, this does not affect the overall operation of the circuit as a CNOT gate. We operate the circuit by injecting pairs of photons from the atomic source into the chip. We test the operation of the circuit with input states corresponding to all four possible combinations of control and target input states in the computational basis, $|0_C 0_T\rangle$, $|0_C 1_T\rangle$, $|1_C 0_T\rangle$ and $|1_C 1_T\rangle$. After performing measurements on the states on the output of the chip, also in the computational basis, the resulting correlations can then be compared to the correlations expected from an ideal CNOT gate. The input/output correlation matrix for an ideal CNOT gate is shown in Fig. (5.15, right, dotted bars). After normalising our data and correcting for detector dark counts, we obtain the correlation matrix shown in Fig. (5.15, right, coloured bars).

To determine the quality of the data, we treat the background[11]-corrected data as a probability distribution. In this way, we can calculate the similarity S with the probability distribution expected from an ideal CNOT operation. The similarity is defined as

$$S = \frac{\sum \sqrt{p_i q_i}}{\sqrt{\sum p_i \sum q_i}}, \tag{5.39}$$

where p_i and q_i are elements of the measured and expected truth tables. The similarity S is a measure of the classical overlap between two probability distributions. Our results show a statistical similarity of S = 94$\pm$1% with the ideal CNOT truth table [84]. As displayed in Fig. (5.12), our linear optical circuit is not representative of an ideal CNOT gate due to the fact that the directional couplers deviate slightly from the ideal values and the interferometer on the target modes has a non-zero phase. Full characterisation of our circuit[12] reveals directional coupler reflectivities of η_{21} = 0.4967, η_{22} = 0.5336, η_{41} = 0.5098, η_{42} = 0.5239 and the phase ϕ inside of the interferometer was found to be $\phi = 0.1\pi$ as shown in Fig. (5.12). Taking into account these imperfections of the device we find that the similarity increases to S = 97$\pm$1% if we account for these non-ideal directional-coupler reflectivities and the phase shift in the interferometer [84].

Due to the long coherence time of the photons, we are able of observing related detection events that are notably separated in time. From these, we determine the similarity with the expected truth table as a function of the detection-time difference. The result can be found in Fig. (5.16). With the coherence length of the photons being three orders of magnitude longer than the equivalent physical length of the chip (10 mm, or 33 ps), the

[11] Please see my colleague Oliver Barter's thesis for a more detailed explanation.
[12] Private communication with Costas Poulios from the Bristol research group.

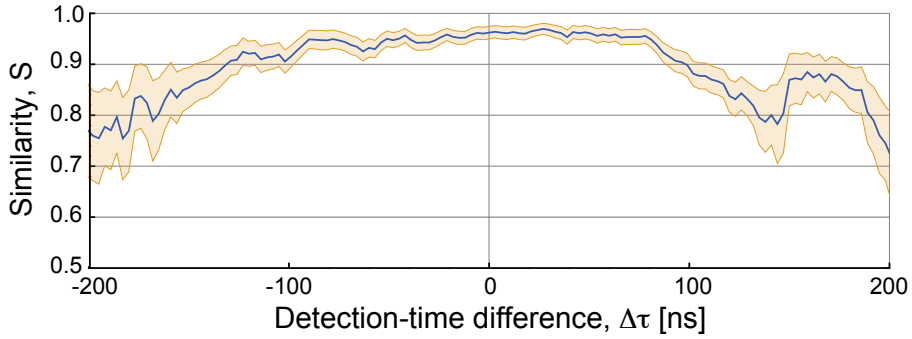

Figure 5.16: Similarity of the truth table [84] with the ideal CNOT as a function of the separation between detections, $\Delta\tau$. Events are considered within $\Delta\tau \pm 30$ ns. The shaded area corresponds to the respective error of Similarity S associated with the respective detection time difference of correlation events. For detections up to 100 ns apart, the similarity exceeds 90%. Beyond that, it drops due to noise dominating the signal. This is evident by correlations arising for which there is no path routing the input photons to those output channels.

gate operates as expected for detections up to 100 ns apart. Beyond that, the event rate is too small compared to noise which then dominates the truth table [84].

Having completed the discussion of how to implement a CNOT functionality on a CNOT4 LOQC circuit, we discuss how to use the circuit in a way it has originally be intended to be used. We generate and verify on-chip entanglement with the help of Sagnac-type interferometers. This is explained in the following.

5.3 On-chip entanglement generation and verification or ‘Sagnac-loops in action’

A defining feature of two-qubit logic is its ability to generate entanglement. Up to this point, we have used our LOQC chip not in a way it was designed to be used but just as a simple CNOT gate. In the following experiment – the on-chip entanglement generation and verification – it is used in a way it was originally designed for, the descriptive nomenclature can be found in Fig. (5.17). Depending on the input states into the CNOT4 circuit,

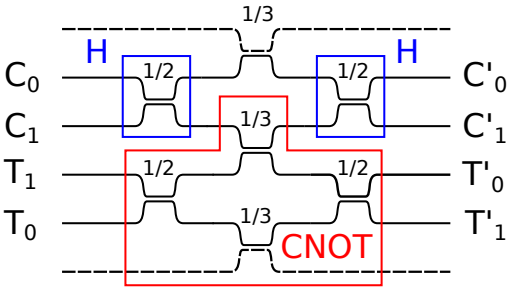

Figure 5.17: For the entanglement generation and verification experiment we use the CNOT4 in a way it was initially designed for. We input a pair of single photons – one photon in the control and one in the target modes – and count correlations in a not straightforward way.

we are able of generating a maximally entangled Bell state. To verify that we produce the Bell state with the help of the circuit, we have to measure in two different sets of bases, namely the $\{|0\rangle, |1\rangle\}$ 'computational basis' [3, 87] and $\{|+\rangle, |-\rangle\}$ 'plus-minus basis', to discriminate all four possible states.

5.3.1 Generating the Bell states – theoretically

We start with different inputs into the CNOT4 chip, these can be $|0_C 0_T\rangle$, $|0_C 1_T\rangle$, $|1_C 0_T\rangle$, or $|1_C 1_T\rangle$. The subscripts $_C$ and $_T$ stand for the state of the control and the target, respectively. To thoroughly discuss the theory, we identify

$$|0\rangle = \begin{pmatrix} 1 \\ 0 \end{pmatrix}, \text{and } |1\rangle = \begin{pmatrix} 0 \\ 1 \end{pmatrix}, \tag{5.40}$$

which are the two basis states of the computational basis in two dimensions [3, 87]. For the input state $|0_C 0_T\rangle$ into the CNOT4 circuit, we find

$$|00\rangle = |0_C 0_T\rangle = \begin{pmatrix} 1 \\ 0 \end{pmatrix} \otimes \begin{pmatrix} 1 \\ 0 \end{pmatrix} = \begin{pmatrix} 1 \\ 0 \\ 0 \\ 0 \end{pmatrix}. \tag{5.41}$$

The first operation that is carried out on chip is the Hadamard operation $\hat{H}_C$ on the

control input for instance marked in blue in Fig. (5.17). The Hadamard operation in general is a one-qubit rotation, mapping the qubit basis states $\{|0\rangle, |1\rangle\}$ onto superposition states with equal amplitudes. The transformed basis states of the computational basis then read

$$\hat{H}|0\rangle = \frac{1}{\sqrt{2}}\Big(|0\rangle + |1\rangle\Big), \text{ and } \hat{H}|1\rangle = \frac{1}{\sqrt{2}}\Big(|0\rangle - |1\rangle\Big), \tag{5.42}$$

hence the matrix of the operation is

$$\hat{H} = \frac{1}{\sqrt{2}}\begin{pmatrix} 1 & 1 \\ 1 & -1 \end{pmatrix}. \tag{5.43}$$

We carry out this Hadamard operation on the control mode of our input state $|0_C 0_T\rangle$ and find

$$\begin{aligned} |0_C 0_T\rangle \xrightarrow{\hat{H}_C} \quad & \frac{1}{\sqrt{2}}\Big(|0_C\rangle + |1_C\rangle\Big) \otimes |0_T\rangle = \\ & = \frac{1}{\sqrt{2}}\Big(|0_C\rangle \otimes |0_T\rangle + |1_C\rangle \otimes |0_T\rangle\Big). \end{aligned} \tag{5.44}$$

The other three potential input states $|1_C 1_T\rangle$, $|1_C 0_T\rangle$ and $|0_C 1_T\rangle$ are transformed by this operation into

$$|1_C 1_T\rangle \xrightarrow{\hat{H}_C} \frac{1}{\sqrt{2}}\Big(|0_C\rangle \otimes |1_T\rangle - |1_C\rangle \otimes |1_T\rangle\Big), \tag{5.45}$$

$$|1_C 0_T\rangle \xrightarrow{\hat{H}_C} \frac{1}{\sqrt{2}}\Big(|0_C\rangle \otimes |0_T\rangle - |1_C\rangle \otimes |0_T\rangle\Big), \tag{5.46}$$

$$|0_C 1_T\rangle \xrightarrow{\hat{H}_C} \frac{1}{\sqrt{2}}\Big(|0_C\rangle \otimes |1_T\rangle + |1_C\rangle \otimes |1_T\rangle\Big). \tag{5.47}$$

At this point, we know we generated superposition states and subsequently apply the CNOT operation between control and target modes. Again, we explicitly carry our the calculation for the $|0_C 0_T\rangle$ input state, and give the result accordingly for the other possible input states. It is well-known that the CNOT operation swaps the target output only if the control input is in state $|1_C\rangle$, leaving the control state unchanged. Therefore, the matrix for this operation reads

$$\hat{CNOT} = \begin{pmatrix} 1 & 0 & 0 & 0 \\ 0 & 1 & 0 & 0 \\ 0 & 0 & 0 & 1 \\ 0 & 0 & 1 & 0 \end{pmatrix}. \tag{5.48}$$

Acting with the CNOT operator on the superposition state of Eq. (5.44), we obtain

$$|0_C 0_T\rangle \xrightarrow{\hat{H}_C} \frac{1}{\sqrt{2}} \begin{pmatrix} 1 \\ 0 \\ 1 \\ 0 \end{pmatrix} \xrightarrow{\hat{CNOT}} \frac{1}{\sqrt{2}} \begin{pmatrix} 1 & 0 & 0 & 0 \\ 0 & 1 & 0 & 0 \\ 0 & 0 & 0 & 1 \\ 0 & 0 & 1 & 0 \end{pmatrix} \begin{pmatrix} 1 \\ 0 \\ 1 \\ 0 \end{pmatrix} = \tag{5.49}$$

$$= \frac{1}{\sqrt{2}} \begin{pmatrix} 1 \\ 0 \\ 0 \\ 1 \end{pmatrix} = \frac{1}{\sqrt{2}} \Big(\begin{pmatrix} 1 \\ 0 \end{pmatrix} \otimes \begin{pmatrix} 1 \\ 0 \end{pmatrix} + \begin{pmatrix} 0 \\ 1 \end{pmatrix} \otimes \begin{pmatrix} 0 \\ 1 \end{pmatrix} \Big) = \tag{5.50}$$

$$= \frac{1}{\sqrt{2}} \Big(|0_C 0_T\rangle + |1_C 1_T\rangle \Big). \tag{5.51}$$

After the action of the Hadamard operation on the control modes and the CNOT operation between control and target modes, the other potential input states $|1_C 1_T\rangle$, $|1_C 0_T\rangle$ and $|0_C 1_T\rangle$ read

$$|1_C 1_T\rangle \xrightarrow{\hat{H}_C,\, C\hat{N}OT} \frac{1}{\sqrt{2}}\Big(|0_C 1_T\rangle - |1_C 0_T\rangle\Big), \tag{5.52}$$

$$|1_C 0_T\rangle \xrightarrow{\hat{H}_C,\, C\hat{N}OT} \frac{1}{\sqrt{2}}\Big(|0_C 0_T\rangle - |1_C 1_T\rangle\Big), \tag{5.53}$$

$$|0_C 1_T\rangle \xrightarrow{\hat{H}_C,\, C\hat{N}OT} \frac{1}{\sqrt{2}}\Big(|0_C 1_T\rangle + |1_C 0_T\rangle\Big). \tag{5.54}$$

From these equations, it is easy to see that the states resulting from the input states are the maximally entangled Bell states [3]

$$|0_C 0_T\rangle \xrightarrow{\hat{H}_C,\, C\hat{N}OT} |\phi^+\rangle = \frac{1}{\sqrt{2}}(|0\rangle \otimes |0\rangle + |1\rangle \otimes |1\rangle), \tag{5.55}$$

$$|1_C 0_T\rangle \xrightarrow{\hat{H}_C,\, C\hat{N}OT} |\phi^-\rangle = \frac{1}{\sqrt{2}}(|0\rangle \otimes |0\rangle - |1\rangle \otimes |1\rangle) \tag{5.56}$$

$$|0_C 1_T\rangle \xrightarrow{\hat{H}_C,\, C\hat{N}OT} |\Psi^+\rangle = \frac{1}{\sqrt{2}}(|0\rangle \otimes |1\rangle + |1\rangle \otimes |0\rangle) \tag{5.57}$$

$$|1_C 1_T\rangle \xrightarrow{\hat{H}_C,\, C\hat{N}OT} |\Psi^-\rangle = \frac{1}{\sqrt{2}}(|0\rangle \otimes |1\rangle - |1\rangle \otimes |0\rangle). \tag{5.58}$$

Please note that up to this point we have solely passed the first Hadamard operation on the control and the CNOT operation between target and control inputs. There is another Hadamard operation between the control modes imprinted in the circuit. This is of great help when we verify the Bell states on chip as we learn in Sec. 5.3.2.

5.3.2 Measuring the Bell states – conceptually

Up to now, we have seen how to generate the maximally entangled Bell states on chip theoretically. However, we also need to experimentally verify their existence. As mentioned above, the states need to be measured in two different bases, the $\{|0\rangle, |1\rangle\}$ and $\{|+\rangle, |-\rangle\}$ basis to discriminate all four possible states. An illustration of the principle can be found

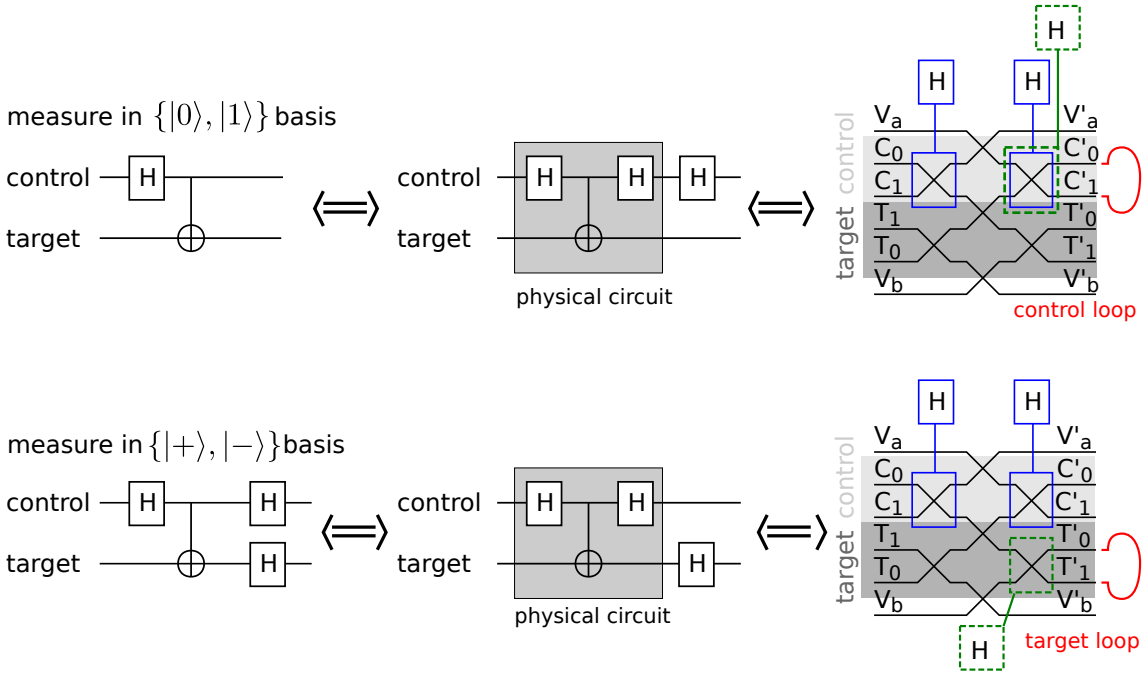

Figure 5.18: Conceptually measuring the Bell states in both the computational basis $\{|0\rangle, |1\rangle\}$ as well as the plus-minus basis $\{|+\rangle, |-\rangle\}$ basis (left). In the $\{|0\rangle, |1\rangle\}$ basis case, we need to externally add a Hadamard gate on the control mode to 'switch off' the Hadamard gate imprinted on the actual circuit. This is possible as two subsequent Hadamard operations restore the initial state (middle). If we want to measure in the $\{|+\rangle, |-\rangle\}$ basis, we need to add a Hadamard operation on the target mode outside the actual circuit. (Right) Actual experimental circuits to both 'switch off' and 'add' a Hadamard on the control and target mode, respectively. We 'loop' the respective control and target outputs to obtain a Sagnac-type interferometer. This is done by joining the end of the fibres together with the help of a simple fibre optics connector. In both cases, the last Hadamard or the last beam splitter in the target interferometer of the CNOT is passed through twice. The respective virtual circuits can be found in Fig. (5.19)

in Fig. (5.18) as well as of the respective virtual circuit in Fig. (5.19).

Conceptually, what we want to measure is the output of the chip in both control and target modes in the $\{|0\rangle, |1\rangle\}$ and $\{|+\rangle, |-\rangle\}$ basis. In the $\{|0\rangle, |1\rangle\}$ basis case, we want the photons to pass through the Hadamard in the control – which creates a superposition state – and then go through the entangling process with the help of the CNOT gate between control and target mode. After that, we want the state to remain unaltered. As there is another Hadamard imprinted in the architecture of the chip, we need to add another Hadamard gate on the control output which 'switches off' the on-chip Hadamard. If we

pass through two Hadamards in a row, the initial state is restored which can be easily seen as the Hadamard transformation is unitary. In the case of the $\{|+\rangle, |-\rangle\}$ basis, we need to add another Hadamard operation on the target mode externally.

Measuring in the $\{|0\rangle, |1\rangle\}$ basis, it is easy to see that if we send the state $|0_\mathrm{C}1_\mathrm{T}\rangle$ into the circuit, after passing through the Hadamard gate on the control modes as well as the CNOT gate between control and target modes, we obtain the maximally entangled Bell state $|\Psi^+\rangle = 1/\sqrt{2}(|0\rangle \otimes |1\rangle + |1\rangle \otimes |0\rangle)$ as deduced in Eq. (5.57). If we now add two Hadamard operations on the control mode, we find

$$\begin{aligned}
\xrightarrow{\hat{H}_\mathrm{C}} \quad & \frac{1}{2}\Big((|0_\mathrm{C}\rangle + |1_\mathrm{C}\rangle) \otimes |1_\mathrm{T}\rangle + (|0_\mathrm{C}\rangle - |1_\mathrm{C}\rangle) \otimes |0_\mathrm{T}\rangle\Big) = \\
& = \frac{1}{2}\Big(|0_\mathrm{C}1_\mathrm{T}\rangle + |1_\mathrm{C}1_\mathrm{T}\rangle + |0_\mathrm{C}0_\mathrm{T}\rangle - |1_\mathrm{C}0_\mathrm{T}\rangle\Big), && (5.59) \\
\xrightarrow{\hat{H}_\mathrm{C}} \quad & \frac{1}{2}\Big((|0_\mathrm{C}\rangle + |1_\mathrm{C}\rangle) \otimes |1_\mathrm{T}\rangle + (|0_\mathrm{C}\rangle - |1_\mathrm{C}\rangle) \otimes |1_\mathrm{T}\rangle + \\
& + (|0_\mathrm{C}\rangle + |1_\mathrm{C}\rangle) \otimes |0_\mathrm{T}\rangle - (|0_\mathrm{C}\rangle - |1_\mathrm{C}\rangle) \otimes |1_\mathrm{T}\rangle\Big) = \cdots && (5.60) \\
& = \frac{1}{\sqrt{2}}\Big(|0_\mathrm{C}1_\mathrm{T}\rangle + |1_\mathrm{C}0_\mathrm{T}\rangle\Big) = |\Psi^+\rangle. && (5.61)
\end{aligned}$$

This indicates that the Bell state is restored and the second Hadamard on the control mode is 'switched off'. Measuring in the $\{|+\rangle, |-\rangle\}$ basis, we start again with the Bell state $|\Psi^+\rangle$ and add a Hadamard operation on the control and the target modes

$$\begin{aligned}
\xrightarrow{\hat{H}_\mathrm{C}\hat{H}_\mathrm{T}} \quad & \frac{1}{2}\Big(\frac{1}{\sqrt{2}}(|0_\mathrm{C}\rangle + |1_\mathrm{C}\rangle) \otimes \frac{1}{\sqrt{2}}(|0_\mathrm{T}\rangle - |1_\mathrm{T}\rangle) + \\
& + \frac{1}{\sqrt{2}}(|0_\mathrm{C}\rangle - |1_\mathrm{C}\rangle \otimes \frac{1}{\sqrt{2}}(|0_\mathrm{T}\rangle + |1_\mathrm{T}\rangle)\Big). && (5.62)
\end{aligned}$$

If we identify the $\{|+\rangle, |-\rangle\}$ basis states with $|+\rangle = 1/\sqrt{2}(|0\rangle + |1\rangle)$ and $|-\rangle = 1/\sqrt{2}(|0\rangle -$

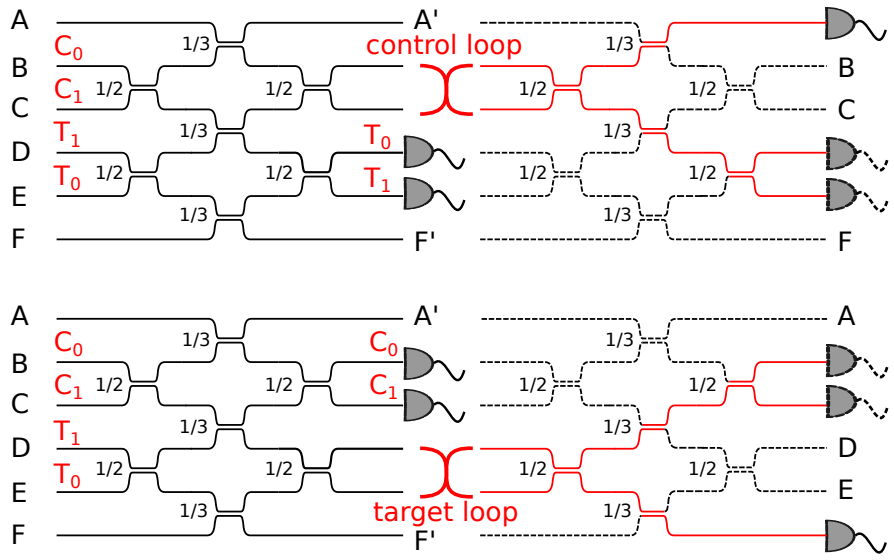

Figure 5.19: 'Virtual' representation of both target-and control-looped CNOT4 circuit: Constructing a Sagnac-type interferometer by coupling the control and target outputs, respectively, we re-use parts of the chip in the backward direction. By observing a combination of in- and outputs of the chip, we can reconstruct the measured state.

$|1\rangle$) and find generated Bell state in this particular basis

$$|\Psi^+\rangle = \frac{1}{\sqrt{2}}(|+_C -_T\rangle + |-_C +_T\rangle). \tag{5.63}$$

Experimentally, the addition and subtraction of Hadamard operations is achieved with a trick: The respective target and control output modes are *looped* by joining the fibre ends with a fibre connector. The only potential problem in this measurement is that there might be too much loss introduced by various couplings into, out of and back into the circuit. Also, the photons can take various paths inside the circuit and we are not able of monitoring all potential output modes which also leads to a dropping correlation count rate. However, these concerns are unfounded experimentally in Sec. 5.3.5.

5.3.3 Control loop - theoretical discussion

Before we take the measurements with either control or target outputs of the CNOT4 circuit joined in a Sagnac loop, we want to learn what result we expect in this experiment. For the sake of clarity, we draw a 'virtual' circuit of the CNOT4 gate whose control outputs are looped. This virtual circuit can be found in Fig. (5.20). To determine the output of the control-looped CNOT4 gate, a representation comprising ten input modes from Q_C to Z_C is chosen. Similarly this is done for the target loop which can be found in Sec. 5.3.4. To not confuse the target- and control-looped cases, we use the subscripts $_C$ and $_T$, respectively. Input modes R_C to W_C are consistent with previously defined input modes A_{in} to F_{in}[13]. Input mode S_C is also consistent with C_0, T_C with C_1, U_C with T_1, and V_C with T_0. We monitor six output or input modes with single-photon counters[14] of which two are vacuum modes. Four of the observed modes which are connected to detectors D1 to D4 are the 'interesting' ones. Detector D1 monitors $A_{in} \equiv Q'_C$, D2 monitors – depending of the input state – $D_{in} \equiv X'_C$ or $E_{in} \equiv Y'_C$, D3 monitors $D_{out} \equiv U'_C$, and D4 $E_{out} \equiv V'_C$. Please note that the control input modes are B_{in} and C_{in} whereas the target modes are D_{in} and E_{in}. The vacuum input modes are A_{in} and F_{in}. This is different from the CNOT operation where A and F are used as the control modes and D and E as the target input modes.

To find the output mode of the CNOT4 circuit, we need to establish a 10 x 10 matrix representation similar to the one introduced for the CNOT operation in Sec. 5.2.3. This output mode leaving the CNOT4 gate is in its most general representation reading

[13] We choose to keep the subscript $_{in}$ for the sake of clarity as in this Section we also need to monitor the *input* modes of the circuit and not just the output modes.

[14] This experiment was carried out before the NQIT grant – four of the six detectors had to be borrowed from Bristol.

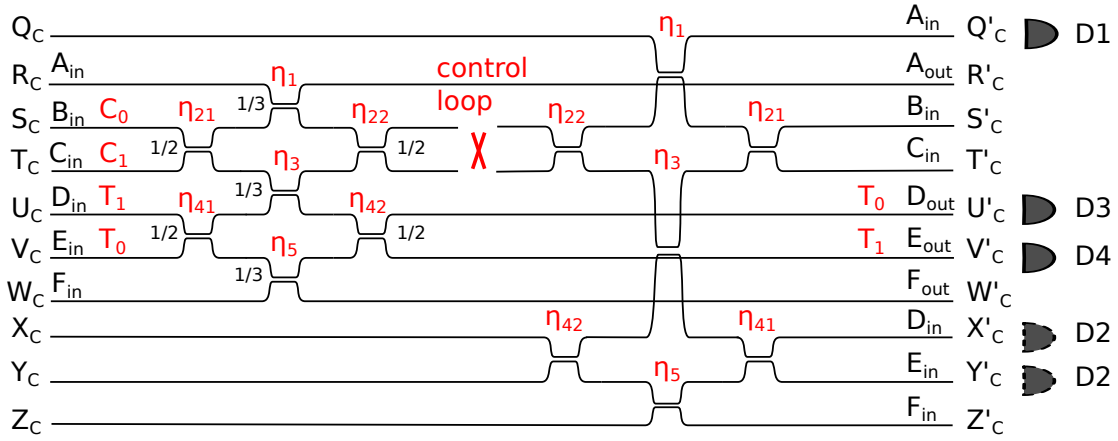

Figure 5.20: As we want to obtain the complete truth table for the control-looped CNOT4 gate, a novel formulation has been chosen comprising 10 input modes Q_C, R_C, S_C, T_C, U_C, V_C, W_C, X_C, Y_C, Z_C not be confused with the A to F inputs for the simple CNOT gate on a CNOT4 circuit. Therefore, we can identify the input of a pair of single photons in each of the following input modes (B_{in}, D_{in}) as (S_C, U_C), (B_{in}, E_{in}) as (S_C, V_C), (C_{in}, D_{in}) as (T_C, U_C) and (C_{in}, E_{in}) as (T_C, V_C). We use the subscript $_C$ to highlight the fact that we are working with the control loop. Similarly, if we use the target loop, all modes have a subscript $_T$.

$$\begin{pmatrix} Q'_C \\ R'_C \\ S'_C \\ T'_C \\ U'_C \\ V'_C \\ W'_C \\ X'_C \\ Y'_C \\ Z'_C \end{pmatrix} = M7_C \cdot M6_C \cdot M5_C \cdot M4_C \cdot M3_C \cdot M2_C \cdot M1_C \cdot \begin{pmatrix} Q_C \\ R_C \\ S_C \\ T_C \\ U_C \\ V_C \\ W_C \\ X_C \\ Y_C \\ Z_C \end{pmatrix}. \tag{5.64}$$

The transformation matrices $M1_C$, $M2_C$, $M3_C$, $M4_C$, $M5_C$, $M6_C$ and $M7_C$ explicitly read

$$M1_{\mathrm{C}} = \begin{pmatrix} \mathbb{1}_2 & 0 & 0 & 0 & 0 & 0 \\ 0 & \sqrt{\eta_{21}} & \sqrt{1-\eta_{21}} & 0 & 0 & 0 \\ 0 & \sqrt{1-\eta_{21}} & -\sqrt{\eta_{21}} & 0 & 0 & 0 \\ 0 & 0 & 0 & \sqrt{\eta_{41}} & \sqrt{1-\eta_{41}} & 0 \\ 0 & 0 & 0 & \sqrt{1-\eta_{41}} & -\sqrt{\eta_{41}} & 0 \\ 0 & 0 & 0 & 0 & 0 & \mathbb{1}_4 \end{pmatrix}, \tag{5.65}$$

$$M2_{\mathrm{C}} = \begin{pmatrix} 1 & 0 & 0 & 0 & 0 & 0 & 0 & 0 \\ 0 & \sqrt{\eta_1} & \sqrt{1-\eta_1} & 0 & 0 & 0 & 0 & 0 \\ 0 & \sqrt{1-\eta_1} & -\sqrt{\eta_1} & 0 & 0 & 0 & 0 & 0 \\ 0 & 0 & 0 & \sqrt{\eta_3} & \sqrt{1-\eta_3} & 0 & 0 & 0 \\ 0 & 0 & 0 & \sqrt{1-\eta_3} & -\sqrt{\eta_3} & 0 & 0 & 0 \\ 0 & 0 & 0 & 0 & 0 & \sqrt{\eta_5} & \sqrt{1-\eta_5} & 0 \\ 0 & 0 & 0 & 0 & 0 & \sqrt{1-\eta_5} & -\sqrt{\eta_5} & 0 \\ 0 & 0 & 0 & 0 & 0 & 0 & 0 & \mathbb{1}_3 \end{pmatrix}, \tag{5.66}$$

$$M3_{\mathrm{C}} = \begin{pmatrix} \mathbb{1}_2 & 0 & 0 & 0 & 0 & 0 \\ 0 & \sqrt{\eta_{22}} & \sqrt{1-\eta_{22}} & 0 & 0 & 0 \\ 0 & \sqrt{1-\eta_{22}} & -\sqrt{\eta_{22}} & 0 & 0 & 0 \\ 0 & 0 & 0 & \sqrt{\eta_{42}} & \sqrt{1-\eta_{42}} & 0 \\ 0 & 0 & 0 & \sqrt{1-\eta_{42}} & -\sqrt{\eta_{42}} & 0 \\ 0 & 0 & 0 & 0 & 0 & \mathbb{1}_4 \end{pmatrix}, \tag{5.67}$$

$$M4_{\mathrm{C}} = \begin{pmatrix} \mathbb{1}_2 & 0 & 0 & 0 \\ 0 & 0 & 1 & 0 \\ 0 & 1 & 0 & 0 \\ 0 & 0 & 0 & \mathbb{1}_6 \end{pmatrix}, \tag{5.68}$$

$$M5_{\mathrm{C}} = \begin{pmatrix} \mathbb{1}_2 & 0 & 0 & 0 & 0 & 0 & 0 \\ 0 & \sqrt{\eta_{22}} & \sqrt{1-\eta_{22}} & 0 & 0 & 0 & 0 \\ 0 & \sqrt{1-\eta_{22}} & -\sqrt{\eta_{22}} & 0 & 0 & 0 & 0 \\ 0 & 0 & 0 & \mathbb{1}_3 & 0 & 0 & 0 \\ 0 & 0 & 0 & 0 & \sqrt{\eta_{42}} & \sqrt{1-\eta_{42}} & 0 \\ 0 & 0 & 0 & 0 & \sqrt{1-\eta_{42}} & -\sqrt{\eta_{42}} & 0 \\ 0 & 0 & 0 & 0 & 0 & 0 & 1 \end{pmatrix}, \tag{5.69}$$

$$M6_{\mathrm{C}} = \begin{pmatrix} \sqrt{\eta_1} & 0 & \sqrt{1-\eta_1} & 0 & 0 & 0 & 0 \\ 0 & 1 & 0 & 0 & 0 & 0 & 0 \\ \sqrt{1-\eta_1} & 0 & -\sqrt{\eta_1} & 0 & 0 & 0 & 0 \\ 0 & 0 & 0 & \sqrt{\eta_3} & 0 & \sqrt{1-\eta_3} & 0 \\ 0 & 0 & 0 & 0 & \mathbb{1}_3 & 0 & 0 \\ 0 & 0 & 0 & \sqrt{1-\eta_3} & 0 & -\sqrt{\eta_3} & 0 \\ 0 & 0 & 0 & 0 & 0 & 0 & \mathbb{1}_2 \end{pmatrix}, \tag{5.70}$$

$$M7_{\mathrm{C}} = \begin{pmatrix} \mathbb{1}_2 & 0 & 0 & 0 & 0 & 0 & 0 \\ 0 & \sqrt{\eta_{21}} & \sqrt{1-\eta_{21}} & 0 & 0 & 0 & 0 \\ 0 & \sqrt{1-\eta_{21}} & -\sqrt{\eta_{21}} & 0 & 0 & 0 & 0 \\ 0 & 0 & 0 & \mathbb{1}_3 & 0 & 0 & 0 \\ 0 & 0 & 0 & 0 & \sqrt{\eta_{41}} & \sqrt{1-\eta_{41}} & 0 \\ 0 & 0 & 0 & 0 & \sqrt{1-\eta_{41}} & -\sqrt{\eta_{41}} & 0 \\ 0 & 0 & 0 & 0 & 0 & 0 & 1 \end{pmatrix}, \tag{5.71}$$

where η_{xy} refers to the respective beam splitter's reflectivity. Accordingly, 1-η_{xy} refers to the respective transmitivity. As it can be seen, these matrices M1$_{\mathrm{C}}$ to M7$_{\mathrm{C}}$ are constructed in a similar way as the non-looped CNOT4 circuit demonstrated in Sec. 5.2.3. To calculate an output state of a general form, we invert the matrices and obtain

$$\begin{pmatrix} Q_{\mathrm{C}} \\ R_{\mathrm{C}} \\ S_{\mathrm{C}} \\ T_{\mathrm{C}} \\ U_{\mathrm{C}} \\ V_{\mathrm{C}} \\ W_{\mathrm{C}} \\ X_{\mathrm{C}} \\ Y_{\mathrm{C}} \\ Z_{\mathrm{C}} \end{pmatrix} = (M7_{\mathrm{C}} \cdot M6_{\mathrm{C}} \cdot M5_{\mathrm{C}} \cdot M4_{\mathrm{C}} \cdot M3_{\mathrm{C}} \cdot M2_{\mathrm{C}} \cdot M1_{\mathrm{C}})^{-1} \cdot \begin{pmatrix} Q'_{\mathrm{C}} \\ R'_{\mathrm{C}} \\ S'_{\mathrm{C}} \\ T'_{\mathrm{C}} \\ U'_{\mathrm{C}} \\ V'_{\mathrm{C}} \\ W'_{\mathrm{C}} \\ X'_{\mathrm{C}} \\ Y'_{\mathrm{C}} \\ Z'_{\mathrm{C}} \end{pmatrix}. \tag{5.72}$$

From this, we can determine the output modes for all four input mode combinations. By switching from the Schrödinger to the Heisenberg picture, we find the creation/annihi-

lation operators for single photons introduced into the respective mode

$$\hat{B}^\dagger \hat{D}^\dagger \equiv \hat{S}_\mathrm{C}^\dagger \hat{U}_\mathrm{C}^\dagger \propto \frac{1}{3\sqrt{3}} \hat{Q}_\mathrm{C}'^\dagger \hat{V}_\mathrm{C}'^\dagger - \frac{1}{3\sqrt{6}} \hat{U}_\mathrm{C}'^\dagger \hat{Y}_\mathrm{C}'^\dagger, \tag{5.73}$$

$$\hat{B}^\dagger \hat{E}^\dagger \equiv \hat{S}_\mathrm{C}^\dagger \hat{V}_\mathrm{C}^\dagger \propto \frac{1}{3\sqrt{3}} \hat{Q}_\mathrm{C}'^\dagger \hat{U}_\mathrm{C}'^\dagger - \frac{1}{3\sqrt{6}} \hat{V}_\mathrm{C}'^\dagger \hat{Y}_\mathrm{C}'^\dagger, \tag{5.74}$$

$$\hat{C}^\dagger \hat{D}^\dagger \equiv \hat{T}_\mathrm{C}^\dagger \hat{U}_\mathrm{C}^\dagger \propto \frac{1}{3\sqrt{3}} \hat{Q}_\mathrm{C}'^\dagger \hat{V}_\mathrm{C}'^\dagger + \frac{1}{3\sqrt{6}} \hat{U}_\mathrm{C}^\dagger \hat{Y}_\mathrm{C}'^\dagger, \tag{5.75}$$

$$\hat{C}^\dagger \hat{E}^\dagger \equiv \hat{T}_\mathrm{C}^\dagger \hat{V}_\mathrm{C}^\dagger \propto \frac{1}{3\sqrt{3}} \hat{Q}_\mathrm{C}'^\dagger \hat{U}_\mathrm{C}'^\dagger + \frac{1}{3\sqrt{6}} \hat{V}_\mathrm{C}'^\dagger \hat{Y}_\mathrm{C}'^\dagger, \tag{5.76}$$

assuming ideal beam splitter reflectivities and post-selecting in the coincidence basis. This 10 x 10 matrix formalism gives us a tool to determine the complete theoretical truth table for the Bell states measurements on a CNOT4 circuit. As we define the transformation matrices $\mathrm{M1_C}$ to $\mathrm{M7_C}$ with arbitrary beam splitter ratios and only switch to ideal beam splitter ratios in the final step, it is easy to also calculate the truth table for the measured reflectivities on the chip. However, for the sake of simplicity, we will only discuss the case of an ideal CNOT4 circuit. As we observe six in- and outputs of the chip we can solely monitor certain detector combinations experimentally. In the control-loop case for the input of a single photon pair $\hat{B}^\dagger \hat{D}^\dagger$, we observe the outputs $\mathrm{A_{out}}$, $\mathrm{D_{out}}$, $\mathrm{E_{out}}$, $\mathrm{F_{out}}$, $\mathrm{A_{in}}$ as well as $\mathrm{E_{in}}$ which corresponds to output modes $\mathrm{R'_C}$, $\mathrm{U'_C}$, $\mathrm{V'_C}$, $\mathrm{W'_C}$, $\mathrm{Q'_C}$, and $\mathrm{Y'_C}$, respectively. The truth table for the ideal CNOT4 and all four different inputs read:

$\hat{B}^\dagger\hat{D}^\dagger$ Input Control Loop	A_{out} $\equiv R'_C$	D_{out} $\equiv U'_C$	E_{out} $\equiv V'_C$	F_{out} $\equiv W'_C$	A_{in} $\equiv Q'_C$	E_{in} $\equiv Y'_C$
$A_{out} \equiv R'_C$	x	0	1/9	1/9	0	1/27
$D_{out} \equiv U'_C$	0	x	1/27	1/18	0	1/54
$E_{out} \equiv V'_C$	1/9	1/27	x	1/18	1/27	0
$F_{out} \equiv W'_C$	1/9	1/18	1/18	x	1/27	1/54
$A_{in} \equiv Q'_C$	0	0	1/27	1/27	x	1/81
$E_{in} \equiv Y'_C$	1/27	1/54	0	1/54	1/81	x

Table 5.1: Expected coincidence probabilities for input $\hat{B}^\dagger\hat{D}^\dagger$ or state $|0_C 1_T\rangle$.

Equivalently, one can determine the ideal truth table for the single photon input pair $\hat{B}^\dagger\hat{E}^\dagger$, $\hat{C}^\dagger\hat{D}^\dagger$ and $\hat{C}^\dagger\hat{E}^\dagger$ inputs.

$\hat{B}^\dagger\hat{E}^\dagger$ Input Control Loop	A_{out} $\equiv R'_C$	D_{out} $\equiv U'_C$	E_{out} $\equiv V'_C$	F_{out} $\equiv W'_C$	A_{in} $\equiv Q'_C$	E_{in} $\equiv Y'_C$
$A_{out} \equiv R'_C$	x	1/9	0	1/9	0	1/27
$D_{out} \equiv U'_C$	1/9	x	1/18	1/18	1/27	0
$E_{out} \equiv V'_C$	0	1/18	x	1/18	0	1/54
$F_{out} \equiv W'_C$	1/9	1/18	1/18	x	1/27	1/54
$A_{in} \equiv Q'_C$	0	1/27	0	1/27	x	1/81
$E_{in} \equiv Y'_C$	1/27	0	1/54	1/54	1/81	x

Table 5.2: Expected coincidence probabilities for input $\hat{B}^\dagger\hat{E}^\dagger$ or state $|0_C 0_T\rangle$.

$\hat{C}^\dagger\hat{D}^\dagger$ Input Control Loop	A_{out} $\equiv R'_C$	D_{out} $\equiv U'_C$	E_{out} $\equiv V'_C$	F_{out} $\equiv W'_C$	A_{in} $\equiv Q'_C$	E_{in} $\equiv Y'_C$
$A_{out} \equiv R'_C$	x	0	1/9	1/9	0	1/27
$D_{out} \equiv U'_C$	0	x	1/18	1/18	0	1/54
$E_{out} \equiv V'_C$	1/9	1/18	x	1/18	1/27	0
$F_{out} \equiv W'_C$	1/9	1/18	1/18	x	1/27	1/54
$A_{in} \equiv Q'_C$	0	0	1/27	1/27	x	1/81
$E_{in} \equiv Y'_C$	1/27	1/54	0	1/54	1/81	x

Table 5.3: Expected coincidence probabilities for input $\hat{C}^\dagger\hat{D}^\dagger$ or state $|1_C1_T\rangle$.

$\hat{C}^\dagger\hat{E}^\dagger$Input Control Loop	A_{out} $\equiv R'_C$	D_{out} $\equiv U'_C$	E_{out} $\equiv V'_C$	F_{out} $\equiv W'_C$	A_{in} $\equiv Q'_C$	E_{in} $\equiv Y'_C$
$A_{out} \equiv R'_C$	x	1/9	0	1/9	0	1/27
$D_{out} \equiv U'_C$	1/9	x	1/18	1/18	1/27	0
$E_{out} \equiv V'_C$	0	1/18	x	1/18	0	1/54
$F_{out} \equiv W'_C$	1/9	1/18	1/18	x	1/27	1/54
$A_{in} \equiv Q'_C$	0	1/27	0	1/27	x	1/81
$E_{in} \equiv Y'_C$	1/27	0	1/54	1/54	1/81	x

Table 5.4: Expected coincidence probabilities for input $\hat{C}^\dagger\hat{E}^\dagger$ or state $|1_C0_T\rangle$.

As mentioned above, we are only interested in the outputs connected to the four detectors D1, D2, D3, and D4. The mapping of detectors to output modes can be found in Fig. (5.20). The following table comprises the expected coincidence probabilities between output modes depending on the respective input. As it can be seen, the probabilities to detect

a correlation in the output are very low already even for an ideal operation of the CNOT4 circuit. An illustration of the ideal truth table can be found in Fig. (5.22, right).

Control Loop Measured in Input	D3, D1	D3, D2	D4, D1	D4, D2
$\hat{B}^\dagger\hat{D}^\dagger \equiv \hat{S}_C^\dagger\hat{U}_C^\dagger$	0	$\left(-\frac{1}{3\sqrt{6}}\right)^2 = \frac{1}{54}$	$\left(\frac{1}{3\sqrt{3}}\right)^2 = \frac{1}{27}$	0
$\hat{B}^\dagger\hat{E}^\dagger \equiv \hat{S}_C^\dagger\hat{V}_C^\dagger$	$\left(\frac{1}{3\sqrt{3}}\right)^2 = \frac{1}{27}$	0	0	$\left(-\frac{1}{3\sqrt{6}}\right)^2 = \frac{1}{54}$
$\hat{C}^\dagger\hat{D}^\dagger \equiv \hat{T}_C^\dagger\hat{U}_C^\dagger$	0	$\left(\frac{1}{3\sqrt{6}}\right)^2 = \frac{1}{54}$	$\left(\frac{1}{3\sqrt{3}}\right)^2 = \frac{1}{27}$	0
$\hat{C}^\dagger\hat{E}^\dagger \equiv \hat{T}_C^\dagger\hat{V}_C^\dagger$	$\left(\frac{1}{3\sqrt{3}}\right)^2 = \frac{1}{27}$	0	0	$\left(\frac{1}{3\sqrt{6}}\right)^2 = \frac{1}{54}$

Table 5.5: Expected coincidence probabilities for measured output combination comprising D1 (A_{in}), D2 (E_{in} or D_{in}), D3 (D_{out}), and D4 (E_{out}). A pictorial representation can be found in Fig. (5.20).

5.3.4 Target loop - theoretical discussion

The target loop is the equivalent to the control loop with the difference that not the control outputs are joined but the target outputs. A schematic drawing can be found in Fig. (5.21). The formalism to calculate the output is similar to the one introduced in Sec. 5.3.3 for the control loop.

To determine the output of the target-looped CNOT4 gate a virtual circuit comprising ten input modes Q_T to Z_T has been chosen similarly to the control loop. For the sake of clarity, all different notations, e. g. from the paper [84] or working nomenclature are

described in the following. Input modes T_T to X_T of the looped-circuit description are consistent with A_{in} to F_{in}. In particular, input mode U_T is also consistent with C_0, V_T with C_1, W_T with T_1, and X_T with T_0. We monitor six output modes with single-photon counters of which two are vacuum modes. Detectors D1 to D4 are the ‘interesting’ ones, as detector D1 monitors – depending of the input state – $B_{in} \equiv R'_T$ or $C_{in} \equiv S'_T$, D2 monitors $F_{in} \equiv Z'_T$, D3 monitors $B_{out} \equiv U'_T$, and D4 monitors $E_{out} \equiv V'_T$.

Carrying out the equivalent calculations as in the control-loop case, we find the creation operators for single photons introduced into the respective mode

$$\hat{B}^\dagger \hat{D}^\dagger \equiv \hat{U}_T^\dagger \hat{W}_T^\dagger \propto \frac{1}{3\sqrt{3}} \hat{V}_T'^\dagger \hat{Z}_T'^\dagger - \frac{1}{3\sqrt{6}} \hat{S}_T'^\dagger \hat{U}_T'^\dagger, \tag{5.77}$$

$$\hat{B}^\dagger \hat{E}^\dagger \equiv \hat{U}_T^\dagger \hat{X}_T^\dagger \propto -\frac{1}{3\sqrt{3}} \hat{V}_T'^\dagger \hat{Z}_T'^\dagger - \frac{1}{3\sqrt{6}} \hat{S}_T'^\dagger \hat{U}_T'^\dagger, \tag{5.78}$$

$$\hat{C}^\dagger \hat{D}^\dagger \equiv \hat{V}_T^\dagger \hat{W}_T^\dagger \propto \frac{1}{3\sqrt{3}} \hat{U}_T'^\dagger \hat{Z}_T'^\dagger + \frac{1}{3\sqrt{6}} \hat{V}_T^\dagger \hat{R}_T'^\dagger, \tag{5.79}$$

$$\hat{C}^\dagger \hat{E}^\dagger \equiv \hat{V}_T^\dagger \hat{X}_T^\dagger \propto -\frac{1}{3\sqrt{3}} \hat{U}_T'^\dagger \hat{Z}_T'^\dagger + \frac{1}{3\sqrt{6}} \hat{V}_T'^\dagger \hat{R}_T'^\dagger. \tag{5.80}$$

An illustration of the ideal truth table can be found in Fig. (5.22, left).

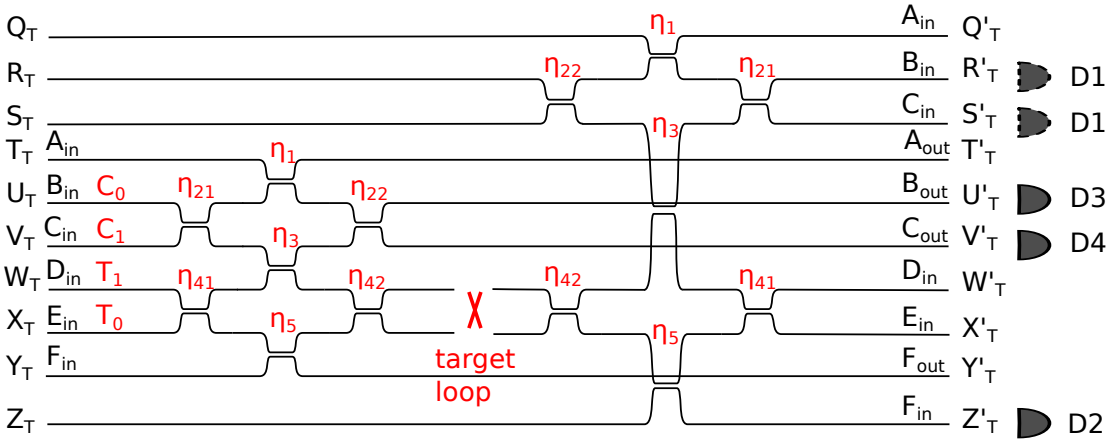

Figure 5.21: Virtual circuit for the target loop experiment: Our formalism comprises ten input modes Q_T, R_T, S_T, T_T, U_T, V_T, W_T, X_T, Y_T, and Z_T as well as ten output modes Q'_T, R'_T, S'_T, T'_T, U'_T, V'_T, W'_T, X'_T, Y'_T, and Z'_T. We can identify the inputs modes (B_{in}, D_{in}) as (U_T, W_T), (B_{in}, E_{in}) as (U_T, X_T), (C_{in}, D_{in}) as (V_T, W_T) and (C_{in}, E_{in}) as (V_T, X_T). We use the subscript $_T$ for all operators and input to avoid confusion with the control loop experiment.

Target Loop Measured in	D2, D3	D1, D3	D2, D4	D1, D4
Input				
$\hat{B}^\dagger\hat{D}^\dagger \equiv \hat{U}_T^\dagger\hat{W}_T^\dagger$	0	$\left(-\frac{1}{3\sqrt{6}}\right)^2 = \frac{1}{54}$	$\left(\frac{1}{3\sqrt{3}}\right)^2 = \frac{1}{27}$	0
$\hat{B}^\dagger\hat{E}^\dagger \equiv \hat{U}_T^\dagger\hat{X}_T^\dagger$	0	$\left(-\frac{1}{3\sqrt{6}}\right)^2 = \frac{1}{54}$	$\left(-\frac{1}{3\sqrt{3}}\right)^2 = \frac{1}{27}$	0
$\hat{C}^\dagger\hat{D}^\dagger \equiv \hat{V}_T^\dagger\hat{W}_T^\dagger$	$\left(\frac{1}{3\sqrt{3}}\right)^2 = \frac{1}{27}$	0	0	$\left(\frac{1}{3\sqrt{6}}\right)^2 = \frac{1}{54}$
$\hat{C}^\dagger\hat{E}^\dagger \equiv \hat{V}_T^\dagger\hat{X}_T^\dagger$	$\left(-\frac{1}{3\sqrt{3}}\right)^2 = \frac{1}{27}$	0	0	$\left(\frac{1}{3\sqrt{6}}\right)^2 = \frac{1}{54}$

Table 5.6: Expected probabilities for measured outputs D1 (B_{in} or C_{in}), D2 (F_{out}), D3 (B_{out}), and D4 (C_{out}). A pictorial representation can be found in Fig. (5.21).

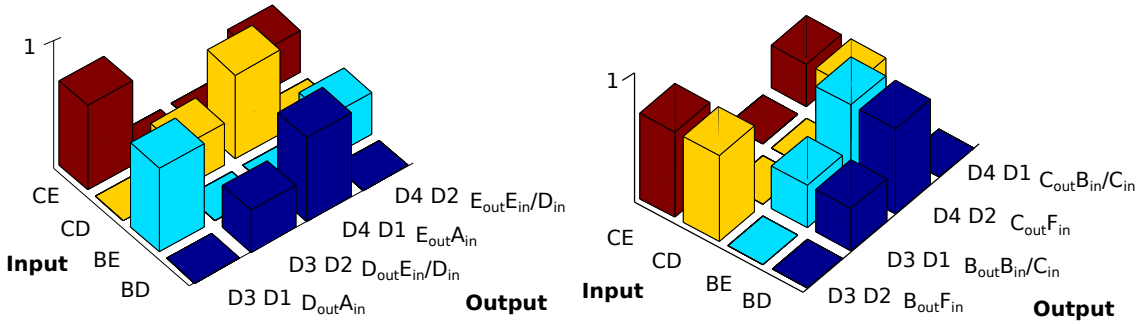

Figure 5.22: Normalised truth table for both Sagnac-looped control (left) and target (right) modes experiments. The respective calculations can be found in Sec. 5.3.3 and 5.3.4. Please note that due to the intrinsic architecture of the chip the bars in the plot are not of the same height even theoretically. Where the factor of $1/\sqrt{2}$ – or 1/2 in the probability – between the bar heights comes from is pictographically explained in Fig. (5.23). As this is only due to the chip's architecture and has nothing to do with the intrinsic physics of the system, this intrinsic imbalance is accounted for in published data [84].

5.3.5 Experimental results and fidelity of a quantum state

Having discussed what we expect to measure for Sagnac-looped target and control modes theoretically starting from simple matrix calculations, we want to interpret the measured data in terms of quantum information processing.

A defining feature of two-qubit logic is the ability to generate entanglement from separable input states. However, as it can be learned from [88, 89], if a composite system is subjected to local measurements, the measurement data will exhibit correlations, whether these systems are classical or quantum. So, in the following, we have to verify that the correlations that we observe are indeed *quantum*.

If we want to measure the system, we need an observable. An observable is described by a Hermitian operator. A suitable choice for an observable are the Pauli-operators. Therefore, a measurement along the z-axis corresponds to the Pauli-z-matrix σ_z which reads

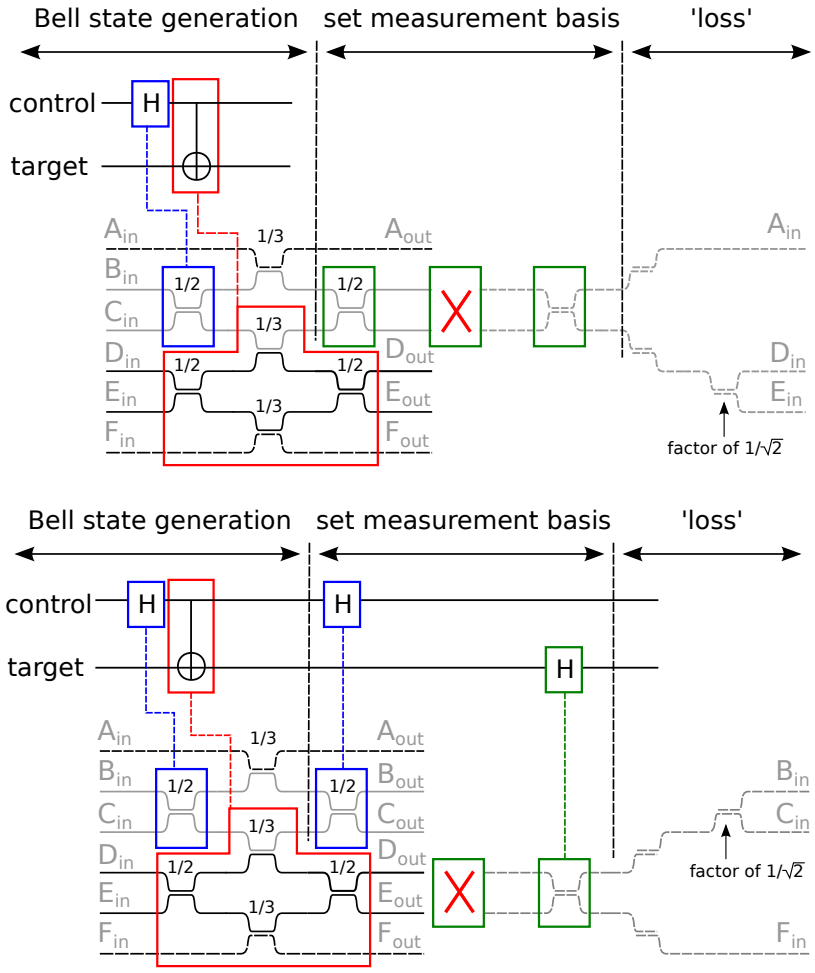

Figure 5.23: Experimental implementation of measuring along the z-axis (upper) and x-axis (lower): The first Hadamard operation (blue) rotates the control qubit from the Z- in the X-basis, after this, control and target qubits are entangled via a CNOT operation and form a maximally entangled Bell state. This is the case for both control and target loop. (Upper) Passing through a Hadamard gate in the control twice with the help of a Sagnac-type interferometer ('loop'), the final measurement basis is set to the computational basis. (Lower) Passing through a Hadamard gate in both the target and control modes separately, the final measurement basis is set to the plus-minus-basis. In both upper and lower illustrations the externally added Hadamard gates are shown in green, the Sagnac loop as a red cross. Passing through the rest of the circuit, the potential paths the photons could take which do no lead towards detectors are considered 'loss'.

$$\sigma_z = \begin{pmatrix} 1 & 0 \\ 0 & -1 \end{pmatrix}, \tag{5.81}$$

which corresponds to a measurement of the observable 'Pauli-z' or 'Z' [84]. $|0\rangle$ and $|1\rangle$ are the eigenvectors of this operator. We already encountered these vectors as the basis states of the computational basis in Sec. 5.3.2. The measurement along the x-axis is different to the one along the z-axis. The eigenvectors of the Pauli-x-matrix σ_x which reads

$$\sigma_x = \begin{pmatrix} 0 & 1 \\ 1 & 0 \end{pmatrix}, \tag{5.82}$$

are $|+\rangle$ and $|-\rangle$, the plus-minus basis states. A measurement along the x-axis corresponds to the measurement of the observable 'Pauli-x' or 'X' [84]. After the measurement, the system is in an eigenvector of the respective observable, the outcome of the measurement being the eigenvalue of the eigenvector. The next step is that we have to identify how we can measure both observables, Z and X in our exact setup. Both in the control-loop case and in the target-loop case we measure in the z-axis and x-axis of control and target modes as it can be seen in Fig. (5.23), respectively.

Therefore, what we measure is $\langle Z_\mathrm{C} \otimes Z_\mathrm{T}\rangle$ and $\langle X_\mathrm{C} \otimes X_\mathrm{T}\rangle$. For an arbitrary two-bit state ρ this indicates in the $\langle Z_\mathrm{C} \otimes Z_\mathrm{T}\rangle$ case

$$\begin{aligned}\langle Z_\mathrm{C} \otimes Z_\mathrm{T}\rangle = \langle 0_\mathrm{C}0_\mathrm{T}|\rho|0_\mathrm{C}0_\mathrm{T}\rangle + \langle 1_\mathrm{C}1_\mathrm{T}|\rho|1_\mathrm{C}1_\mathrm{T}\rangle - \langle 1_\mathrm{C}0_\mathrm{T}|\rho|1_\mathrm{C}0_\mathrm{T}\rangle \\ - \langle 0_\mathrm{C}1_\mathrm{T}|\rho|0_\mathrm{C}1_\mathrm{T}\rangle,\end{aligned} \tag{5.83}$$

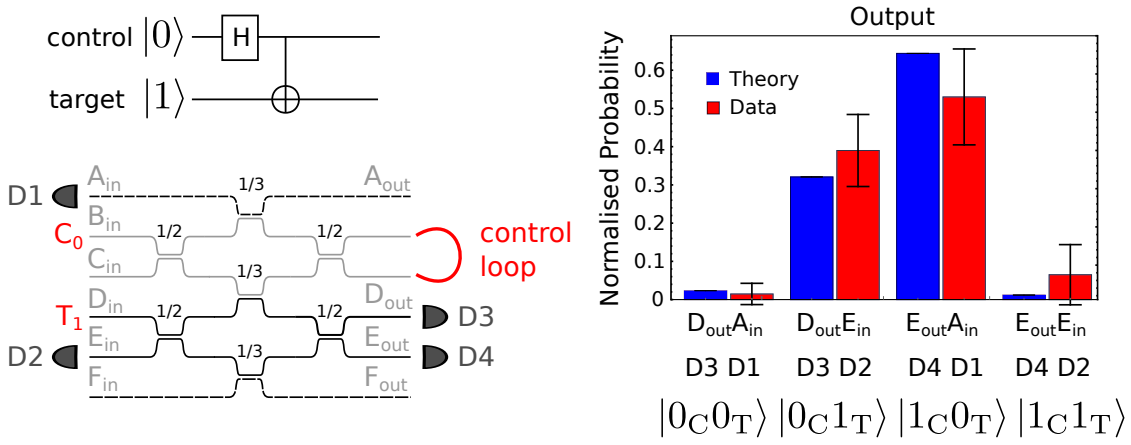

Figure 5.24: Measuring a Bell state in the $\{|0\rangle, |1\rangle\}$ basis with the help of a control-looped CNOT4 circuit: (Upper left) Circuit diagram of what we aim to measure as introduced in Sec. 5.3.2. (Lower left) To determine whether we can observe entanglement we fibre-couple the control output modes C'$_0$ and C'$_1$, which form a Sagnac loop. (Right) Ideal (blue) and measured (red) data for the $|0_C1_T\rangle$ input state, corresponding to the creation operators $\hat{B}^\dagger\hat{D}^\dagger$: We count correlations between $D_{out}A_{in}$, $D_{out}E_{in}$, $E_{out}A_{in}$, $E_{out}E_{in}$ corresponding to coincidence measurements between detectors D3 and D1, D3 and D2, D4 and D1 as well as D4 and D2. For the theory values we assume non-ideal beam splitters that we note for instance in Fig. (5.12).

and for $\langle X_C \otimes X_T\rangle$ case it reads

$$\begin{aligned}\langle X_C \otimes X_T\rangle &= \langle +_C +_T |\rho| +_C +_T\rangle + \langle -_C -_T |\rho| -_C -_T\rangle \\ &+ \langle -_C +_T |\rho| -_C +_T\rangle + \langle +_C -_T |\rho| +_C -_T\rangle = \\ &= \langle 1_C1_T|\rho|0_C0_T\rangle + \langle 0_C0_T|\rho|1_C1_T\rangle + \langle 0_C1_T|\rho|1_C0_T\rangle \\ &+ \langle 1_C0_T|\rho|0_C1_T\rangle. \end{aligned} \tag{5.84}$$

For the $\hat{B}^\dagger\hat{D}^\dagger$ input in the control-loop case, we count correlations between detectors D3 and D1 which correspond to $\langle 0_C0_T|\rho|0_C0_T\rangle$, between D3 and D2 corresponding to $\langle 1_C0_T\rho|1_C0_T\rangle$, between D4 and D1 corresponding to $\langle 0_C1_T|\rho|0_C1_T\rangle$ as well as between D4 and D2 corresponding to $\langle 1_C1_T|\rho|1_C1_T\rangle$. The result as well as the ideal outcome are shown in Fig. (5.24). Please note that due to the circuit's intrinsic architecture, the amount

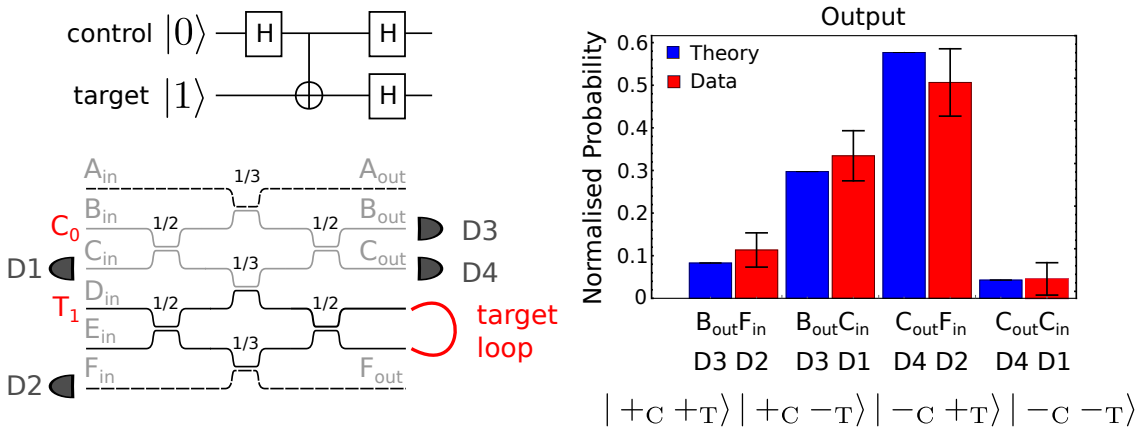

Figure 5.25: Target-looped CNOT4 circuit – measuring in the $\{|+\rangle, |-\rangle\}$ basis: (Upper left) Circuit diagram of what we aim to measure as introduced in Sec 5.3.2. (Lower left) To determine whether we can observe entanglement we fibre-couple the control output modes T'$_0$ and T'$_1$, which form a Sagnac loop. (Right) Ideal and measured data for the $|0_C 1_T\rangle$ input state, corresponding to the creation operators $\hat{B}^\dagger \hat{D}^\dagger$: We count correlations between $B_{out}F_{in}$, $B_{out}C_{in}$, $C_{out}F_{in}$, $C_{out}C_{in}$ which is equivalent to coincidence measurements between D3 and D2, D3 and D1, D4 and D2 as well as D4 and D1. (Right) Ideal (blue) and measured (red) data. For the theory values we assume non-ideal beam splitters that we note for instance in Fig. (5.12).

of correlations between D4 and D1 are twice as high as the amount of correlation between detectors D3 and D2.

For the same input but with Sagnac-looped target outputs, we measure correlations between detectors D3 and D2 corresponding to $\langle +_C +_T |\rho| +_C +_T\rangle$, between D3 and D1 corresponding to $\langle +_C -_T |\rho| +_C -_T\rangle$, between D4 and D2 corresponding $\langle -_C +_T |\rho| -_C +_T\rangle$ as well as between D4 and D1 corresponding to $\langle -_C -_T |\rho| -_C -_T\rangle$ and the result can be found in Fig. (5.25). Please note that due to the circuit's intrinsic architecture, the amount of correlations between D3 and D1 are half as high as the amount of correlation between detectors D4 and D2. As in the control-loop case this is due to the circuit's intrinsic architecture, already hinted at in Fig. (5.23).

The displayed theory data in both control- and target-loop cases has been obtained not from the model concerning a circuit with *ideal* beam splitters imprinted on it but with the

real beam splitter ratios determined in an auxiliary measurement with the same wavelength of laser light (780 nm) as we use in our measurements.

Coming back to the initial question whether we really observe quantum entanglement, we reconstruct the probability distributions for our measurements of $X_C \otimes X_T$ and $Z_C \otimes Z_T$ using maximum-likelyhood estimation (MLE)[15], with the data normalised to the logical two-bit basis. The correlations show similarities of $97\pm3\%$ and $94\pm2\%$ with the ideal distributions.

To determine the 'quantumness' of our measurements, we want to determine the fidelity between the ideal quantum Bell state and the data we measure. To do so, we choose the input into modes (B, D) corresponding to input state $|0_C 1_T\rangle$. From [90], we learn that if we obtain a fidelity $F_{|\Psi^-\rangle}$ of the measured state with the maximally entangled, ideal Bell state $|\Psi^-\rangle$ of $F_{|\Psi^-\rangle} \geq 1/2$, we have an entanglement witness. The fidelity $F_{|\Psi^-\rangle}$ to a given qubit state ρ reads

$$\begin{aligned} F_{|\Psi^-\rangle} &= \langle\Psi^-|\rho|\Psi^-\rangle = \\ &= \frac{1}{2}\Big(\langle 0_C 1_T|\rho|0_C 1_T\rangle + \langle 1_C 0_T|\rho|1_C 0_T\rangle - \langle 0_C 1_T|\rho|1_C 0_T\rangle - \langle 1_C 0_T|\rho|0_C 1_T\rangle\Big), \end{aligned} \tag{5.85}$$

as the Bell state is $|\Psi^-\rangle = 1/\sqrt{2}\Big(|0_C 1_T\rangle - |1_C 0_T\rangle\Big)$. The fidelity for a different Bell state, $|\phi^+\rangle = 1/\sqrt{2}\Big(|0_C 0_T\rangle + |1_C 1_T\rangle\Big)$ reads

$$\begin{aligned} F_{|\phi^+\rangle} &= \langle\phi^+|\rho|\phi^+\rangle = \\ &= \frac{1}{2}\Big(\langle 0_C 0_T|\rho|0_C 0_T\rangle + \langle 1_C 1_T|\rho|1_C 1_T\rangle + \langle 0_C 0_T|\rho|1_C 1_T\rangle + \langle 1_C 1_T|\rho|0_C 0_T\rangle\Big). \end{aligned} \tag{5.86}$$

[15] Please find more information on this topic my colleague Oliver Barter's thesis.

From the fidelity definition above, and the knowledge of what we can actually measure in the lab, it is clear that we cannot determine $F_{|\Psi^-\rangle}$ directly. However, what we can directly calculate from our measurement data is

$$F_{\text{min}} = -\frac{1}{2}\Big(\langle Z_{\text{C}} \otimes Z_{\text{T}}\rangle + \langle X_{\text{C}} \otimes X_{\text{T}}\rangle\Big), \tag{5.87}$$

a lower bound for our fidelity. By doing the maths, we find that F_{min} can be rewritten as

$$F_{\text{min}} = F_{|\Psi^-\rangle} - F_{|\phi^+\rangle} \quad \Rightarrow \quad F_{\text{min}} \leq F_{|\Psi^-\rangle}, \tag{5.88}$$

and so we measure a lower bound for $F_{|\Psi^-\rangle}$. If $F_{|\Psi^-\rangle} \geq 1/2$, we have an entangled state. Evaluating our measurement data yields $F_{|\Psi^-\rangle} \geq 0.82 \pm 0.1$. Similar to the evaluation in Fig. (5.16), we can determine the degree of entanglement in the process of time. As shown in Fig. (5.26) [84], the degree of entanglement is largely insensitive to the detection-time difference. We are able to observe non-classical correlations between pairs of photons that are projected onto states that could not have occupied the optical chip simultaneously. The 60 m (or 200 ns) coherence length of our photons exceeds the very short dimensions of the linear optical network by at least three to four orders of magnitude. This shows that quantum interference is unaffected by photon localisation in time or space that one could otherwise associate with the two separate photon detections.

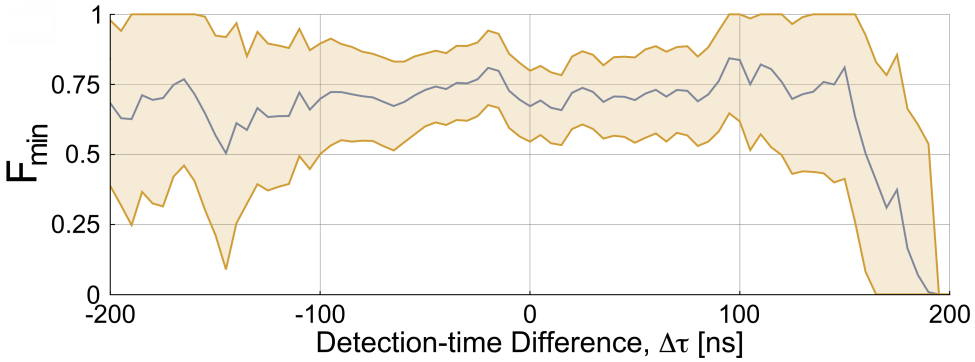

Figure 5.26: Graph similar to Fig. (5.16): Detection-time-dependent variation of fidelity bound $F_{\min}$ for Bell state $|\Psi^-\rangle$ when considering only a subset of the detections, separated by $\Delta\tau \pm 50$ ns. The shaded area corresponds to the error of $F_{\min}$ for the respective detection-time difference $\Delta\tau$.

5.4 CNOT operation with twin-peak photons

Having demonstrated the ability of encoding time-binned qubits, qutrits and ququads in single photons in Chapter 4 as well as the operation of a LOQC chip with long atom-cavity photons in Secs. 5.2.3 and 5.3, we combine these two separate experiments by sending temporally encoded qubits into the CNOT4 circuit. A related experiment has been carried out already as a preliminary measurement shown in Sec. 5.1.3, where we have used time-bin encoded qubits to operate a CNOT circuit. However, due to the lack of a proper normalisation in our first attempt, this data is recorded again. When doing so, an additional aim is to investigate the CNOT functionality depending on various imprinted phase shifts between the time bins as opposed to only one specific phase shift in the preliminary data. Here, we describe this novel two-qubits experiment in detail. In particular, we briefly characterise our twin-peak photons with the help of the hybrid source-chip system in Sec. 5.4.1, discuss two ways of imprinting a phase shift onto the spatio-temporal envelope of the photons in Sec. 5.4.2, show how the CNOT functionality depends on various different

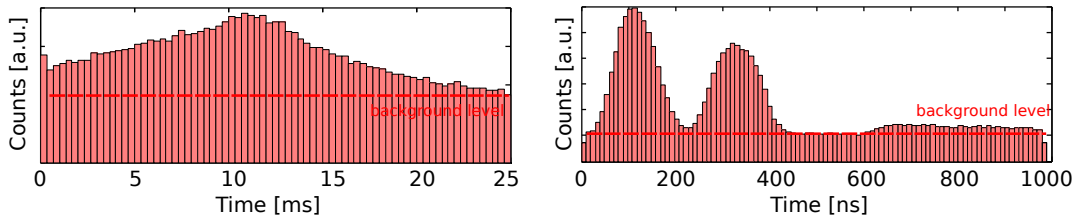

Figure 5.27: (Left) Characterising the experimental parameters such as speed of the cold atom cloud and (right) spatio-temporal envelope of the twin-peak photons: We see the envelope of the atom cloud passing through the cavity. The diagram shows all the counts registered by the SPCMs histogramed and summed up over all MOT throws. It takes the centre of the cloud of atoms 11 ms to reach the cavity as we see from the peak in the data. From these atoms, we produce time-binned qubit photons where each time bin has a temporal length of 230 ns. The plateau towards the end of the pulse originates from the repumping process of the atoms after every single photon emission.

phases imprinted between the time bins of the qubits in Sec. 5.4.3 and conclude in Sec. 5.4.4.

5.4.1 Quantum-homodyne measurements – on chip

Along the lines of Sec. 5.2.2 in which we characterise the hybrid source-chip system with the help of the system itself, we determine the properties of the twin-peak photons or temporally encoded qubits in the following. Inside our cavity, we shape each photon's spatio-temporal envelope into two peaks, which is shown in Fig. (5.27, right). By doing so, we put each photon in a coherent superposition of these two time bins of 230 ns length. Also, to probe the interaction time of the atom-cavity system, we show a histogram of all counts registered per MOT throw in Fig. (5.27, left). This histogram shows the MOT cloud travelling through the cavity and emitting photons. We find that the cloud is sufficiently slow as it takes the centre of the atomic cloud 11 ms to reach the cavity.

For further characterisation, we determine the indistinguishability of the photons on

chip by sending a pair of twin-peak photons into the circuit. This is similar to the measurement carried out with single-peaked photons in Sec. 5.2.2. This time, we regard one photon of the pair as a reference and the other one as a signal photon, where the reference photon does not exhibit a phase shift between its time bins and the signal photon does exhibit a phase shift of $\phi = \pi$. As introduced in Sec. 4.2, this measurement extends simple Hong-Ou-Mandel interference and is referred to as quantum homodyning [65]. We send the signal and reference photons into input modes A and D/E of the circuit and count correlations between output modes B' and C' as depicted in Fig. (5.28, left). The measured time-resolved on-chip quantum-homodyne data is displayed in Fig. (5.28, right). As a reference, we also send indistinguishable photons of perpendicular polarisation into the circuit. Because the signal of the temporally encoded qubits has a phase shift of π imprinted between its time bins, we observe that the number of cross-correlations detected between adjacent time bins increases in the same way as with a quantum-homodyne measurement using a fiber beam splitter in Fig. (4.10). The visibility V between signal and reference photons of perpendicular polarisation for detections in the same time bin yields $\approx 80\%$, with the visibility being defined as

$$V = 1 - \frac{\int_{\text{same TB}} \Phi_{\text{Signal}}(\Delta\tau)\, d\Delta\tau}{\int_{\text{same TB}} \Phi_{\text{Reference}}(\Delta\tau)\, d\Delta\tau}\,, \tag{5.89}$$

where $\Phi_{\text{Signal}}(\Delta\tau)$ and $\Phi_{\text{Reference}}(\Delta\tau)$ correspond to the fitted functions to the reference and signal measurement data, respectively. Please note that we integrate over the centre time bin only. The data is shown in Fig. (5.28, right). Having demonstrated the quantum-homodyne measurement on chip, we continue with the demonstration of a CNOT func-

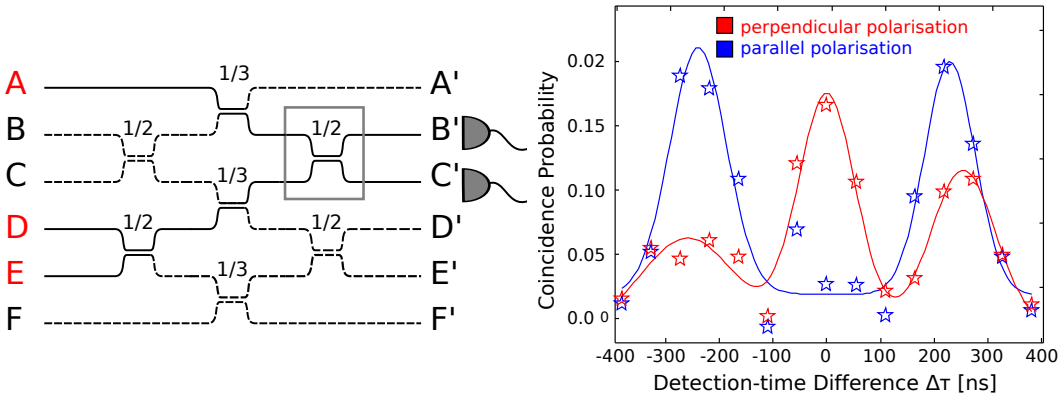

Figure 5.28: Time-resolved quantum homodyning *on chip* as a test of indistinguishability of the photons: We send a pair of single twin-peak photons into the circuit via input modes A and D/E and measure in the output modes B' and C' (left). As only a fraction of complete pairs of single photons reach the marked beam splitter, the measurement time on chip is increased by a large amount as opposed to the measurement on a fiber beam splitter. One photon of the pair of photons serves as a reference and one as a signal. The reference photon exhibits no phase shift between its time bins whereas the signal photon has a phase shift of $\phi = \pi$ imprinted between its time bins. Therefore, to determine the indistinguishability of the photons we can only measure the visibility in the centre time bin which yields $\approx 80\%$ (right). Nevertheless, it can be seen clearly that the amount of correlations measured in the ± 1 time bins increase by twice the amount detected in the reference measurement with perpendicular photons. The data displayed in this graph is taken in 13,000 MOT throws which is equivalent to less than 3 hours of pure measurement time.

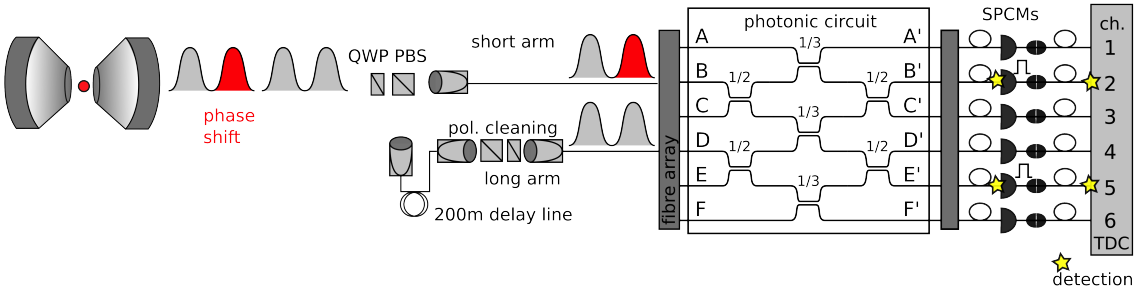

Figure 5.29: Potential experimental setup of measuring the CNOT operation with two time-binned photons: Two qubits are produced from the atom-cavity system alternatingly with and without a phase shift between their time bins. They are coupled into the long and the short arm of the photon pistol which are connected to the input modes of the LOQC circuit. We use input combinations that we also use in Sec. 5.2 when testing the CNOT functionality on a CNOT4 circuit and monitor all six output modes.

tionality with twin-peak photons.

5.4.2 Different experimental possibilities

To demonstrate the CNOT functionality on a CNOT4 chip with to twin-peak photons, we re-use the same circuit as introduced in Sec. 5.2. To obtain the complete truth table, we send pairs of photons into the input modes (A, E), (A, D), (E, F) and (D, F) corresponding to the modes C_0T_0, C_0T_1, C_1T_0 and C_1T_1 in the standard CNOT notation.

The question is now how to prepare the qubits in our atom-cavity source. Clearly, the obvious way is to have two twin-peak photons subsequently emitted from the cavity, where one photon exhibits a pre-defined phase shift of ϕ between its time bins and the other one does not. A potential experimental setup to do so is depicted in Fig. (5.29). However this approach suffers from a substantial disadvantage. We set the phase we choose to measure once and we cannot switch to another one during one experimental run[16]. This

[16]We traditionally refer to 1,500 to 2,000 MOT throws as 'one' experimental run. This sums up to 15-25 minutes of measurement time.

means, long-term drifts in the whole system as for instance in the laser or cavity resonance frequency affect only one phase measurements and not another one that is taking place at a different time. This would lead to a systematic error affecting all data which we have to avoid. To circumvent this problem, we use an inherently different approach of imprinting the phase onto the photons.

In the following, the photons are *not* produced as a pair of photons consisting of a signal and a reference where the signal exhibits a phase shift between its time bins an the reference does not. Instead, there are solely 'signal' photons produced with pseudo-random phases imprinted between their two time bins. Each registered count in a detector is assigned to the imprinted phase *difference* it originated from. In this way, all measured phases are affected by long term drifts in the same way. This technique is discussed in the following Section.

5.4.3 Multiple phase differences in one go

To avoid any long-term drifts in our setup affecting measurements in a systematic way, we choose a novel way of imprinting the phases onto our twin-peak photons. In previous measurements, we have generated a pair of single photons of which one was the reference and one the signal photon exhibiting a phase shift. Now, each generated photon exhibits a randomly chosen phase shift ϕ_n between its two time bins. An outline of this principle and the experimental arrangement can be found in Fig. (5.30). We send two twin-peak photons into the input modes E and F corresponding to the input modes C_1 and T_0 in the standard CNOT notation and monitor all six output modes. Here, we restrict our discussion to this particular setting as sending single photons into the input modes (A, E) and (A, F) does

not provide any further insight into the physics of this experiment and (D, F) mimics the result of the (E, F) case.

The phase shifts ϕ_1, ϕ_2... as for instance shown in Fig. (5.30) are generated in the following way: We choose how many equally spaced phase values between [0, 2π] we want to measure before each run. These values are pseudo-randomly distributed over an array of pre-defined length and saved in a 'lookup' table which is used to generate the RF-photon emission pulses that are imprinted on the STIRAP pump light with the help of an AOM. Hence, each of the photon trigger pulses has a pseudo-random phase imprinted on it. We monitor all six outputs of the circuit and at the same time register the *phase difference*[17] between the two twin-peak photons for each detected click in the SPCMs. In this way, we can evaluate quantum-homodyne-type data for the CNOT operation during post-processing.

Similar to the preliminary measurements in Sec. 5.1.3, Fig. (5.6), we evaluate the data for correlation events between the same as well as different time bins. However, we do not present the data in form of the well-known truth table but as a histogram as a function of $\Delta\phi$. For sending photon pairs into input modes E and F, we choose to imprint various phase differences between [0, 2π] with a step size of π/4

$$\begin{aligned} \Delta\phi \quad \in \quad & \{-2\pi, -7\pi/4, -3\pi/2, -5\pi/4, -\pi, -3\pi/4, -\pi/2, -\pi/4, 0, \\ & \pi/4, \pi/2, 3\pi/4, \pi, 5\pi/4, 3\pi/2, 7\pi/4, 2\pi\} \end{aligned} \tag{5.90}$$

between the time bins of our twin-peak photons. In Fig. (5.31), we present the theoret-

[17] As we are well aware which phase belongs to which pulse number of the photon emission trigger.

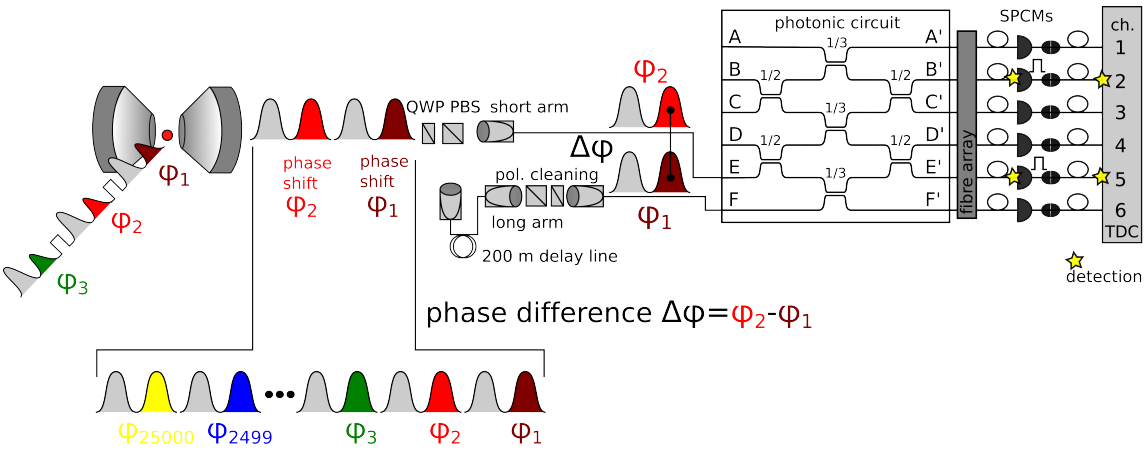

Figure 5.30: Experimental setup of measuring the CNOT operation with two time-binned photons: Two qubits are produced from the atom-cavity system with a pseudo random phase shift between their respective two time bins. A pair of twin-peak photons is coupled into the respective input modes of the CNOT4 circuit. We use input combinations that we also use in Sec. 5.2 when testing the CNOT functionality on a CNOT4 circuit and monitor all six output modes. In addition to the information that is traditionally registered, we also record the phase difference $\Delta\phi$ between the two photons. This gives us the possibility of comparing all measured phase data because slow systematic drifts of the setup do affect all phase settings equally.

ical as well as measured coincidence probability between output modes D' and F'. For detections within the same time bin, the imprinted phase difference is not relevant and the CNOT functionality behaves as expected. However, when we evaluate the data with respect to correlation events between different time bins we observe a sinusoidal behaviour of the coincidence probability in outputs (D', F') as shown in Fig. (5.31, blue trace) with a maximum at $\Delta\phi = \pi$.

The reason why our data does not perfectly match the theory curve is mainly due to the limited coherence time of our photons. This limitation is caused by the laser system used in our experiment and the drift of the cavity's resonance frequency. We remind ourselves that the cavity is not actively locked when the photon generation process takes place. Additionally, changes in the magnetic environment in the laboratory also reduce the coherence time of our photons. This is beyond our control.

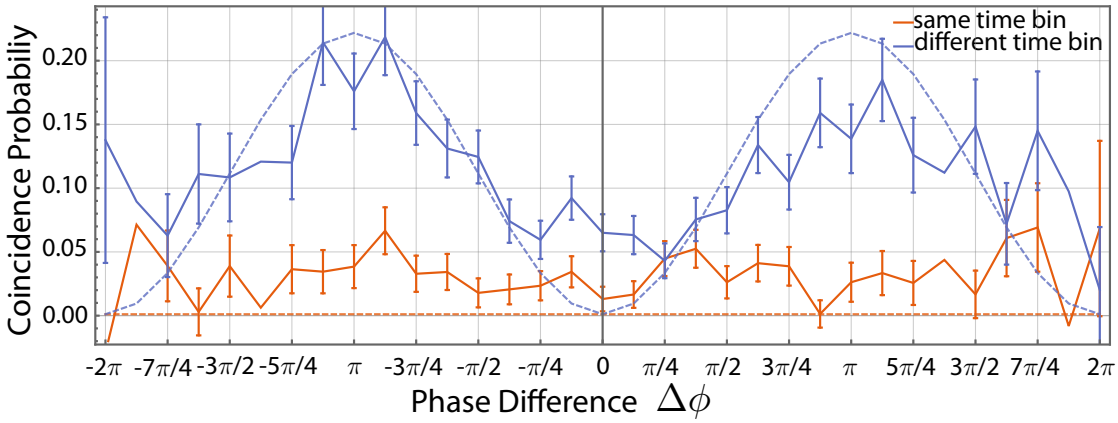

Figure 5.31: Measured data for the input of a twin-peak photon pair exhibiting various of phase differences $\Delta\phi$: We choose the input modes (E, F) of our CNOT4 circuit and monitor all six output modes. The data displayed is the evaluation of the data for correlation events between output modes D' and F'. The yellow data shows the evaluation for detections in the same time bin whereas the blue data shows detections in different time bins. In the case of a phase difference of π we expect twice the correlation events as in the same time-bin case for counting correlations between output modes (E', F').

5.4.4 Potential interpretation and outlook

There are two reasons why we carry out these type of experiments – an esoteric and a technical one. The esoteric one is that we can make our photons behave like bosons and fermions at the same time [83], depending on the time bins we use to correlate events. Having quantum feedback experiments in mind, the combination of complex integrated circuits with time-bin encoding on several hundred nanoseconds long photons opens the way to a new class of experiments, exploring conditional quantum interference such as switching between symmetric and antisymmetric entangled states in large interferometer circuits. This is further discussed in the outlook.

The technical reason is to study how the CNOT performance in function of the phase is affected by de-phasing processes. So we can comparatively as well as systematically study the de- and re-phasing of quantum states as well as the the effects of time-varying

internal phases on the fidelity and errors of photonic quantum circuits. This is subject to further investigation[18].

[18]The data presented in this Section is not yet published.

Chapter 6

Conclusion and outlook

Wir stehen selbst enttäuscht und sehn betroffen den Vorhang zu und alle Fragen offen. [Brecht]

The main focus of this DPhil thesis[1] was both to gain insight into a very intriguing deterministic single photon source and its application in modern quantum technology experiments.

Regarding our first set of experiments, we have seen that we can prepare and on-demand deliver single photons in arbitrary quantum superpositions of various temporal modes [65, 66]. We have made use of the spatio-temporal sub-division into time bins to reliably encode a selection of various quantum bits of information into single photons. Photon-generation efficiencies of up to $\eta = 85\%$ and state-preparation fidelities

[1]The actual work carried out in the past four years was to obtain a stable photon pistol experiment which could operate for several hours/days/months in a row without any failure of e.g. a laser diode, AOM electronics etc. It worked.

of F = 94% in the qutrit case have been found by quantum homodyning [65, 66]. We have demonstrated that time-bin encoding takes place upon photon generation which is inherently non-probabilistic, versatile, reconfigurable and not subject to systematic photon losses. There are substantial advantages of our scheme compared to approaches that are probabilistic. These probabilistic approaches can be for instance based on spontaneous parametric down conversion and are subject to intrinsic photon loss if they rely on variable amplitude attenuation [91], phase modulation [92] or interferometric techniques for photon shaping [69]. The availability of time bins as an additional degree of freedom in an essentially deterministic photon-generation scheme is a big step towards large-scale quantum computing in photonic networks [93].

The slow ('adiabatic') photon generation process, coupled with small photonic circuits and fast detectors, also allows for real-time feedback during the production of single photons. As an outlook, the quantum feedback experiment as well as very preliminary data has been presented. The latest results can be found in Oliver Barter's thesis as it is beyond the scope of this project.

In a second set of experiments, our single photon source has been used to seed a variety of chip-integrated quantum logic gates. This work has been carried out in a collaboration with the Jeremy O'Brien group in Bristol. We have shown the reliable operation of two-qubit linear optical quantum gates and generated photon-photon entanglement applied to photons emitted from a single atom strongly coupled to a cavity, the latter with a quantum state fidelity of $F \geq 82\%$ [84]. We strongly believe that this approach paves the way to quantum technology that utilises both narrowband single-photon sources and integrated quantum photonics, such as networked quantum computing, narrow linewidth quantum

enhanced sensing and atomic memories.

However, there is still a lot to do. To improve the overall efficiency of the hybrid source-chip system, deterministic loading of atoms into cavities necessary to increase the capability of this system to larger photon numbers. To do so, one could think of an intra-cavity dipole trap [61, 94, 95] and/or optical tweezers to put one single atom between the mirrors of a high-finesse optical cavity. One could even go one step further and not use conventional high-finesse optical but fibre-tip cavities. The advantage in this case is that the two fibre tips can be brought close together, yielding a much smaller mode volume as standard cavities. Hence, the atom-cavity coupling strength can be boosted by an order of magnitude [37].

Moreover, another potential research area besides the LOQC experiments could be to fabricate a second cavity[2] and transfer information between two distant atoms. The idea has been introduced by Kimble as the *quantum internet* [96]. Quantum bits of information are generated, processed and stored in quantum nodes which are linked by quantum channels to transfer quantum information from point to point inside a quantum system. Exporting this scenario to our experiment, the atoms in the cavities represent *nodes* which can also be referred to as stationary qubits. Flying qubits imprinted into single photons are emitted from one atom and can be re-absorbed by the second atom in a cavity, as it has been theoretically shown in [97]. A similar experiment has been already carried out at the MPQ in Munich [98].

[2]This project is also underway, please refer to my colleague Thomas Barrett's transfer report.

Chapter 7

Appendix: Detection of non-classical CV light

Measurements in continuous variable (CV) quantum optics experiments mainly deal with quantum noise detection [99]. In an experiment, it is impossible to measure noise properties at all frequencies. Therefore, what one does is measuring at a given frequency Ω with a bandwidth of $\delta\Omega$. However, Ω can not be the optical carrier frequency $\omega = 2\pi c/\lambda$ due to the fact that ω oscillates too fast to be measured. The solution is to measure at the optical sidebands, at $\omega \pm \Omega$. The measured mode can be described by the following relation

$$\hat{a}(t) \propto \alpha e^{i\omega t} + \delta\hat{a}_{-\Omega} e^{i(\omega-\Omega)t} + \delta\hat{a}_{+\Omega} e^{i(\omega+\Omega)t}, \tag{7.1}$$

where the time-dependent annihilation operator is used in a linear form and where $\pm\Omega$ indicates the distance from the carrier frequency ω. As the noise properties of the sidebands are of interest in order to carry out quantum optics experiments, it has to be stated that the photons in the sidebands are carrying all the information. Consequently, a single mea-

surement is quantum mechanically speaking a projection onto the photon number operator $\hat{n}(t) = \hat{a}^\dagger \hat{a}$. If one inserts Eq. (7.1) into the expression for $\hat{n}(t)$, one can approximate

$$\begin{aligned}
\hat{n}(t) &= |\alpha|^2 + \alpha(\delta\hat{a}_{-\Omega} e^{-i\Omega t} + \delta\hat{a}_{+\Omega} e^{i\Omega t} + \mathcal{O} + \delta\hat{a}_{-\Omega} e^{i\Omega t} + \delta\hat{a}^\dagger_{+\Omega} e^{-i\Omega t} + \mathcal{O}) = \\
&\approx |\alpha|^2 + \alpha \Big(\cos\Omega t(\delta\hat{a}_{-\Omega} + \delta\hat{a}_{+\Omega} + \delta\hat{a}^\dagger_{-\Omega} + \delta\hat{a}^\dagger_{+\Omega}) \\
&\quad + i \sin\Omega t(-\delta\hat{a}_{-\Omega} + \delta\hat{a}_{+\Omega} + \delta\hat{a}^\dagger_{-\Omega} - \delta\hat{a}^\dagger_{+\Omega}) \Big) = \\
&= |\alpha|^2 + \alpha \Big((\delta\hat{X}_{+\Omega} + \delta\hat{X}_{-\Omega}) \cos\Omega t + (\delta\hat{Y}_{+\Omega} - \delta\hat{Y}_{-\Omega}) \sin\Omega t \Big) \\
&= \underbrace{|\alpha|^2}_{\text{intensity } \langle \hat{n}(t) \rangle} + \underbrace{\alpha\delta\hat{X}'}_{\text{intensity fluctuations } \delta\hat{n}} ,
\end{aligned} \tag{7.2}$$

which is the square of the "classical" amplitude and equivalent to the intensity and the fluctuations of the intensity. In this Equation, we have used the definition of a quantum quadrature operators

$$\hat{X} = \hat{a}^\dagger + \hat{a}, \qquad \text{as well as} \qquad \hat{Y} = i(\hat{a}^\dagger - \hat{a}), \tag{7.3}$$

and the Euler equation

$$e^{i\phi} = \cos\phi + i \sin\phi. \tag{7.4}$$

There are two different ways of detecting CV non-classical light: The direct and the ho-

modyne measurement techniques.

7.1 Direct and balanced direct detection

For the *direct* detection, a simple setup in which the beam is impinging on a single photodetector is used. The photodetector acts as a converter of an optical beam into an electric signal via the photoelectric effect. If the energy of the photons $E = \hbar\omega$ is higher than a certain threshold, they emit electrons out of the material they interact with. This means the number of photons is transformed into an electrical current $i(t)$ [100], where

$$i(t) = e\eta\frac{P(t)}{\hbar\omega}. \tag{7.5}$$

$P(t)$ is the optical power of the incident beam, $\hbar\omega$ the energy of one photon with the wavelength ω, therefore the fraction $\frac{P(t)}{\hbar\omega}$ indicates the number of photons per time unit. η refers to the quantum efficiency of the diode and e is the electron charge. Although the electrical signal $i(t)$ is totally classical, it does contain the quantum statistics of the incident field which are necessary to determine the quantum noise properties $\delta\hat{n}(t)$. In reality, the quantum efficiency is always $\eta < 1$ due to imperfections in the system and therefore the photocurrent does not contain full information about the state of light. However, η will be regarded as 1 in the following for the sake of simplicity.

In principle, the noise of quantum states is characterised by its optical noise spectrum, which can be measured with the help of an electronic spectrum analyser (ESA) which is illustrated in Fig. (7.1). This instrument measures the spectral power density $S(\Omega, B)$ of a stochastic variable $\delta x(t)$ with the bandwidth B within a frequency $\Omega \pm \frac{1}{2}B$, which means

the power at a certain spectral component of the optical beam. The electronic spectral noise density is proportional to the spectral power density within a given optical sideband [101]

$$\begin{aligned} S(\Omega, B) &\propto Var_{\Omega\pm\frac{1}{2}B}(i(t)) \propto Var_{\Omega\pm\frac{1}{2}B}(\hat{n}(t)) \\ &\propto Var_{\Omega\pm\frac{1}{2}B}(\delta\hat{n}(t)) = \alpha^2(t)_{\Omega\pm\frac{1}{2}B} Var_{\Omega\pm\frac{1}{2}B}(\delta\hat{X}'(t)). \end{aligned} \tag{7.6}$$

From this, it can be seen that the spectral density $S(\Omega, B)$ is equivalent to a time domain measurement of noise variance photocurrent.

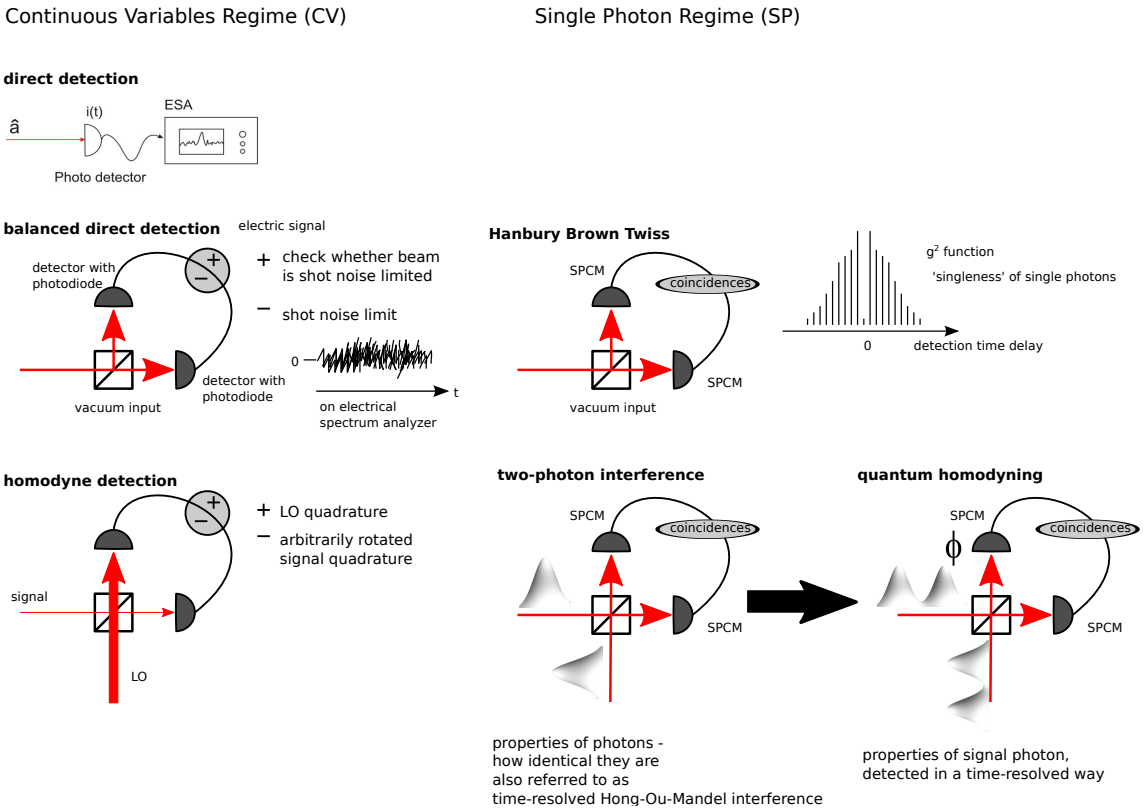

Figure 7.1: In this picture, the standard CV and SP measurement techniques are compared.

An extension to this straight-forward direct detection scheme is the so-called *balanced* direct detection which is depicted in Fig. (7.1). In this case, it is possible to obtain the noise of a coherent vacuum state in order to compare it to the noise of the measured beam. The incoming beam is sent on a 50:50 beamsplitter which is characterised by the transmission rate T = 1/2 and the reflected rate R = 1/2. Due to conservation reasons, T and R sum up to $T + R = 1$. The output beams then read

$$\hat{c} = \sqrt{T}\hat{a} + \sqrt{R}\hat{b}, \qquad \hat{d} = \sqrt{R}\hat{a} - \sqrt{T}\hat{b}, \tag{7.7}$$

where $\hat{c}$ is impinging on one of two balanced photo diodes and $\hat{d}$ on the other one. The AC signal of both detectors can be added or subtracted. Due to the fact that the incoming light beam is split equally on the 50:50 BS both beams $\hat{c}$ and $\hat{d}$ have the same noise in both detector signals. If one takes the "-" operation on both signals, the result is supposedly zero. However, the "-" signal is not zero since the incoming beam interferes on the beam splitter with the vacuum state in the second input port. Consequently, the vacuum input is $\hat{b} = \delta\hat{b}$. The photon numbers in the output ports of the beam splitter are

$$\hat{n}_1 = \hat{c}^\dagger\hat{c} = \frac{1}{2}(\alpha^2 + \alpha\delta\hat{n}_1), \qquad \hat{n}_2 = \hat{d}^\dagger\hat{d} = \frac{1}{2}(\alpha^2 + \alpha\delta\hat{n}_2), \tag{7.8}$$

where the annihilation operator $\hat{a}$ has been used in the approximation of a bright beam $\hat{a} = \alpha + \delta\hat{a}$.

Therefore, the sum signal can be calculated as

$$\delta\hat{n}_1 + \delta\hat{n}_2 = \alpha\delta\hat{X}_{\mathrm{a}}, \tag{7.9}$$

and the difference signal is

$$\delta\hat{n}_1 - \delta\hat{n}_2 = \alpha\delta\hat{X}_{\mathrm{vac}}. \tag{7.10}$$

From Eq. (7.9) and (7.10) it is clear that the sum and difference signal describe the input beam with respect to a coherent beam with the same field amplitude. The advantage of this balanced direct detection is the fact that one can measure the "+" and "-" operation between both detector signals at the same time and therefore determine the standard quantum limit or shot noise level of a beam. However, the downside of this detection is that one can only measure in the amplitude quadrature direction. In terms of amplitude squeezed light this scheme is suitable but in terms of quadrature squeezed states a more advanced setup is needed. One possibility is the *homodyne* detection.

7.2 Homodyne detection

The homodyne detection setup is in principle the same as the balanced direct detection in which the vacuum input port $\hat{b}$ has been replaced by a bright beam of the same frequency as the input beam $\hat{a}$. This second input beam is much brighter than the first one $|\alpha_{\mathrm{b}}| >> |\alpha_{\mathrm{a}}|$ and is called local oscillator (LO). Consequently, the interference of a signal and a LO on the beam splitter is exploited. As an arbitrary phase shift between signal and LO can be

introduced, $\hat{b}$ can be written

$$\hat{b} = \alpha_{\mathrm{b}} + \delta\hat{b}e^{i\theta}. \tag{7.11}$$

The sum and difference photon number fluctuations are

$$\delta\hat{n}_1 + \delta\hat{n}_2 = \alpha_{\mathrm{b}}\delta\hat{X}_{\mathrm{b}}, \qquad \delta\hat{n}_1 - \delta\hat{n}_2 = \alpha_{\mathrm{a}}\delta\hat{X}_{\mathrm{a}}(\theta), \tag{7.12}$$

therefore one sees that the quadrature $\delta\hat{X}(\theta)$ at any angle θ of the signal beam is measurable. This feature of homodyne detections makes it inevitable in experiments dealing with the measurement of non-classical CV beams.

Bibliography

[1] R. Feynman. Simulating physics with computers. *Int. J. Theor. Phys.*, 21(6/7):467–488, 1982.

[2] D. Deutsch. Quantum theory, the Church-Turing principle and the universal quantum computer. *Proc. R. Soc. Lond. A*, 400:97–117, 1985.

[3] M. A. Nielsen and I. L. Chuang. *Quantum Computation and Information*. Cambridge University Press, 2000.

[4] G. Leuchs and T. Beth. *Quantum Information Processing*. Wiley-VCH Verlag, 2005.

[5] D. P. DiVincenzo. The physical implementation of quantum computation. *Fortschr. Phys.*, 48:771, 2000.

[6] C. Kurtsiefer, S. Mayer, P. Zarda, and H. Weinfurter. Stable solid-state source of single photons. *Phys. Rev. Lett.*, 85:290–293, 2000.

[7] M. Förtsch, J. U. Fürst, C. Wittmann, D. Strekalov, A. Aiello, M. V. Chekhova, C. Silberhorn, G. Leuchs, and C. Marquardt. A versatile source of single photons for quantum information processing. *Nat Commun*, 4:133602, 2013.

[8] A. Kuhn, M. Hennrich, and G. Rempe. Deterministic single-photon source for distributed quantum networking. *Phys. Rev. Lett.*, 89:067901, 2002.

[9] C. Kurtsiefer, P. Zarda, M. Halder, H. Weinfurter, P. M. Gorman, P. R. Tapster, and J. G. Rarity. A step towards global key distribution. *Nature*, 419:450, 2002.

[10] C. Gobby, Z. L. Yuan, and A. J. Shields. Quantum key distribution over 122 km of standard telecom fiber. *Appl. Phys. Lett.*, 84(19):3762, 2004.

[11] R. Braunstein. Nonlinear optical effects. *Phys. Rev.*, 125:475–477, 1962.

[12] P. A. Franken, A. E. Hill, C. W. Peters, and G. Weinreich. Generation of optical harmonics. *Phys. Rev. Lett.*, 7:118–119, 1961.

[13] E. Knill, R. Laflamme, and G. J. Milburn. A scheme for efficient quantum computing with linear optics. *Nature*, 409:46–52, 2001.

[14] T. B. Pittman, B. C. Jacobs, and J. D. Franson. Demonstration of nondeterministic quantum logic operations using linear optical elements. *Phys. Rev. Lett.*, 88:257902, 2002.

[15] J. L. O'Brien, G. J. Pryde, A. G. White, T. C. Ralph, and D. Branning. Demonstration of an all-optical quantum controlled-NOT gate. *Nature*, 426:264–267, 2003.

[16] J. C. F. Matthews, A. Politi, A. Stefanov, and J. L. O'Brien. Manipulation of multiphoton entanglement in waveguide quantum circuits. *Nat. Photon.*, 3:346, 2009.

[17] T. C. Ralph, N. K. Langford, T. B. Bell, and A. G. White. Linear optical controlled-not gate in the coincidence basis. *Phys. Rev. A*, 65:062324, 2002.

[18] C. Cohen-Tannoudji, J. Dupont-Roc, and G. Grynberg. *Photons and Atoms: Introduction to Quantum Electrodynamics*. Wiley-Interscience, 1997.

[19] M. D. Eisaman, J. Fan, A. Migdall, and S. V. Polyakov. Invited review article: Single-photon sources and detectors. *Rev. Sci. Instrum.*, 82:071101, 2011.

[20] R. Alleaume, F. Treussart, G. Messin, Y. Dumeige, J.-F. Roch, A. Beveratos, R. Brouri-Tualle, J.-P. Poizat, and P. Grangier. Experimental open-air quantum key distribution with a single-photon source. *New J. Phys.*, 6(1):92, 2004.

[21] T. Gaebel, I. Popa, A. Gruber, M. Domhan, F. Jelezko, and J. Wrachtrup. Stable single-photon source in the near infrared. *New J. Phys.*, 6(1):98, 2004.

[22] A. J. Shields. Semiconductor quantum light sources. *Nat Photon*, 1:215, 2007.

[23] S. Strauf, N. G. Stoltz, M. T. Rakher, L. A. Coldren, P. M. Petroff, and D. Bouwmeester. High-frequency single-photon source with polarization control. *Nat Photon*, 1:704, 2007.

[24] M. Hennrich, T. Legero, A. Kuhn, and G. Rempe. Photon statistics of a non-stationary periodically driven single-photon source. *New J. Phys.*, 6:86, 2004.

[25] C. Maurer, C. Becher, C. Russo, J. Eschner, and R. Blatt. A single-photon source based on a single Ca+ ion. *New J. Phys.*, 6:94, 2004.

[26] M. Steiner, A. Hartschuh, R. Korlacki, and A. J. Meixner. Highly efficient, tunable single photon source based on single molecules. *Appl. Phys. Lett.*, 90(18):183122, 2007.

[27] S. Chen, Y. Chen, T. Strassel, Z. Yuan, B. Zhao, J. Schmiedmayer, and J. Pan. Deterministic and storable single-photon source based on a quantum memory. *Phys. Rev. Lett.*, 97:173004, 2006.

[28] E. Waks, E. Diamanti, and Y. Yamamoto. Generation of photon number states. *New J. Phys.*, 8(1):4, 2006.

[29] A. Soujaeff, T. Nishioka, T. Hasegawa, S. Takeuchi, T. Tsurumaru, K. Sasaki, and M. Matsui. Quantum key distribution at 1550 nm using a pulse heraldedsingle photon source. *Opt. Express*, 15(2):726–734, 2007.

[30] A. B. U'Ren, C. Silberhorn, K. Banaszek, and I. A. Walmsley. Efficient conditional preparation of high-fidelity single photon states for fiber-optic quantum networks. *Phys. Rev. Lett.*, 93:093601, 2004.

[31] J. Fan and A. Migdall. A broadband high spectral brightness fiber-based two-photon source. *Opt. Express*, 15(6):2915–2920, 2007.

[32] E. A. Goldschmidt, M. D. Eisaman, J. Fan, S. V. Polyakov, and A. Migdall. Spectrally bright and broad fiber-based heralded single-photon source. *Phys. Rev. A*, 78:013844, 2008.

[33] J. B. Spring, P. S. Salter, B. J. Metcalf, P. C. Humphreys, M. Moore, N. Thomas-Peter, M. Barbieri, X.-M. Jin, N. K. Langford, S. Kolthammer, M. J. Booth, and I. A. Walmsley. On-chip low loss heralded source of pure single photons. *Opt. Express*, 21(11):13522–13532, 2013.

[34] A. Kuhn, M. Hennrich, T. Bondo, and G. Rempe. Controlled generation of single photons from a strongly coupled atom-cavity system. *Appl. Phys. B*, 69:373–377, 1999.

[35] M. Hennrich, T. Legero, A. Kuhn, and G. Rempe. Vacuum-stimulated Raman scattering based on adiabatic passage in a high-finesse optical cavity. *Phys. Rev. Lett.*, 85:4872–4875, 2000.

[36] A. Kuhn and D. Ljunggren. Cavity-based single-photon sources. *Contemp. Phys.*, 51:289–313, 2010.

[37] A. Predojević and M.W. Mitchell. *Engineering the Atom-Photon Interaction: Controlling Fundamental Processes with Photons, Atoms and Solids*. Nano-Optics and Nanophotonics. Springer International Publishing, 2015.

[38] E. M. Purcell. Spontaneous emission probabilities at radio frequencies. *Phys. Rev.*, 69:681, 1946.

[39] H. J. Carmichael. Photon antibunching and squeezing for a single atom in a resonant cavity. *Phys. Rev. Lett.*, 55:2790–2793, 1985.

[40] F. De Martini, M. Marrocco, and D. Murra. Transverse quantum correlations in the active microscopic cavity. *Phys. Rev. Lett.*, 65:1853–1856, 1990.

[41] E. T. Jaynes and F. W. Cummings. Comparison of quantum and semiclassical radiation theories with application to the beam maser. *Proc. IEEE*, 51:89–109, 1963.

[42] M. Fox. *Quantum Optics*. Oxford University Press, 2006.

[43] A. Messiah. *Quantum Mechanics*. J. Wiley & Sons, NY, 1958.

[44] G. Rempe, R. J. Thompson, R. J. Brecha, W. D. Lee, and H. J. Kimble. Optical bistability and photon statistics in cavity quantum electrodynamics. *Phys. Rev. Lett.*, 67:1727–1730, 1991.

[45] G. S. Vasilev, D. Ljunggren, and A. Kuhn. Single photons made-to-measure. *New J. Phys.*, 12:063024, 2010.

[46] C. J. Foot. *Atomic Physics*. Oxford University Press, 2005.

[47] E. Raab, M. Prentiss, A. Cable, S. Chu, and D. E. Pritchard. Trapping of neutral sodium atoms with radiation pressure. *Phys. Rev. Lett.*, 59:2631, 1987.

[48] P. D. Lett, W. D. Phillips, S. L. Rolston, C. E. Tanner, R. N. Watts, and C. I. Westbrook. Optical molasses. *J. Opt. Soc. Am. B*, 6(11):2084–2107, 1989.

[49] D. A. Steck. Rubidium-87 d line data.

[50] D. W. Preston. Dopplerfree saturated absorption: Laser spectroscopy. *American Journal of Physics*, 64(11):1432–1436, 1996.

[51] E. D. Black. An introduction to Pound-Drever-Hall laser frequency stabilization. *American Journal of Physics*, 69:79–87, 2001.

[52] P. Nisbet-Jones. Shaping single photons. *D. Phil. Thesis, Oxford*, 2012.

[53] J. Dilley. A single photon source for quantum networking. *D. Phil. Thesis, Oxford*, 2012.

[54] J. McKeever, J. R. Buck, A. D. Boozer, and H. J. Kimble. Determination of the number of atoms trapped in an optical cavity. *Phys. Rev. Lett.*, 93:143601, 2004.

[55] M. Khudaverdyan, W. Alt, I. Dotsenko, T. Kampschulte, K. Lenhard, A. Rauschenbeutel, S. Reick, K. Schörner, A. Widera, and D. Meschede. Controlled insertion and retrieval of atoms coupled to a high-finesse optical resonator. *New J. Phys.*, 10(7):073023, 2008.

[56] Noliac A/S. Linearity CSA.

[57] R. W. Fox, C. W. Oates, and L. W. Hollberg. Chapter 1 – Stabilizing diode lasers to high-finesse cavities. *Experimental Methods in the Physical Sciences: Cavity-Enhanced Spectroscopies*, 40, 2003.

[58] M. Meucci, E. Mariotti, P. Bicchi, C. Marinelli, and L. Moi. Light-induced atom desorption. *Europhys. Lett.*, 25(9):639, 1994.

[59] C. Klempt, T. van Zoest, T. Henninger, O. Topic, E. Rasel, W. Ertmer, and J. Arlt. Ultraviolet light-induced atom desorption for large rubidium and potassium magneto-optical traps. *Phys. Rev. A*, 73:013410, 2006.

[60] P. B. R. Nisbet-Jones, J. Dilley, D. Ljunggren, and A. Kuhn. Highly efficient source for indistinguishable single photons of controlled shape. *New J. Phys.*, 13:103036, 2011.

[61] T. Puppe, I. Schuster, A. Grothe, A. Kubanek, K. Murr, P. W. H. Pinkse, and G. Rempe. Trapping and observing single atoms in a blue-detuned intracavity dipole trap. *Phys. Rev. Lett.*, 99:013002, 2007.

[62] T. C. Ralph, A. G. Witte, W. J. Munro, and G. J. Milburn. Simple scheme for efficient linear optics quantum gates. *Phys. Rev. A*, 65:012314, 2001.

[63] P. Kok, W. J. Munro, K. Nemoto, T. C. Ralph, J. P. Dowling, and G. J. Milburn. Linear optical quantum computing with photonic qubits. *Rev. Mod. Phys.*, 79(1):135–174, 2007.

[64] J. L. O'Brien. Optical quantum computing. *Science*, 318:1567, 2007.

[65] P. B. R. Nisbet-Jones, J. Dilley, A. Holleczek, O. Barter, and A. Kuhn. Photonic qubits, qutrits and ququads accurately prepared and delivered on demand. *New J. Phys.*, 15:053007, 2013.

[66] A. Holleczek, O. Barter, G. Langfahl-Klabes, and A. Kuhn. Qubits, qutrits, and ququads stored in single photons from an atom-cavity system. *Proc. SPIE*, 9377:937709–937709–6, 2015.

[67] J. D. Franson. Bell inequality for position and time. *Phys. Rev. Lett.*, 62:2205–2208, 1989.

[68] J. Brendel, N. Gisin, W. Tittel, and H. Zbinden. Pulsed energy-time entangled twin-photon source for quantum communication. *Phys. Rev. Lett.*, 82:2594–2597, 1999.

[69] I. Marcikic, H. de Riedmatten, W. Tittel, V. Scarani, H. Zbinden, and N. Gisin. Time-bin entangled qubits for quantum communication created by femtosecond pulses. *Phys. Rev. A*, 66:062308, 2002.

[70] M. Hennrich. Kontrollierte Erzeugung einzelner Photonen in einem optischen Resonator hoher Finesse. *PhD Thesis. Technische Universität München, Max Planck Institut für Quantenoptik*, 2003.

[71] T. B. Pittman, B. C. Jacobs, and J. D. Franson. Demonstration of non-deterministic quantum logic operations using linear optical elements. *Phys. Rev. Lett.*, 88:257902, 2002.

[72] W. Wasilewski, P. Kolenderski, and R. Frankowski. Spectral density matrix of a single photon measured. *Phys. Rev. Lett.*, 99:123601, 2007.

[73] C. K. Hong, Z. Y. Ou, and L. Mandel. Measurement of subpicosecond time intervals between two photons by interference. *Phys. Rev. Lett.*, 59:2044–2046, 1987.

[74] H. P. Yuen and V. W. S. Chan. Noise in homodyne and heterodyne detection. *Opt. Lett.*, 8(3):177–179, 1983.

[75] T. Legero, T. Wilk, A. Kuhn, and G. Rempe. Time-resolved two-photon quantum interference. *Appl. Phys. B*, 77:797–802, 2003.

[76] T. Legero, T. Wilk, M. Hennrich, G. Rempe, and A. Kuhn. Quantum beat of two single photons. *Phys. Rev. Lett.*, 93:070503, 2004.

[77] T. Legero, T. Wilk, A. Kuhn, and G. Rempe. Characterization of single photons using two-photon interference. *Adv. At. Mol. Opt. Phys.*, 53:253, 2006.

[78] E. Knill, R. Laflamme, and G. Milburn. Thresholds for Linear Optics Quantum Computation. *ArXiv:quant-ph/0006120v1*, 2000.

[79] H. F. Hofmann and S. Takeuchi. Quantum phase gate for photonic qubits using only beam splitters and postselection. *Phys. Rev. A*, 66:024308, 2002.

[80] A. Politi, M. J. Cryan, J. G. Rarity, S. Yu, and J. L. O'Brien. Silica-on-silicon waveguide quantum circuits. *Science*, 320(5876):646–649, 2008.

[81] M. A. Pooley, D. J. P. Ellis, R. B. Patel, A. J. Bennett, K. H. A. Chan, I. Farrer, D. A. Ritchie, and A. J. Shields. Controlled-not gate operating with single photons. *Appl. Phys. Lett.*, 100(21):211103, 2012.

[82] A. Politi, J. C. F. Matthews, M. G. Thompson, and J. L. O'Brien. Integrated quantum photonics. *Selected Topics in Quantum Electronics, IEEE Journal of*, 15(6):1673–1684, 2009.

[83] J. C. F. Matthews, K. Poulios, J. D. A. Meinecke, A. Politi, A. Peruzzo, N. Ismail, K. Wörhoff, M. G. Thompson, and J. L. O'Brien. Observing fermionic statistics with photons in arbitrary processes. *Scientific Reports*, 3:1539, 2013.

[84] A. Holleczek, O. Barter, A. Rubenok, J. Dilley, P. B. R. Nisbet-Jones, G. Langfahl-Klabes, G. D. Marshall, C. Sparrow, J. L. O'Brien, K. Poulios, A. Kuhn, and J. C. F. Matthews. Photonic Quantum Logic with Narrowband Light from Single Atoms. *arXiv:1508.03266v1*, 2015.

[85] P. J. Shadbolt, M. R. Verde, A. Peruzzo, A. Politi, A. Laing, M. Lobino, J. C. F. Matthews, M. G. Thompson, and J. L. O'Brien. Generating, manipulating and measuring entanglement and mixture with a reconfigurable photonic circuit. *Nat. Photonics*, 6:45, 2008.

[86] R. Hanbury Brown and R. Q. Twiss. A test of a new type of stellar interferometer on sirius. *Nature*, 178:1046, 1956.

[87] B. Schumacher. Quantum coding. *Phys. Rev. A*, 51:2738–2747, 1995.

[88] K. M. R. Audenaert and M. B. Plenio. When are correlations quantum? verification and quantification of entanglement by simple measurements. *New J. Phys.*, 8(11):266, 2006.

[89] H. Wunderlich and M. B. Plenio. Quantitative verification of entanglement and fidelities from incomplete measurement data. *J. Mod. Opt.*, 56(18-19):2100–2105, 2009.

[90] B. M. Terhal and P. Horodecki. Schmidt number for density matrices. *Phys. Rev. A*, 61:040301, 2000.

[91] P. Kolchin, C. Belthangady, S. Du, G. Y. Yin, and S. E. Harris. Electro-optic modulation of single photons. *Phys. Rev. Lett.*, 101(10):103601, 2008.

[92] H. P. Specht, J. Bochmann, M. Mücke, B. Weber, E. Figueroa, D. L. Moehring, and G. Rempe. Phase shaping of single-photon wave packets. *Nat. Photonics*, 3:469–472, 2009.

[93] A. J. Bennett, D. G. Gevaux, Z. L. Yuan, A. J. Shields, P. Atkinson, and D. A. Ritchie. Experimental position-time entanglement with degenerate single photons. *Phys. Rev. A*, 77(2):023803, 2008.

[94] P. Maunz, T. Puppe, I. Schuster, N. Syassen, P. W. H. Pinkse, and G. Rempe. Cavity cooling of a single atom. *Nature*, 428:50–52, 2004.

[95] J. McKeever, J. R. Buck, A. D. Boozer, A. Kuzmich, H.-C. Nägerl, D. M. Stamper-Kurn, and H. J. Kimble. State-insensitive cooling and trapping of single atoms in an optical cavity. *Phys. Rev. Lett.*, 90:133602, 2003.

[96] H. J. Kimble. The quantum internet. *Nature*, 453:1023–1030, 2008.

[97] J. Dilley, P. Nisbet-Jones, B. W. Shore, and A. Kuhn. Single-photon absorption in coupled atom-cavity systems. *Phys. Rev. A*, 85:023834, 2012.

[98] S. Ritter, Ch. Noelleke, C. Hahn, A. Reiserer, A. Neuzner, M. Uphoff, E. Figueroa, J. Bochmann, and G. Rempe. An elementary quantum network of single atoms in optical cavities. *Nature*, 484:195–200, 2012.

[99] H.-A. Bachor and T. C. Ralph. *A guide to experiments in quantum optics*. Wiley-VCH Verlag, Weinheim.

[100] J. Heersink. Experimental characterization of nonclassical polarization states of intense light. *PhD Thesis. Institut für Optik, Information und Photonik der Universität Erlangen-Nürnberg, Max Planck Forschungsgruppe*, 2006.

[101] J. Milanovic. Generation of nonclassical polarization states of intense light using photonic crystal fibers. *PhD Thesis. Institut für Optik, Information und Photonik der Universität Erlangen-Nürnberg, Max Planck Institut für die Physik des Lichts*, 2012.

Verehrtes Publikum, los, such dir selbst den Schluss!
Es muss ein guter da sein, muss, muss, muss! [Brecht]

Im Sinne Brechts möchte ich zum Schluss meiner Arbeit einer Institution und mehreren Personen aus meinem akademischen und privaten Leben in Oxford danken

- zunächst dem Oxforder University College für das generöse funding, das ich erhalten habe – sogar inklusive einem vierten Jahr.
- meinem Betreuer Axel Kuhn, ohne dessen Vertrauensvorschuss und Unterstützung ich diese Arbeit nicht hätte anfertigen können.
- Costas Poulios, ohne den es unser cavity-LOQC Experiment weder gegeben, und ohne dessen Optimismus es dann, als es schließlich begonnen hatte, nicht so gut über die Bühne gegangen wäre.
- Gunnar Langfahl-Klabes, der mir in Labor das 'Laufen' beigebracht hat und ohne den ich nie erfahren hätte, dass man alle Schraubenschlüssel zum Laserreparieren auswendig kennen kann.
- Oliver Barter für seine Lebenszeit hinter dem Computer.
- Dustin Stuart dafür, dass man sich immer auf ihn verlassen konnte, sogar Sonntag Nachmittag.
- Graham Quelch, der immer ein offenes Ohr für meine kleineren und größeren Sorgen und Nöte hatte.

Natürlich und vor allem gilt mein größter Dank meiner Familie, meinen Eltern und meinem großen Bruder Thomas, ohne die ich es nicht geschafft hätte an einer Stelle in meinem Leben zu sein, diese Danksagung verfassen zu müssen.

Abschliessend gilt mein Dank Hrn. Dr. Müller – für sein Vertrauen, seine Vernunft und vermutlich am meisten für seine unabänderbaren Grundsätze[1].

[1] und natürlich auch für alle hart erarbeiteten Flugmeilen; das nächste Mal ist es eine MiG-29 Fulcrum. Versprochen.